Title
Nuclear Fallout Formation in Iron Rich Environments

Permalink
https://escholarship.org/uc/item/2bk101m8

Author
Genda, Timothy

Publication Date
2022

Nuclear Fallout Formation in Iron Rich Environments

by

Timothy Genda

A dissertation submitted in partial satisfaction of the

requirements for the degree of

Doctor of Philosophy

in

Nuclear Engineering

in the

Graduate Division

of the

University of California, Berkeley

Committee in charge:

Professor Peter Hosemann, Chair
Professor Michael Manga
Prof. Rebecca Abergel
Dr. Bethany Goldblum

Fall 2022

Nuclear Fallout Formation in Iron Rich Environments

Abstract

Nuclear Fallout Formation in Iron Rich Environments

by

Timothy Genda

Doctor of Philosophy in Nuclear Engineering

University of California, Berkeley

Professor Peter Hosemann, Chair

Above-ground nuclear explosions that interact with the surface of the earth entrain materials from the surrounding environment, influencing the resulting physical and chemical evolution of the fireball. These influences can effect how hazardous radionuclides fractionate and are dispersed in the environment as fallout particles, and can affect their final chemical phase and mobility. The interaction of iron with a nuclear explosion is of specific interest due to the potential for iron to act as a redox buffer and because of the likelihood of significant masses of metals to be present in urban environments. We investigated glassy fallout from a historic surface interacting nuclear explosion conducted on a steel tower and report the discovery of widespread and diverse iron-rich micro-structures preserved within the samples, including crystalline dendrites and micron-scale iron-rich spheres with liquid immiscibility textures. We assert these micro-structures (termed 'amoeboids') reflect local redox conditions and cooling rates and can inform interpretation of high temperature events, enabling new insights into fireball condensation physics and chemistry when metals from the local environment (i.e., structural steel) are vaporized or entrained. Amoeboids likely form as a result of decomposition of a single liquid and/or from the emulsification of two compositionally distinct liquids. Amoeboid compositional comparison to computational phase diagram calculations produced using the CALPHAD (CALculation of PHAse Diagrams) method and to silicate liquid immiscibility measurements in other systems suggest they reflect non-equilibrium processes, complicating efforts to make quantitative inferences on fireball conditions. A phase field method (PFM) model shows that the variety of amoeboid morphologies are consistent with a decomposition hypothesis. Principal component analysis (PCA) and multivariate curve resolution (MCR) approaches to spatially resolved compositional measurements of samples were used to estimate the compositions of four distinct precursors and relative contributions to complex melt mixing during formation. These results also suggest that amoeboids may form as a result of spontaneous emulsification between a relatively Fe-poor, well mixed melt (all four precursors) and late entry of one Fe-rich precursor. While radioactive Pu has traditionally been associated with FeCaMg-rich glass in nuclear fallout, MCR models coupled with nano-scale secondary ion mass spectrometry (NanoSIMS) and autoradiography data highlighted inconsistent relationships between these elements in this work. Limited NanoSIMS data on amoeboids and immiscibility textures show that Pu (< 20 ppm) is primarily associated with the relatively Fe-poor phase of amoeboids, which generally supports an emulsification hypothesis. In summary, this work outlines key processes that may be unique to Fe-rich fallout formation, including variations in the relationships of Fe concentrations to other elements of interest, liquid immiscibility, widespread iron oxide crystallization, and limited evidence of intermediate oxygen environments. These processes may offer constraints on fireball conditions as the thermodynamics and kinetics of silicate immiscibility is better understood, and influence the distribution of radionuclides in the environment following a nuclear explosion. These processes should be considered in future quantitative models of fallout formation and radiochemical fractionation.

Contents

List of Figures

List of Tables

Acknowledgments

Thank you to my committee for for providing valuable insight and advice during all phases of my time at Berkeley. In particular, thanks to my advisor Peter Hosemann for his guidance and being willing to be flexible with me and enable me the autonomy to work on the research I was interested in. Thanks to Bethany Goldblum for her invaluable efforts in the beginning of my program to get me situated in Berkeley, reviewing an editing manuscripts, and preparing me for my qualifying exams which made this process much easier. Thanks to Michael Manga and Rebecca Abergel for their advice during my exams and while trying to submit and publish my research. I also want to especially thank Kim Knight at Lawrence Livermore Laboratory who I worked the most closely with during all of my research. Her guidance for me in learning how to form good research questions and spending countless hours working through my dissertation and publications was fundamental to my completion of this dissertation. In addition, there are not many people working in the nuclear fallout field, so having someone with her expertise was critical for me to avoid going down too many rabbit holes. Thanks to those that helped me collect data for this work, including Jenny Matzel, Peter Weber, Zurong Dai, and Christy Ramon. Thanks also to Emily Moore for her expertise and work conducting CALPHAD simulations which were an essential part of this work. Thanks to all the aforementioned people as well as Enrica Balboni and Marc Fitzgerald for their valuable guidance and advice during the writing and editing process of my manuscripts and my thesis. Thank you to my colleagues I worked with in the Air Force prior to coming to Berkeley that helped stimulate in me a passion for this field. And finally, thanks to my friends, family, and fellow students who were an integral part of my PhD by offering emotional support and encouraging me to finish my PhD at Berkeley when I was very discouraged. It has been a truly wonderful experience for me and this work could not have been completed without everyone's help.

The author wrote this dissertation in support of requirements for the degree of Doctor of Philosophy in Nuclear Engineering at the University of California, Berkeley. The research is funded in part by the LLNL Lawrence Graduate Scholar Program, and is not a deliverable for any United States government agency. The views and opinions expressed are those of the author, and do not state or reflect those of the United States government or Lawrence Livermore National Security, LLC.

Chapter 1

Motivation and Background

1.1 Motivation

In an above-ground, near-surface nuclear explosion, energy is released that can be millions of times more powerful than the largest conventional explosion, vaporizing both the device and surrounding material and forming a fireball that rises and cools in a matter of seconds [33]. As the vapor condenses, additional proximate material may be entrained, creating fallout particles that are a mixture of environmental materials and condensed bomb vapor [1, 24]. An understanding of how the cooling rate and fireball chemistry fractionates radionuclides during this process is necessary for predictions of fallout distributions used in preparing for and responding to nuclear explosions [23, 62, 85, 13, 64, 57, 25, 84] and for models of radionuclide environmental transport [49, 41]. The extent to which variations in local environments may influence cooling and chemistry behavior in fireballs remains ill constrained.

Current fallout formation models are semi-empirical and based on observations from above-ground nuclear weapons testing and compositional analysis of fallout in the 1940s-1960s representing a limited range of environments [33, 1, 24, 23, 62, 85]. Such models assume a homogeneous, fully oxygenated fireball [23, 62, 85], and largely ignore differences in the local settings of the nuclear event. Recent efforts applying modern tools to re-investigate historic fallout [16, 8, 5, 70, 46, 94, 3] challenge many fallout formation assumptions with evidence of reduced conditions [8, 5, 70], heterogeneous vapors [46], and unexpected volatility behavior[94], motivating research into how and to what extent entrained materials may influence the fireball environment, affecting chemical speciation and partitioning during fallout formation. The interaction of iron with a nuclear explosion is of specific interest on account of the potential for iron to act as a mineral redox buffer [60] affecting the chemical behavior of condensing radioactive species [8] and because of the likely presence of masses of metals in the case of an explosion in an urban environment. This work focuses on studying fallout formed in relatively iron-rich conditions, focusing on understanding formation mechanisms that are unique to such environments.

1.2 Nuclear Explosions and Fallout Formation

A nuclear explosion occurs when a mass of fissile actinide material (primarily ^{235}U or ^{239}Pu) is rapidly assembled into a configuration such that it can sustain a chain reaction of neutron-induced fission, resulting in a release of energy that is larger than that produced by traditional chemical explosions. As the chain reaction takes place, a massive amount of energy (about 200 MeV per fission) is released until the mass of actinide material is disassembled (i.e., 'explodes') where it is no longer in a configuration that can sustain the fission chain reaction. This energy is released in the form of an initial shockwave, initial nuclear radiation (often referred to as "prompt" radiation), thermal radiation, and residual nuclear radiation [33].

Within about one microsecond, the fission chain reaction is complete. As the fission products and radiation released in the fission events interact with and heat the surrounding matter via scattering and absorption events, some of the energy is converted into thermal energy. This material continually absorbs and re-emits thermal (X-ray) radiation, and some of the energy is converted into kinetic energy in the form of a destructive shock wave. The partition of energy between thermal and kinetic energy will depend on the properties and quantity of materials in the device and immediately surrounding the explosion and the yield of the device. The thermal radiation forms a spherical fireball consisting of vaporized materials that can reach temperatures over 10^7 K, which expands over time and cools rapidly (on the order of seconds to minutes depending on the size of the explosion). This vapor contains the radioactive fission products and unfissioned actinides that are the primary radioactive contributors of concern in a post-detonation environment. Non-radioactive material within the device and in the surrounding environment can also be activated from the intense prompt radiation. These activation products can contribute significantly to fallout radiation dose at early times, but are generally short lived compared to fission products which have decay timescales ranging from milliseconds up to millions of years.

As the fireball expands and the vaporized material cools to temperatures of $\sim$2000-4000 K, the vapor condenses into radioactive particles. For air-bursts, this process is driven by nucleation into condensate droplets from the vapor, growth, and agglomeration of the condensates, resulting in particles with compositions reflecting the initially vaporized material. In the case of a ground burst or a height of burst that is low enough to interact with the surface of the earth, there is added complexity during the condensation of the vaporized material. The hot fireball is buoyant and rises over time, drawing additional material up into the fireball over time in a process known as "entrainment". Entrained material may be vaporized, fully molten, partially molten, or unaltered depending on the time and temperature at which it is drawn into the fireball. Entrained material serves as condensation sites for the condensing radioactive vapor or may scavenge already condensed particles, and also may be continually vaporized, re-condensed, or agglomerate during turbulent mixing as the fireball rises into the air. The complex and poorly understood process of entrainment results in a particles reflecting varying degrees of both the condensed vapor and locally entrained material. Entrainment can also result in the production of larger radioactive particles which fall to the earth more rapidly. This effect results in a more significant local radioactive hazard than for bursts without the entrainment of local material (such as an air-burst), whereas smaller particles may remain airborne for months or years and become more diffuse over time with less significant immediate radioactive hazard..

1.3 Radiochemical Fractionation

Radiochemical fractionation can be defined as "the alteration of the radionuclide composition occurring between the time of detonation and the time of radiochemical analysis which causes the debris sample to be non-representative of the detonation product taken as a whole" [25]. Studies of fallout during the 1950s and 1960s noted particle size dependent fractionation trends for many radionuclides of interest. This particle size effect is important because as fallout is deposited, larger particles enriched in refractory radionuclides are deposited closer to ground zero, and smaller particles enriched in volatile radionuclides are deposited further from ground zero, resulting in spatial variation of radionuclide inventories in fallout that have the potential to alter radioactive exposure rates for the public and first responders after a nuclear attack [12].

The complex processes by which radionuclides fractionate in fallout are not well understood, but it is hypothesized that these trends are caused primarily by volatility-driven effects during the condensation of the radioactive vapor. Elements that are more refractory condense first, with volatile elements condensing later, which result in a particle-size dependent fractionation. The volatility behavior of a given radionuclide is not only a function of it's own chemical volatility, but also a function of the volatility of it's radioactive precursors, independent fission chain yields, and the cooling rate of the vapor. Because of the rapid decay of (and changing chemical properties of) the radioactive fission products, a refractory fission product which would be expected to condense at high temperatures may still exhibit volatile behavior within fallout if it's volatile radioactive parents are the primary elements present at the time of condensation. Thus entire fission product mass chains are referred to as being refractory vs. volatile for a given data set rather than individual radionuclides. While mass chains can generally be identified as refractory or volatile [38] the extent of fractionation for a given mass chain is not theoretically predictable for a given event using current fallout formation models and known chemical and nuclear properties of of fissions products.

Because of the complexities of fallout formation, fallout researchers have relied on empirical relationships between these mass chains and particle sizes from data collected from a variety of fallout particles sourced from nuclear testing conducted in the 1940s-1960s. These relationships formed the basis for semi-empirical models representing a limited range of environments [33, 1, 24, 23, 62, 85]. A detailed overview of these models and their limitations in predicting fractionation behavior is offered by Lewis [47]. Some examples of the deficiencies of these models include the deviations in fractionation trends for large particles [63], variations in uranium volatility in different environments [24, 13], and the failure of volatility of mass chains to correlate to cooling timelines that would be expected if fractionation was governed by mass chain volatility alone [14]. In addition, Recent efforts applying modern tools to re-investigate historic fallout [16, 8, 5, 70, 46, 94, 3] challenge many fallout formation assumptions with evidence of reduced conditions [8, 5, 70], heterogeneous vapors [46], and unexpected volatility behavior [94]. Better understanding of the validity of these assumptions as well as accounting for other formation processes (i.e., agglomeration, re-evaporation, time-dependent entrainment, etc.) may better predict unexplained fractionation behavior and increase confidence in extrapolating these models into untested environments.

The failure of models to theoretically predict fractionation behavior and recent studies of historic fallout particles suggest an incomplete picture of volatility-controlled processes, and may also suggest the influence of other formation processes. The extent to which variations in local environments influence deviations from empirical radio-chemical fractionation patterns is unknown. This motivates a deeper understanding of fallout formation mechanisms in different environments to enable predictions of fallout formation in untested environments.

1.4 Environmental Influence on Fallout Formation

Observations of fallout collected from historic nuclear tests demonstrate that the local environment influences the resulting morphology, composition, and size distribution of fallout. These influences have been pointed to as the cause for observed deviations from semi-empirical fractionation trends, and introduce sufficient complexity that initial attempts to predict chemical fractionation relied on semi-empirical vs. theoretical models. There are two potential means that the environment has the potential to influence fractionation behavior: (1) the influence of environmental composition on condensation, solidification, and cooling behavior, and (2) the location of environmental material in relation to the detonation location (i.e., emplacement).

The influence of environmental composition is not surprising since fallout particles are primarily composed of the materials initially vaporized and/or entrained into the fireball. Historical studies have documented variations in size distributions, color, morphology, and composition that is associated with nuclear tests in a variety of local compositions, including silicate-rich desert environments [55], calcium-rich ocean atolls [2], iron-rich towers [13], iron-rich barges [19], and airbursts containing little local environmental material beyond the bomb casing [24]. While variations in fallout characteristics were historically documented, access to modern tools allows more detailed investigation of formation processes today. The mechanisms by which environmentally-driven formation processes may influence radiochemical fractionation is unclear, but some possibilities include alterations in the freezing temperatures of particles, variations in vapor speciation, and perturbing the cooling rates of the fireball.

The solidification temperatures of particles is relevant because, as theorized by Miller [57], it represents the transition in condensation behavior between refractory and volatile mass chains. Under this model, particle size-dependent fractionation effects are due to the refractory mass chains condensing during and/or prior to particle formation resulting in volumetric distribution within particles, and with volatile mass chains condensing after particle formation and being distributed on the surface area of particles. This results in volatile mass chains being enriched in smaller particles with higher surface are to volume ratios, and refractory mass chains being enriched in larger particles. Semi-empirical fractionation models have been developed with some success (for example, Miller[57] and Martin [55]) for silicate environments . While these models remain semi-empirical due to the complexity of formation processes, it is reasonable to assume that different freezing temperatures in non-silicate environments could influence fractionation behavior of each given mass chain.

Current fallout formation models assume condensation behavior that is governed by fully oxidized gaseous radionuclides. The extent to which this assumption holds true is unclear. Fission product behavior studied by Cassata [8], differences in uranium volatility between air and ground bursts [13] and between silicate and calic enviornments [13], and actinide speciation that suggests dramatically different redox environments across different environments [70] has motivated hypotheses that environmental material may constrain the oxidation behavior for condensing radionuclides for at least a portion of their condensation history. This has motivated work into gaseous speciation of uranium, iron, and aluminum in different environments by Koroglu [44], but the magnitude of such an effect for different environments remains unclear. In particular, it has been hypothesized that large quantities of metallic material (such as Fe) may buffer the oxidation environemnt, influencing condensation temperatures of some fission product mass chains.

It is also possible that the composition of the environment may influence cooling rates of the fireball which influences fractionation behavior as the time of condensation of a given specie competes with the radioactive decay of the mass chain. Calculations by Izrael [38] argue that the heat of condensation and solidification of environmental material has the potential to change the cooling rate of the fireball for timescales (0.6-1.6 seconds) and temperatures (1700-3000K) at which mass chain decay is competing with condensation of precursors of varying volatility. The magnitude of this delay will depend (for similar quantities of vaporized and molten material) on the composition of the vaporized and molten material, and thus affect fractionation of mass chains with decay similar decay timescales.

The influence of emplacement on fractionation is also well documented, though difficult to predict. The height of burst influences the quantity of entrained material in the fallout cloud [82]. This entrainment effects results in differences in fractionation ground bursts (which are significantly fractionated) and air bursts (which are less fractionated). This effect is due to the level to which nearby environmental material enters the vapor phase or is entrained into the fireball after initial vaporization, influencing the initial vapor composition, particle size distributions, and particle formation processes. Variations in particle size distributions between air and ground bursts (unimodal lognormal vs. bimodal and trimodal lognomoral distributions) are a result of different formation mechanisms (as opposed to condensation only) and/or timing of entrained material with the cloud [36]. These size distributions are sensitive to the height of burst, which influences the quantity and timing of entrained material. Models of the size distribution via condensation processes predict that the partitioning between the two particle size lognormal modes is sensitive to the amount of entrained particles present in the fireball when condensation takes place [85] which will also vary with the height of burst. The timing and quantity of entrained material has an effect on these particle size distributions, influencing not only empirical fractionation trends along particle size, but atmospheric transport and dispersion of produced particles which result in fractionation. Larger particles formed in surface bursts (mm-scale) have been shown to exhibit more volatile behavior than the semi-empirical models predict and have been hypothesized to be a result of agglomeration processes currently not accounted for [47].

In summary, there is evidence that the environment influences fundamental formation properties of fallout. However, the complexity of these processes makes predictions of fallout and important radio-chemical fractionation processes difficult. Accounting for the role of these processes in fractionation is beyond the scope of this work. However, the possibility for their influence on fractionation behavior motivates a systematic investigation into the basic physics and chemistry of fallout formation in different environments using modern micro-analytical techniques. The interaction of iron with a nuclear explosion is of specific interest on account of the potential for iron to act as a mineral redox buffer [60], affecting the chemical behavior of condensing radioactive species[8] and because of the likely presence of masses of metals in the case of an explosion in an urban environment. As part of a larger systematic investigation of fallout formed in different environments, this work focuses on studying fallout formed in iron-rich environments to understand general fallout formation processes, with a focus on those that are unique to iron-rich environments.

1.5 Dissertation Objective and Outline

It is hypothesized that iron in the environment influences fundamental fallout formation processes, highlighting the importance that the local environment has on fallout formation. This work aims to understand the formation of fallout in iron-rich environments by characterizing and interpreting a set of 26 mm-scale nuclear fallout particles that were formed in a near-surface nuclear explosion conducted on a steel tower. During characterization, novel micro-scale spherical microstructures reflecting liquid immiscibility processes were discovered and are unique to Fe-rich silicate environments. Such microstructures have not been incorporated into fallout formation models, and are the primary focus of this work. These microstructures are termed “amoeboids” after immiscible amoeboid inclusion textures [75] due to their morphological resemblance to biological amoebas. The sensitivity of silicate liquid immiscibility to parameters of interest for fallout such as oxygen fugacity and temperature highlight the importance of amoeboids to understanding complex fallout formation processes. The exact formation mechanism of amoeboids is not clear, but is necessary to using them to infer fireball conditions. Some potential formation mechanisms are explored in this work including formation via decomposition from a single, miscible liquid, and emulsification of two chemically distinct liquids. Because good evidence exists that amoeboids represent non-equilibrium processes, establishing their mechanism of formation is important because it allows differing interpretations of the fireball environment under which they formed.

Chapter 2 describes the analytical techniques used to characterize the fallout particles in this work. The results of the characterization work is presented in Chapter 3, with a focus on the characterization of amoeboids, and a discussion is offered for the two hypotheses for their formation processes: via either decomposition from a single homogeneous liquid or via emulsification of two chemically distinct liquids. In Chapter 4, the possibility that amoeboids represent high temperature chemical equilibrium compositions and thus may be able to provide redox and temperature constraints is explored using a computational thermodynamics approach, and evidence for non-equilibrium compositions is presented. Chapters 5 and 6 explore amoeboid formation hypotheses using two different computational approaches. In Chapter 5, a phase field method model is used to evaluate whether decomposition can result in the range of observed amoeboid morphologies. In Chapter 6, a multivariate un-mixing method is applied to sample compositional measurements from Chapter 3 to interpret compositional relationships within the fallout. This method is used to discuss whether amoeboid two-phase compositions may directly reflect the emulsification of distinct precursor liquids. Finally, in Chapter 7, this work is summarized, key findings are highlighted, and suggestions for further work are offered.

Chapter 2

Analytical Techniques

It is hypothesized that fallout formation differs in iron rich environments, but the extent to which it does and the mechanisms for potential differences are not well understood. To establish how fallout formation differs, an important first step is to investigate the physical properties of such fallout. To accomplish this, this work utilizes a variety of common materials characterization techniques. This chapter presents a brief conceptual overview of each characterization technique, and provides an overview of the methods and instrument parameters used for data collection and analysis. The results of these techniques are presented in Chapter 3, with some limited results described here to give the reader an understanding of each technique. Materials characterization techniques used in this study included autoradiography, scanning electron microscopy (SEM), transmission electron microscopy (TEM) and nano-scale secondary ion mass spectrometry (NanoSIMS).

2.1 Sample Selection and Preparation

Samples of mm-scale nuclear fallout samples were isolated from soil samples collected near the detonation site of an historic near-surface nuclear weapons test. Isolation of samples from the soil was conducted visually by selecting grains that exhibited some degree of glassy luster which has been historically associated with fallout particles that have experiences interaction with the high temperature fireball [32]. Collection IDs were assigned in the format FLD-17-11-XX, where XX represents a two digit identifier from 01-35. For brevity, samples in this study are refered to in the format FXX. Samples F1-F8, and F10 were selected for other analyses which were not the focus of this study, resulting in a final sample set of twenty six individual samples (F9, F11-35). Specimens were optically characterized using the bright field imaging mode of an Olympus SZ61 Stereo-microscope System. They were then fixed to an SEM stub with double sided sticky tape, coated with 10-15 nm of carbon, and imaged using an FEI Inspect F SEM. Samples were then removed from the SEM stub and mounted in eponate araldite epoxy within five stainless steel round mounts and hand-polished to expose approximate mid-plane cross sections to a 1 μm surface roughness using a range of

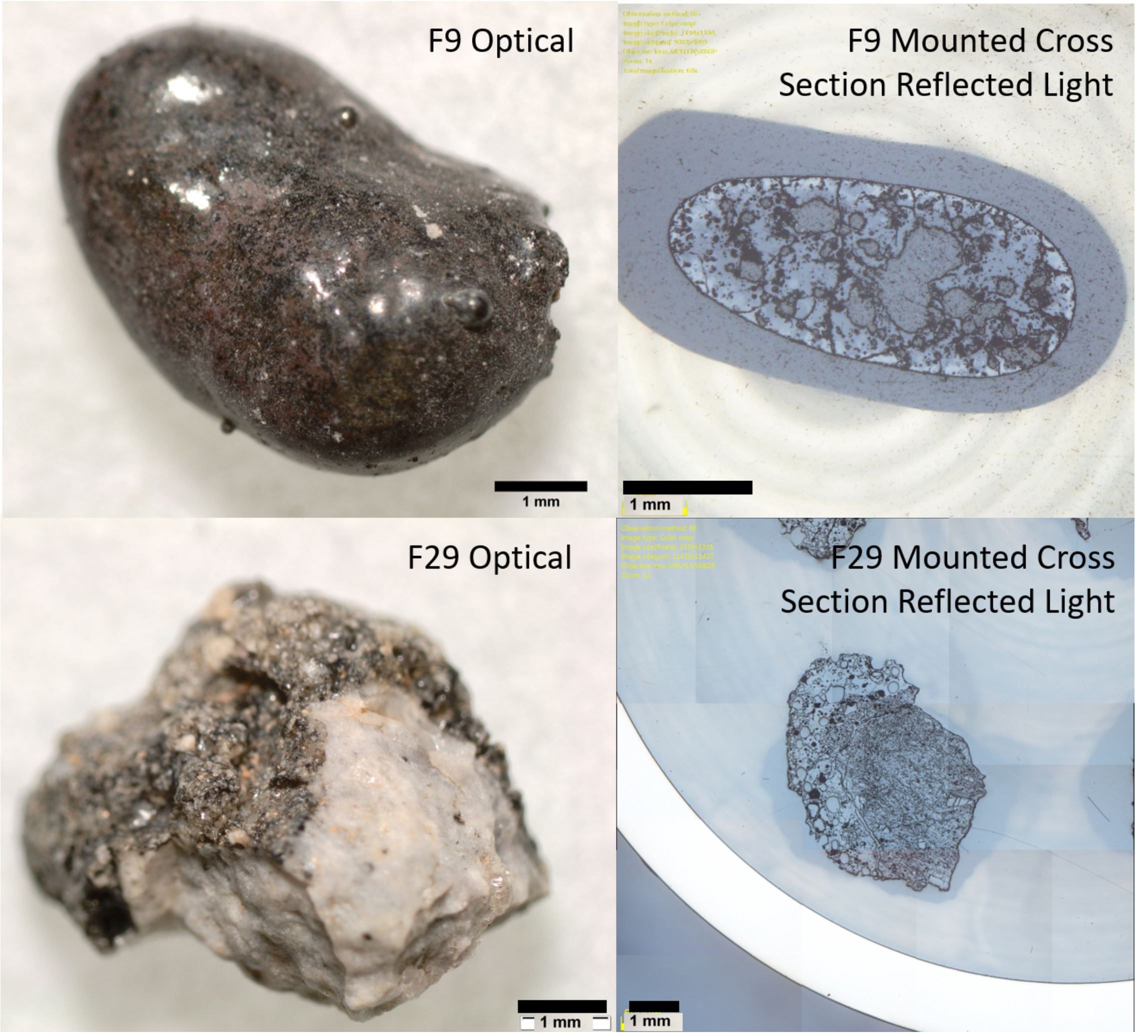

Figure 2.1: Examples of two different optical methods used to characterize samples for this study. The left column contains optical images of two samples (F9 and F29), at right, reflected light images of the same samples after polishing. Shadows in the cross section optical images are objects below the surface of mounting epoxy.

sandpaper grits, 3 μm and 1 μm diamond paste, and 1 μm alumina powder. Ultrasonication between each step was used to remove residual grit. Optical imaging was used to inspect the polished cross sections, and exposed vesicles were backfilled with epoxy and re-polished. Exposed cross section mounts were then coated with 10-15 nm of carbon and analyzed using autoradiography, SEM and NanoSIMS techniques. Finally, a focused ion beam (FIB) was used to prepare 100 nm thick 'lift-outs' of several microstructures within the exposed cross sections which were analyzed using an FEI Titan TEM/STEM. Examples of optical images of both the bulk samples and sample mounts with exposed cross sections of the samples are shown in Figure 2.1. All optical images are provided in the appendix. The following sections give an overview of each techniques and methods used.

2.2 Autoradiography Imaging

In order to measure the level of radioactive species in the samples in this study, digital autoradiography techniques were used, described in detail by Parsons-Davis *et al*[71] This method employs photosensitive phosphor digital imaging plates which contain photosensitive grains with an emulsion of europium-doped barium fluorohalides. Radiation oxidizes the europium into a higher oxygen state, bumping electrons into the conduction band where they are trapped in fluorohalide vacancies. After exposure, plates are then stimulated by laser, allowing the electrons to return to the europium atom, which releases characteristic light which can be detected by a photomultiplier tube and resolved spatially. The captured image reflects a qualitative distribution of radioactivity in the sample, which is primarily from alpha particles at or near (within ∼50 μm) of the sample surface or beta particles (within a few millimeters of the samples surface, depending on the the particle energy and sample material). Gamma and neutron radiation can also be detected on the imaging plates, but are usually more diffuse due to their ability to their longer path length of interaction in the sample (and thus be sourced from anywhere in the sample volume rather than just the surface), and decreased likelihood of interaction with the thin imaging plate. The resulting image predominately reflects alpha and beta particles near the sample surface that is in contact with the imaging plate.

In this study, all five polished sample mounts were placed face down on a Fujifilm BAS-SR phosphor storage imaging plate with an approximate spatial resolution of 50 μm in a light tight box for six hours. The imaging plate was then scanned using a GE typhoon FLA 7000 scanner in phosphor-imaging mode. Because all samples were exposed and imaged simultaneously, the relative intensity of the pixels in the image represents the relative radioactivity present between and within each sample. Pixel intensity was converted to a cyan color scale using ImageJ software [77], and an image of collected auto-radiography for all samples in their mounted puck geometry is shown in Figure 2.2.

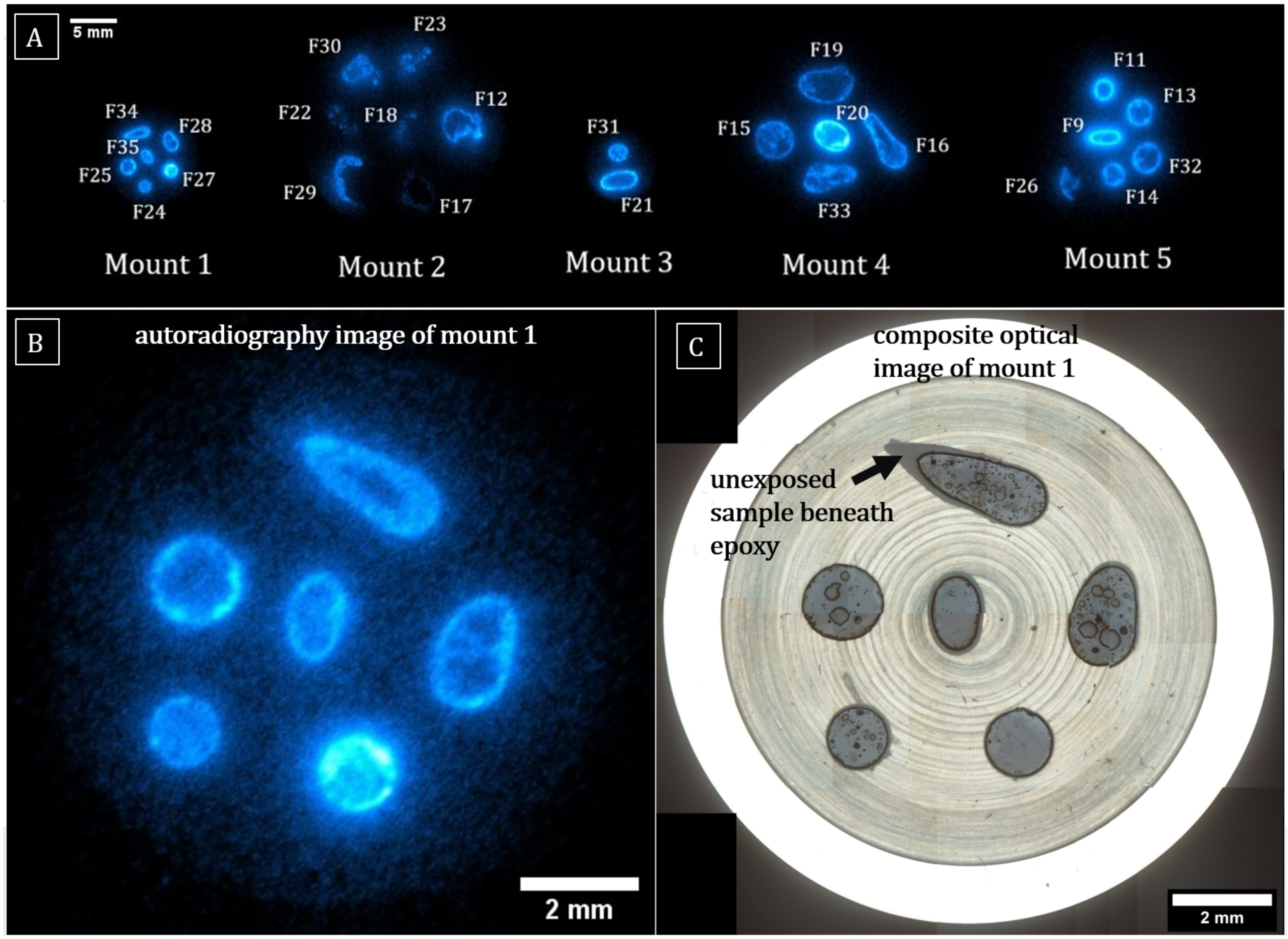

Figure 2.2: Auto-radiography image of the cross section of all samples used in this study. (A) Radiography image of all mounts displayed in false cyan color scale, with sample locations annotated - all images were taken from a single exposure, so intensity is comparable between images. (B) A closer view of mount 1 with (C) a composite optical image of mount 1 for comparison. Note the clear radioactive-rich rims present in most samples. Mount 1 shows a radioactive region that matches well with the exposed region of sample F34, suggesting radioactive signals in the bulk sample beneath the epoxy do not significantly contribute to the autoradiography signal. This suggest the majority of the signal is due to alpha radiation that only reaches the imaging plate from within the top 50 μm layer of sample surfaces.

2.3 Electron Microscopy

Electron microscopy is a well-established technique for materials characterization which uses an electron beam source to interrogate samples [17]. Electrons are generated from an electron source, and accelerated and focused to a point using a variety of voltage sources and electron optics. In a scanning electron microscope (SEM), scanning coils are then used to change the direction of the beam, allowing rapid scans across areas of the sample. Spatially correlated signals that are emitted in the form of electrons or X-rays as a result of electron beam interrogation can be used to determine the material properties of the sample, and are measured using a variety of electron and X-ray detectors. In an SEM, the electron beam is typically on the order of 10-30 keV is used to interrogate a bulk sample, and signals that are emitted out of the bulk sample are detected to provide a variety of information about the sample. In a transmission electron microscope (TEM), an electron beam of 200-300 keV is used to interrogate a very thin sample ($\sim$50-100 nm), and electrons that pass through the sample are also detected using a CCD camera on the beam path which provides additional information about the sample.

SEM Imaging and EDS Analysis

In this work, an FEI Inspect F Scanning Electron Microscope was use with an Everhart-Thornley secondary electron (SE) detector and an annular solid-state silicon backscatter electron (BSE) detector to produce images of each sample. For imaging analysis, an electron beam of 20 keV was used. In these images, SE imaging gives better topological information, but BSE imaging highlights chemical heterogeneities, where brighter regions represent higher Z or higher density regions. Since this work primarily investigates chemical heterogeneity of polishes samples, SEM images are all BSE images unless otherwise noted.

In an SEM, upon interaction with the bulk sample, electrons forward-scatter in the direction of the primary electron beam, and result in a volume of material within the bulk sample known as the excitation volume. The size of this volume is dependent on e-beam voltage and material properties of the sample, and is generally inversely proportional to sample density and/or atomic number (Z).

Some atoms in the excitation volume are ionized as a result of electrons inelastically scattering, releasing low energy electrons ($\sim$ 50 eV). Due to their low energy only the electrons within the top few nanometers of the sample surface escape from the bulk sample and are accelerated towards an Everhart-Thornley secondary electron (SE) detector within the sample chamber. The electrons that reach the detector are multiplied, resulting in a display brightness proportional to the number of electrons that reached the detector, which varies as the electron beam is scanned across the region of interest. The number of secondary electrons is dependent on beam geometry in relation to the sample surface. Thus contrast in images from SE detection primarily reflect surface topography. Due to the small region of SE origination, SE detection can offer spatial resolution on the order of nanometers.

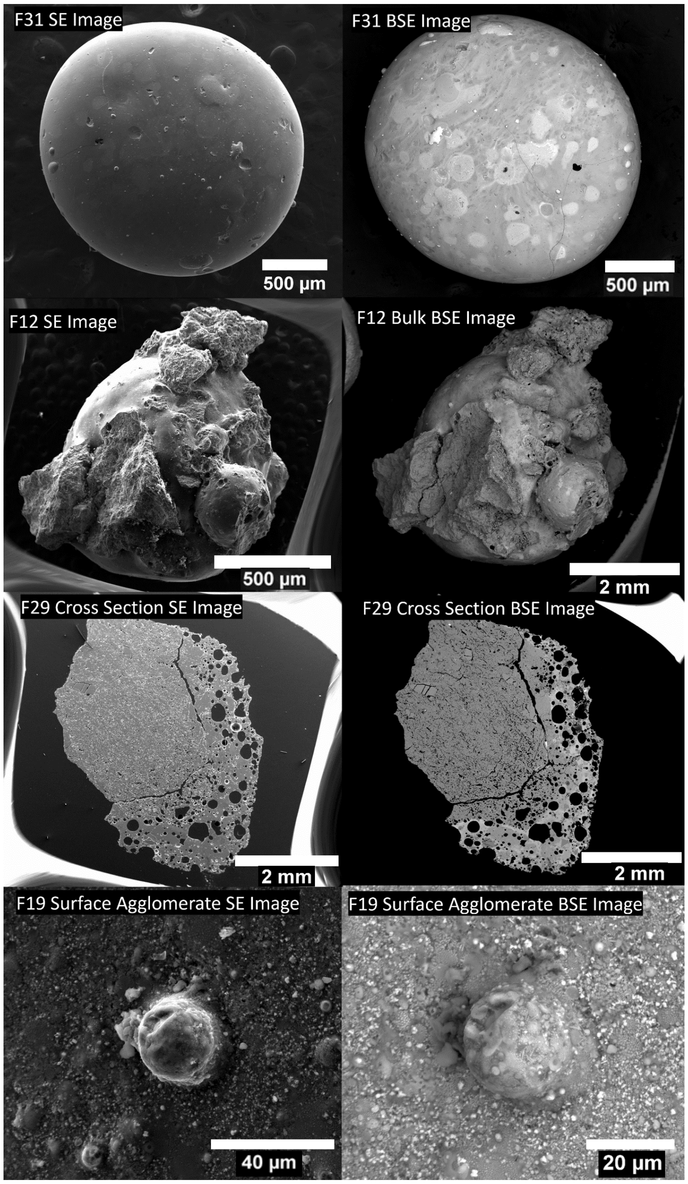

Figure 2.3: Examples of secondary electron (SE) images (left) and backscatter electron (BSE) images (right) representing a range of scales and sample preparation. Shown are samples (from top to bottom) F31, F12, F29 (polished cross section), and F19 (surface feature). Note the more resolved topographical features in the left column versus the contrast reflecting compositional heterogeneity in the right column. It is easy to distinguish topographical features from compositional heterogeneity in samples without significant topography such as sample F31. When significant topographical features exist, such as in sample F12, compositional variation becomes convoluted with topographical variation. Polishing samples (F29) removes topographical interference, allowing better capturing of compositional variation.

Beam electrons that are elastically scattered are higher energy than secondary electrons, and so can escape from a larger portion of the excitation volume, and are known as backscatter electrons (BSE). Since BSE are most strongly scattered at near 180 degrees, a solid-state silicon BSE detector is located annularly around the in-going beam. The intensity of backscatter is proportional to the sample orientation, the initial beam energy, and the atomic number (Z) of the sample or its density. Thus, for a flat sample with constant electron beam energy, the contrast in BSE images reflect variations in chemical composition or sample density. Thus BSE signals are more reflective of chemical heterogeneity and less sensitive to surface topology, though at the expense of decreased spatial resolution. Example SE and BSE images from this study are shown in Figure 2.3.

The interaction of the electron beam with the sample also results in the generation of X-rays which can be used to estimate the composition of the sample. X-rays are produced throughout the excitation volume, and are after escaping from the bulk sample, are detected using XFlash 6-60 Silicon Drift Detector (SDD) within the sample chamber. The energy of each X-ray is recorded and added to a histogram that displays the counts per second as a function of energy, as shown in Figure 2.4. Interpreting this spectrum, known as Energy Dispersive Spectroscopy (EDS), and involves subtracting background caused by continuum X-rays, as well as identifying the X-ray emission caused by excitation of electrons in different energy-level shells (K,L, and M) in different elements. Because X-rays are sourced from the entire excitation volume, the spatial resolution of EDS varies with the sample properties and beam energy. For SEM analysis on a bulk sample, this is typically on the order of 0.5-1 μm. Using lower beam energies increases the spatial resolution, but if the beam energy is below the threshold of primary K-shell energies of elements in the sample, this complicates quantification efforts.

In order to quantify the composition of the sample, the background X-rays must be subtracted, and peaks fit to known intensities of each element's X-ray peaks, accounting for deviations from theoretical peak intensities caused by X-ray interactions in the sample excitation volume. For SEM-EDS, one widely used method for quantification is the standardless ZAF method. This method accounts for the atomic number effect (Z) which affects the deceleration of the beam into the sample. The self-absorption effect (A) affects X-ray intensities as a function of energy and sample composition as they escape the excitation volume. The fluorescence effect (F) corrects for secondary X-rays emitted as a result of primary X-rays interacting with elements in the excitation volume. By making an initial estimation of the composition, a ZAF correction factor can be applied, which causes a new estimation of composition. This is done iteratively until the composition converges and best fits the EDS spectrum. This work uses correction factors that are calibrated to pure-element standards specific to the machine geometry and detectors. Standardless ZAF correction results in semi-quantitative measurements. By using well-polished, flat samples, we increase the accuracy of the measurements, which can yield results accurate within +/- 1-2% for major (10 wt%) and minor (1-10 wt%) elements.

SEM-EDS was used for two purposes in this study. First, one hour qualitative SEM-EDS maps of sample cross sections were collected (referred to as a cross section map).

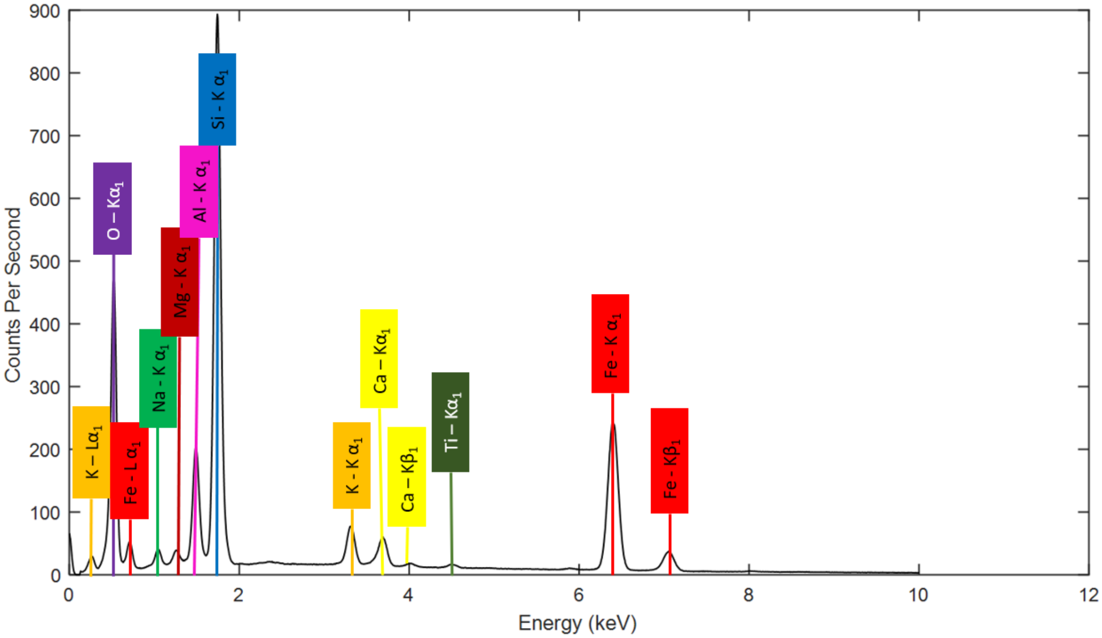

Figure 2.4: Representative EDS spectra from a localized point EDS analysis in sample F11. Each spectral peak can be associated with a characteristic elemental X-ray peak. Such peaks are deconvolved and quantified using the ZAF method to estimate the composition where the spectra was collected.

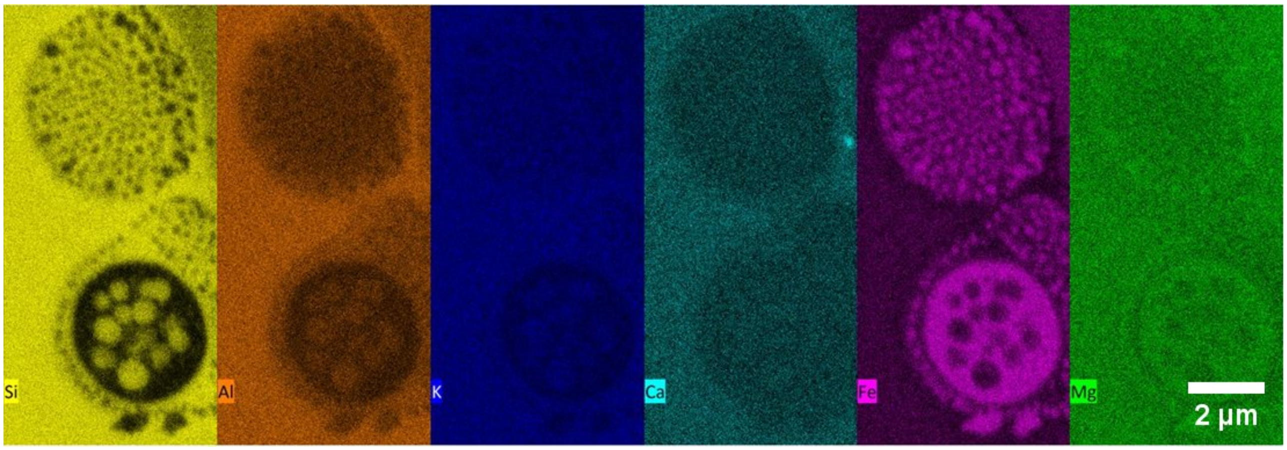

Figure 2.5: Examples of a qualitative SEM-EDS map of two ameoboid microstructures preserved in the exposed cross section of sample F28. Because relative intensities are not consistent from image to image, these maps allow us to understand variation for each element within the map, but are not quantified between elements.

Second, SEM-EDS maps and localized EDS points ('spot' analyses) were collected from many microstructures of interest. Spot analysis involves collected a spectrum at a single point. Spot analyses give the best spatial resolution, but care must be taken to find the right balance of collection time. Longer dwell time can heat the sample and result in the loss of volatile elements such as K or Na, whereas too short of a collection time results in insufficient statistics for good quantitative estimations.

Mapping involves a raster over a large area, with a spectra collected at each pixel and deconvolved with adjacent pixels to arrive at the best estimate of composition for each pixel location. Mapping allows us to understand compositional spatial information over large areas, but data collection can take a long time, and beam to sample orientation angle changes with mapping over a large area can affect quantification accuracy.

Because samples studied here contain significant amounts of iron (K-alpha X-ray energy=6.4 keV), energies <10 keV provide insufficient counting statistics. For cross section maps and for microstructure maps with features $\sim 1\ \mu m$, a 20 keV beam energy was used. For analysis of microstructures with features $<1\ \mu m$ a 10 keV beam was used to optimize spatial resolution. In addition, 11 aerodynamic glass samples and 2 ground glass samples with high microstructure diversity were selected for semi-quantitative mapping. Semi-quantitative maps were measured for 12 hours each, and converted to pixel by pixel compositional estimates using the ZAF method in the Quantax Esprit 2.0 EDS software. Representative maps for one sample (F9) are shown in Figure 2.5, and the rest are included in the appendix.

The EDS techniques were also used for characterization of the microstructure in this study, including both mapping, raster analysis, and spot analysis. Raster analysis involves defining a region of interest and a raster of the beam over the entire are to collect a single spectrum which is quantified to estimate the average composition in the raster area. Raster methods have lower spatial resolution, but experience less significant volatile loss of alkali elements from beam heating. In order to determine if volatilization may play a significant role in this work, sequential point and $2\ \mu m$ x $2 \mu m$ raster analyses were taken in a region of sample F20. A new point/raster location was chosen in the same general region for each set of sequential runs, and each set was measured for either 10 seconds, 30 seconds, or 2 minutes, with the hypothesis that longer analyses times should volatilize more alkali, resulting in decreased Na concentrations for later runs. The hypothesis was that raster analyses, by scanning over a larger surface area, should reduce the level of heating in the bulk sample and thus reduce the amount of volatilisation. Results (Fig 2.7) show that all measurements, with the exception of one 2 min raster, were within 1-σ of the average concentration, with no clear systematic decrease in Na wt% for later runs. Variation in Na wt% between sets of analyses are attributed to local chemical heterogeneity. While these results suggest that alkali loss was not a significant source of error in EDS quantification used in this study, features $<1\ \mu m$ utilized spot analyses to optimize spatial resolution, whereas features $>1\ \mu m$ utilized raster analyses.

SEM imaging documented a wide range of micro-structure morphologies in the exposed cross sections of samples. Composition maps of many of these structures were collected to understand the general partitioning behavior of elements. One category of semi-spherical

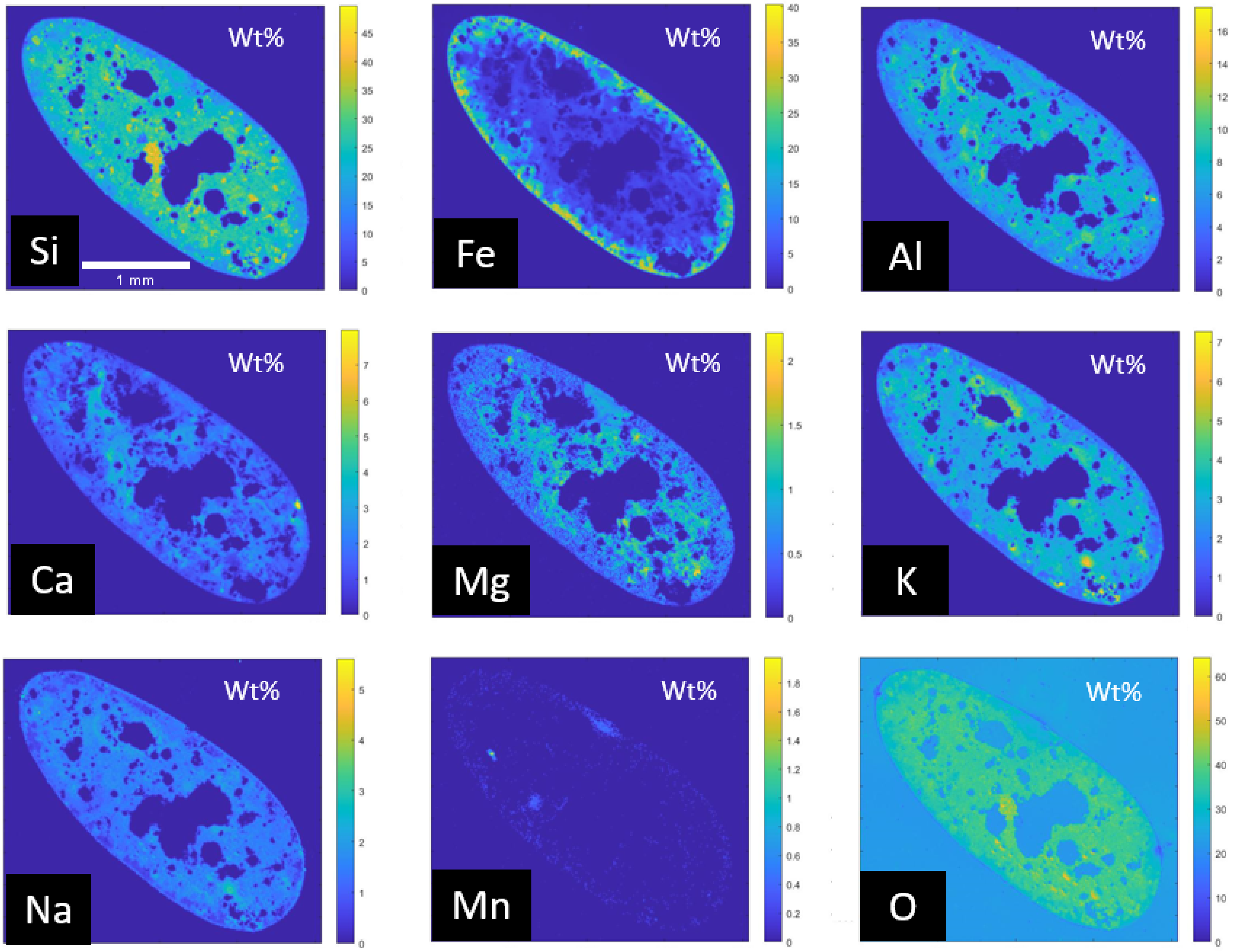

Figure 2.6: Examples of semi-quantitative SEM-EDS maps for sample F9, which show element absolute weight% within a sample cross section. Note scale bars are different for each image. Although relative compositional variation for a given element are evident in a qualitative map, semi-quantitative maps enable improved comparison between elements. Compositions below 0.5% are less reliable (i.e., the Mn map).

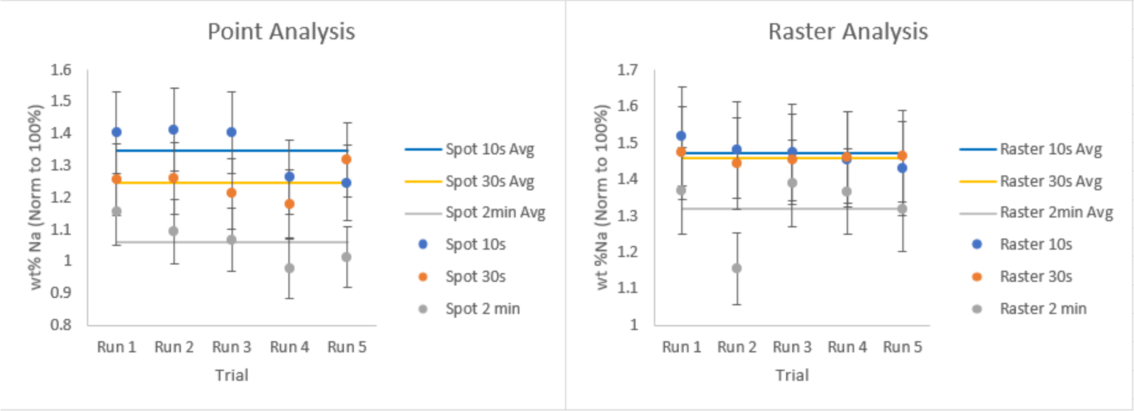

Figure 2.7: Na concentrations for sequential point and raster analyses for regions of Fe-rich glass in sample F20 demonstrating effects of volatile loss. Raster analyses were conducted using a 2 μm x 2 μm square region. With the exception of a single raster analyses, all measurements were within error bars of the average suggesting volatile loss is not significant for these samples during EDS analyses.

two-phase microstructures referred to as ”amoeboids” were of primary interest, and 42 total amoeboids in samples F34 and F28 were selected for analysis. Their two phases are theorized to represent two immiscible liquids, one of which is more Si-rich and Fe-poor and the other more Si-poor and Fe-rich, and are referred to as L_{Si} and L_{Fe}, respectively. See chapter 4 for further discussion on liquid immiscibility. Circular raster EDS spectra were collected over exposed amoeboid cross sections to approximate the average compositions of individual amoeboids, and point spectra were collected in different locations at 10 keV within the amoeboid to approximate compositions of L_{Si} and L_{Fe} phases. Because the size of the L_{Si} features is typically on the scale of the approximate excitation volume of the electron beam in the matrix, electron-beam mixing may exist between analyses of the L_{Si} and L_{Fe} phases when their domain size is small ($\sim$ 1 μm. This effect would result in overestimation of iron content in the L_{Si} phase or underestimation of iron content in the L_{Fe} phase. However, using an electron beam of 10 keV, the Fe Kα X-ray at an energy of 6.5 keV should produce X-rays from a depth of 0.7 μm according to the Anderson-Hasler range equation [28], which is less than the domain size of most L_{Si} phases analyzed, minimizing the impact of electron beam mixing. For amoeboids with phases $< 1\mu m$, raster spectra of overall amoeboid composition were collected but no two-phase spectra. Uncertainties in EDS compositions are reported as the uncertainty from the ZAF calculated fit for individual analyses. For amoeboids where >5 measurements were taken of each phase, the average composition is reported (see appendix) with uncertainty as the standard error of the mean.

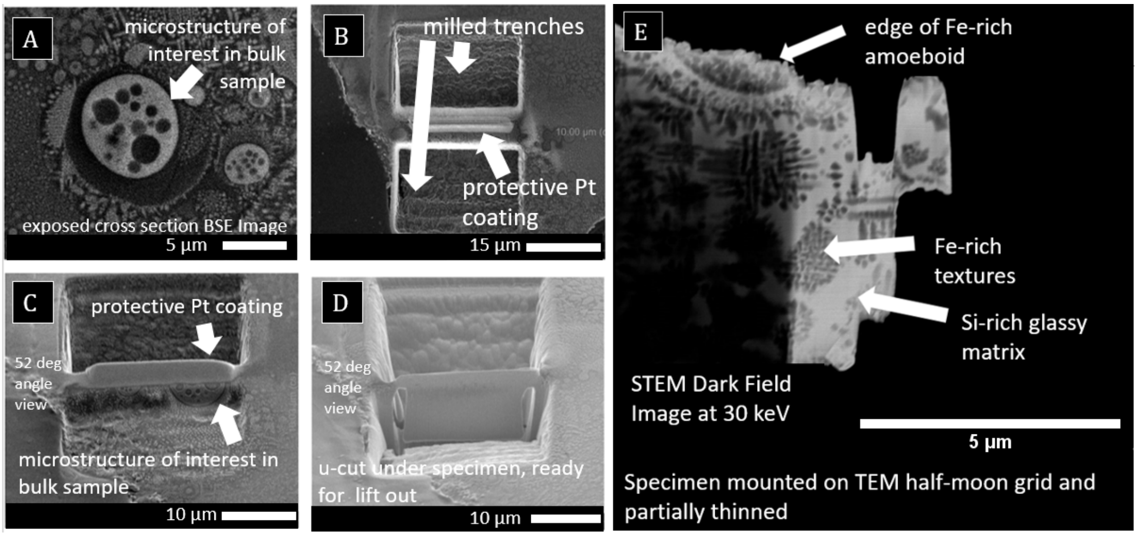

Figure 2.8: Images from proof-of-principle FIB liftout of an amoeboid micro-structure. (A) BSE image of the exposed cross section of a microstructure of interest in the bulk sample. (B) The milled trenches and protective Pt coating. (C) The milled trenches and protective Pt coating from an e-beam angle of 52 degrees. (D) Amoeboid specimen ready for lift-out from the sample after the u-cut. (E) A STEM DF image of the lifout after initial thinning. Note the protective Pt coating has been ablated away. Better thinning technique and a higher quality instrument was used for subsequent thin section preparations.

Focused Ion Beam Liftouts

Because amoeboid microstructures have phases present with spatial domains on the order of SEM-EDS spatial resolution, TEM-EDS data, which have sub-μm spatial resolution were collected. In order to conduct TEM analysis, samples must be sufficiently thin to allow electron transmission. In this work, a FIB-SEM workstation comprised of a primary SEM column, a focused ion beam (FIB), a micromanipulator, and a platinum deposition needle was used to fabricate lamellas (or 'liftout') specimens of microstructures of interest. In brief, this method deposits a protective platinum coating over the microstructure. Then, by rotating the stage that the sample is mounted on, a Ga^+ ion beam then used to mill out trenches on each side of the sample and under the microstructure. The micromanipulator is welded to the top protective Pt bar using additional Pt, and the Ga^+ ion beam finishes cutting the specimen out of the sample. The specimen is then mounted on a TEM grid using Pt, and the Ga^+ ion beam is used to thin the sample to 50-100 nm. A detailed overview of this method can be found in Mayer et al [56].

In this study, a total of 6 FIB sections were analyzed, and referred to as T1-T6. T1 was a proof of concept liftout prepared at the Biomolecular Nanotechnology Center (BNC) cleanroom facility in Stanley Hall on the UC Berkeley campus. Figure 2.8 shows some

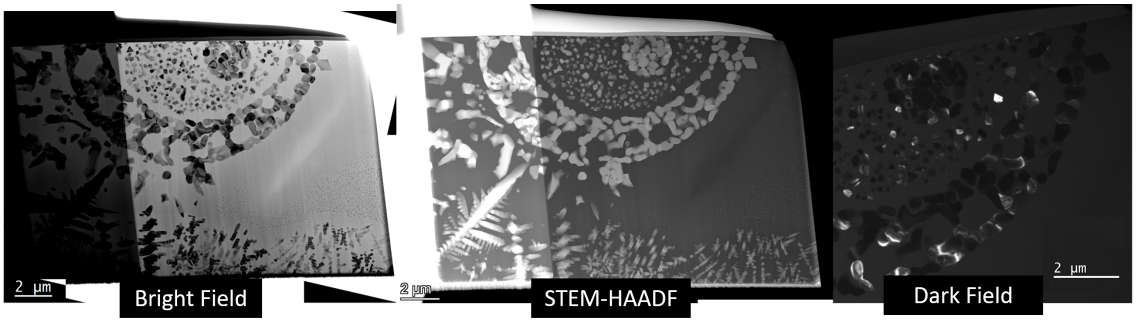

Figure 2.9: Example TEM BF and HAADF images from specimen T2 from sample F11. In the bright field image, the unscattered electron beam is collected and scatter electrons are blocked using an aperture, with dark areas reflecting either crystalline or high mass materials. In STEM-HAADF, an annular detector is used to collect scattered electrons, and represents the inverse in contrast from bright field, but with improved resolution. Similarly, conventional dark field imaging shows scattered electrons which are selected using an aperture.

images collected during a first attempt at the FIB liftout process. Due to poor Ga^+ ion beam quality, the protective Pt coating has been fully ablated, and sample is not of uniform thickness, making this a poor quality specimen. Because of the poor quality of sample T1, samples T2-T6 were prepared using a FEI Helios 600i Dual Beam FIB-SEM at Lawrence Livermore National Laboratory with improved beam quality, which allow addition TEM data collection.

TEM Imaging and EDS Analysis

In a TEM, imaging modes are feasible that are not available to SEM, to include bright field (BF) imaging, dark field (DF) imaging, and selected area diffraction pattern (SADP) imaging. For scanning TEMs (STEM), high angle annual dark field (HAADF) imaging can also be performed. These techniques rely on the electron beam to pass through the sample, and require a thin sample and high electron beam energy. In BF and DF imaging an objective aperture is placed in the back focal plane of the objective lens to select either the forward-scattered or diffracted beams. For BF, the forward-scattered electrons are allowed to pass through the aperture and are captured on the charged coupled device (CCD), resulting in contrast that reflects variations in crystalline phase, density, or composition. DF captures the diffracted beam on the CCD and blocks the forward-scattered beam, reflecting similar contrast as BF, but with lower noise and additional detail. For HAADF, an annular detector is used to directly detect scattered electrons rather than selecting individual beams of scattered electrons using an aperture.

In addition, a condensed beam can be rastered across the sample to provide scanning transmission electron microscopy (STEM) for collecting compositional maps. STEM is performed on collected spectra similar to SEM-EDS. The advantage to STEM (vs. SEM) on thinned samples is that the excitation volume is on the order of nanometers rather than microns when done on bulk samples. STEM results in improved spatial resolution for EDS maps appropriate for use in analyzing nano-scale liquid immiscibility features identified using SEM-EDS. With 50-100 nm thin samples, absorption and fluorescence effects can be ignored. Thus, the ZAF quantification method is not used. Rather, the Cliff-Lorimer method [11] applies a factor that calculates relative concentrations of elements from their integrated peak intensities. This factor is calibrated to the specific TEM instrument.

In this study, transmission electron microscopy (TEM) of specimens T1-T6 were conducted using an FEI Titan STEM/TEM located at Lawrence Livermore National Laboratory and was operated at 300 keV. BF and high angle annular dark field (HAADF) images were collected for each sample. Example images are shown in Figure 2.9. STEM EDS maps were collected for T2-T6 only, since T1 was of poor quality with re-deposition of Pt on the sample and inconsistent thickness. A variety of ROIs were selected after mapping that approximate each presumed L_{Si} and L_{Fe} phase. Individual crystal grain ROIs within the L_{Fe} phase ROIs were also selected, as well as ROIs that encompass the entire exposed amoeboid to approximate bulk amoeboid composition. Spectra from each of these ROIs were then used for quantification. Bulk amoeboid composition was estimated using the ROI over the entire amoeboid region of the liftout, and L_{Si} and L_{Fe} phases were estimated taking the average of each L_{Si} and L_{Fe} phase ROI. For amoeboids with 5 ROIs for each phase, the uncertainty was calculated taking the standard error of the mean (SEOM).

TEM Diffraction Analysis

While SEM-EDS provides compositional information, it does not directly identify the the phases present in the excitation volume. With TEM selected area diffraction patterns (SADP), the measurement of the crystalline structure of the sample can identify what phases are present. An aperture is placed over a region of interest so that the electron beam only passes through that area. The sample is tilted until the electron beam is passing perpendicular to one crystal plane (i.e., zone axis) and the electron beam diffracts off the crystal planes. These diffracted electrons interfere with each other, providing bright spots in the imaging plane which represent interference from different crystal planes. The distance and angles between each diffraction spot for multiple zone axes are compared to reference databases to determine the indices of each diffraction spot and identify the phase.

In this study, SADPs were recorded for specimen T2. A selected aperture was used to select individual crystal grains or glass regions and diffraction patterns were collected using the Gatan Digital Micrograph software. For crystalline regions, the sample was tilted to collect a DP from a second major zone axis so that phases could be identified. Diffraction patterns for crystals inside the amoeboid and outside the amoeboid were collected and analyzed. Example diffraction patterns are shown in Figure 2.10.

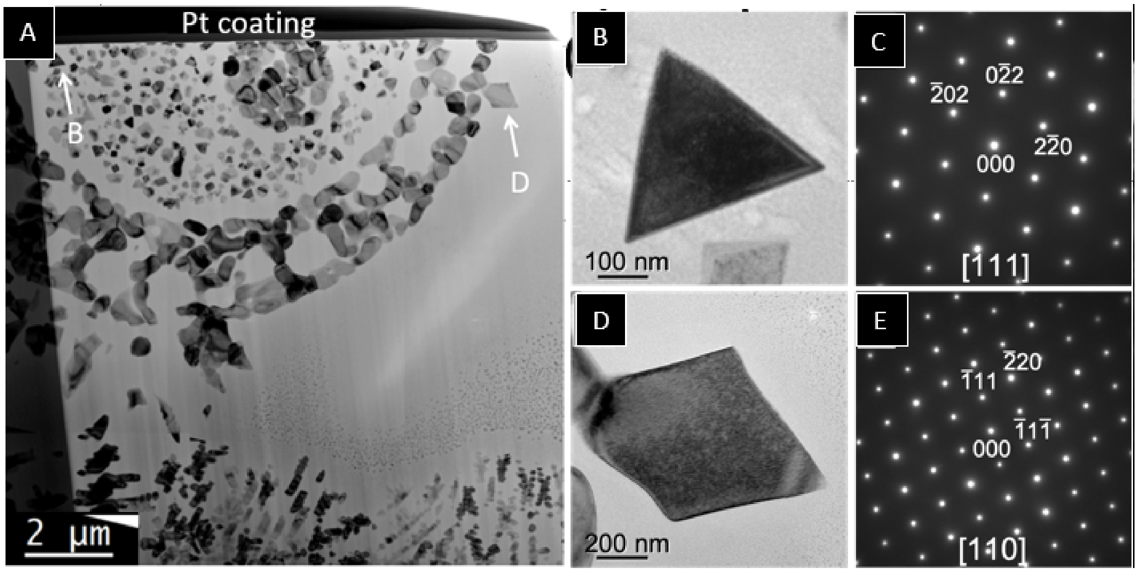

Figure 2.10: Selected area diffraction patterns from specimen T2. (A) Bright field image of the T2 thin section with two crystals used for SADP collection. (B) BF image of a triangular projection crystal inside the amoeboid with (C) its associated SADP. (D) A diamond projection crystal located on the amoeboid shell with (E) its associated SADP. All electron diffraction patterns match the inverse spinel structured magnetite (Fe_3O_4: Fd-3m, a = 8.3985 Å)[22].

2.4 Nano-scale Secondary Ionization Mass Spectrometry

Secondary ion mass spectrometry (SIMS) is a technique that can measure elemental and isotopic compositions in a sample using a mass spectrometer. In this method, a primary ion beam is used to probe a sample with sufficient energy to ionize the atoms in the sample. These secondary ions are then accelerated away from the sample surface and into a mass spectrometer. The charge to mass ratios of each isotope results in collection into different ion detectors and counted. Additional details on NanoSIMS can be found in [66]. In this study, a Cameca NanoSIMS 50 instrument was used to analyze a variety of regions in sample F27, F29, and F34. A primary O- ion beam was used with a current of 500 pA with a beam diameter of $\sim 1\ \mu$m. A variety of species were measured using electron multipliers, of which $^{30}Si^+$, $^{42}Ca^+$, $^{54}Fe^+$, $^{63}Cu^+$, and $^{239}Pu^+$ are reported in this study. The detector collecting $^{30}Si^+$ was saturated using these beam conditions, and so for some measurements it is not reported. The secondary beam mass resolving power was $\sim$ 3600. The ^{54}Fe mass peak had an interference from $^{27}Al_2$, and ^{63}Cu had interference from $^{23}Na^{40}Ca$, $^{24}Mg^{39}K$, and $^{23}Na^{24}Mg^{16}O$, but were resolvable by collecting ions on the shoulders of the mass peak where

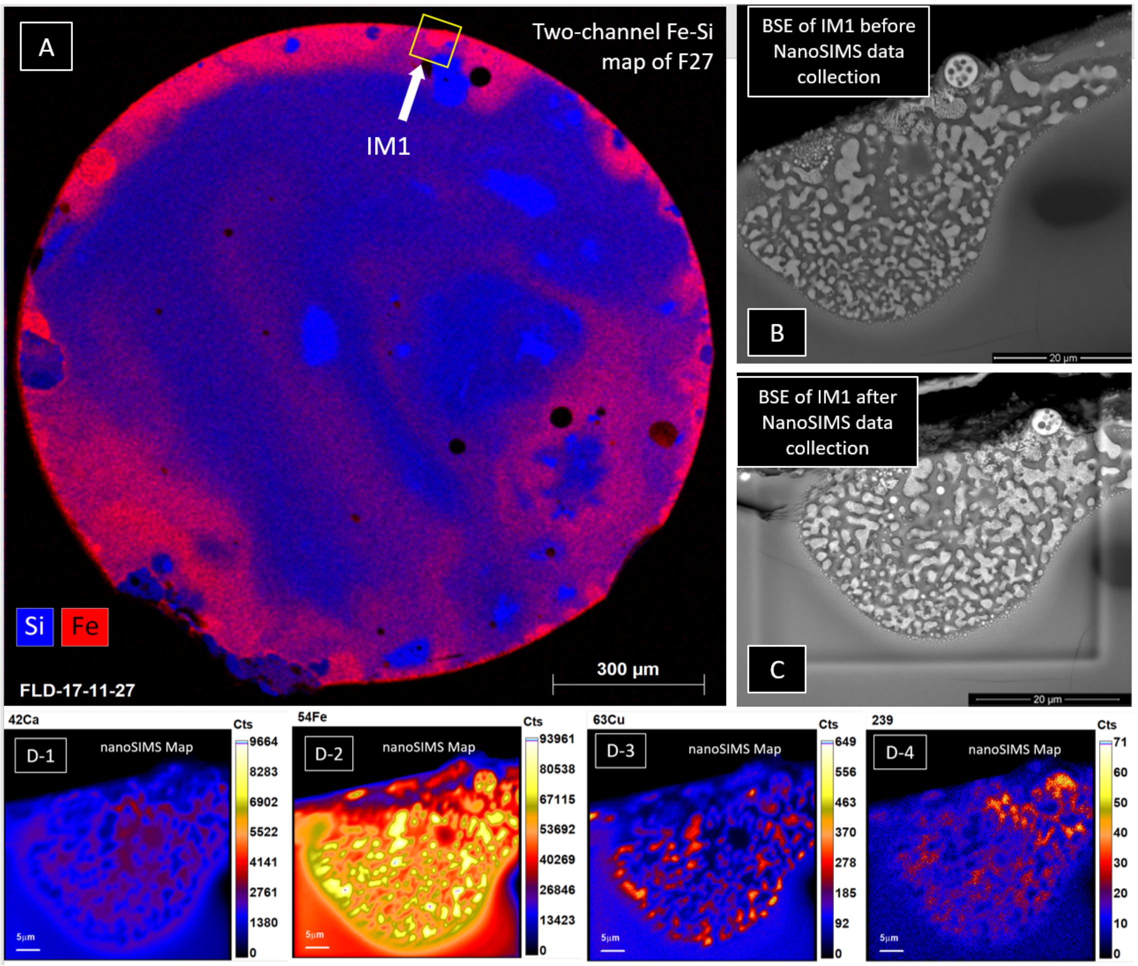

Figure 2.11: Example of NanoSIMS analysis. (A) Two-channel Fe-Si map of sample F27 with the location of NanoSIMS map IM1 annotated. The before (B) and after (C) BSE iamges of the IM1 region are shown. Note the destructive nature of ion beam rastering, which can affect spatial resolution between the two observable phases as the ion beam ablates material for analysis. Fe-rich phases (brighter regions) and Fe-poor phases (darker regions) in the BSE images are characteristic of immiscible textures (see chapter 3 for further discussion). Bottom row shows four ion maps (D-1 through D-4) that were collected, where pixel intensity represents the qualitative spatial distribution of of each ion present in the region.

Table 2.1: Overview of collected NanoSIMS maps. 'Glass' refers to regions without immiscible textures. Each cycle is a single raster over the ROI.

NanoSIMS Map	Sample	Raster Size	Description	Number of cycles
R1	F27	10 x 10 μm^2	Glass	40
R2	F27	10 x 10 μm^2	Glass	40
R3	F27	10 x 10 μm^2	Glass	40
R4	F27	10 x 10 μm^2	Glass	40
R5	F27	10 x 10 μm^2	Glass	40
R6	F27	10 x 10 μm^2	Glass	40
IM1	F27	40 x 40 μm^2	Immiscible Textures	22
IM2	F29	40 x 40 μm^2	Immiscible Textures	60
IM3	F29	40 x 40 μm^2	Immiscible Textures	60
R7	F29	10 x 10 μm^2	Glass	25
IM4	F34	15 x 15 μm^2	Immiscible Textures	40

the interference is not present.

Data Collection

In this study, a total of 11 NanoSIMS maps were collected and are summarized in Table 2.1. Each map is constructed by aligning and summing multiple cycles, where a cycle is a single raster of the region of interest. Seven maps from glassy regions without immiscible textures were collected: Six in sample F27, and one in sample F29. All of these maps were collected using a raster area of 10 μm x 10 μm. Four maps from immiscible regions were collected: one from sample F27, and two from sample F29, and one from sample F34. These maps were constructed using a raster area of 40 μm x 40 μm in samples F27 and F29, and 15 μm x 15 μm in sample F34. Map R7 was not initially planned, but during collection of IM2 and IM3, no significant Pu was detected. To ensure this absence of Pu was real and not an instrument error, a glassy region in F29 with higher radioactivity levels (according to autoradiograph measurements) was measured.

ROI and Cycle Selection

Ion maps were processed using the L'image software [66]. To make quantitative estimates, a constant concentration of ions must be present, and so early cycles that are not in sputtering equilibrium were rejected from analysis. For each map in this work, sputtering equilibrium was not achieved until after the first 3-5 cycles (due to sputtering of the surface carbon coating), and so these cycles were rejected for each analysis. To correct for beam drift, image alignment was conducted using the $42Ca^+$ images for maps IM1-IM4. For R1-R7, no features were readily observed that could be aligned on so no image alignment was used. For R1-R7, a 5μm x 5μm ROI in the interior of the ROI was chosen to avoid the influence of the trench wall effects. Cycles 6-28 for R1, 6-40 for R2-R5, 4-40 for R6, and 5-40 for R7 were selected for use in quantification.

For the IM1 40μm x 40μm raster, a region that was associated with the nearby mounting epoxy showed increased counts of each ion species and is attributed to re-deposition, and so was excluded from all ROIs. An ROI corresponding to the region of *in situ* immiscible textures (excluding the exterior amoeboid) was manually selected. Using ^{54}Fe count histogram binning, a threshold was selected that created two ROIs that best matched the sharp phase boundaries observed in the BSED. This resulted in three total ROIs: one capturing the entire region, one highlighting the identified *in situ* L_{Fe}, and one highlighting the identified *in situ* L_{Si}. An *ex situ* amoeboid ROI was isolated from the region by hand, and then a ^{239}Pu threshold was selected that approximately matched the boundary of the amoeboid and its halo. Due to sputtering through the smaller L_{Si} domains (Fig 2.12) in the *ex situ* amoeboid, summation of cycles resulted in loss of spatial resolution. Accordingly, no separate ROIs were created to distinguish between L_{Fe} and L_{Si}. For both the IM2 and IM3 a 40 μm x 40 μm raster and ROI corresponding to the region of immiscible textures was manually selected. Using ^{54}Fe count histogram binning, a threshold was selected that created two ROIs that best matched the sharp phase boundaries observed in the BSED. This resulted in three total ROIs for IM2 and IM3: bulk, L_{Fe}, and L_{Si}. For IM4, the sputtering rate burned through the immiscible amoeboid microstructure rapidly, which impeded the ability to sum cycle counts together in a way that preserved the spatial resolution of the amoeboid structure. Bins of 5 cycles were summed and for each bin image, the boundary was manually selected as a separate ROI. ^{63}Cu, ^{54}Fe, ^{42}Ca, and ^{239}Pu were extracted in counts/pixels-sec for analysis.

Plutonium Quantification

To quantify the Pu concentration in each selected ROI, the procedure described by Weisz [93] was used with a Pu-bearing silicate glass standard known as UPI, with major and minor element composition described in Table 2.2. Pu concentration in the UPI glass was 50+/-1 ppm. ^{239}Pu was 94% of total Pu, so a standard value of 47.2+/-1 ppm was used for ^{239}Pu. Unfortunately, Pu-bearing silicate glass standards are rare, and so the UPI standard is not well matched to the sample matrix. The most significant difference is in Fe concentration, which has been shown to significantly affect relative ion yields. Because the magnitude of the matrix effect is unknown, measurement uncertainties are reported but underestimate true uncertainty. To investigate whether nonlinear RSF effects could account for unexpected behavior in the data results, REE RSFs calculated across a range of Fe concentration in Fe-rich glass were used [45].

The concentration of ^{239}Pu in each ROI is calculated using the following equation:

$$C_{ROI}^{^{239}Pu} = (\frac{^{239}Pu}{^{42}Ca})_{ROI} * C_{ROI}^{Ca} * RSF_{Pu} * \frac{A_{^{239}Pu}}{A_{^{42}Ca}} \tag{2.1}$$

where $\frac{^{239}Pu}{^{42}Ca})_{ROI}$ is the measured ratio of ^{239}Pu to ^{42}Ca in the ROI, C_{ROI}^{Ca} is the concentration of Ca in wt% in the ROI measured using EDS, RSF_{Pu} is the relative sensivity factor of Pu

Table 2.2: Major element oxides in wt% in UPI standard glass.

UPI Major Oxides	**SiO_2**	**Al_2O_3**	**K_2O**	**Na_2O**	**Fe_2O_4**	**CaO**	**MgO**	**MnO**	**TiO_2**
(wt%)	56.48	12.55	7.05	0.09	0.28	16.29	7.21	0.01	0.08

in relation to Ca measured using the UPI standard under the same anlytical conditions, and $A_{^{239}Pu}$ is the isotope abundance of ^{239}Pu in the standard (measured), and $A_{^{42}Ca}$ is the natural isotopic abundance of ^{42}Ca. The RSF is defined as:

$$RSF_{Pu} = \frac{(C_{Pu}/C_{Ca})_{Standard}}{(I_{Pu}/I_{Ca})_{Standard}} \tag{2.2}$$

where C_{Pu} and C_{Ca} are the known ^{239}Pu and ^{42}Ca concentrations in the standard, and I_{Pu} and I_{Ca} are the measured count rates of ^{239}Pu and ^{42}Ca in the standard using repeated measurements. The RSF in the UPI standard was calculated to be 19.5+/-0.4. This uncertainty only represents the measurement uncertainty, and does not quantify the uncertainty in RSF due to the difference in matrix in the samples.

In order to calculate the ^{239}Pu concentration according to equation 2.2, the Ca concentration is needed for each ROI. For R1-R7, two SEM-EDS spectra per ROI were collected using 5 μm x 5 μm rasters after NanoSIMS data collection was completed. One spectra was collected inside each NanoSIMS crater, and one immediately adjacent to the crater. Rasters adjacent to the craters were not significantly different in composition and had better quantification (greater than 95%), so they were used for Ca wt% values. For IM1, ROI Ca composition was estimated using averages of multiple spot analyses taken prior to NanoSIMS analysis. L_{Fe} composition was calculated using an average of 7 spot analyses taken from different locations, and L_{Si} was calculated using an average of 5 spot analyses in different locations. A raster over the exposed cross section of the *ex situ* amoeboid ROI was used to estimate its Ca composition. Spot analyses were used to estimate Ca composition of ROIs in IM2 and IM3 (sample F29) and are reported in Chapter 3, but are not used for quantification since Pu values were insignificant. An estimation of the amoeboid ROI in IM4 (sample F34) was collected by EDS raster. High sample sputtering caused the boundary of the amoeboid to shrink over sputtering time, making Pu quantification of the entire amoeboid unreliable. All collected EDS data and NanoSIMS data are reported in Chapter 3.

Measurement errors are propagated through these calculations, but the effect of poor matrix match is not known. To address this issue, two approaches were used. First, the range of possible non-linear RSF values is used to apply conservative error bars to the data. Systematic variation of Pu RSFs according to Fe concentration in glass has not been conducted. However, Lehmann [45] systematically investigated the effect of trace REE RSFs as a function of Fe concentration ranging from values close to that of the UPI standard to Fe concentrations in this study. While trace REEs will have different RSF behavior than Pu, and Lehmann used basis of Si instead of Ca, this approach estimates the general magnitude

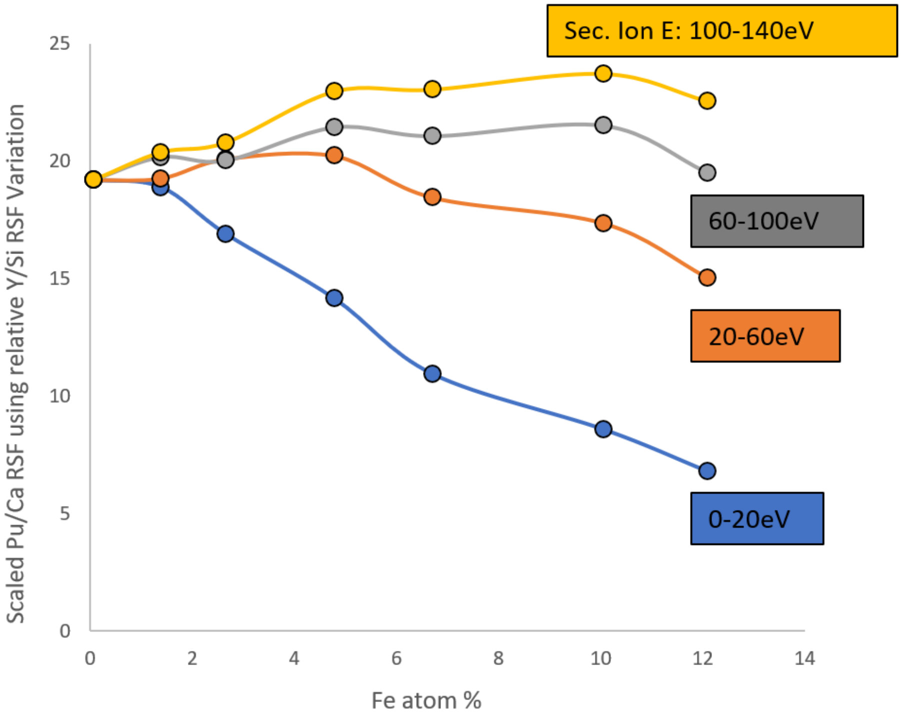

Figure 2.12: Influence of Fe content on relative sensitivity factors in Fe-rich silicate matrices. Lehmann RSF variation as a function of Fe atom%. Pu/Ca RSF is calculated based on relative variation in Y/Si RSFs. Each curve represents RSF variation for a given bin of secondary ion energies. The nonlinear behavior of Pu/Ca will be different from that of REEs referenced to Si but data are limited. This approach gives the reader a general idea of how variations in local Fe concentrations my influence final Pu concentration estimations.

of the effect for trace species. Lehmann analyzed the nonlinearity of RSFs as a function of the secondary ion energies using a voltage offset approach. The Cameca NanoSIMS 50 instrument does not currently have the ability to discriminate between secondary ion energies, so we calculate conservative bounds on the Pu ppm values by taking the absolute minimum/maximum RSFs across all Fe concentrations and secondary ion energies. In the Lehmann study, each REE saw varying levels of variation. In this study, the RSF with the largest variation was chosen (Y/Si). For Y/Si, RSFs deviated by +24% at 10 atom % Fe for 100-140 eV secondary ions and -65 % at 12 atom % Fe for 0-20 eV secondary ions. These large uncertainties are presented with NanoSIMS quantification in chapter 3.

A second way to address the matrix mismatching is to investigate what effect the observed nonlinearity of RSFs in the Lehamnn study would have on any conclusions on trends in the data if similar RSF trends exist for Pu RSFs. To do this, for each ROI, the Fe concentration was used to predict RSFs for each secondary ion energy bin and for each REE. This percent deviation from the predicted RSF at Fe concentrations in the standard was calculated to estimate a new Pu concentration. This correction was applied to each ROI and plotted to determine if nonlinearities in the RSF for any single REE/energy bin combination altered the conclusions made about Pu data trends. The Pu/Ca RSF change with increased Fe atom% used in this study in shown in Figure 2.12 for the Y/Si Lehamann data. Since these data were analyzed using separate bins of secondary ion yield energies, there is an implicit assumption that secondary ion yield energy distributions do not significantly vary as a function of Fe concentration. Additional nonlinear behavior of Pu RSFs associated with changed in secondary ion yield, are not addressed in this study.

Chapter 3

Iron-Rich Fallout Characterization

A first step in understanding the influence of iron on a nuclear explosion is to characterize the record preserved in fallout formed in Fe-rich environments. This chapter details the results of characterization done on Fe-rich fallout using the methods described in Chapter 2, and provides the motivation for the work explored in Chapters 4-6. In Section 3.1 a general overview of the samples used in this study is provided. Section 3.2 discusses the chemical composition for a subset of those samples selected for semi-quantitative SEM-EDS. Section 3.3 describes the variety of micro-structures and textures observed within the samples using electron microscopy. In Section 3.4, SEM and TEM measurements of chemical compositions and structures are presented for a subset of the observed micro-structures referred to as 'amoeboids'. Section 3.5 describes the spatially resolved measurements of radioactivity in the samples and some relationships between radioactivity and chemical composition. Section 3.6 discusses two possible theories for amoeboid formation, the range of evidence for each, and implications of each hypothesis on understanding amoeboid formation. In Section 3.7, key findings and interpretations on the influence of iron on fallout formation are summarized.

3.1 Sample Overview

A total of 26 samples collected from a single historical event were characterized in this study and range in mass from 3 mg to 94 mg with diameters of 1-6 mm. Sample morphologies included spheres, teardrops, elongated spheroids, partially melted soil grains, and vesiculated glass. Of the 26 samples, 19 samples with smooth continuous surfaces are referred to as 'aerodynamic'. These surface features are believed to be formed as a result of air-quenched melts [20, 5]. The remaining 7 irregular samples are referred to as 'non-aerodynamic'. Though they may have underwent some level of airborne transport, their surfaces did not become sufficiently molten to result in aerodynamic quench surface textures. Figures 3.5 - 3.13 demonstrate the diversity of sample morphology using 6 select samples, with an optical image, a BSE image, a BSE image of the exposed cross section, and an autoradiograph of the exposed cross section. These samples are shown in the main text because of either their

Figure 3.1: Optical images of all fallout samples used in this study. Samples with smooth continuous surfaces are labeled ‘Aero.’ for aerodynamic, and samples with irregular surfaces are labeled ‘Non-Aero.’ for non-aerodynamic.

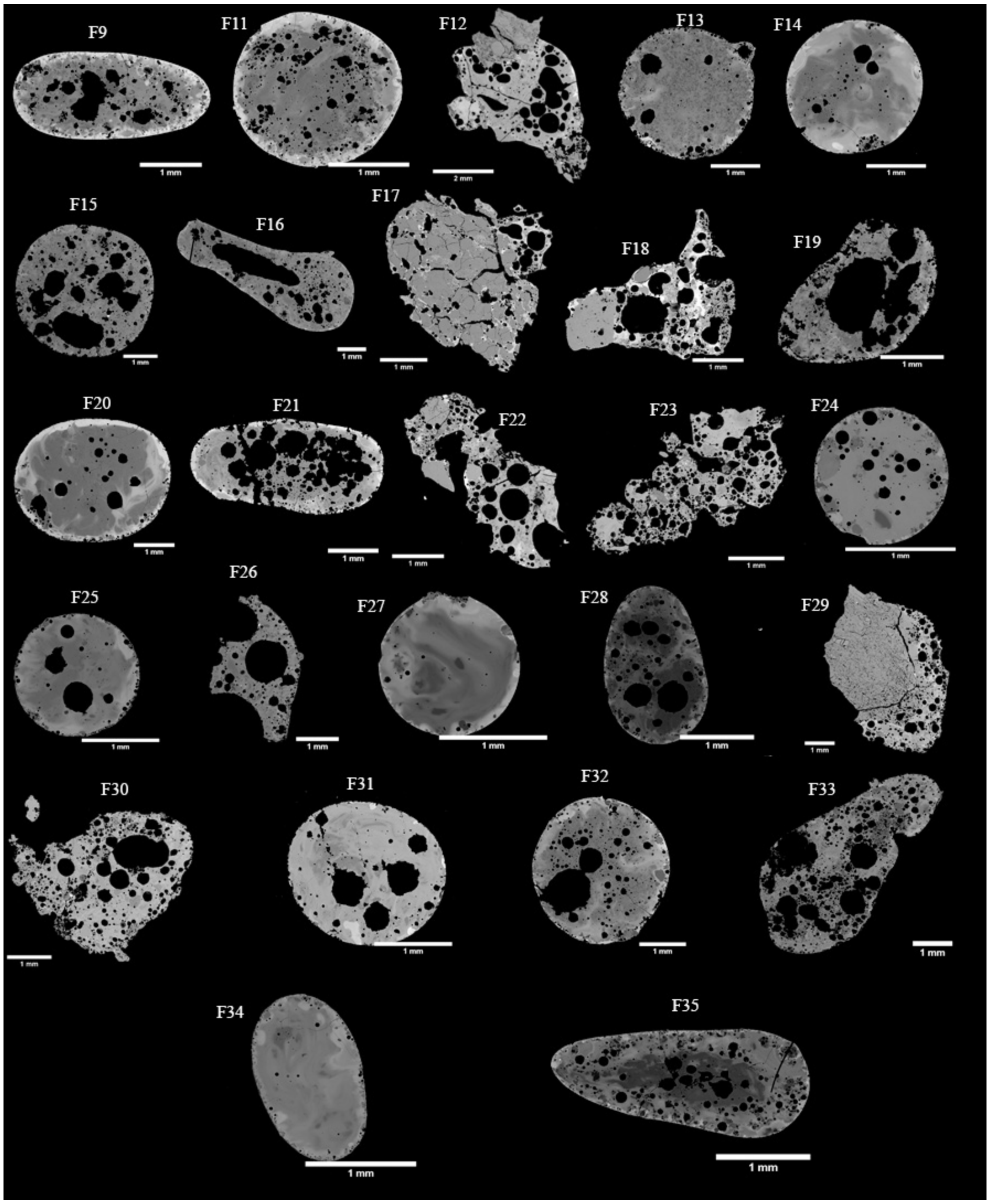

Figure 3.2: BSE images of cross sections of all samples following mounting and polishing. Each image is scaled for contrast, so contrast is not comparable between different images.

unique features (F13, F20, F31, F34), because of their use in NanoSIMS analysis (F27, F29, F34, see Section 3.5), or because they were samples for which more detailed amoeboid SEM analysis was conducted (F28, F34). Characterization images for all samples are provided in the appendices.

Auto-radiography of cross sections of all samples (Figure 3.3) revealed varying levels of

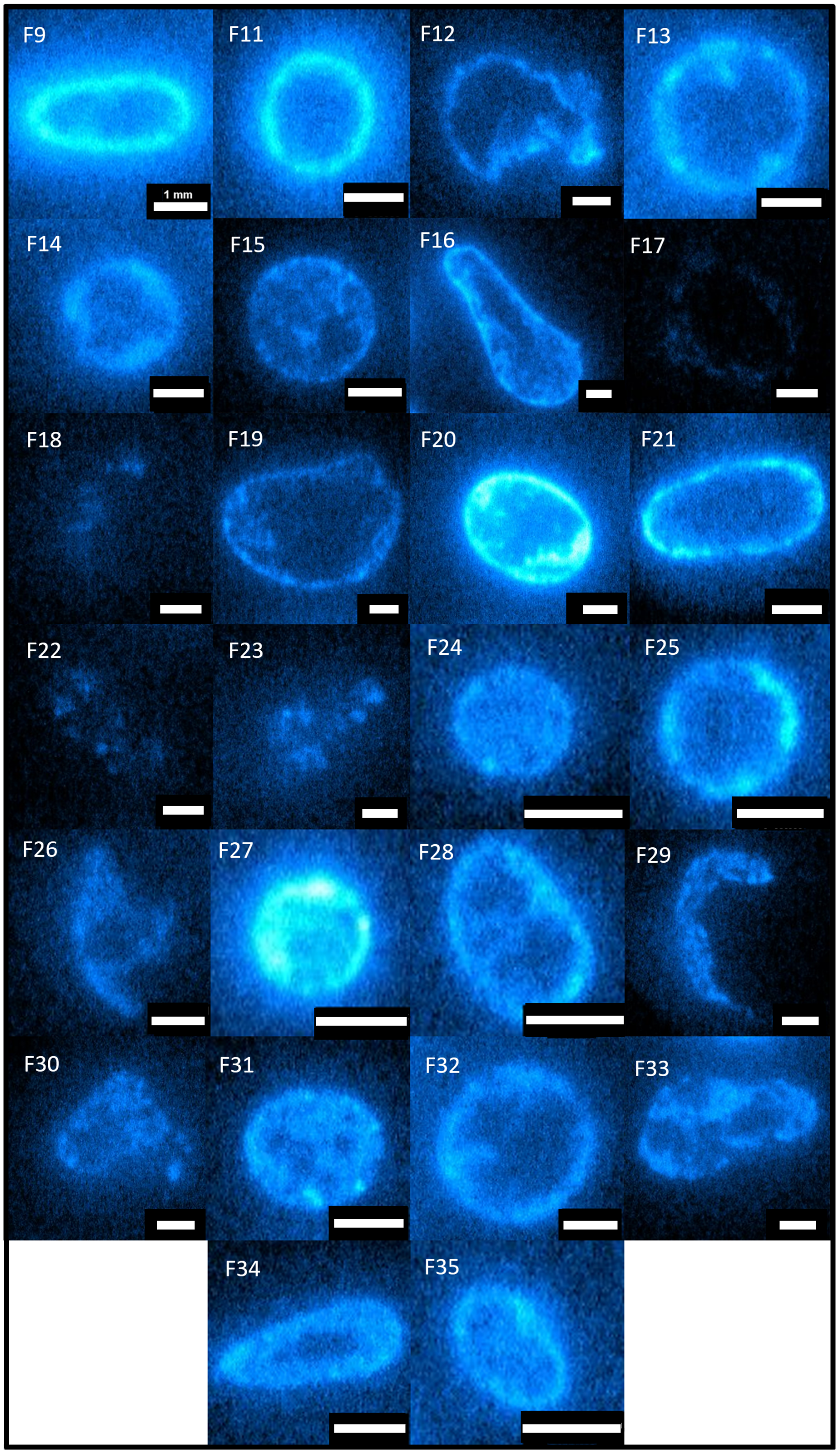

Figure 3.3: Autoradiography images of the exposed cross sections of each sample. All images were taken using the same exposure length, so pixel brightness is comparable between images. Scale bars on each image are 1 mm.

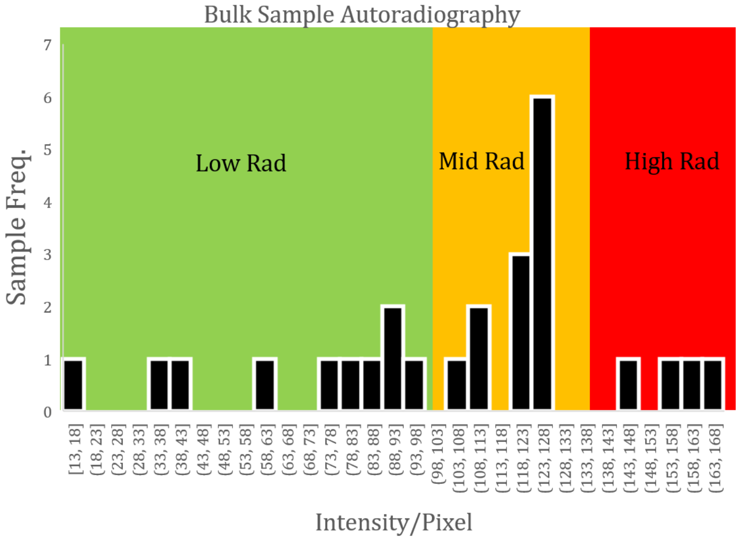

Figure 3.4: Histogram of autoradiograph measure of total radioactivity in Fe-rich samples. Radioactivity was measured by taking the sum of intensities for all pixels within the boundary of a given sample and divided by the total number of pixels. Samples were classified as low-activity (below 100), mid-activity (100-130), and high-activity (above 130) to distinguish between the primary peak of radioactivity and those in the tails of the distribution. All non-aerodynamic samples and two aerodynamic samples (F15, F19) are classified as low rad. F19, F11, F20, and F27 are classified as high rad. All the rest of the samples are classified as mid-activity.

radioactivity within the samples represented by pixel brightness. Most aerodynamic samples have radioactivity located along the their rims, though some (F24, F28, F31) were more homogeneous and lacked clear radionuclide rim-structure. The non-aerodynamic samples are less radioactive, with little to no radioactivity in un-melted grains, but still exhibit radioactivity in the glassy regions. A faint radioactive rim structure is present in one non-aerodynamic sample (F17). Comparison to BSE cross section images (Figure 3.2) reveals that the radioactive regions in fallout matches that of brighter contrast, higher Z/density regions of fallout in both aerodynamic and non-aerodynamic samples. These regions are best correlated to Fe concentration according to SEM-EDS maps and are here all amoeboid micro-structures are located. There is also a correlation to Ca and Mg in some samples, which is consistent with recent observation of actinide concentrations correlating to a Fe-Ca-Mg-rich glass [5]. This data suggests the presence of a radioactive, Fe-rich precursor that was deposited on the surface of aerodynamic samples, and is also the source (or rapidly mixed with melt) of glassy regions of non-aerodynamic samples. The connection between radioactivity and precursors will be more thoroughly investigated in Chapter 6.

The range of radioactivity varied significantly in these samples. Total intensity/pixel values for exposed cross sections for each sample was used as a metric to measure the concentration of radioactive species in each sample. A histogram of this metric (Figure 3.4) can be divided into three qualitative categories: low-radioactivity, mid-radioactivity, and high-radioactivity. Mid-radioactivity is defined as the region that encompasses the primary peak modal abundance (100-130 arb. units/pixel), while low radioactivity is values <100 and high radioactivity is >130. All non-aerodynamic samples and two aerodynamic samples (F15, F19) are classified as low-activity. Four aerodynamic samples (F9, F11, F20, and F27) are classified as high-activity.

Aerodynamic samples (F9, F11-F16, F19-21, F24-F27, F28, F31-F35, Figure 3.1) are black or reddish-black in color and have either a dull, metallic, or glassy luster. Samples F27 (Figure 3.5, 3.6) and F28 (Figure 3.8) have a unique mottled red and black surface. F12 has some surface irregularities caused by agglomeration of partially molten minerals and a portion of the glassy surface that has fractured off after formation, revealing an interior that appears to contain minerals that have not been melted. The majority of it's surface is still a smooth glassy surface, so this sample is still categorized as aerodynamic. F26 is not fully spherical, and has one side that exhibits a smooth curved surface, while the other side shows many exposed vesicles. This sample is most likely a fractured piece of an aerodynamic sample.

Some aerodynamic morphologies are categorized as spheres (F11, F12, F13, F14, F15, F20, F24, F25, F27, F31, F32). Three of these samples appear to have been broken or fractured after formation as spheres, revealing a white mineral core (F12) a clear glassy core (F20, Figure 3.9), and a black vesiculated glassy core (F26). Other aerodynamic samples are categorized as oblong spheroids (F9, F16, F19, F21, F28, F33, F35), and one aerodynamic sample is categorized as a teardrop (F34, Figure 3.10). There is evidence of smaller agglomerates on most sample surfaces in the form of spheres, half spheres, or globules that have been partially or fully subsumed into the sample. Agglomeration processes have been hypothesized to explain the inability of models to predict activity-size and size distribution of fallout. A study of their prevalence and compositions can be found in work by Lewis [46, 47]. Lewis found that agglomerate compositions were more homogeneous than their hosts, but were similar in overall composition. Interfaces between agglomerates and their hosts often preserve compositionally distinct boundary layers representing condensation from vapors rich in Si or rich in Fe, Ca, Mg, and bomb-derived U.

Non-aerodynamic samples (F17, F18, F22, F23, F26, F29, F30, Figure 3.1) have irregular surfaces and expose white, clear, or grey grains. These samples have glassy textures that suggest they underwent some degree of melting, but melting was insufficient to form continuous smooth surfaces characteristic of aerodynamic samples. Internally observed grains are often surrounding by a black glassy matrix (F17, F18, F22, F23, F30). Sample F29 is unique in that it is primarily composed of a singular white angular material with limited evidence of melting, and partially surrounded with dark glassy material (F29, Figure 3.12).

All sample cross sections reveal the presence of spherical vesicles in their interiors ranging form 10s of μms to 2.6 mm in diameter. One oblong sample (F16) contains a long elliptical vesicle 3.3 mm in length with a major axis oriented along the major axis of the sample. In non-aerodynamic samples, vesicles are present in glassy regions but are not present in un-melted regions (F29, Figure 3.12). Two aerodynamic samples (F27, Figure 3.5 and F34, Figure 3.10) are notable for their relative sparsity of vesicles. The few vesicles present in F27 and F34 are all less than 60 μm in diameter.

Generally, glassy regions of samples exhibit evidence of complex mixing processes, including evidence of viscous mixing in the form of schlieren textures[26], and some chemically distinct parcels reflecting un-melted or partially melted minerals, or melt parcels that were not well mixed with the rest of the samples. BSE images exhibit high-Z rim structures (brighter pixels) on 13 of the 19 aerodynamic samples. Glassy regions of non-aerodynamic samples are also associated with high-Z material. SEM-EDS analysis of samples (see Appendix B for qualitative SEM-EDS maps) revealed the high-Z rims to be greatly enriched in Fe. In some samples, rims are also enriched in Ca or Mg. Fe is the only element that was correlated to BSE image brightness in every sample. Spherical or spheroidal agglomerates observed on the surface of samples in optical and BSE imaging. In cross section, similar agglomerate features are observe, some of which appear to be partially or fully subsumed into sample interiors. Descriptions of characteristic samples are discussed further below.

Sample F27 (Figure 3.5) is an example of a spherical aerodynamic spherical sample with a mottled red/black metallic luster that is unique to this sample set and has not been reported in other fallout literature. Cross section images show the presence of one subsumed agglomerate, and pronounced schlieren textures with evidence of mixing of the Fe-rich rim into the sample interior. Relative compositional variation using qualitative SEM-EDS maps of F27 (Figure 3.6) reveal several examples of chemically distinct SiO_2 melt parcels are observed in the interior. The rim is enriched in both Fe and radionuclides, but lacks enrichment of Ca and Mg associated with the Fe-rich rim in other samples. Ca and Mg concentrations are relatively homogeneous throughout the interior, though still show evidence of viscous mixing. The subsumed agglomerate, however, if both Fe and Ca rich, but lacks notable Mg enrichment. Note that qualitative SEM-EDS maps in Figure 3.6 only show relative elemental distribution throughout the sample, and pixel brightness does not represent absolute concentrations. Remaining qualitative SEM-EDS maps are shown in the appendix, and a subset of samples selected for semi-quantitative analysis are discussed in section 3.2. This sample was also partially characterized using NanoSIMS techniques (section 3.5).

In contrast to F27, sample F31 (Figure 3.7) is an example of a spherical aerodynamic sample with a glassy luster on its surface. BSE imaging reveals the surface is compositionally heterogeneous, which is not readily observable with optical imaging techniques. Surface heterogeneity observed in BSE imaging is unique to this sample, and may reflect agglomerates that were incompletely subsumed into the sample. Some of these Fe-rich, radionuclide-rich agglomerates can be seen in the exposed cross section and are also enriched in Ca and Mg, and restricted to the rims of the sample. Schlieren textures similar to those observed in F27 are present. Vesicles up to 100s of μm in diameter are present that are quasi circular but lack smooth boundaries observed in most other vesicles in this study. Radioactivity

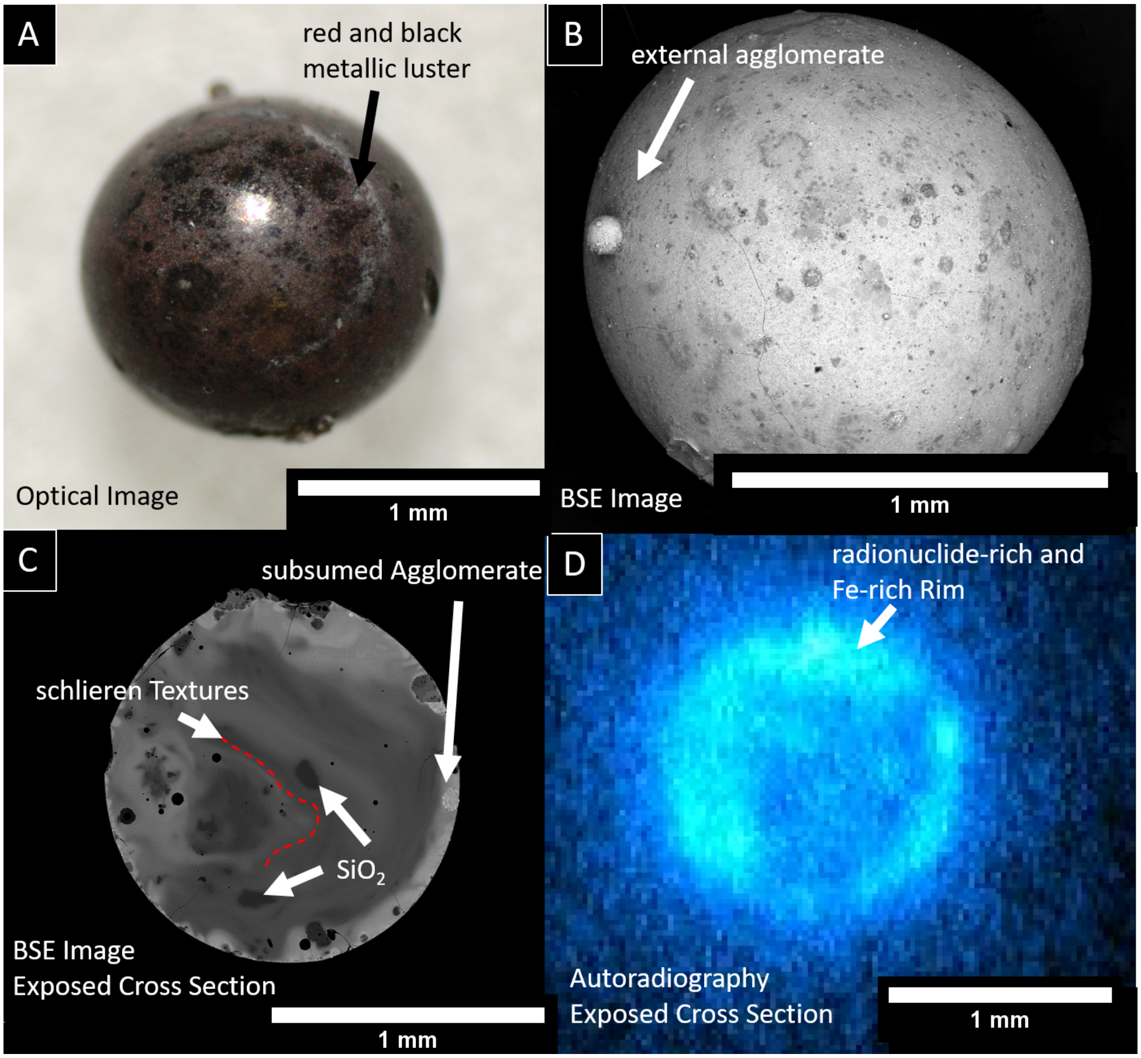

Figure 3.5: Overview of sample F27. (A) Optical image (B) BSE image (C) BSE image of the exposed cross section (D) autoradiography of the exposed cross section. Note the unique mottled red/black surface, and the presence of a spherical agglomerate. This sample has limited vesiculation, schlieren flow textures and relict SiO_2. Also present is evidence of a Ca-rich, Fe-rich spherical agglomerates that was subsumed into the interior of the sample. A radionuclide-rich rim also correlates well to the Fe-rich rim but lacks Ca and Mg enrichment associated with Fe-rich rims in some samples.

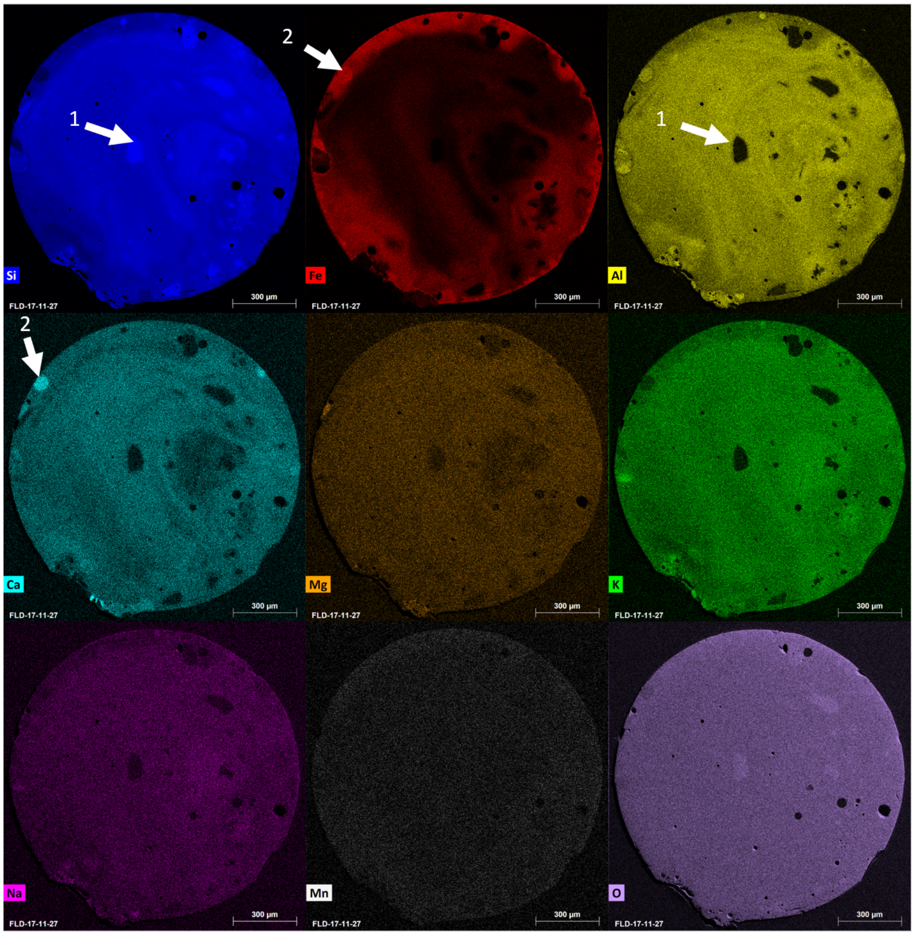

Figure 3.6: Qualitative SEM-EDS maps of sample F27. Each image represents relative concentrations of an element, but pixel intensities are not quantitative and should not be compared between element images. Euhedral Si-rich features depleted in other elements (arrow 1) are interpreted as relict quartz grains. The Mn and O maps are shown but the Mn signal is weak and O is prone to surface defect effects. F27 has an Fe-rich rim that contains an Fe-rich subsumed agglomerate (arrow 2), with bands of Fe enrichment along schlieren. No Ca or Mg enrichment is observed along the Fe-rich rim, but the subsumed agglomerate is enriched in Ca. Scale bars are 300 μm.

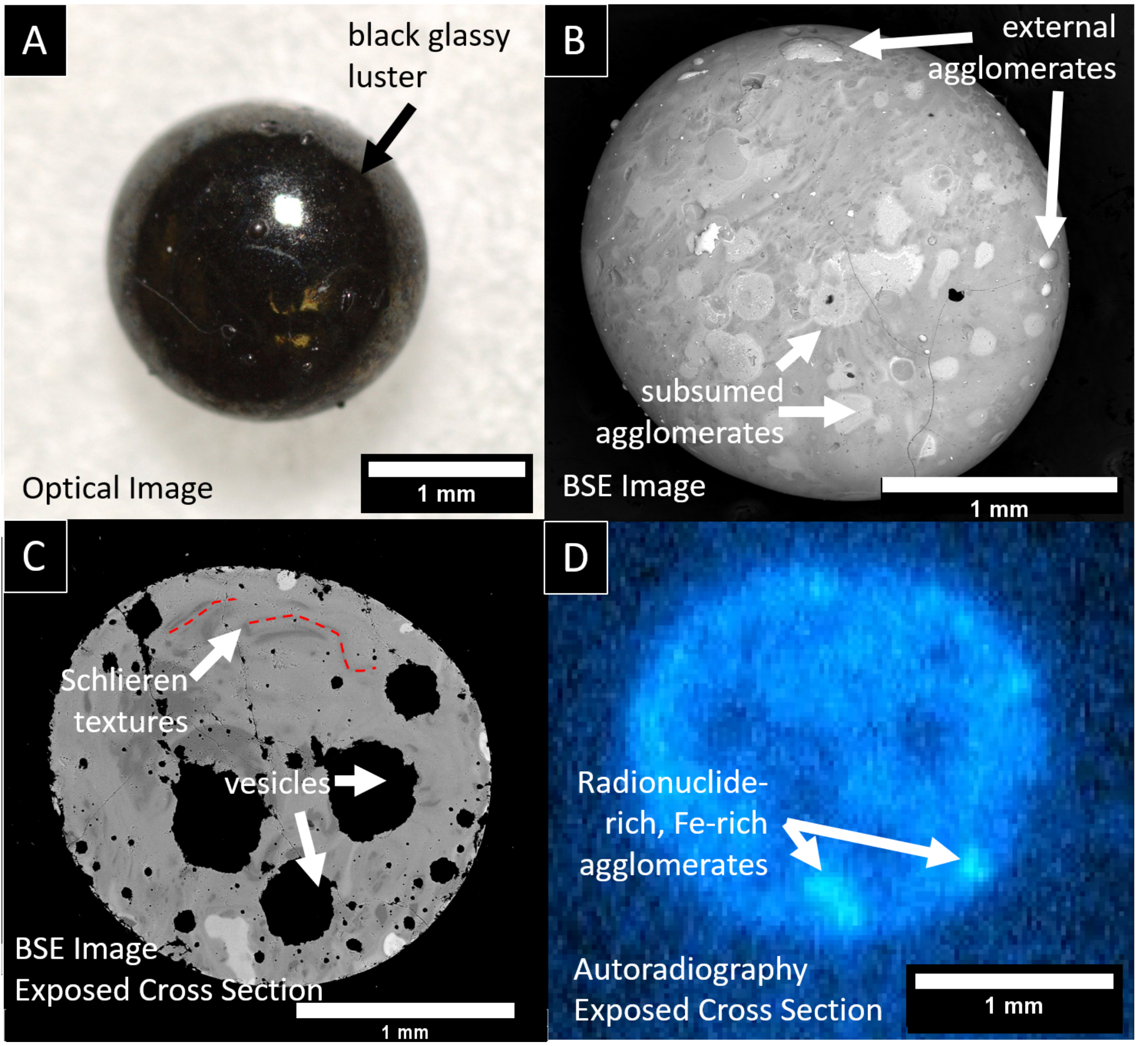

Figure 3.7: Overview of sample F31. (A) Optical image (B) BSE image (C) BSE image of the exposed cross section (D) autoradiography of the exposed cross section. Note the highly heterogeneous surface features in the BSE image which are not observable using optical imaging, and likely reflect chemically distinct agglomerates. Interior of the sample has vesicles that are 100s of μm in diameter and schlieren flow textures. Radioactivity is correlated with Fe, as can be seen in the radionuclide-rich, Fe-rich subsumed agglomerates (arrows in D). The radioactivity signature in this sample is more homogeneous than F27 and lacks the Fe-rich, radioactive rim observed in most other aerodynamic samples in this study.

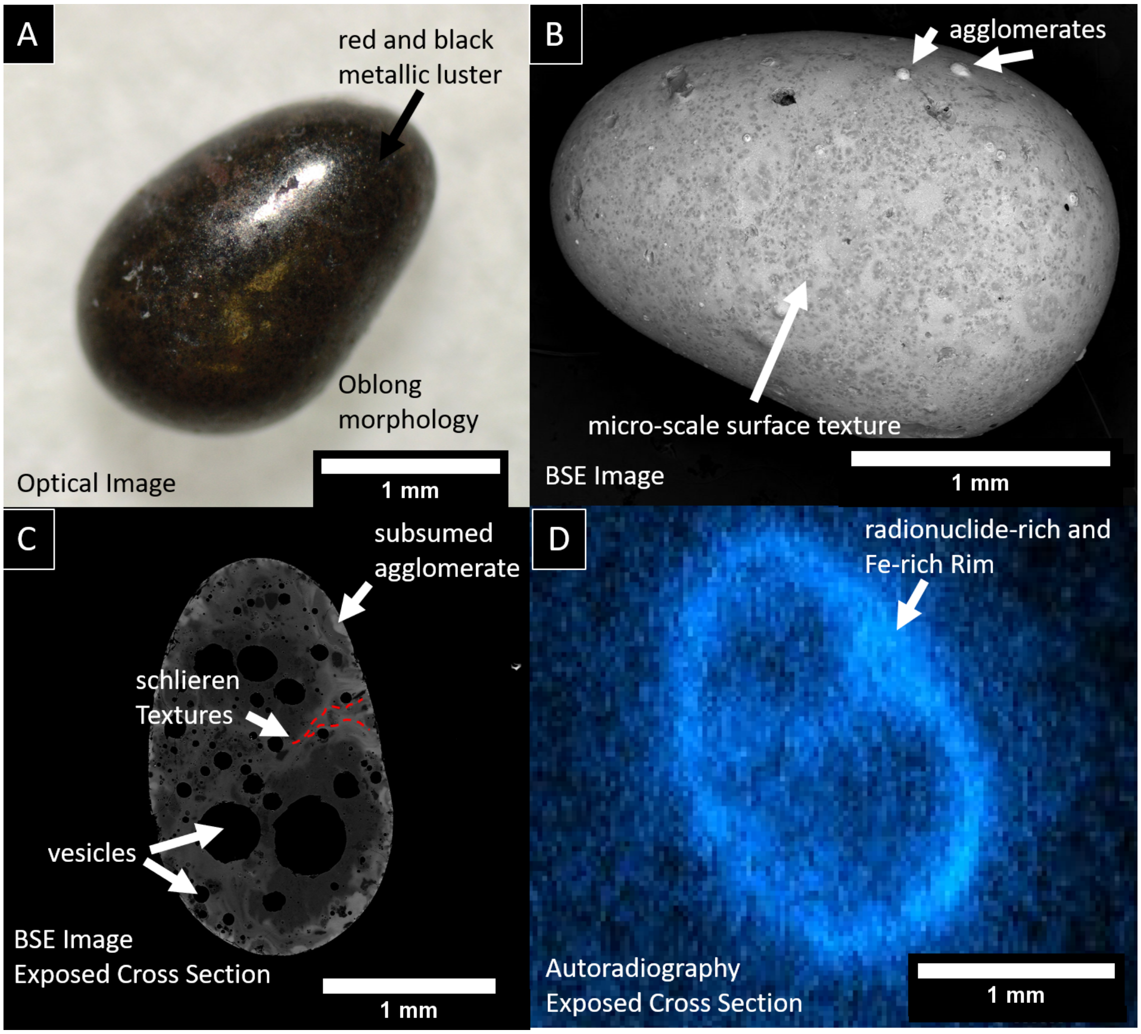

Figure 3.8: Overview of sample F28. (A) Optical image (B) BSE image (C) BSE image of the exposed cross section (D) autoradiography of the exposed cross section. Note the surface textures and presence of agglomerates. The interior contains vesicles and schlieren flow textures. The rim is enriched in Fe and radionuclides.

has a more homogeneous distribution in this sample compared to F27 and lacks the Fe-rich, radionuclide-rich rim structure. There is a positive correlation in radionuclides and Fe concentration in the Fe-rich subsumed agglomerates.

Sample F28 (Figure 3.8) is an example of an oblong aerodynamic morphology with a mottled red/black metallic surface similar to sample F27. Some micro-scale surface textures and agglomerates are shown in the BSE image. The cross section preserves similar schlieren textures and vesicles observed in other samples. This sample has an Fe-rich, radionuclide rich rim. K and Na are enriched around vesicles. This sample was used for additional analysis

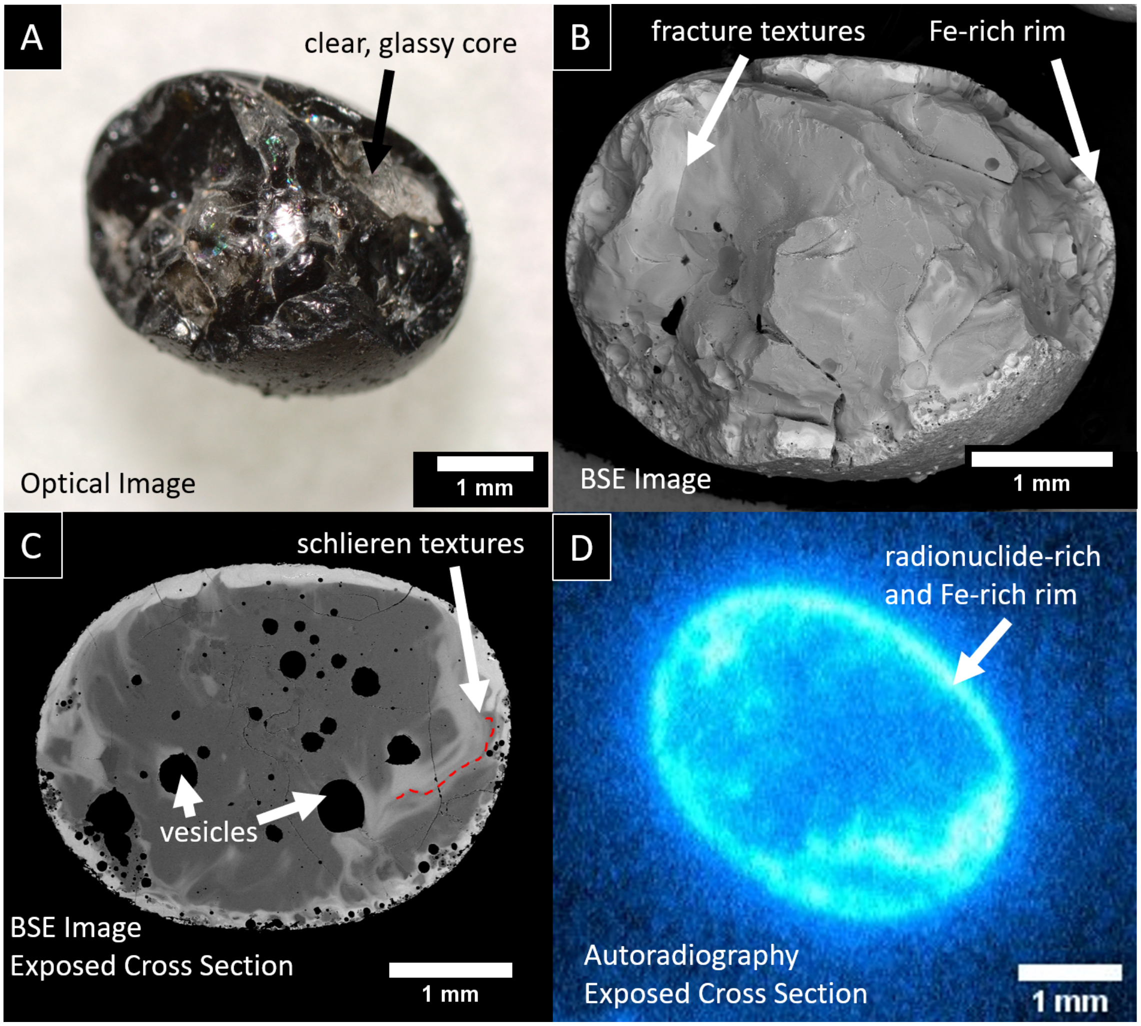

Figure 3.9: Overview of sample F20. (A) Optical image (B) BSE image (C) BSE image of the exposed cross section (D) autoradiography of the exposed cross section. Note in the optical image the presence of a clear glassy core and black surface which correlates to the Fe-rich rim observed in the BSE images, and which also correlates to radioactvity. Vesicles and schlieren flow textures are also present in the interior of this sample.

because of the micro-structural characteristics of the rim (Section 3.3).

Sample F20 (Figure 3.9) is an example of a spherical aerodynamic sample that fractured after formation. Optical images show a dull metallic sheen on the sample surface and a colorless glassy core with conchoidal fracture textures. Optical image of the interior appear dark because of the opaque shell. BSE cross section images and SEM-EDS maps reveal this rim structure is enriched in Fe, Ca, and Mg. This is in contrast to previous sample rims which were enriched in Fe but not in Ca and Mg. The prominent schlieren textures in the

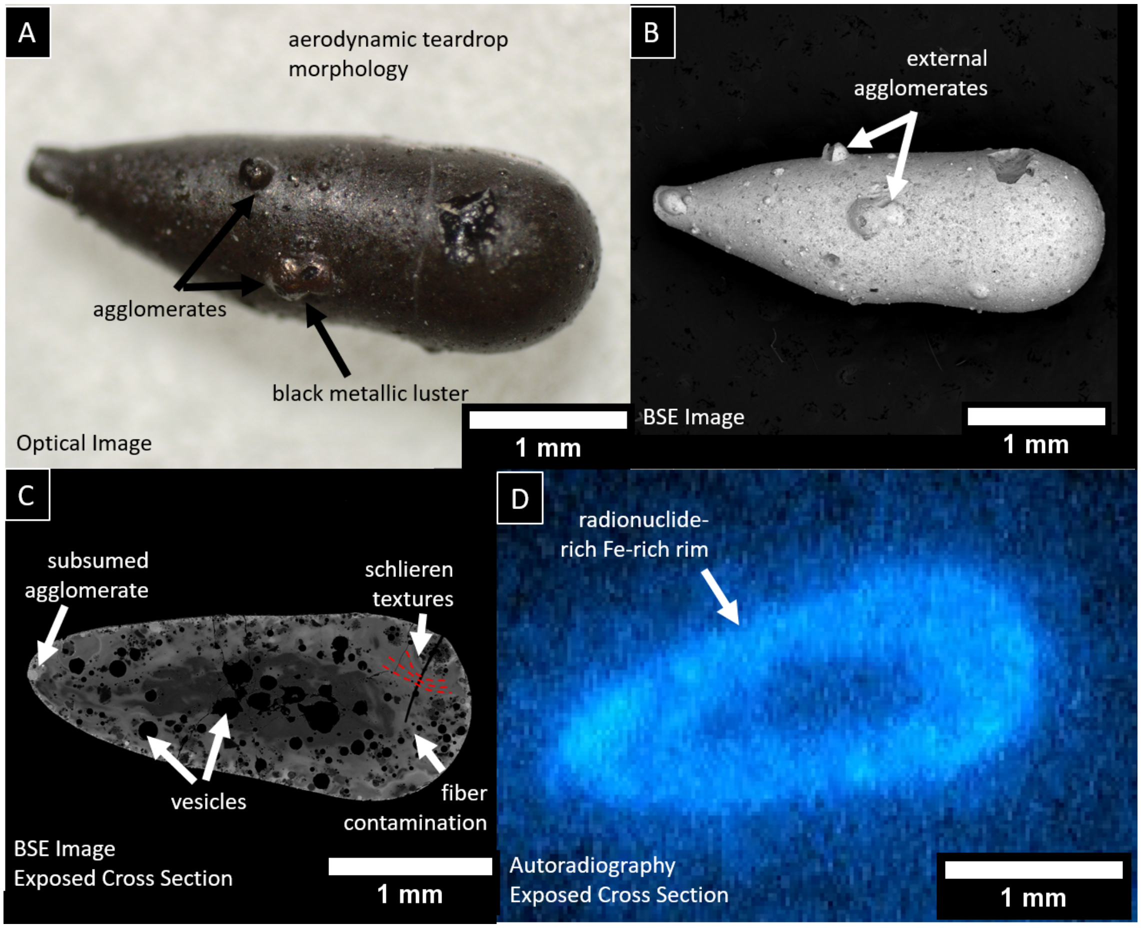

Figure 3.10: Overview of sample F34. (A) Optical image (B) BSE image (C) BSE image of the exposed cross section (D) autoradiography of the exposed cross section. Note the aerodynamic teardrop morphology and presence of spherical agglomerates. Interior features show subsumed agglomerates, vesicles, and schlieren textures. The linear dark feature in (C) is not a feature of the sample, but is a piece of non-fallout contamination (fiber) that was deposited on the sample after carbon coating. Radioactivity is correlated to Fe content.

exposed cross-section are consistent with mixing of the Fe-rich rim into the interior prior to quench. Sample F20 is significantly more radioactive than other samples (Figure 3.3).

Sample F34 (Figure 3.10) is an example of an aerodynamic teardrop sample with black metallic luster. The leftmost side of the sample exhibits evidence of fracture. Sample interior contains unique concentric layering. Rather than a simple Fe-rich rim, this sample has three diffuse compositional layers with evidence of viscous mixing between each layer. The core is enriched in Si, Al, Na, and K. Surrounding that core is a middle layer that is radionuclide-rich and is enriched in Fe, Ca, and Mg. The outer rim of the sample is Fe-rich but lacks co-located relative enrichment in Ca and Mg observed in the middle layer and in the rim of F20.

Sample F13 (Figure 3.11) is an example of a black spherical aerodynamic sample with an dull opaque luster with several spherical agglomerates attached to its surface. White flecks observed on the surface (approximately coincident with black speck features in the BSE image) appear consistent with adhered, un-melted dust particles. This sample contained enrichment of Ca and Mg in the Fe-rich rim similar to F20. The sample interior exhibits limited schlieren textures, but is notable for the abundant micro-scale euhedral Si-rich features dispersed throughout. Although dispersed Si-rich features are observed in other samples from this study (see F27), the scale and fairly uniform distribution of these features are unique to this sample. Interior vesicles are present, with one vesicle located within the agglomerate cross section. Autoradiography shows enrichment in radionuclide concentration along the Fe/Ca/Mg-rich rim and within schlieren textures. The agglomerate is not enriched in radionuclides and exists outside the radionuclide-rich rim, suggesting agglomeration after the sample incorporated significant radioactive vapor.

Sample F29 (Figure 3.12) is an example of a non-aerodynamic sample preserving melted grains and surrounded in part with dark glassy material. Qualitative SEM-EDS maps (Figure 3.13) reveal that the glassy material is enriched in Fe, Ca, and Mg relative to the entire sample. Vesicles revealed in the exposed cross section but are absent from the non-glassy core. This non-glassy core contains sanidine grains that preserve crystalline fracture patterns. The measured SEM-EDS composition is consistent with that of sanidine. These features together suggest this region is composed of un-melted sanidine. An intermediate region between the Fe-Ca-Mg-rich glass and un-melted sanidine exhibits diffuse compositional boundaries and spherical vesicles suggesting a transition from fully melted to unmelted host material. Sample F29 is one of the less radioactive samples - a result that is not surprising given the sample is dominated by un-melted sanidine. This sample was partially characterized using NanoSIMS (section 3.5).

3.2 Sample Major Element Characteristics

Samples are primarily composed of Si, Fe, Al, Ca, Mg, K, Na, and O as measured by qualitative SEM-EDS mapping of their exposed cross sections (see Appendix B). All aerodynamic sample rims and glassy regions of partially molten non-aerodynamic samples have some level of Fe enrichment. In some cases (F13, F14, F20, F21, F28, F32, and portions of F34) the Fe-rich regions are also enriched in Ca and Mg. A subset of the samples were analyzed using longer (12 hour) SEM-EDS mapping techniques to acquire semi-quantitative estimates of composition. Si-rich, Al-poor features are likely un-melted or incompletely mixed relict quartz grains. Otherwise, Si is generally associated with the Al, Na, and K, indicative of aluminosilicate minerals. Fe, Ca, and Mg show variable behavior, with spatial correlations observed in some samples. Fe-rich rims are common, but some are not spatially correlated to Ca or Mg concentrations.

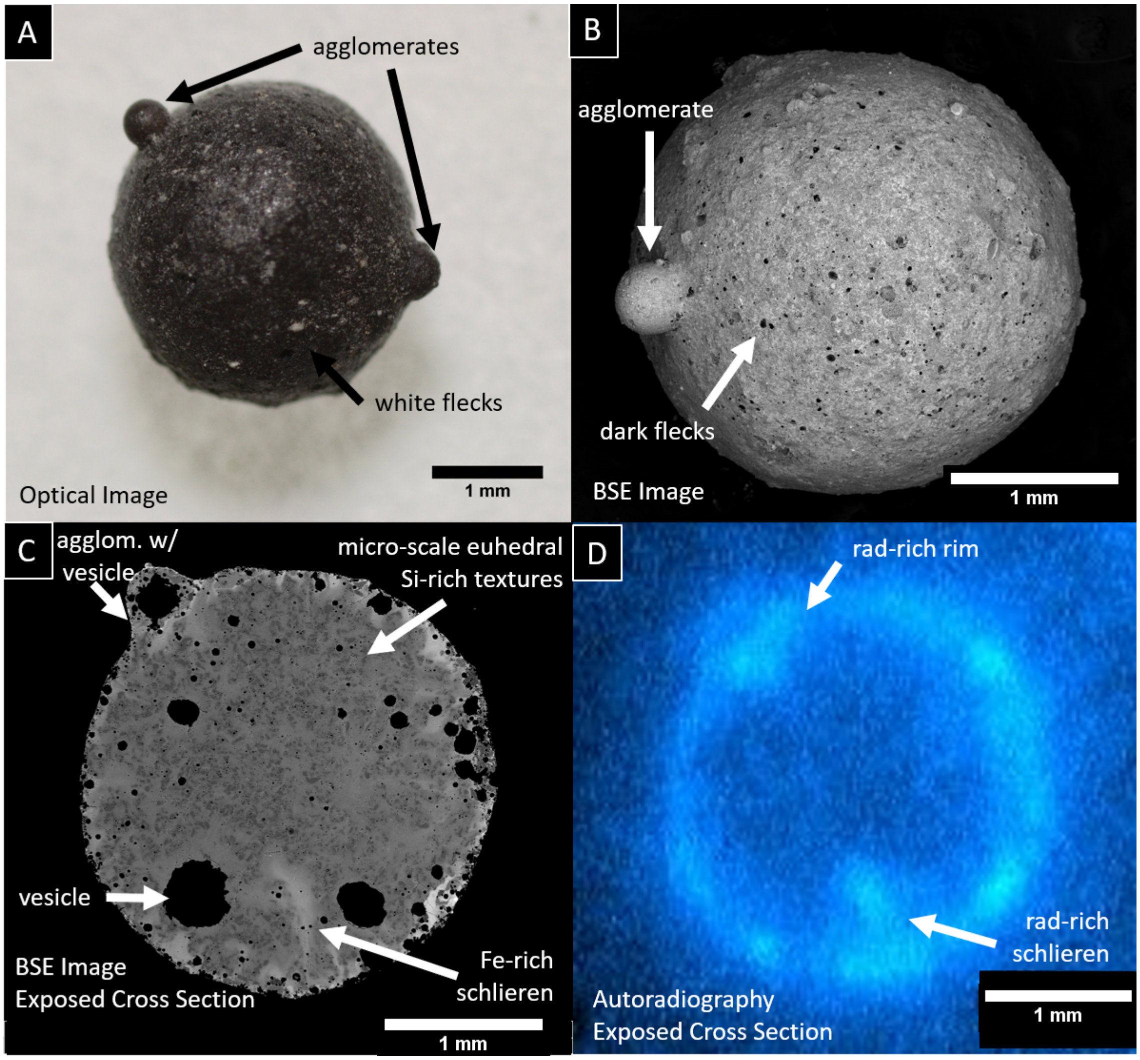

Figure 3.11: Overview of sample F13. (A) Optical image (B) BSE image (C) BSE image of the exposed cross section (D) autoradiography of the exposed cross section. Note the presence of smaller surface spherical agglomerates, interior vesicles (including a vesicle in one agglomerate). Micro-scale white flecks in optical and black flecks in BSE images are seen on the surface of the sample. Sample interior exhibits micro-scale compositional heterogeneity with a dispersion of euhedral Si-rich features. Interior vesicles are present from 10s of μms to 100s of μms and the rim of the sample is enriched in radionuclides.

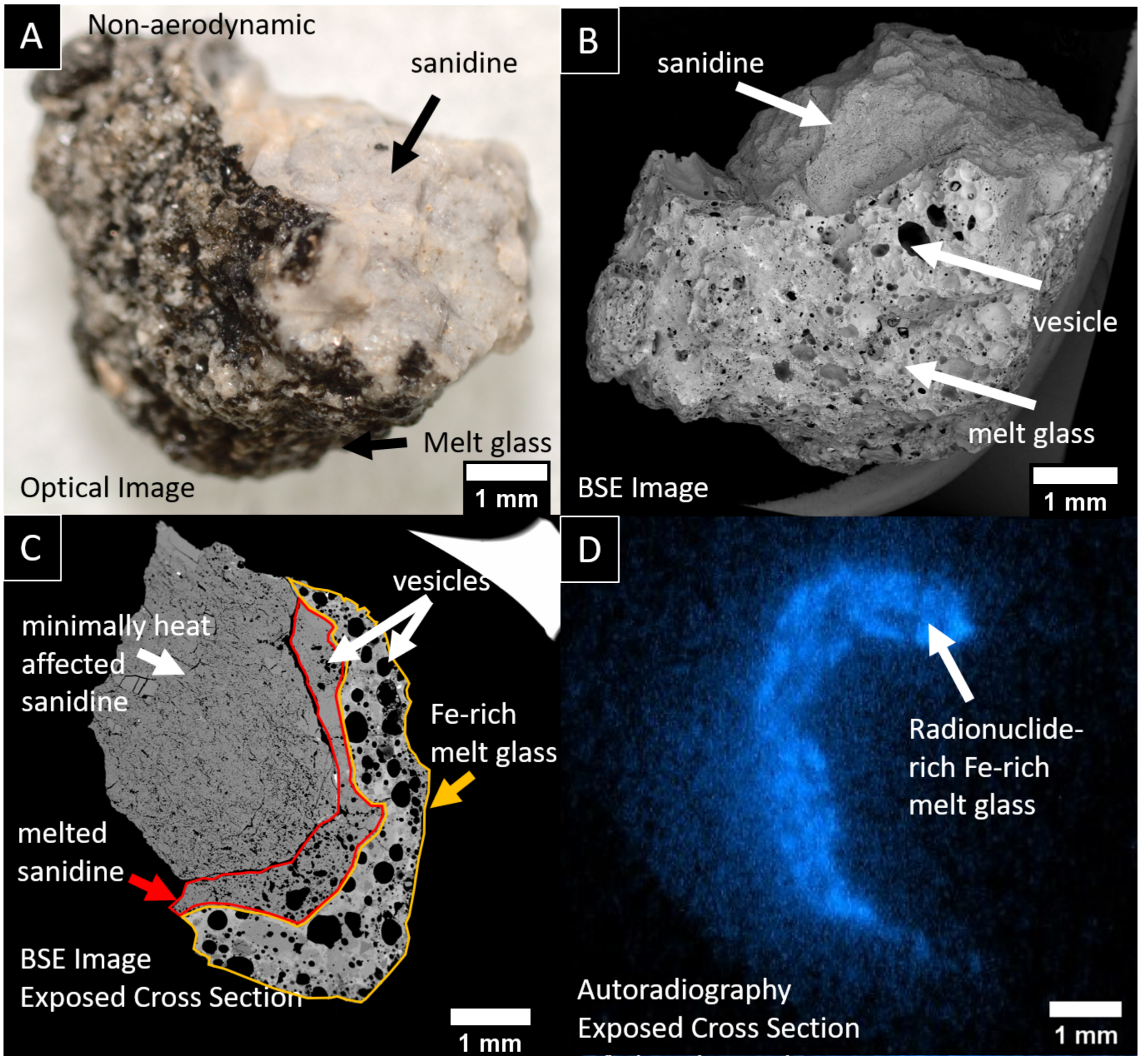

Figure 3.12: Overview of sample F29. (A) Optical image (B) BSE image (C) BSE image of the exposed cross section (D) autoradiography of the exposed cross section. Note the minimally heat-affected sanidine grain without vesicles in this non-aerodynamic sample which contains no measurable radioactivity (via autoradiograph) in contrast to the radioactivity-rich glassy region with significant vesicularity. The boundary between the glassy region and un-melted sanidine matches sanidine composition but has vesicles. This regions represents a transition where the sanidine was melted but did not significantly mix with the radioactive, Fe-rich source term.

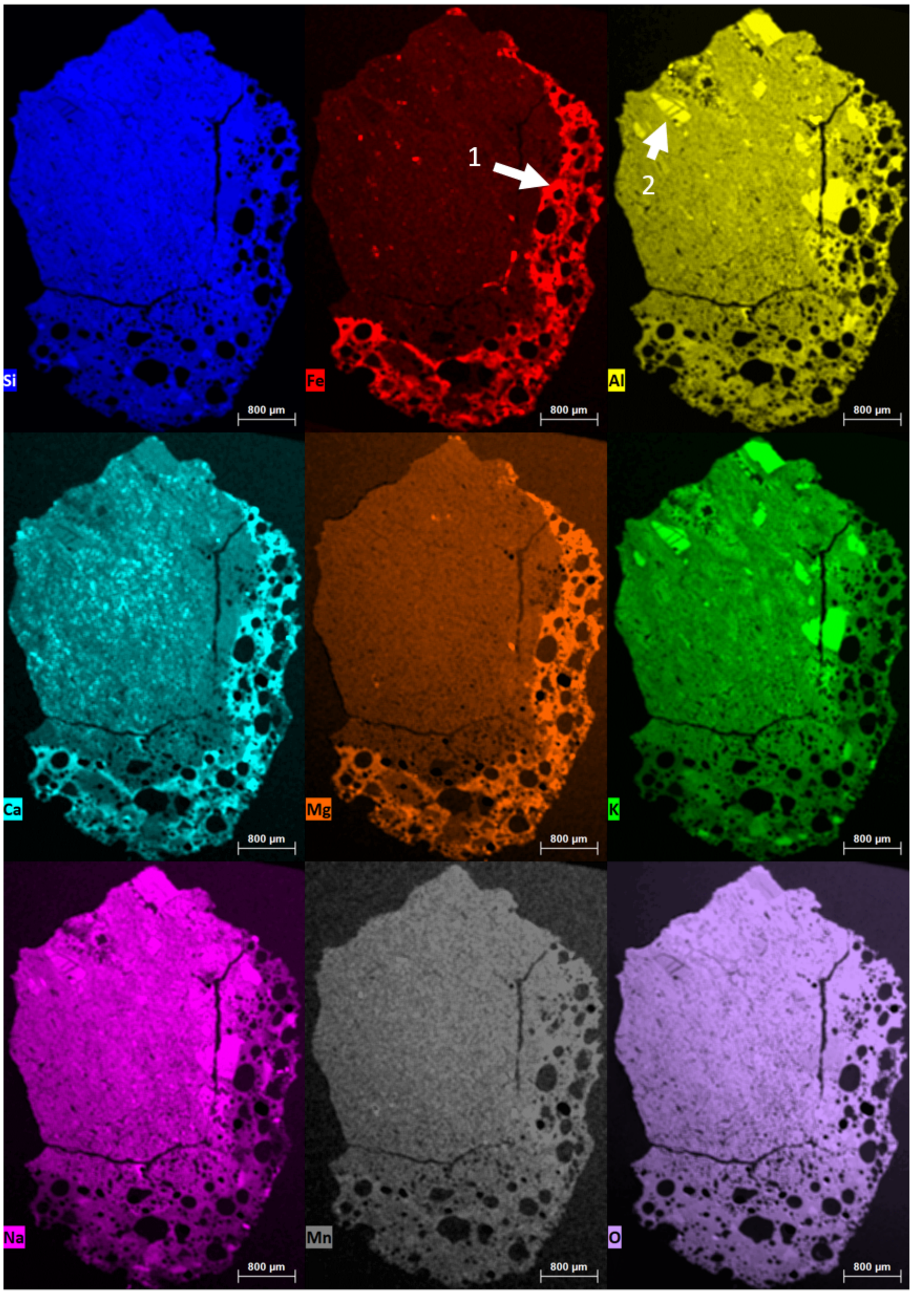

Figure 3.13: Qualitative SEM-EDS maps of sample F29. Each image represents relative concentrations of an element, but pixel intensities are not quantitative and should not be compared between element images. The glassy, vesicular region (arrow 1) is enriched in Fe, Ca, and Mg relative to the rest of the sample. The un-melted region of the sample contains euhedral grains with crystalline planar fractures (arrow 2) and compositions matching sanidine. The intermediate region with vesicularity but lacking Fe-Ca-Mg-enrichment suggests the melt did not incorporate the Fe-rich radioactive source. The Mn map signal is very weak and O is prone to surface defect effects.

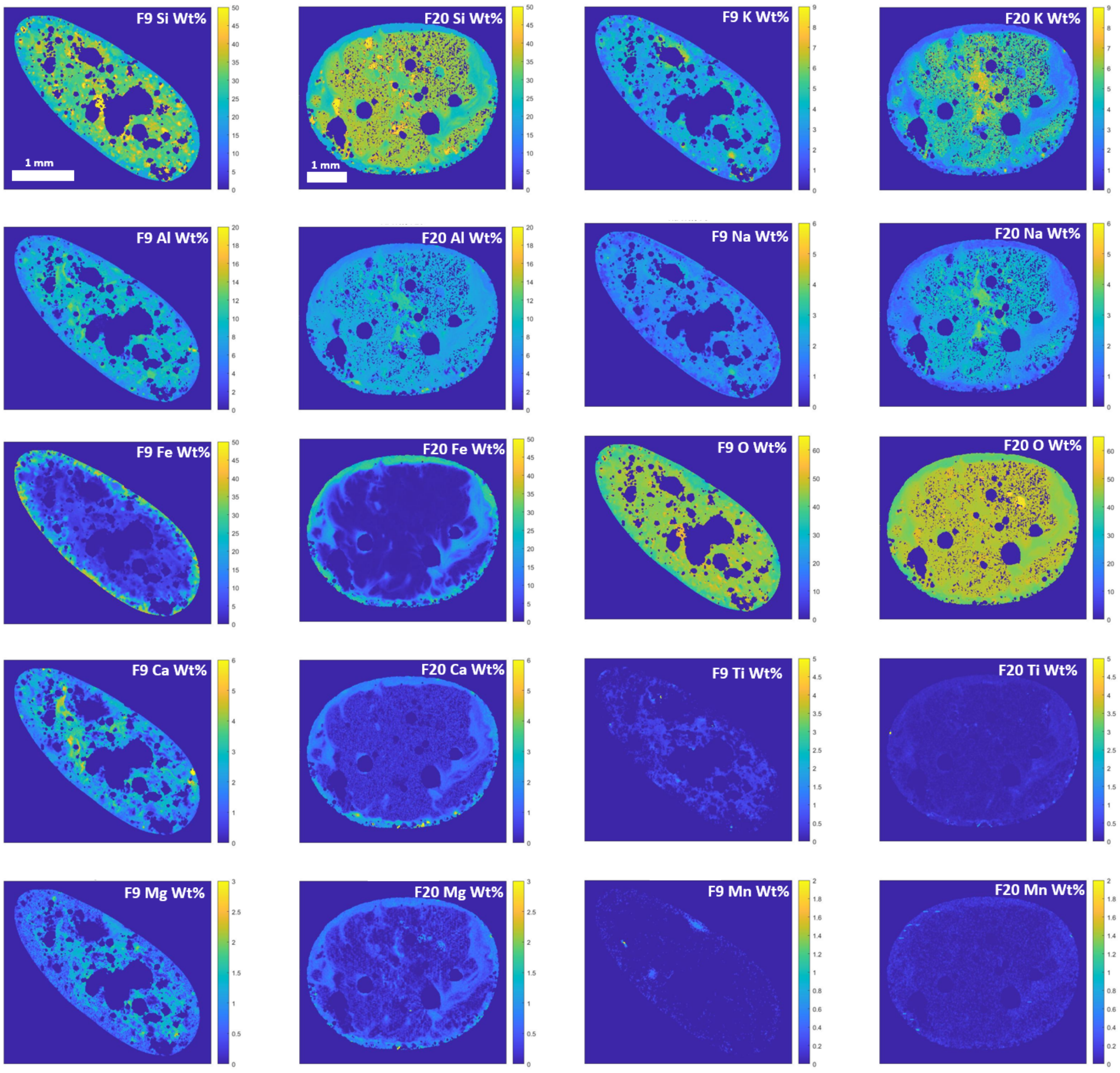

Figure 3.14: Semi-quantitative SEM-EDS Maps of F9 and F20. Maps for each sample can be found in the appendix. Scale bars are the same between samples, but different for each element. F9 shows an Fe-rich rim without a co-located Ca and Mg enrichment. In F20, the Fe-rich rim has a co-located Ca and Mg enrichment. In general, compositions $< 0.5\%$ (most Mn and Ti measurements) are not reliable for quantitative estimations.

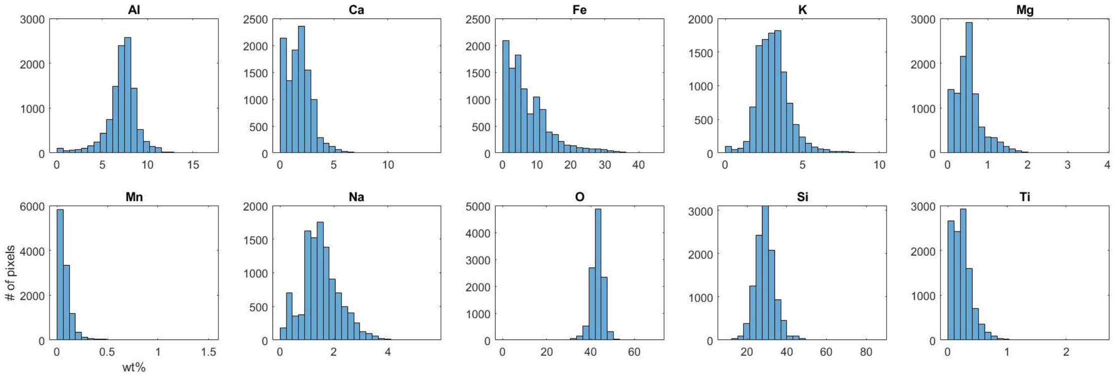

Figure 3.15: Histograms of each major element present in the 13 samples selected for semi-quantitative analysis. Each sample is represented by 1000 data-points randomly selected from each sample. Median values are provided in Table 3.1. The dominant elements present are Si, Fe, and Al. Si and Al have a quasi-gaussian distribution which suggests a static contribution, but the Fe distribution is non-gaussian and suggests a dynamic contribution.

Two examples (F9 and F20) of semi-quantitative maps are presented in Figure 3.14, with the remainder of the maps shown in Appendix C. Sample F9 shows an example of a sample with an Fe-rich rim, but no associated Ca or Mg enrichment. In contrast, F20 shows a rim that is enriched in Fe, Ca, and Mg. In general, compositions <0.5% (for example, most Mn and Ti measurements) are not reliable for quantitative estimations. Spatial elemental heterogeneity in fallout sample has been shown to be a result of incomplete mixing of materials entrained into the fireball and the bomb vapor [20]. Identifying precursors as well as understanding their contribution to final sample heterogeneity is important for interpreting the evolution of the fireball composition. A more detailed investigation of precursors in the samples using spatially resolved data are presented in Chapter 6 using multi-component regression techniques.

The elemental abundance of all 13 samples selected for semi-quantitative mapping are shown in Figure 3.15. This figure displays histograms for each element from the summation of 1000 data-points selected at random from non-epoxy regions of each sample. Median elemental concentration in wt% is shown in Table 1, as well as bulk dissolution chemistry measurements from both local soils and similar aerodynamic glassy samples [43]. These values are generally in agreement with typical silicate mineral lithologies, with the exception of Fe, which has concentrations in excess of known major mineral compositions. These high Fe concentrations likely stem from anthropogenic structural Fe, a reasonable assumption in light of the fact that these samples were chosen from nuclear detonation that interacted with significant anthropogenic iron. Summed totals for measured EDS data for each data-point ranged from 80-93 wt%. Inspection of the collected spectra suggest that these low summation values are due to insufficient counting statistics rather than failure to account

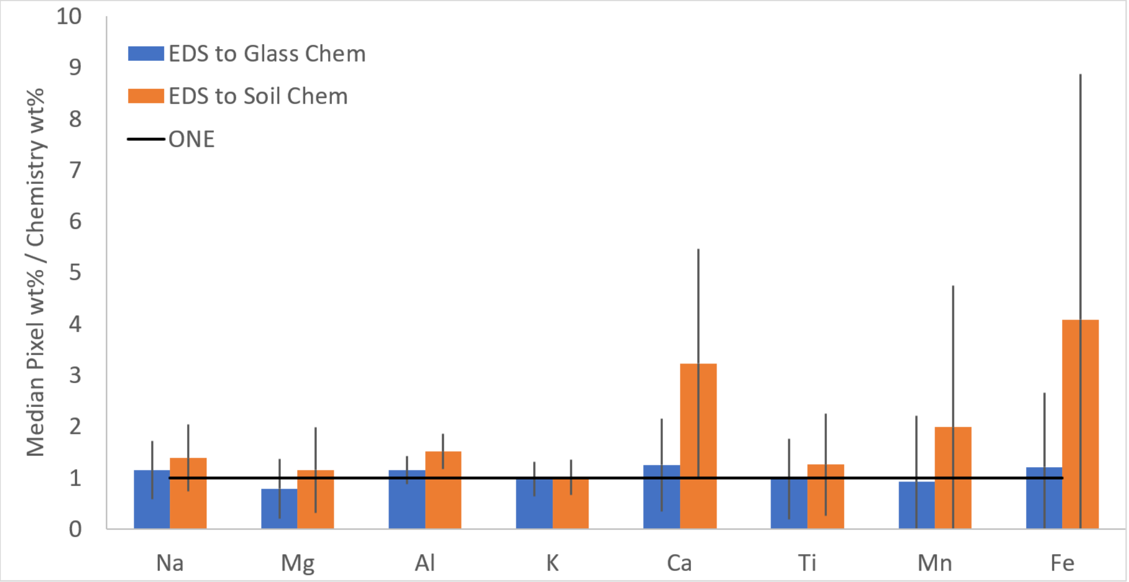

Figure 3.16: Comparison of SEM-EDS pixel median values to dissolution chemistry values of glassy aerodynamic debris (blue) and local soil (orange). SEM-EDS results are consistent with dissolution chemistry values of glassy aerodynamic debris. The results are also consistent with dissolution chemistry values of soil with the exception of Al, Ca, and Fe, which are enriched. These results show show that fallout composition is dominated by the local soil with minor contributions from the bomb vapor.

for major elements in the samples. All EDS measurements are normalized to 100 wt% in this work.

Median compositions were compared to bulk dissolution chemistry measurements (Table 1) from both local soils and similar aerodynamic glassy samples (Figure 3.16). Median SEM-EDS elemental compositions are within 1-σ (using the standard deviation of SEM-EDS data-points) of bulk chemistry data for aerodynamic glass, which increases the confidence in the quality of these semi-quantitative data. Median SEM-EDS elemental compositions are significantly enriched compared to soil chemistry for Al, Ca, and Fe. Dissolution chemistry data show a similar trend for aerodynamic glass compared to soil composition.

The Fe concentration based on bulk chemical dissolution (4.8 wt %) and baed on median SEM-EDS Fe concentration (5.8 wt%) are both higher than other recent measurements of fallout glass. Work by Lewis [46] studies an explosion from a near surface test that resulted in samples only 2.6 wt % (reported as 3.7 wt% Fe_2O_3). A detonation involving significant iron was the Trinity nuclear test which occurred on top of a steel tower. Reports of the maximum Fe concentration of 11.8 wt% [5] in trinitite are much smaller than the maximum concentration measured in the SEM-EDS data of 57 wt%. Other studies of trinitite by Eby *et al* reported concentrations of Fe in 'red trinitite' of 3.6 wt% (reported as 4.7 wt% FeO) and

Table 3.1: Element median SEM-EDS measurement values compared to bulk chemistry data. 1-σ values in the dissolution data represent measurement uncertainty, and in the SEM-EDS data represents the standard deviation of the 1000 measurements in each sample.

Wt%	**Al**	**1σ**	**Ca**	**1σ**	**Fe**	**1σ**	**K**	**1σ**	**Mg**	**1σ**	**Mn**	**1σ**	**Na**	**1σ**	**O**	**1σ**	**Si**	**1σ**	**Ti**	**1σ**
Dissolution Glass	6.865	0.412	1.474	0.329	4.793	1.193	3.345	0.221	0.666	0.102	0.066	0.005	1.350	0.195	NM		NM		0.244	0.036
Dissolution Soil	5.210	0.013	0.571	0.004	1.419	0.002	3.227	0.005	0.454	0.002	0.031	0.00002	1.115	0.004	NM		NM		0.190	0.0002
F9	8.22	2.11	1.91	0.92	6.15	9.34	3.50	0.97	0.73	0.39	0.00	0.09	1.72	0.45	43.84	3.63	30.52	5.66	0.08	0.24
F11	7.72	2.07	1.70	0.83	4.41	8.47	3.35	0.95	0.39	0.23	0.06	0.06	1.95	0.65	47.38	3.19	31.13	5.64	0.17	0.16
F13	6.68	2.22	0.10	0.56	4.24	3.48	3.34	0.79	0.69	0.43	0.03	0.03	0.39	0.28	48.89	1.75	34.35	4.74	0.43	0.23
F14	7.66	1.22	2.22	0.93	5.19	6.34	3.60	1.07	0.33	0.21	0.07	0.05	2.19	0.57	47.41	2.45	30.18	4.39	0.14	0.09
F18	7.89	2.12	1.50	4.12	4.65	7.89	3.67	1.69	0.84	0.61	0.05	0.09	1.32	1.07	47.09	3.17	30.68	6.12	0.23	0.20
F20	7.64	1.48	0.52	0.69	2.36	8.66	4.36	1.42	0.29	0.27	0.06	0.06	2.24	0.71	47.09	2.64	33.54	5.56	0.12	0.12
F24	8.66	1.75	3.13	0.97	11.35	3.56	2.43	0.85	0.57	0.25	0.08	0.05	1.19	0.47	44.34	2.53	27.87	4.13	0.29	0.13
F25	7.76	1.34	1.90	1.02	4.67	4.93	3.58	0.79	0.49	0.34	0.08	0.08	1.72	0.49	46.69	2.39	32.06	3.67	0.25	0.14
F27	7.87	1.58	1.97	0.72	6.86	7.27	3.10	0.74	0.54	0.19	0.09	0.06	1.50	0.30	46.55	3.23	30.26	4.51	0.28	0.14
F28	8.31	1.84	1.43	0.91	4.46	4.53	3.50	0.99	0.45	0.33	0.06	0.05	1.82	0.63	47.23	2.35	31.83	4.47	0.23	0.18
F29	7.79	1.58	0.82	0.95	0.61	2.36	4.78	1.53	0.15	0.40	0.05	0.07	2.73	0.74	48.40	1.20	33.88	2.99	0.09	0.21
F34	8.41	1.85	3.27	1.69	9.02	6.49	3.33	1.40	0.82	0.52	0.07	0.05	1.37	0.49	45.30	3.05	27.01	4.78	0.25	0.16
F35	7.63	1.68	2.08	1.06	6.03	3.96	2.78	0.75	0.56	0.27	0.07	0.06	1.21	0.36	47.51	2.71	31.39	4.04	0.28	0.11
All Data	**7.88**	**1.84**	**1.74**	**1.68**	**5.39**	**6.76**	**3.35**	**1.25**	**0.51**	**0.41**	**0.06**	**0.07**	**1.60**	**0.78**	**46.92**	**3.06**	**31.19**	**5.05**	**0.22**	**0.19**
Aerodyanmic Only	**7.90**	**1.83**	**1.83**	**1.26**	**5.87**	**6.68**	**3.25**	**1.08**	**0.52**	**0.37**	**0.06**	**0.06**	**1.55**	**0.70**	**46.71**	**3.11**	**30.93**	**5.02**	**0.23**	**0.18**

some Fe-rich blebs with concentrations as high as 31 wt% (reported as 40.1 wt% FeO)[16]. The Eby data are more Fe-rich than those reported by Bonamici, but local concentrations observed in fallout are much higher in the samples used for this study. Samples in this study are among the most Fe-rich samples reported to date in glassy fallout, highlighting their value to understanding fallout formation in Fe-rich environments. Deviations from Fe-Ca-Mg relationships reported in other studies of fallout glass are of interest and are discussed in Chapter 6.

3.3 Micro-structures in Iron-Rich Nuclear Fallout

One of the most notable features of this sample set was the observation of diverse and abundant microstructures on samples surfaces (Figure 3.17B) and throughout sample interiors (Figure 3.17A,C). These micro-structures are most visible using BSE imaging that highlights compositional heterogeneity relative to the glassy matrix due to high Fe concentration. Some of these micro-structures have never been reported in the fallout literature. These Fe-rich structures are of interest because of the correlations between Fe and radioactivity (in this study and previous fallout work), and because of the potential of Fe existing in multiple oxidation states to provide evidence that Fe may buffer the oxidation environment of the fireball during fallout formation (as discussed in Chapter 1).

Upon mounting and polishing to sample mid-planes, these micro-structures and textures were found to be predominant along the iron-rich radioactive sample rims within 200 μm of sample surfaces (Figure 3.17A,C). The relatively iron-poor sample interiors lack significant micro-structure and exist primarily as a glass, with evidence of partially molten mineral grains or unmixed molten grains in some samples. Rim micro-structures significantly deviate from fallout observations in the literature, both in micro-structure prevalence and in morphological diversity. Micro-structures are also sometimes present in iron-rich glassy regions of non-aerodynamic samples, but are less abundant than in aerodynamic samples.

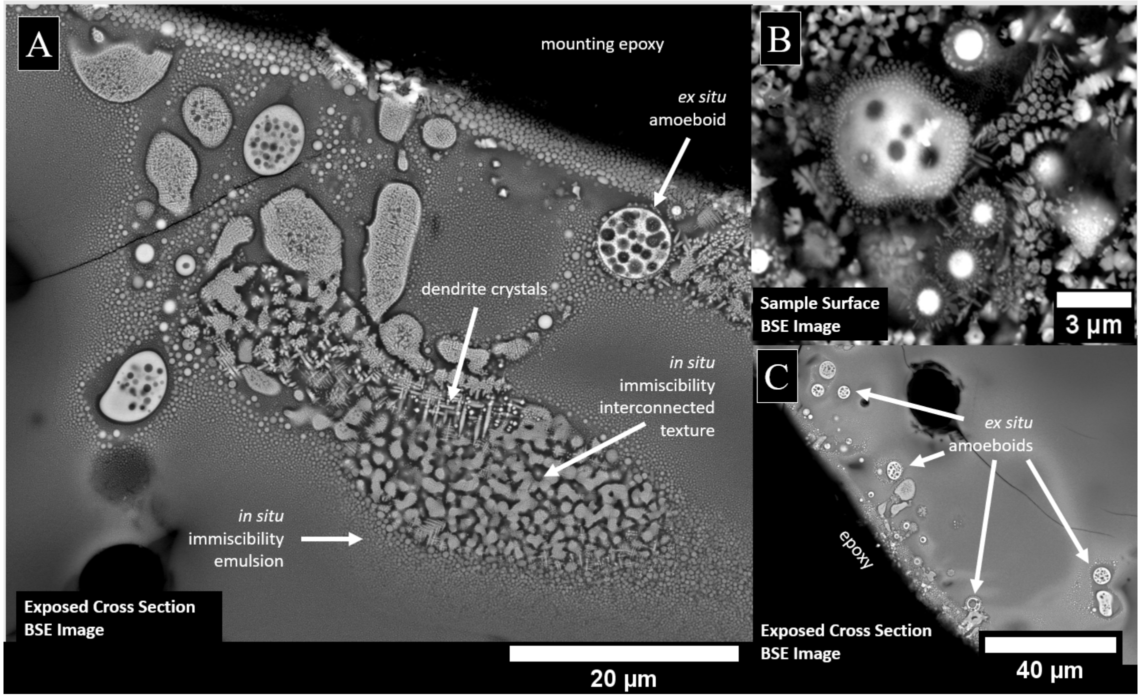

Figure 3.17: Micro-structures preserved in the rims of Fe-rich fallout. A range of heterogeneous textures including immiscibility textures, dendritic crystal growth, and *ex situ* amoeboids micro-structures are present within ∼200 μm of aerodynamic sample surfaces, and can be seen in BSE images of the exposed cross section of F9 (A,C) or directly on the surface of sample F21 (B). All samples in these images are primarily silicate glass, with brightness in BSE images reflect higher Fe content.

Observed rim micro-structures and textures occur as two primary categories: (1) immiscibility textures consisting of interconnected and emulsion two-phase textures, and (2) crystalline growth textures, including micron-scale dendrites and nano-scale crystals. The location and frequency of each microstructure morphology is not reported, but an overview of the diversity of of morphologies is presented. In addition, observations of several metallic globules and altered relict zircons are also described. This work further subdivides immiscibility textures into those that reflect *in situ* formation within the sample glass, and those that reflect *ex situ* formation, followed by agglomeration and sub-summation into the glass. The delineation of *ex situ* and *in situ* is further discussed in section 3.6 and is a focus of discussion for this thesis.

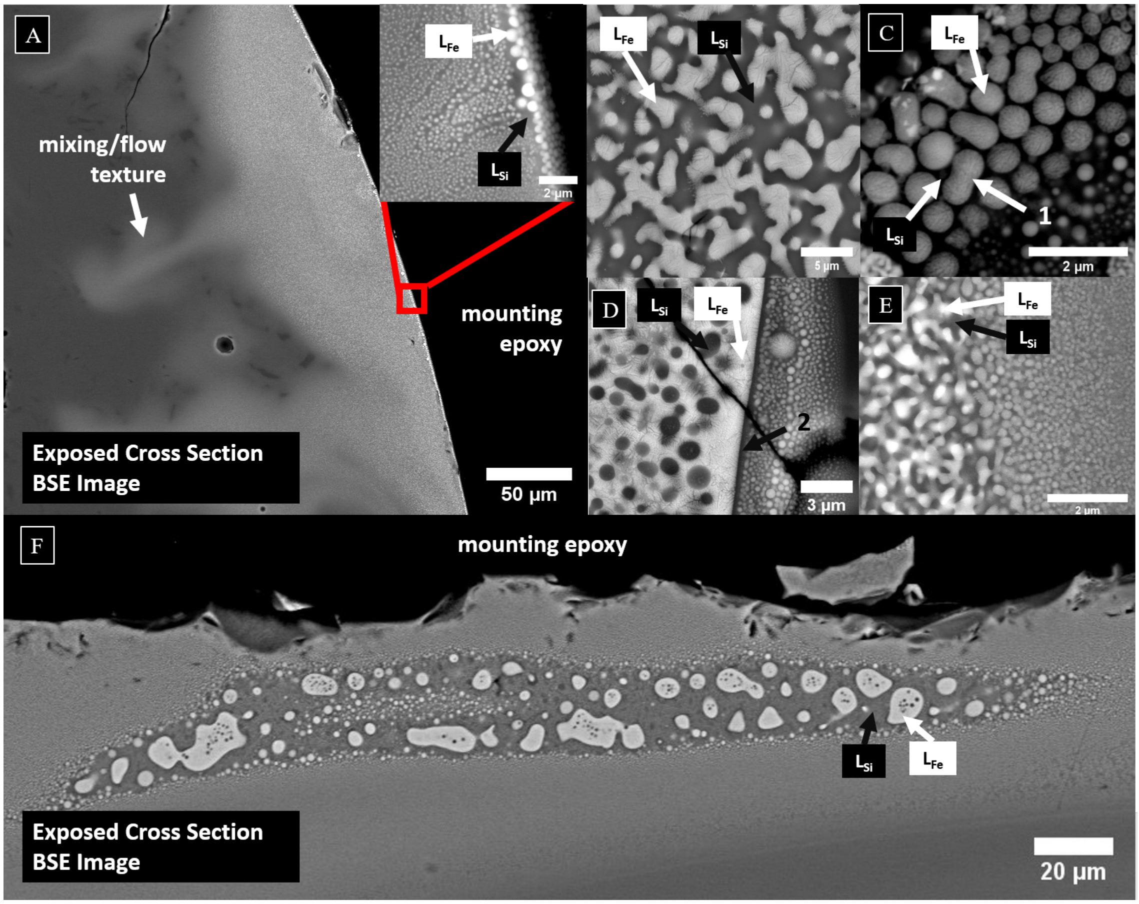

Figure 3.18: Immiscibility textures in Fe-rich fallout. Samples with Fe-rich (brighter regions in BSE images) regions contain significant immiscibility textures such as (A) sample F12, with emulsions of spheres (inset). (B) An example of interconnected Fe-rich (L_{Fe}) and Si-rich (L_{Si}) immiscibility textures in sample F20. (C) An example of merging and/or splitting of L_{Fe} spheres in sample F9. (D) An example of L_{Si} spheres emulsifed in a L_{Fe} matrix in sample F29. (E) A boundary region between nano-scale interconnected and nano-scale emulsion textures in sample F21). (F) A large band of immiscibility textures present in sample F20

Liquid Immiscibility Textures

Interconnected and emulsion textures observed in this suite of samples range from the nano-scale to the micron-scale (Figure 3.18). Interconnected textures (Figure 3.18B, E) consist of networks of iron-rich/silica-poor and iron-poor/silica-rich phases. L_{Fe} and L_{Si} are used to refer to the distinct iron-rich and silica-rich phases present in this study. In some samples (F9, F20, F27), large bands ($\sim$100s of μms) of immiscibility texture with features 10-20 μm in scale are present (Figure 3.18F). In some cases, L_{Fe} and L_{Si} have solidified as a mixture of glass and nano-scale crystals. In these cases, L_{Fe} and L_{Si} are still used to refer to their presumed boundaries while liquid, prior to solidification. Emulsion textures consist primarily of L_{Fe} spheres dispersed in and L_{Si} matrix (Figure 3.18C). Occasionally, emulsions of L_{Si} within a matrix of L_{Fe} are present (Sample F29, Figure 3.18D). The emulsion textures are widespread throughout the iron-rich regions of all sample rims, with local gradations in sphere sizes ranging from several μms to the nano-scale (where they are not resolvable using SEM imaging techniques).

Whereas in emulsion regions there is a gradation in spherical L_{Fe} phases, many distinct micron-scale (2-20 μm) iron-rich spheres lack local gradations in size in the surrounding matrix. These distinct spherical features consist of two L_{Fe} and L_{Si} phases with sharp phase boundaries and tend to be concentrated at or near (<50 µm) sample surfaces (Figure 3.19). Because of their resemblance to immiscible amoeboid inclusion textures [75, 35] these distinct micro-scale spheres are referred to as amoeboids in this work to distinguish them from other emulsion and solidification micro-structures.

Amoeboids are predominantly spherical, though they occasionally show evidence of deformation along local flow textures. These deformation morphologies suggest amoeboids are not always fully solidified prior to agglomeration onto the host samples, or are heated after agglomeration such that they can be deformed during viscous mixing. Some amoeboids are observed partially or fully protruding from sample surfaces, providing good evidence for *ex situ* formation.

Amoeboids observed in this sample suite can be classified into four primary morphological categories: Type 1 amoeboids where the minority L_{Si} phase is dispersed within the L_{Fe} phase (Figure 3.19A-D), type 2 amoeboids where the minority L_{Fe} phase is dispersed within the L_{Si} phase (Figure 3.19E-D), type 3 amoeboids with complex multi-layer core-shell morphologies alternating between L_{Fe} and L_{Si}, and type 4 amoeboids with interconnected L_{Si} and L_{Fe} phases. Type 3 amoeboids are further divided into type 3A (Figures 3.19G,H) with 2-3 layers of L_{Fe} and L_{Si} and type 3B, where a dispersion of L_{Si} is present in the outermost L_{Fe} rim. The most common amoeboids observed in these samples are types 1 and 2 (on the order of 100s-1000s of amoeboids in the exposed cross sections), whereas type 3 are more rare (10-20 amoeboids), and type 4 was very rare (4 amoeboids).

Amoeboids had varying prevalence from sample to sample. They were observed in 12 of the 19 aerodynamic samples, with the highest number observed in samples F9, F11, F20, F28 and F34. Sample F16 which was an oblong spheroid with a long eliptical vesicle along its major axis was of note as most amoeboids preserved in it's rim had non-spherical

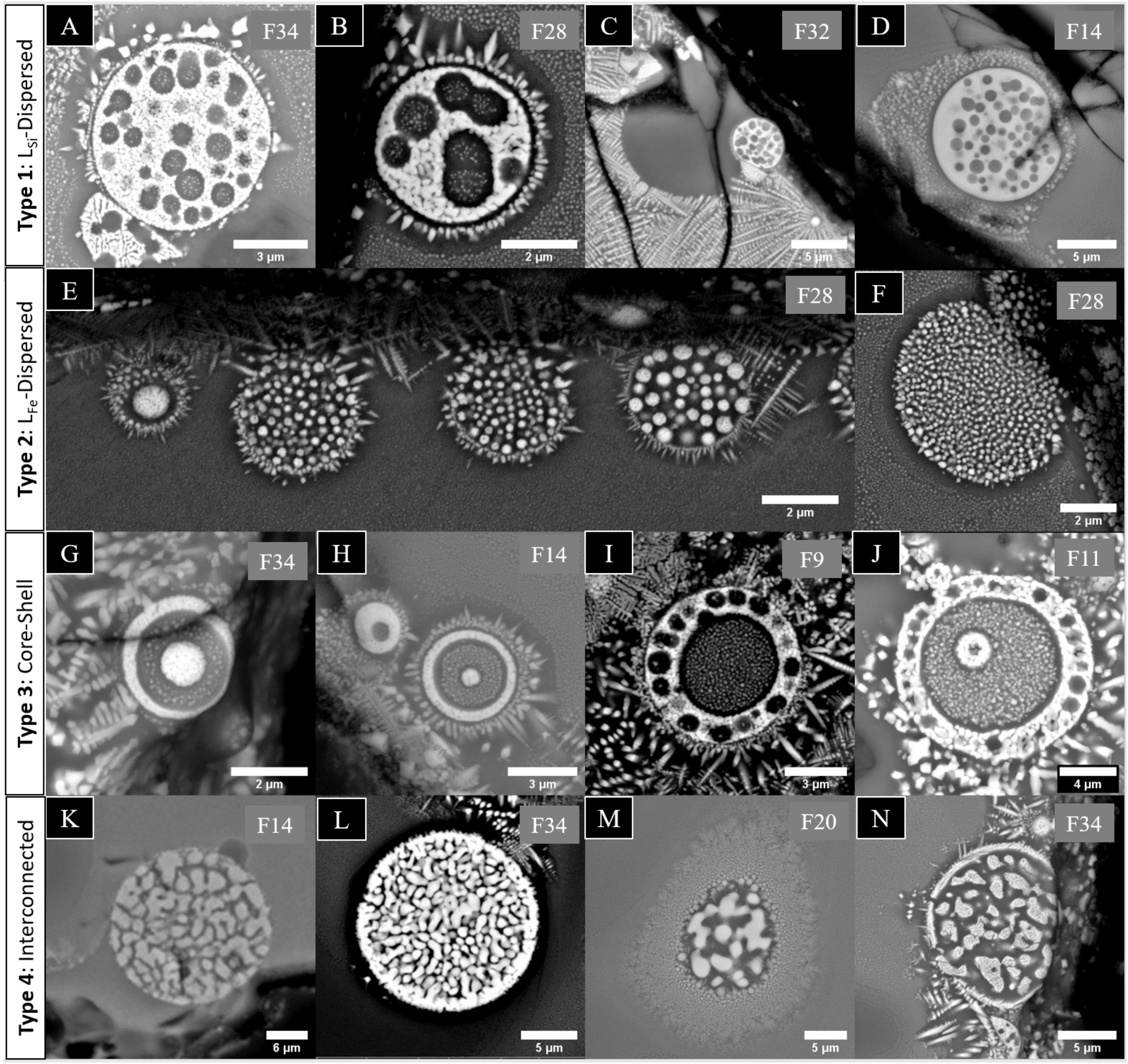

Figure 3.19: Amoeboid micro-structure morphologies exist in four primary categories in order of prevalance. Type 1 (top row) is the most prevalent with the minority L_{Si} phase dispersed within the L_{Fe} phase. Type 2 (2nd row) has the minority L_{Fe} phase dispersed within the L_{Si} phase. Type 3 (3rd row) has complex multi-layer core-shell morphologies alternating between L_{Fe} and L_{Si} phases. Type 4 (bottom row) interconnected L_{Si} and L_{Fe} phases. Halo features around amoeboids either due to chemical diffusion equilibration, dendritic growth, or other *ex situ* formation processes are sometimes present (B, D, H,M).

morphologies indicating deformation while still in the molten state. These defomration textures are consistent with the hypothesis that this morphology of sample resulted from stretching during turbulent mixing as a result of rapid spinning or kinetic ejection from the fireball. All aerodynamic samples without amoeboids (F12, F15, F19, F25, F26, F31, F33) have less obvious Fe-rich rims than those with amoeboids.

Amoeboids were only observed in two of the six non-aerodynamic samples. In sample F22, a single 5 μm amoeboid was observed wedged in a crack between non-melted mineral grains as opposed to the typical preservation within the glassy matrix of aerodynamic samples. In sample F29 a 10 μm oblong amoeboid was observed within a glassy matrix with proximate flow textures (see nanoSIMS analysis in Figure 3.32D) with a unique morphology a continuous L_{Fe} phase in contrast to the L_{Fe} in other amoeboids that consist of much sharper phase boundaries and an L_{Fe} phase that appears to be a single continuous phase in contrast to most amoeboids where the L_{Fe} consists of a multitude of nano-scale iron oxide grains. The F29 amoeboid also had sharper phase boundaries between L_{Fe} and L_{Si}.

The large number of amoeboids in over half the samples (14/26) suggest their formation is widespread and that their formation processes may provide insight into general formation mechanisms of micro-scale fallout particles. Their high iron content as well as association with samples with more Fe-rich rims make them a good feature to investigate formation processes associated with and influenced by the presence of iron in the fireball. Furthermore, their near surface location suggests their agglomeration at late times, and so reflect formation processes that occur at late times in mm-scale formation, such as scavenging of micro-scale fallout particles by entrained material.

Magnetite Crystals

There was evidence of crystalline growth or crystalline structures within Fe-rich glassy regions in every sample. These features have been noted in fallout before [7, 49] but are not reported in most recent studies of fallout. Evidence of Fe oxide crystalline growth was noted in 24/26 samples (all except F15 and F26). Sample F26 had evidence of nano-scale Zr-rich precipitate crystals. Crystalline growth was generally associated with local regions of high Fe concentrations which primarily exist in sample rims. Some particularly Fe-rich samples samples (F9, F11, F20, F34) ware noted for the high level of crystalline growth. While crystalline growth is present in each sample, samples volumes are dominated by silicate and thus regions of Fe oxide growth contributes only a very small percentage to the overall volume (<1%).

Evidence of crystalline growth within samples exists in the form of widespread dendrite crystal growth throughout sample rim glass (Figures 3.20A-C) reflecting non-equilibrium growth of an iron-oxide phase within the iron-rich silicate melt. Some dendrite regions have larger dendrite arms near the surface with a preferential primary axis orthogonal to the sample surface, suggesting growth started near the sample surface and grew inwards (Figure 3.20A). Some dendrites appear to have nucleated from proximate interconnected immiscibility textures (Figure 3.20B). Other regions of dendrites consist of closely packed

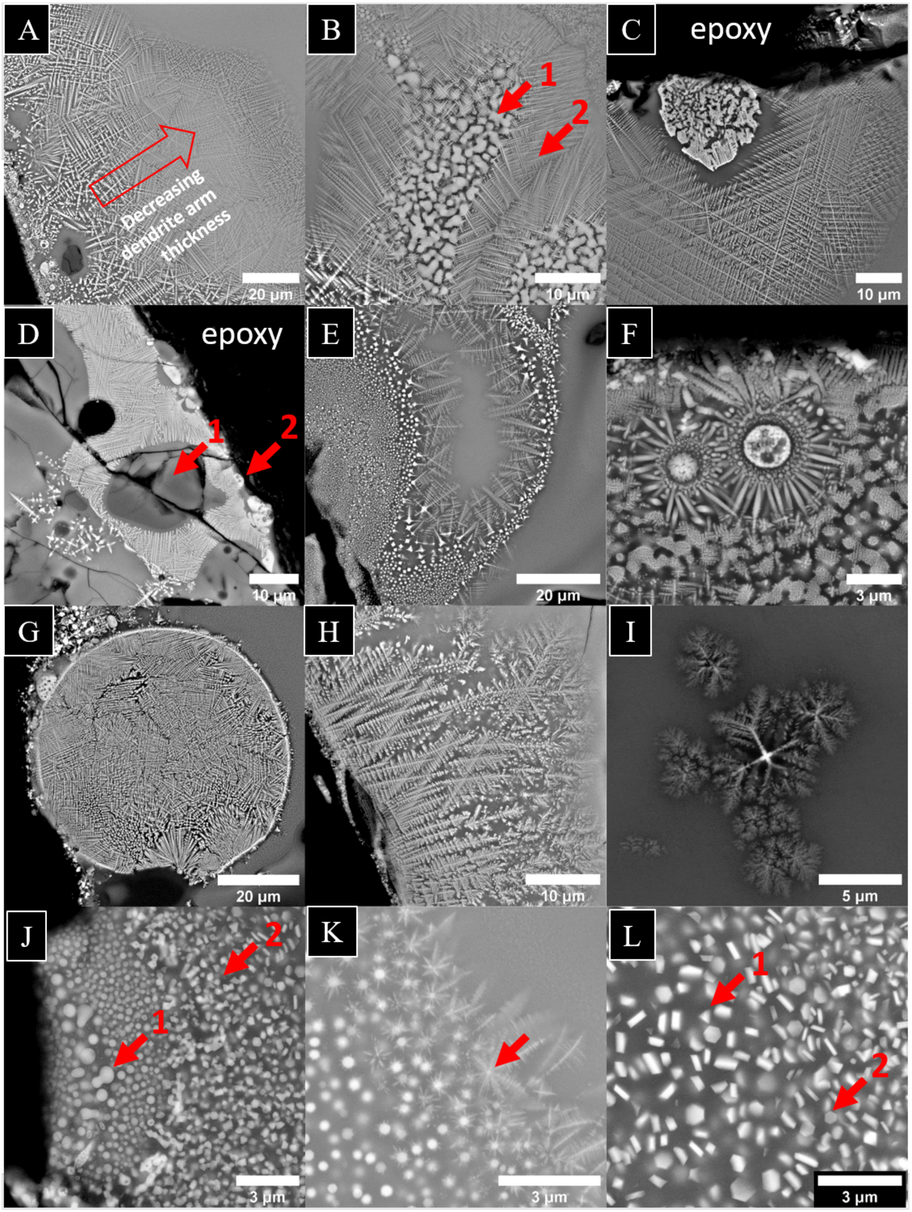

Figure 3.20: Crystalline features in Fe-rich fallout glass. (A) Dendritic magnetite with decreasing dendrite arm size towards sample F11 interior. (B) Dendritic magnetite growth nucleating from interconnected spinodal texutres in sample F20. (C) Fields of interlocking dendrites proximate to an iron-oxide agglomerate in F20, (D) Relict quartz (arrow 1) within a field of dendrite growth, with nearby amoeboids (arrow 2) in F32. (E) Dendrite growth resulting in complex chemical heterogeneities in sample F20. (F) Radial dendrites nucleated near amoeboid surfaces in F9. (G) A large ($\sim 50\ \mu$m) agglomerate consists entirely of dendritic growth in F34. (H) complex 'feather' dendrites with non-orthogonal arms growing from F22 surface. (I) complex 'snowflake' dendrite in F22. (J) Nano-scale immiscibility emulsions (arrow 1) proximate to nano-scale euhedral crystal growth (arrow 2) in F21. (K) nano-scale emuslions serving as nucleation sites for dendrite growth in F17. (L) hexagonal and triangular prism euhedral crystals in F21.

dendrite growth (Figure 3.20C) which in one case surrounded a chemically distinct melt parcel with a quartz composition (Figure 3.20D). Some complex dendrite growth orientations result in interesting chemical heterogeneity (Figure 3.20E). Dendrites are frequently observed in a radial orientation emanating from curved surfaces such as *ex situ* amoeboids (Figure 3.20F), presumably due to the ease of crystal nucleation at interfaces with curvature. Some large (~50 μm) agglomerates consist of closely packed dendrites throughout their interior (Figure 3.20G). While the majority of dendrites exist with orthogonal secondary arms, in some rare cases, other dendrite morphologies are present (Figures 3.20H,I).

Nano-scale faceted crystals are also observed dispersed within the glass proximate to emulsion textures (Figure 3.20J). These emulsion textures also occasionally serve as nucleation sites for radial dendrites (Figure 3.20K). Closer inspection of the faceted nano-scale crystals reveal they consist of hexagonal and triangular prism morphologies (Figure 3.20L). Figure 3.20L also appears to contain rectangular crystals but this may be an image artifact due to the orientation of dispersed prism crystal morphologies.

The immiscible L_{Fe} and L_{Si} phases also contain Fe oxide crystals. Transmission electron microscope selected area diffraction pattern (TEM SADP) analysis of a thin section of a type 3 amoeboid (T2) from F11 (Figure 2.10) confirms the amorphous nature of the L_{Si} glass and that the L_{Fe} regions and nearby dendrites crystallize into grains of inverse spinel structured iron-oxide matching magnetite (Fe_3O_4) [22]). TEM high angle annular dark field (TEM-HAADF) imaging of amoeboids allow better resolution of the features (Figure 3.21). In particular, individual non-faceted magnetite oxide grains within L_{Fe} regions are readily observed in amoeboids T2-T5. The L_{Fe} regions of amoeboids sometimes solidify as an apparently single homogeneous phase (Figure 3.19D), but usually consist of networks of closely packed non-faceted crystal grains of magnetite within a silicate glass matrix (Figure 3.19B, 3.21). TEM-EDS of a variety of L_{Si} and L_{Si} regions of amoeboids from these thin sections have better spatial resolution than SEM-EDS amoeboid measurements (see Section 3.4). Because of the finite thickness of the thin section, some dispersed L_{Fe} and L_{Si} globules have intermediate contrast since the image reflects both L_{Fe} and L_{Si} domains. Nano-scale faceted crystals within the L_{Si} regions of amoeboids are similar to those occasionally dispersed in the host melt (Figure 3.20L). These nano-scale crystals exist as both hexagonal and triangular prism morphologies.

Transmission electron microscopy (TEM) and electron diffraction analyses of a core-shell amoeboid cross-section (T2) from sample F11 confirms the amorphous nature of the L_{Si} glass and that the L_{Fe} regions crystallize into grains of inverse spinel structured iron-oxide matching magnetite (Fe_3O_4)[22]). This TEM data along with oxygen concentrations in SEM-EDS measurements of Fe throughout samples suggest that iron in these samples is overwhelmingly present in oxide form, note that a few metallic, non-oxidized Fe globules were observed in the exposed cross sections of samples F17 and F18, both of which are non-aerodynamic samples (Figure 3.22). In one case, a metallic globule of Fe was observed with smaller metallic Cu regions on is periphery, with textures that suggest liquid flow, and possible Fe/Cu liquid immiscibility (Figure 3.22D). The presence of metals suggests local reduced environments. However, samples F17 and F18 were non-aerodynamic and are some

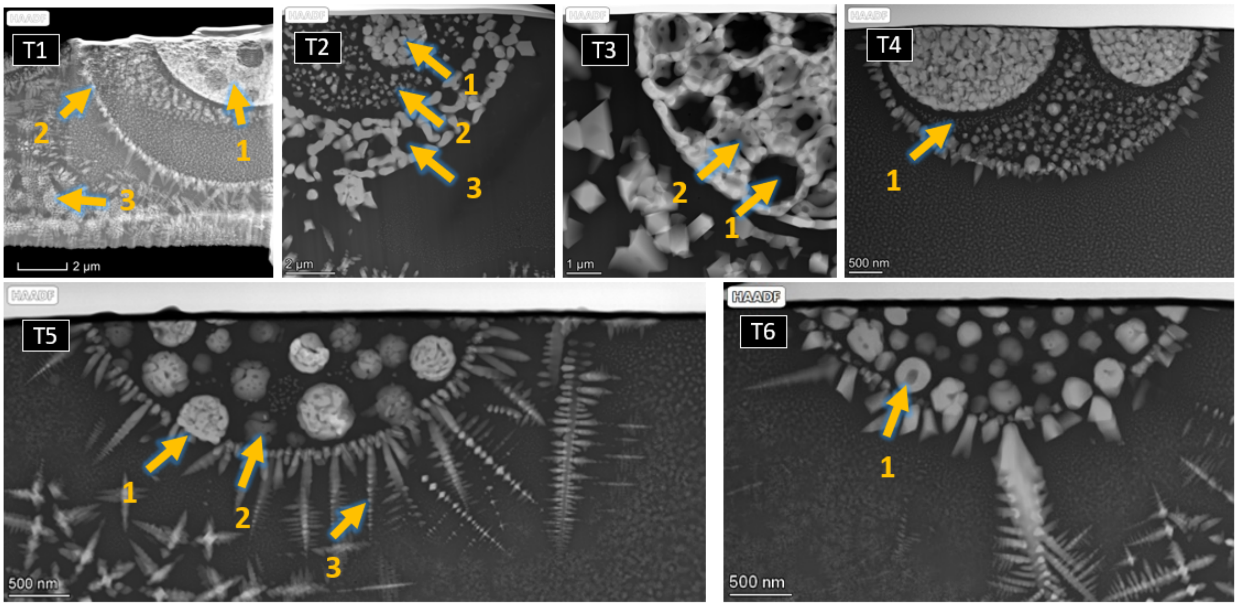

Figure 3.21: TEM HAADF images of thin sections prepared for amoeboid characterization. T1 is a type 1 amoeboid (arrow 1) from F9 with a L_{Si} halo (arrow 2), with *in situ* interconnected textures in the local matrix (arrow 3). T1 was damaged and the quality of thinning was insufficient to collect TEM-EDS data. T2 is a type 3 amoeboid from F11 with a central L_{Fe} core (arrow 1), inner shell composed of glass and dispersed nano-scale magnetite crystals (arrow 2), and outer L_{Fe} shell composed of glassy L_{Si} globules (arrow 3) dispersed throughout. T3 is a type 1 amoeboid from F11 with glassy L_{Si} globules (arrow 1) dispersed in L_{Fe}. Because of the finite thickness of the thin section, some globules (arrow 2) have intermediate contrast since the image reflects both L_{Fe} and L_{Si} domains. T4 is a type 2 amoeboid from F28 with two primary L_{Fe} globules and many nano-scale L_{Fe} globules dispersed within L_{Si}. The boundary of the large globules have a boundary region approximately 200nm thick that is either free of or contains much smaller L_{Fe} globules. T5 is a type 2 amoeboid from F28 with L_{Fe} globules dispersed within L_{Si}, one of which shows wetting behavior on the surface of the amoeboid (arrow 1). Because of the finite thickness of the thin section, some globules (arrow 2) have intermediate contrast since the image reflects both L_{Fe} and L_{Si} domains. Radial dendrite growth nucleated from the amoeboid surface are also present (arrow 3). T6 is a type 2 amoeboid from F28 with L_{Fe} globules (arrow 1) dispersed within L_{Si}.

of the least radioactive in this study, suggesting that they likely had limited interaction with the radioactive fireball. It is difficult to use these metallic globules to make broader claims of the fireball vapor oxygen environment, but it does highlight that there is a spectrum of Fe oxidation within these samples. No metallic globules were observed within the higher radioactivity, aerodynamic samples.

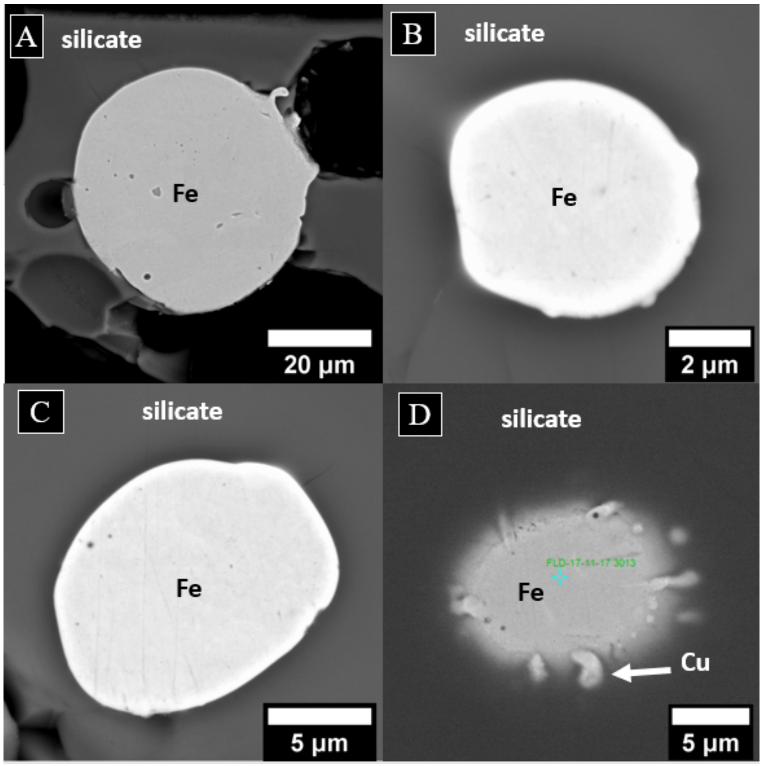

Figure 3.22: Metallic globules observed in Fe-rich fallout. 5-50 μm metallic Fe globules were observed in samples F18 (A-C) and F17 (D). SEM-EDS shows these are reduced iron without the presence of oxygen. The F17 globule (D) also had Cu rim features with textures suggesting liquid flow or Fe-Cu immiscibility.

Altered Relict Minerals

The presence of unaltered, partially altered, and fully altered mineral grains in fallout offers unique time-temperature records of the host melt environment. Work on trinitite glass by Lussier *et al* [52] studied zircons ($ZrSiO_4$) with halos of baddeleyite (ZrO_2), a high temperature decomposition product of zircons. Zircon decomposition can begin at lower temperatures (1200-1600 °C) but with sluggish kinetics. Decomposition kinetics increase by several orders of magnitude at higher temperatures (1550-1675 °C). Several zircons were observed in these samples (Figure 3.23), with compositions confirmed by SEM-EDS mapping. These zircons exhibit a range of decomposition behavior, with halos resembling textures documented in the Lussier work, composed of a mixture of baddeyelite and SiO_2.

One un-melted zircon is present in F17 (Figure 3.23A). Two zircons have fibrous baddeyelite halos (5-10 μm) surrounding an unaltered zircon core (Figure 3.23B), both of which were in non-aerodynamic samples (F29 and F22). One zircon in sample F29 (Figure 3.23A) had two regions of decomposition baddeyelite. One region contains baddeyelite fibers that are still

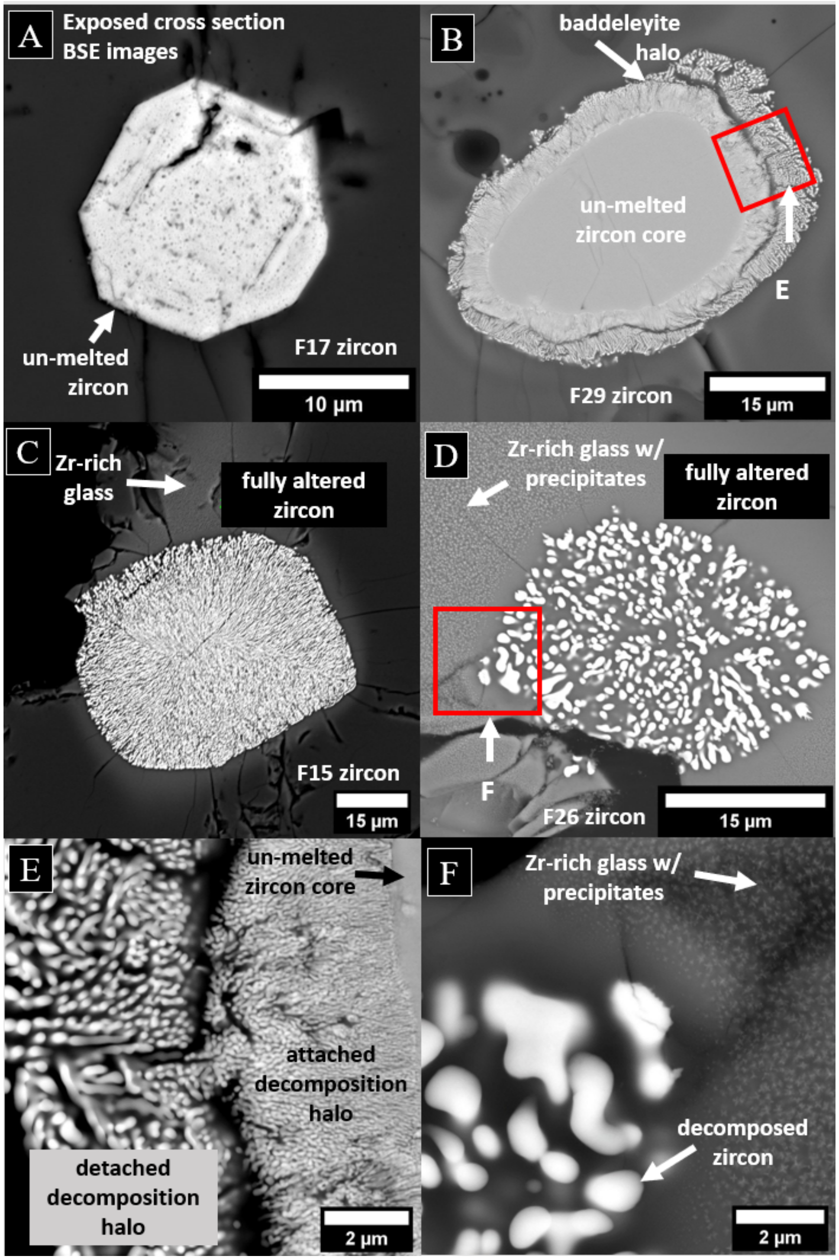

Figure 3.23: Thermally altered zircons provide local time-temperature information. BSE images of zircons in this study are shown, with example from sample F29 (top left), F22 (top right), F15 (bottom left), and F26 (bottom right). Samples F29 and F22 are both non-aerodynamic samples which likely saw lower time-temperature histories, as evidenced by outer halos of fibrous baddeleyite 5-10 μm in thickness. Sample F15 is an aerodynamic sample, and F26, while non-aerodynamic, is primarily composed of glass, and both likely saw higher time-temperature histories, as evidenced by the lack of unaltered zircon cores, with fibrous baddeleyite at least 15 μm in both samples. Local regions of Zr-rich glass were also observed for the fully altered F15 and F26 zircons.

attached to the unaltered core. Another region is separated from he rest of the zircon by a silicate glass region (Figure 3.23E).

Two zircon regions are preserved with fully altered textures throughout their exposed cross sections in two aerodynamic samples (F15 and F26, Figures 3.23C-D). The lack of an un-melted core and the zircon diameters suggests time-temperature histories were sufficient to alter rims >15 μm. This distance is greater than the thickness of halos observed in the zircons preserved in non-aerodynamic F29 and F22. Both of the fully decomposed zircons had local regions of Zr-rich glass as far as 30 μm away from the zircon boundary. This region features nano-scale microlites (Figure 3.23F) dispersed in glass, with compositions that are not resolvable using SEM-EDS techniques. Such features may be a result of diffusion of dissolved Zr in the melt follow by precipitation. Fully altered textures and the presence of Zr in the surrounding glass suggests higher local time-temperature histories than the (non-aerodynamic) F29 and F22 zircons. A higher time-temperature history for zircons in (aerodynamic) F15 and F26 is not surprising because these samples are assumed to have experienced more significant heating than non-aerodynamic samples.

3.4 Chemistry of Immiscible and Crystalline Micro-structure

Each micro-structure morphology, size, and composition is dependent on the chemical and thermal conditions under which they formed. Of primary interest are micro-structures that may have directly interacted with the radioactive vapor term, as they can provide insight into processes during the condensation and incorporation of radionuclides of interest into these samples.

Crystalline growth has the potential to influence the distribution of radionuclides in the phases present within fallout. There is some evidence that dendritic growth can effect distribution of species within the melt. The positive correlation between Fe, Ca, and Mg noted in the literature and observed in some SEM-EDS data (Figure 3.13) are not present in regions of significant dendrite growth (Figure 3.24). Crystalline growth of magnetite occurs at lower temperatures (<1600 °C) and tend to be formed within the melt as it cools, suggesting they are less useful as records of fireball vapor dynamics. The remainder of this section neglects the study of crystalline features, and focuses on the chemical makeup of *ex situ* amoeboids.

Since liquid immiscibility occurs at higher temperatures than solidification, features resulting from liquid immiscibility likely represent processes closer in temperature to vapor phase dynamics, and so are a preferred option to infer vapor conditions. In particular, the amoeboids reported in this study are distributed at or near the sample fallout surfaces, and are most likely to have initially formed outside the host matrix (*ex-situ*). Their *ex situ* formation and small size suggests they are most likely to have been in equilibrium with the cooling radioactive vapor compared to *in situ* immiscibility textures. It is even possible

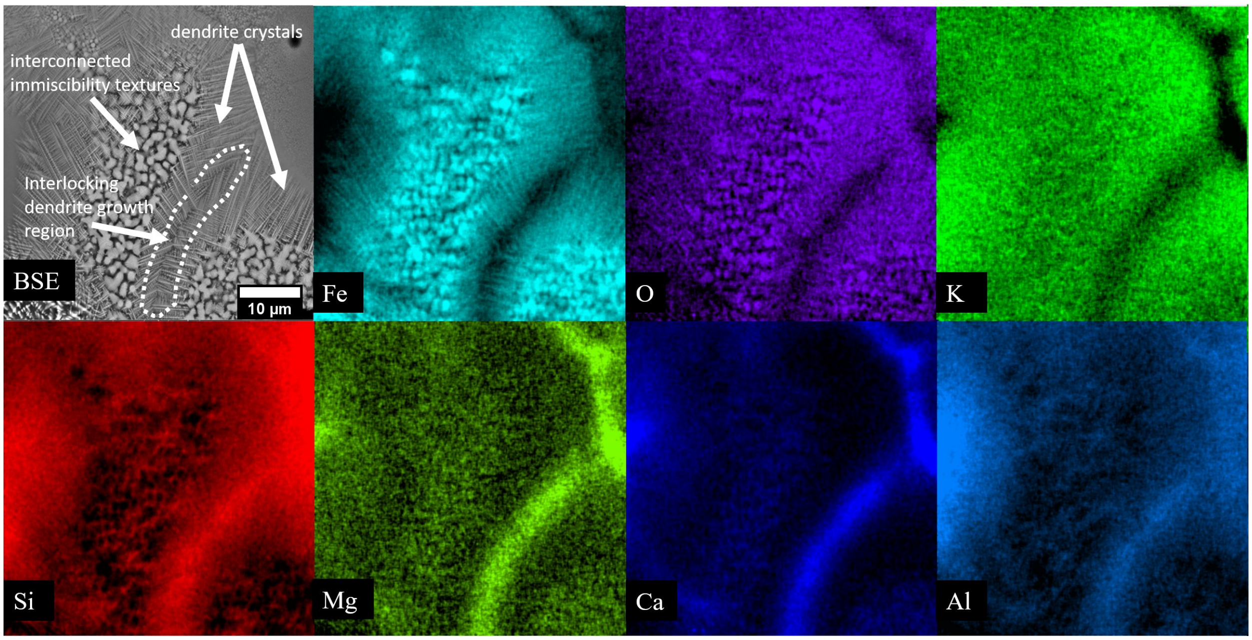

Figure 3.24: Qualitative elemental EDS maps of a region in sample F20 with both immiscibility textures and dendritic growth. Dendrites are nucleated from the immiscible region phase boundaries, likely because of increased nucleation rates on curved surfaces. The Fe-Ca-Mg correlations expected in the bulk melt are not present in regions of dendritic growth, with evidence that Si, Mg, Ca, and Al are rejected at the interfaces of growing crystals, and 'trapped' between interlocking dendrites, represented by the bands of enrichment in the bottom row. Notably, K is not enriched in this region.

that amoeboids may be direct condensates or agglomerates of direct condensates from the vapor. Amoeboid size distributions are on the same scale as particulates formed in non ground-interacting nuclear tests (*i.e.*, was fully vaporized) [83].

A total of 32 amoeboids in sample F28 and 10 amoeboids in sample F34 were selected for SEM-EDS analysis. Type 1 and 2 amoeboids were selected in F28 but only type 1 were selected in F34. Type 3 and type 4 amoeboids (Figure 3.19G-N) were not analyzed further. Amoeboid compositions and their two phase compositions are reported in Figures 3.25 and 3.26 using standard oxide stoichiometry and normalized to 100% to maintain consistency with the silicate immiscibility literature. Data is displayed in the form of a pseudoternary 'MAS' diagram that has been used in the literature to present silicate immiscibility data. The vertices in a MAS diagram reflect modifying cations (M), alumina+alkalis (A) and silica (S).

Shown for comparison with amoeboid data are a sub-selection of SEM-EDS data points from their host samples. In both F28 and F34 sample SEM-EDS data, there exists an apparent mixing line between an Fe-rich end-member and the average of the host melt glass,

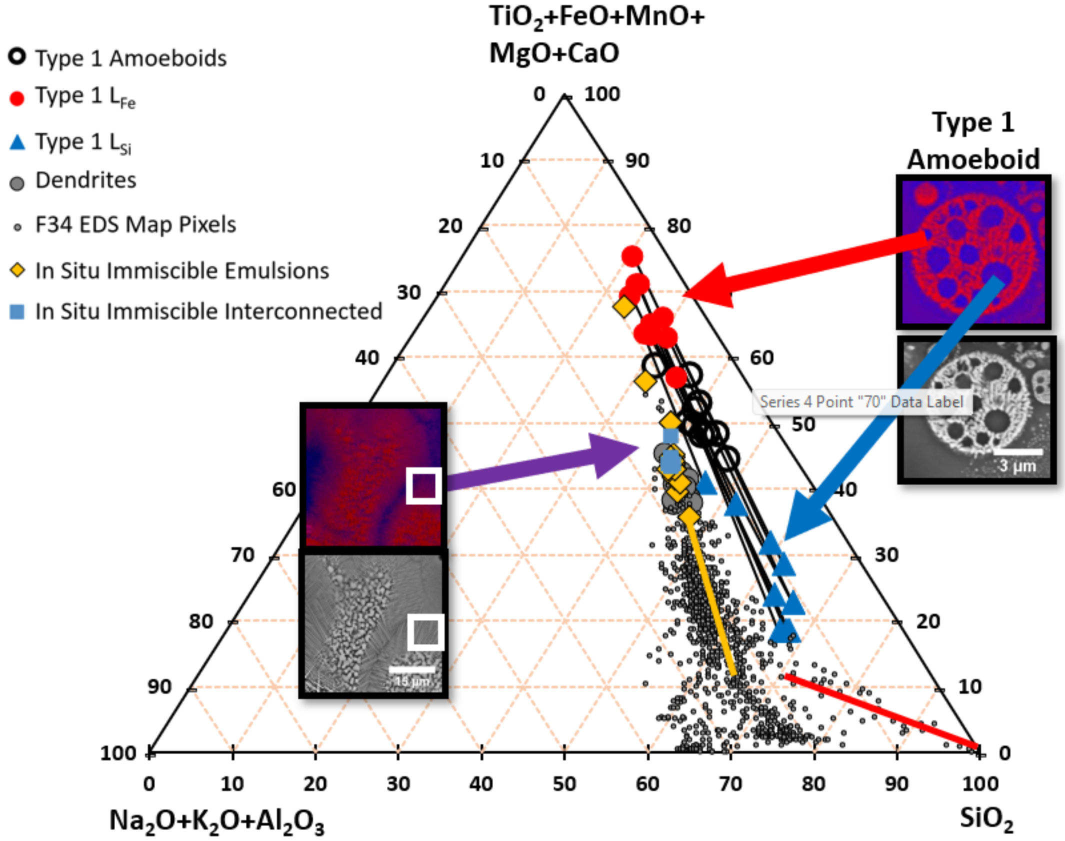

Figure 3.25: Pseudoternary plot of F34 amoeboid SEM-EDS data. Vertices on the MAS pseudoternary reflect modifying cations (M), alumina+alkalis (A) and silica (S). Silicate immiscibility separates into compositions along the MS axis. F34 EDS map pixels represent semi-quantitative 12 hour maps over the entire exposed F34 cross section, and are the result of the complex mixing behavior between local minerals and anthropogenic iron. Amoeboid compositions are alkali and alumina poor compared to the F34 data, including *in situ* immiscibility and dendrite regions. Orange line represents the general mixing line between the average melt composition and Fe-oxide. The red line represents the general mixing line between the average melt composition and quartz.

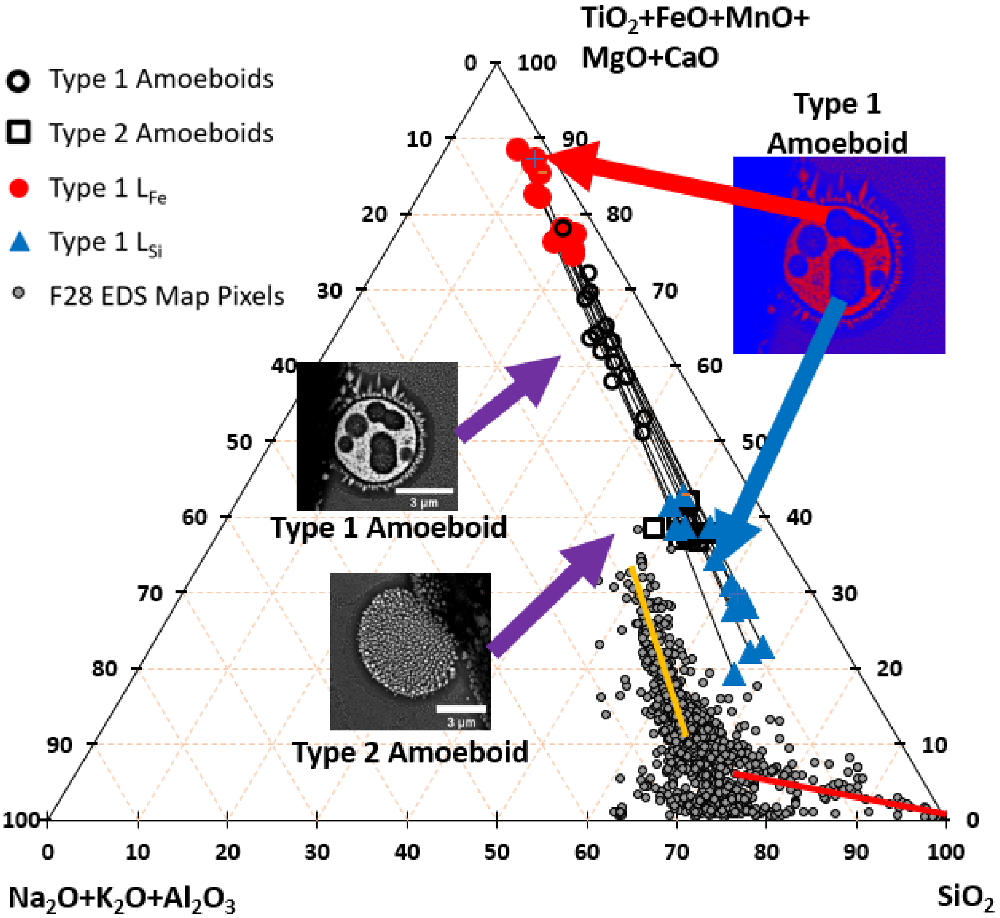

Figure 3.26: Pseudoternary plot of F28 amoeboid SEM-EDS data. Vertices on the MAS pseudoternary reflect modifying cations (M), alumina+alkalis (A) and silica (S). Silicate immiscibility separates into compositions along the MS axis. F28 EDS map pixels represent semi-quantitative 12 hour maps over the entire exposed F28 cross section, and are the result of the complex mixing behavior between local minerals and anthropogenic iron. Amoeboid compositions are alkali and alumina poor compared to the F28 data. Orange line represents the general mixing line between the average melt composition and Fe-oxide. The red line represents the general mixing line between the average melt composition and quartz. Type 1 (empty black circles) and Type 2 (empty black squares) compositions are shown in comparison, as well as the L_{Fe} (red circles) and L_{Si} (blue triangle) compositions of Type 1 ameoboids.

as well as a mixing line between a pure SiO_2 end-member and the average of the host melt glass (Figure 3.26 and 3.23). SEM-EDS measurements of dendrite regions and *in situ* immiscibility regions fall on the mixing line between the Fe-rich end-member and bulk glass (Figure 3.26).

For type 1 amoeboids (with L_{Si} features on the scale of 1 μm), SEM-EDS resolution likely underestimates the difference in Fe and Si between L_{Si} and L_{Si}. For type 2 amoeboids only overall composition is reported and not L_{Fe} and L_{Si}, because the dispersed L_{Fe} phases are too small (submicron) to spatially resolve their compositions using SEM-EDS. Amoeboid measurements in sample F28 (Figure 3.26) highlight the compositional difference between type 1 and type 2 amoeboids. Type 1 amoeboids are more Fe-rich than type 2. In contrast to the *in situ* micro-structures, amoeboid compositions are chemically distinct (alkali and alumina-poor) from the mixing line observed in host sample SEM-EDS measurements, supporting an *ex situ* formation hypothesis. Resolution limitations to these data blur the compositional differences between L_{Fe} and L_{Si} phases.

To remedy the resolution limitations of amoeboid two-phase compositions 5 thin sections of amoeboids (T2-T6) were prepared for TEM analysis. This included one Type 1 (LSi-dispersed) amoeboid, three type 2 (LFe-dispersed) amoeboids, and one type 3 (core-shell) amoeboid (Figure 3.27). In each case, multiple regions of interest (ROIs) were selected in each amoeboid as independent estimates of L_{Fe} and L_{Si}. As noted in section 3.3, the finite thickness of the thin section cause some ROIs of the dispersed L_{Fe} and L_{Si} phases to reflect a combination of L_{Fe} and L_{Si} domains. This results in the spread of data observed in Figure 3.27, specifically in L_{Fe} ROIs in type 2 amoeboids T5 and T6. It is assumed that the most contrasting compositions are the best estimate of L_{Fe} and L_{Si} in the TEM thin sections.

TEM measurements confirm the observation made with SEM-EDS data that amoeboid compositions are chemically distinct from their host melts and do not fall along the host sample melt/Fe-rich precursor mixing line. However, the higher resolution data reveals that the L_{Si} compositions fall on the boundary of the host melt compositional space, where data-points are aluminum-poor and alkali-poor. The TEM-EDS measurements of L_{Si} follows the curve of data as the Fe mixing trends towards the pure SiO_2 vertex. This trend supports the theory that, though amoeboids are formed *ex situ* from the bulk sample, their L_{Si} component may be initially sourced from the aluminum-poor, alkali-poor portion of the melt, and are mixed with the the same Fe precursor independently of the mixing of Fe with the bulk melt.

3.5 Spatial Relationships Between Iron and Plutonium

This study investigates the spatial distribution of radioactive species in these samples in order to gain a better understanding of how they correlate to other spatially resolved data.

Auto-radiography measurements (section 3.1) provide low resolution spatial information (~50 μm) but do not tell us which species are present. To complement auto-radiograph

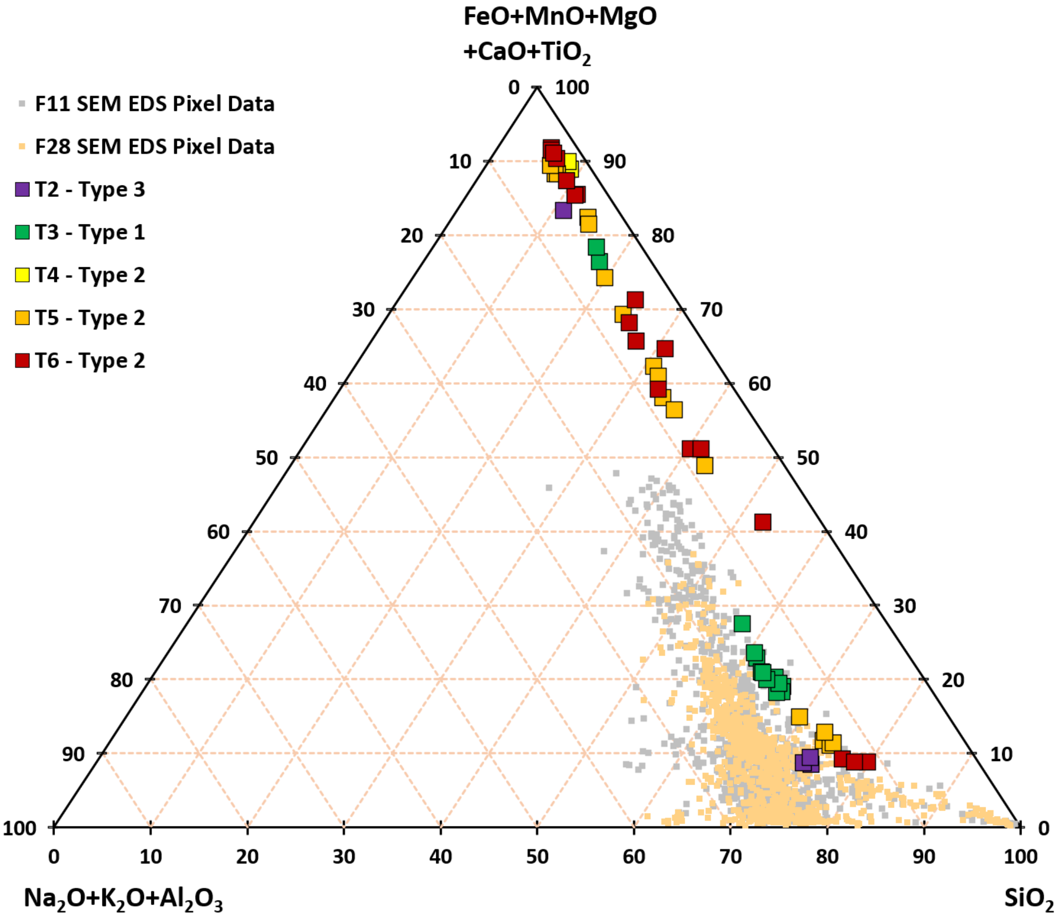

Figure 3.27: TEM-EDS data for 5 different amoeboid thin sections. Small yellow and gray data represent SEM-EDS data for individual pixels downselected from the semi-quantitative maps taken of sample F11 (from which T2 and T3 are sourced) and F28 (from which T4-T6 are sourced). SEM-EDS map data represent a mixing between the vertices of SiO_2, Alkali Feldspar, and Fe-rich component. Clear mixing lines of the majority of the data and both the Fe-rich and SiO_2 vertices are seen. Amoeboid compositions fall off this mixing line, but L_{Si} compositions are consistent with the alumina-poor, alkali-poor regions of F11 and F28, and follow the curve of the boundary of the data as it trends towards the SiO_2 vertex. L_Fe compositions in type 2 amoeboids that were not measurable using SEM-EDS are shown (T4-T6) with T5 and T6 showing significant variability due to phase domains that do not extend through the entire thickness of the thin sections.

measurements, NanoSIMS techniques can be used to measure particular trace radionuclide of interest with better spatial resolution (here, of order 1 μm). In this study, ^{239}Pu concentrations were estimated from NanoSIMS data and compared to major element concentrations. Samples were selected to study the effect of immisciblity on the distribution of radionuclides in these fallout samples. F27 was selected to study because it is a high-activity sample and contains both *in situ* and *ex situ* immiscibility textures. A mid-activity sample with *ex situ* immiscibility textures (F34) and a low-activity sample with *in situ* immiscibility textures (F29) were selected for comparison.

Sample F27 was a high-activity samples, had both *in situ* immiscibility and *ex situ* amoeboids, and was selected to study relationships between Pu and major elements traditionally associated with radioactive glass in fallout such as Fe and Ca (Figure 3.28). The correlation with Mg (often associated with Fe and Ca in radioactive fallout glass) was not investigated due to the lower concentrations compared to Ca and higher uncertainties. Data from 6 regions (R1-R6, Figure 3.29C) were collected in a high-activity region of the sample (as observed by autoradiography) across a contrast gradient observed in the reference BSE image. The location of the map with *in situ* and *ex situ* immiscibility (IM1, Figure 3.29D) is on the opposite edge of the sample, but also in a high-activity region. The BSE image of this region (Figure 3.29D) shows a region of two-phase *in situ* immiscibility textures with an *ex situ* amoeboid agglomerate with a relatively iron-deficient rim protruding from the sample surface. The ion maps show that the amoeboid is Ca-deficient, Cu-deficient, and Pu-rich relative to the *in situ* immiscibility textures and surrounding host matrix glass. The ion maps show general partitioning behavior between the *in situ* immiscible phases for ^{42}Ca, ^{54}Fe, ^{63}Cu, and ^{239}Pu. Ca and Pu are co-located in the *in situ* region. This co-location is not as strong in the relatively Ca-poor amoeboid. The Fe and Cu are co-located throughout the map.

The trends observed in the F27 map are shown in Figure 3.30 for each selected ROI using calculated estimates of ^{239}Pu concentrations using relatives sensitivity factors in a matrix (see section 2.4). Error bars represent the counting uncertainty. Approximate ^{239}Pu quantification is shown on the right axes of Figures 3.30F and 3.30G, but the error on these estimates are unknown due to uncertain matrix effects. The *in situ* ROI was selected by hand. This region was then divided in to an L_{Fe} and L_{Si} ROI by using ^{54}Fe count thresholds to match phase boundaries observed in the BSE image.

There is a weak positive trend between Ca and Pu in the R1-R6 regions (Figures 3.30F). The *in situ* region on the opposite side of the sample and the associated *ex situ* amoeboid do not fall along this trend, though the *in situ* L_{Fe} and L_{Si} phases do support a local positive correlation between Ca and Pu. There exists local positive trends between Ca and Pu but throughout the sample as a whole there likely is a negative trend between Ca and Pu.

There is also a weak positive trend between Fe and Pu in the R1-R6 data (Figure 3.30G). In contrast to the Ca data, the *in situ* region on the opposite side of the sample and its associated *ex situ* amoeboid do follow this positive correlation. However, the *in situ* region L_{Fe} and L_{Si} phases show a negative correlation between Fe and Pu, in contrast to the Ca data. While map resolution was insufficient to separate the *ex situ* amoeboid into L_{Fe}

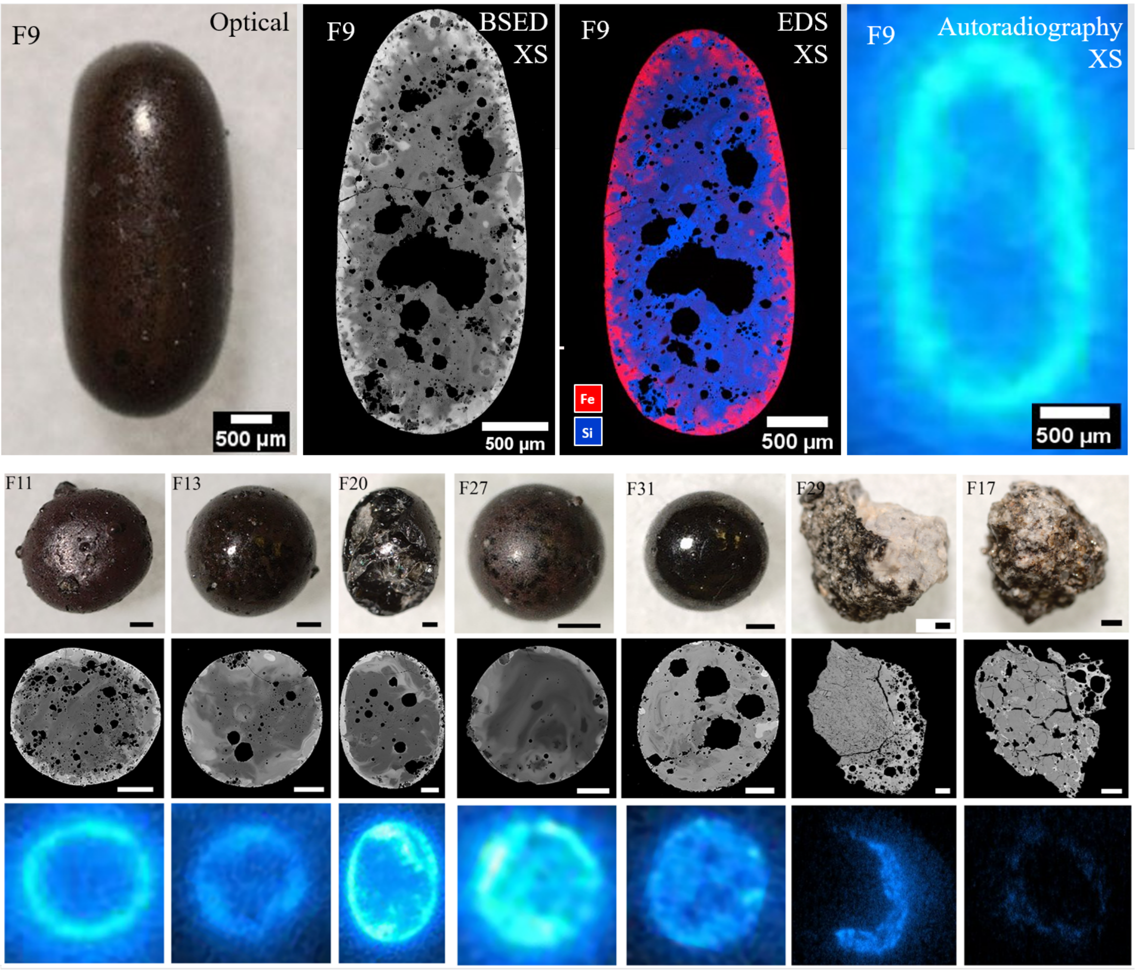

Figure 3.28: Spatial correlation of radionuclides to chemical composition in Fe-rich fallout. The top row displays an optical image of F9, an exposed cross section backscatter electron (BSE) image, an exposed cross section energy dispersive x-ray spectroscopy (EDS) map of Fe and Si, and exposed cross section autoradiography image. In these samples, BSE brightness corresponds most strongly to higher iron concentration, as shown by EDS mapping of sample F9. Each BSE image is contrast adjusted, so comparisons of iron concentration should not be made between images. Pixel brightness in autoradiography images correspond to relative alpha and beta radioactivity. Because all radiographs were collected in a single exposure, relative intensities are comparable between samples. Optical, BSED and autoradiography images of some other samples are shown in the bottom three rows, and EDS maps showed similar correlations between Fe concentration and BSED contrast. Note the strong correlation between regions of high iron content and radioactivity. Non-aerodynamic samples (like F29 and F17 in this image) showed lower levels of radioactivity, with little to no radioactivity within the un-melted mineral grains, but with varying levels of radioactivity in the glass rims or cementation glass. All scale bars are 500 µm.

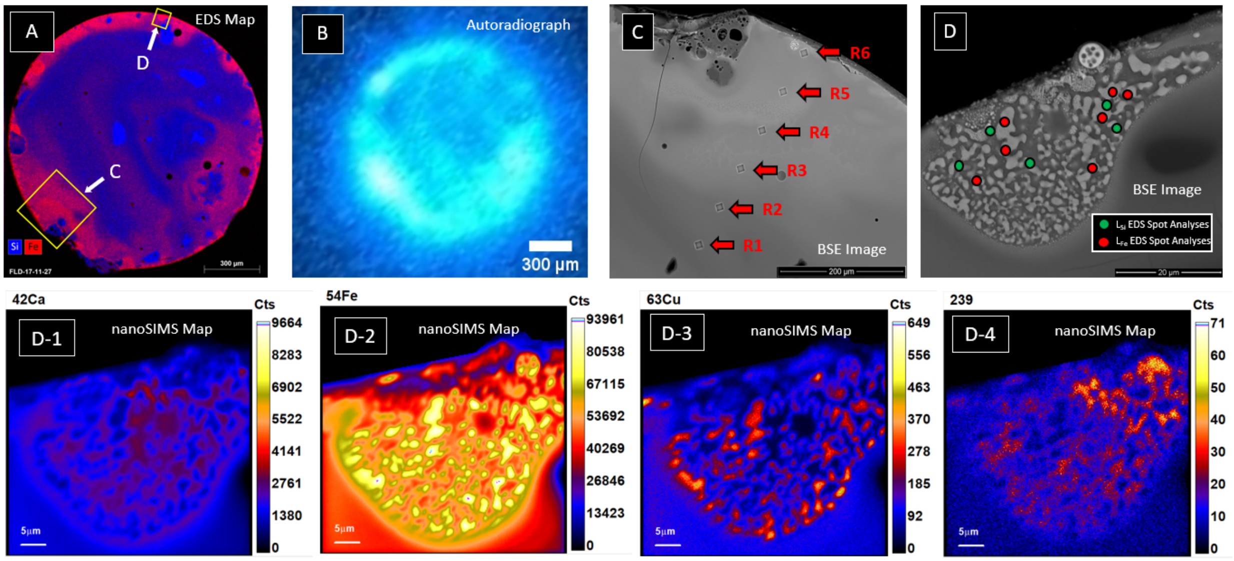

Figure 3.29: NanoSIMS maps in sample F27. (A) SEM-EDS maps of Si and Fe showing the regions of collection for R1-R6 and the F27 NanoSIMS Map. (B) Autoradiograph of F27 cross section; analyses were located in radioactive-rich, Fe-rich rims. (C) BSE image of locations of R1-R6. (D) BSE image of region where the NanoSIMS map was collected. SEM-EDS point spectra analyses locations noted were used to estimate L_{Si} (green) and L_{Fe} (red) compositions. NanoSIMS maps of the region for ^{42}Ca (D-1), ^{54}Fe (D-2), ^{63}Cu (D-3), and ^{239}Pu (D-4). Pu and Ca are co-located in the *in situ* region, but the amoeboid has higher Pu levels without a similar increase in Ca. Fe and Cu are co-located.

and L_{Si} ROIs, the ^{239}Pu ion map most closely matches the boundary of the Fe-deficient rim. There is a negative correlation of ^{239}Pu and ^{54}Fe within the amoeboid ROI, suggesting that the *ex situ* amoeboid has similar elemental partitioning to that of the *in situ* region. This variable behavior in Fe, Ca, and Pu may provide insight into the variable Fe and Ca correlations (Figure 3.14) observed in radionuclide-rich rims.

One NanoSIMS map of an *ex situ* amoeboid was collected from the mid-activity sample F34 (Figure 3.31). This map contained one amoeboid with what appears to be an agglomerated half-spherical second amoeboid. The matrix was rapidly ablated during data collection such that the amoeboid boundary shrunk for each cycle. This made summation of cycles into a single map to improve counting statistics infeasible. It also means that defining ROIs to match the L_{Fe}-L_{Si} phase boundaries was infeasible, similar to the amoeboid measured in F27. ROIs were defined by hand on the amoeboid boundary for bins of 5 cycles each, which resulted in estimations of ^{239}Pu ranging from 1.3-2.1 ppm. This concentration is significantly less than the 19.6 ppm amoeboid in F27, and shows that Pu content varies between amoeboids. With comparable Fe concentrations (40.6 wt% vs 43.4 wt% in the F27 amoeboid),

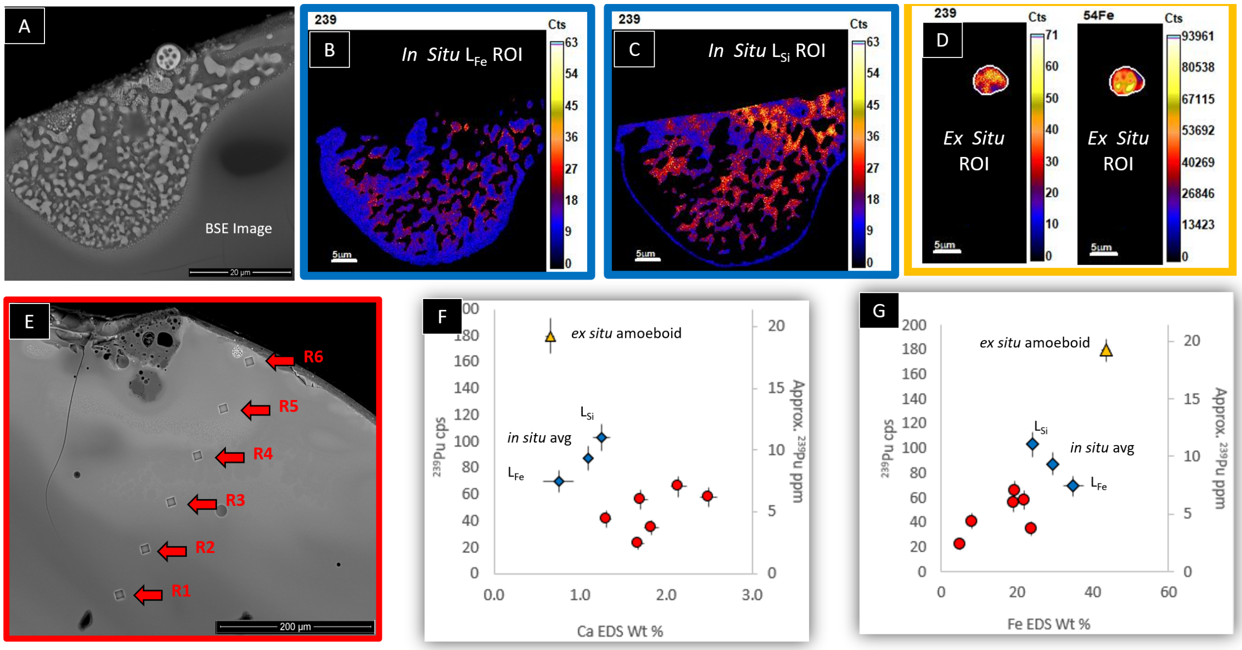

Figure 3.30: F27 NanoSIMS regions of interest. A threshold concentration of ^{54}Fe was used to define ROIs that matched the phase boundaries visible in BSE (A). The L_{Fe} ROI (B) shows lower levels of ^{239}Pu than the L_{Si} ROI (C). A threshold concentration of ^{239}Pu was used to define the *ex situ* amoeboid ROI. This ROI more closely matches the L_{Si} rim surrounding the amoeboid than the spherical L_{Fe} phase (D). The R1-R6 locations are shown in (E). The R1-R6 data (in red) are compared to the (in blue) *in situ* data with two defined ROIs (L_{Fe} and L_{Si}) and and a combined common ROI. in a Pu vs. Ca plot (F) and a Pu vs. Fe plot (G). Localized positive trends between Ca and Pu do not hold throughout the sample as a whole. The positive trend between Fe and Pu is reversed within the *in situ* immiscibility ROI.

this amoeboid does not fall along the general Fe-Pu trend observed in the F27 sample data.

In the low-activity sample (F29), the Fe-rich region has one area (R7) with a ^{239}Pu concentration of approximately 3 ppm. This value is consistent with the R1-R6 Pu-Fe values. The R7 region is more Ca-rich (3.4 wt%) than R1-R6 regions (1.3-2.5 wt%) but with only 3.5 ppm Pu, which is within the lower range of values observed in R1-R6. This datum fits the trends between Pu and Ca described in F27. In the non-glassy, low-activity region of the sample, two NanoSIMS maps (IM2 and IM3) containing immiscibility textures were collected (Figure 3.32). No significant ^{239}Pu was measured in these regions. Cu is also co-located with the L_{Fe}, and Ca is co-located with the L_{Si}. These Cu and Ca trends are both observed in the Pu-rich immiscibility regions of F27. If the positive Fe-Pu correlation observed in F27 holds throughout this sample suite, these regions (L_{Fe} with 40.9 wt% Fe

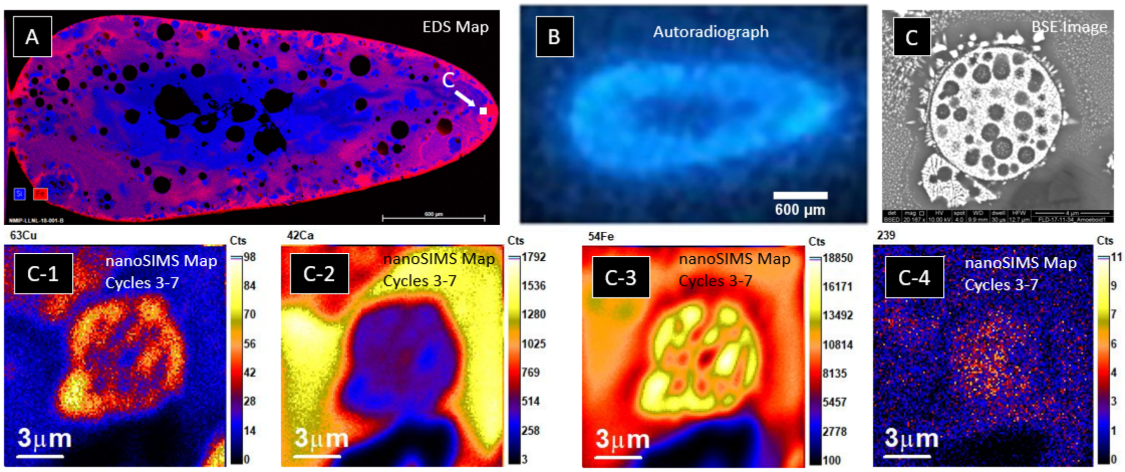

Figure 3.31: NanoSIMS map in sample F34. (A) SEM-EDS maps of Fe and Si, with the location of the *ex situ* amoeboid map annotated. (B) Autoradiograph showing a correlation between radioactivity and Fe concentration. (C) BSE image of the amoeboid used in NanoSIMS analysis. C-1 through C-4 show ion maps for cycles 3-7 for ^{63}Cu, ^{42}Ca, ^{54}Fe, and ^{239}Pu. Concentration of ^{239}Pu within the amoeboid ranged from 1.3-2.1 ppm. ^{239}Pu concentration estimates specific to the L_{Fe} and L_{Si} could not be made, but their image map suggest a weak inverse correlation between Fe and Pu.

and L_{Si} with 26.7 wt% Fe) would be expected to contain 5-15 ppm. The lack of detectable Pu suggests non-radioactive Fe may contribute to at least some of the Fe-rich features in this sample suite.

The presence of other transition metals in fallout such as Cu in fallout is of interest as it may co-condense with with the Fe. There is no measured value for Cu in the UPI glass (the Pu-containing standard glass used for these analyses), so quantification of relative concentrations is not feasible. Even so, in all NanoSIMS data, the measured counts of ^{63}Cu was well correlated with that of ^{54}Fe. This may be because it is a trace metal in the Fe source, or because Cu exhibits similar fractionation processes during evaporation and condensation. The strength of the correlation, however, varies between regions with and without detectable Pu. In Figure 3.33, ^{63}Cu/^{42}Ca is plotted vs ^{54}Fe/^{42}Ca. Fe and Cu are ratioed to Ca to attempt to minimize matrix effects. The data in F27 and F34 with measurable ^{239}Pu had much higher ^{54}Fe/^{63}Cu ratios compared to data in F29 where no ^{239}Pu was measured. All data collected in radioactive, aerodynamic regions (in both F27 and F34) fall on a similar trend-line, with a ^{54}Fe/^{63}Cu ratio of 3.6E-3. Data from non-radioactive, non-aerodynamic regions have a significantly smaller ^{54}Fe/^{63}Cu ratio of 2E-4. The two different populations could be a result of distinct source materials or could reflect varying degrees of chemical fractionation between Fe and Cu caused by distinct thermal histories.

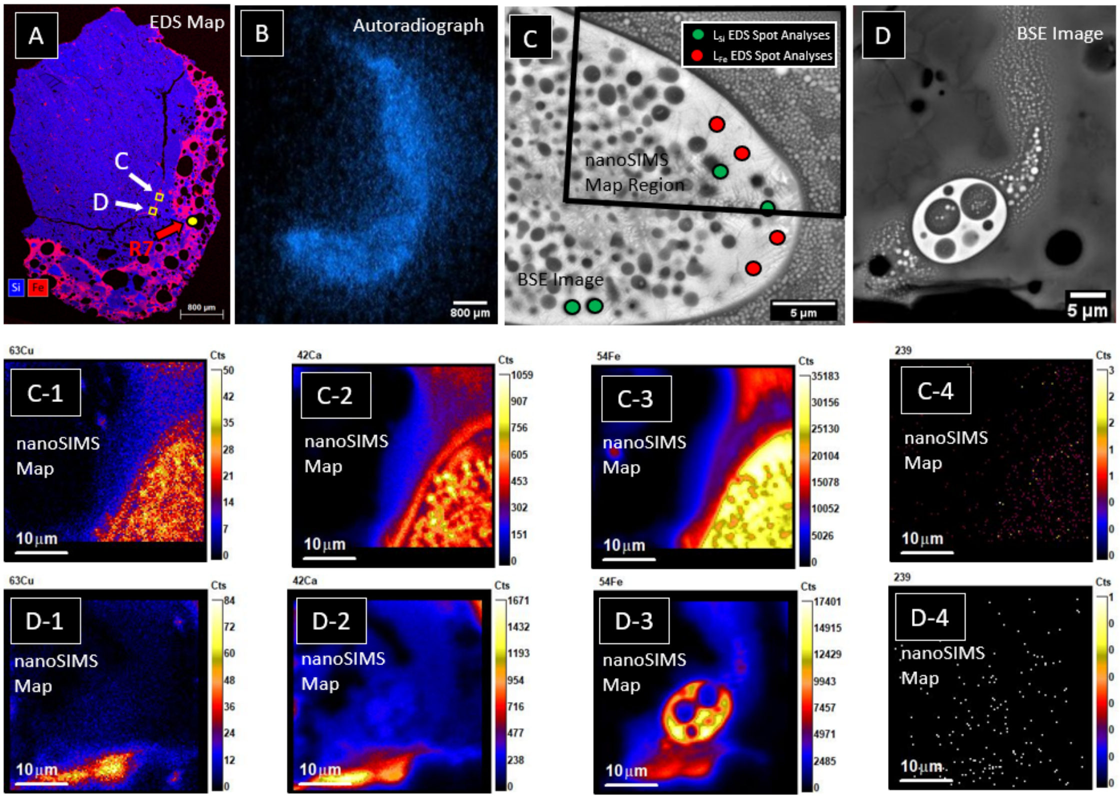

Figure 3.32: NanoSIMS maps collected in sample F29. (A) SEM-EDS qualitative map showing the distribution of Fe and Si in sample F29 and locations of a NanoSIMS measurement of the radioactive glass (R7) and of two collected NanoSIMS maps. (B) Autoradiograph measurements show radioactivity is primarily associated with the Fe-rich glassy region. (C) BSE image of the IM2 NanoSIMS ROI, with point analysis location used in estimation of L_{Fe} and L_{Si} composition. (D) BSE image of the IM3 NanoSIMS ROI - an amoeboid microstructure within a flow texture. ^{42}Ca (C-1), ^{54}Fe (C-2), ^{63}Cu (C-3), and ^{239}Pu (C-4) ion maps are shown for the first ROI, and D-1 through D-4 for the second ROI. No significant ^{239}Pu was detected in these regions.

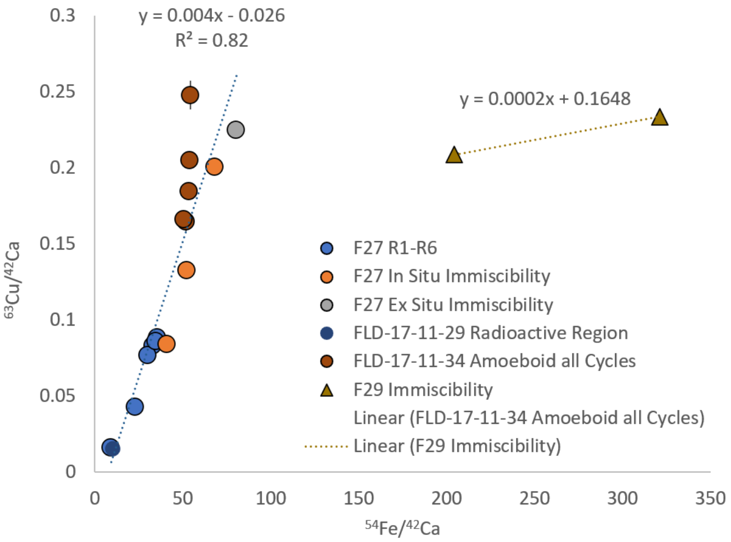

Figure 3.33: Copper and iron trends in fallout. ^{63}Cu/^{42}Ca is plotted vs ^{54}Fe/^{42}Ca. Fe and Cu are ratioed to Ca to attempt to minimize matrix effects. Two different relationships are seen in the radioactive, aerodynamic regions (circles) and the non-radioactive, non-aerodynamic regions (triangles).

3.6 Two Theories for Amoeboid Formation

This works focuses primarily on *ex situ* amoeboid for a variety of reasons. First, they are novel micro-structures that have never been observed in fallout (with some morphologies never having been observed in any system), and so their uniqueness warrant further study. Second, the known sensitivity of silicate liquid immiscibility to melt composition, temperature, and oxygen fugacity suggest that understanding these processes in fallout may enable better constraints on fireball histories. This reason for studying amoeboids also applies to *in situ* textures, which have larger spatial domains and so can be more easily studied using techniques that have limited spatial resolution. Although there are compositional differences between *in situ* and *ex situ* immiscibility textures, it is assumed that both textures are formed via similar immiscibility processes. In some cases, the *in situ* textures are used to infer *ex situ* processes (for example, NanoSIMS Pu behavior in section 3.5), but if this assumption does not hold, these inferences may not hold. Finally, amoeboid locations, textures, and compositions suggest a more intimate association with the radioactive vapor. This means they can better inform vapor dynamics where important chemical fractionation processes likely take place. Recent work [94] showed that mm-scale glass is not likely to reach thermal and chemical equilibrium with the fireball, highlighting the importance of studying

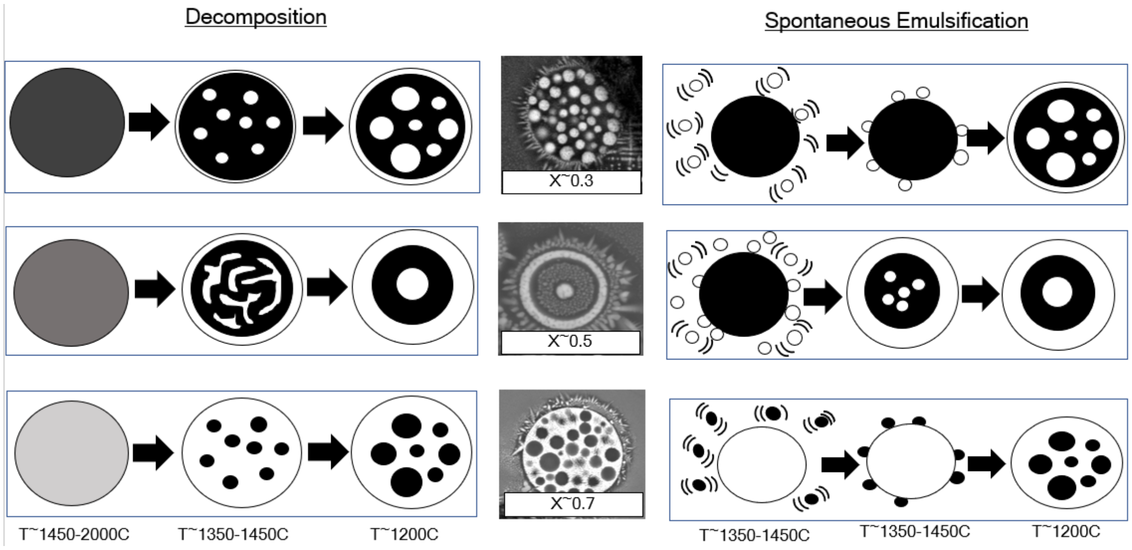

Figure 3.34: Two theories for the formation of immiscible *ex situ* amoeboids. The center greyscale images are BSE images of type 2 (top row), type 3 (middle row), and type 1 (bottom row) amoeboids. Black represents a Si-rich, Fe-poor L_{Si} composition, and white represents a Fe-rich, Si-poor L_{Fe} composition. Grey represents intermediate compositions. The left side of the image shows hypothetical amoeboid formation via decomposition from a miscible, homogeneous liquid. The righ side shows hypothetical ameoboid formaiton via emulsification of two chemically distinct liquids at immiscible temperatures. It is unknown which (or if both) of these processes contribute to amoeboid morphologies.

micro-scale features that are more likely to have achieved equilibrium withe the fireball and which offer better probes of the vapor than the mm-scale glass itself.

Given the observations made in this chapter and assuming the two-phases of amoeboids represent liquid immiscibility processes, two hypotheses for formation are offered (Figure 3.34): decomposition and emulsification. Each hypothesis results in differing implications and interpretations for fallout formation in Fe-rich environments, which are described below.

In the decomposition hypothesis, amoeboids form first by direct condensation or condensate/melt agglomeration in the vapor at temperatures greater than the solvus of the immiscibility region (>1540 K) [75] where they exist as a miscible, homogeneous melt droplets. This temperature bound may vary since the temperature of the solvus depends on the composition of the melt and is not well characterized for complex multi-component melts. As these droplets cool into the liquid immiscibility region, they spontaneously decompose into stable compositions reflecting the evolving temperature and redox environments. Their two phases then coarsen over time and finally solidify into a primarily glass matrix with occasional dispersions on nano-scale crystals (for L_{Si}) or primarily crystal grains within a glass matrix (for L_{Fe}).

In the emulsification approach, two distinct liquids of immiscible compositions are mixed and spontaneously emulsify [81] at temperatures and compositions at which they are immiscible. Their compositions may continue to change in response to the evolving fireball conditions. This process can occur in non-equilibrium systems where significant external mechanical energy results in emulsification, or if a small positive entropy of dispersion is sufficient to overcome a smaller Gibbs energy barrier (compared to equilibrium compositions). Solidification then proceeds in a similar manner to the decomposition hypothesis.

If amoeboid liquid phases reach compositional and morphological equilibrium, it would be impossible to distinguish between these two processes. However, if kinetics limits the achievement of equilibrium, it may be possible to distinguish between these processes, and to use amoeboids to make a different set of inferences if one hypothesis holds true versus the other. In Chapter 4, evidence is presented that amoeboids do not reflect equilibrium processes, highlighting the importance in distinguishing between these hypotheses. For example, if amoeboids are formed by decomposition, their compositions evolving in response to the cooling fireball may result in non-equilibrium compositions that can be used as a geospeedometry metric to infer relative quench rates [29, 96]. On the contrary, if amoeboids are formed by emulsification, their non-equilibrium compositions that reflect individual liquids that more closely match distinct precursors than can be estimated using well mixed melts. Thus, these emulsified immiscible liquids could offer more robust constraints on precursor compositions, which increases our understanding of complex energetic melt mixing within the fireball. It is difficult to distinguish between these two hypotheses at this time, as there is varying levels of evidence for each process, which is summarized below.

The evidence for decomposition is primarily textural. Examples of dispersion and interconnected textures of immiscible phases in the silicate melt literature such as from meteorite impact melts [35], lunar impact melts [75], and terrestrial magmas [74] have all been interpreted as having resulted from decomposition from an initially miscible liquid. Because nuclear fireball temperatures are known to reach temperatures far above the solvi of silicate liquid immiscibility, it is reasonable that this process could result in the observed textures. In addition, experiments in other immiscible systems applicable to industrial alloys such as Fe-Sn [50], Fe-Cu [90], and Fe-Cu-Cr [90] have produced similar immiscible textures and morphologies through decomposition to those documented in this work. In particular, these studies have resulted in core-shell morphologies analogous to type 3 amoeboids that have not been observed in fallout to date. Interconnected morphologies seen in type 4 amoeboids and in many *in situ* immiscibility textures (Figures 3.18B, 3.18E,3.20B 3.24) are attributed to a process known as spinodal decomposition, which results from the spontaneous phase separation from a homogeneous liquid. In addition, local gradations in emulsified sphere sizes of *in situ* textures are best explained with a decomposition theory with size gradations caused by local compositional or thermal gradients. These gradients would be difficult to explain using emulsification alone.

The evidence for emulsification is primarily compositional. The TEM-EDS data of amoeboid L_{Si} phases (Figure 3.27) follow the boundary of the bulk mm-scale glass composition. It would be a strange coincidence indeed if a homogeneous *ex situ* droplet experienced decomposition such that the phase separated L_{Si} compositions matched with portions of the bulk melt. If significant quantities of L_{Si} were produced via decomposition and mixed with the bulk melt, it could be that the alumina-alkali-poor portions of the host melt are just reflections of a significant L_{Si} contribution. However, this explanation would require a much higher mass contribution of phase separated L_{Si} to the bulk mm-scale sample than was observed. Thus, the TEM-EDS data supports the theory that emulsification occurred between two liquids: (1) an Fe-rich liquid (L_{Fe}) that is some mixture of pure iron or iron oxide precursor and a portion of the average melt composition sourced from the local silicate lithology and (2) the alkali-alumina poor portions of the bulk melt that has been somewhat chemically fractionated via evaporation or condensation. The L_{Fe} may represent a non-radioactive Fe source (possibly late entrained or sourced from a continually melting/evaporating Fe source), whereas the L_{Si} is the portion of the melt that has been fractionated and already incorporated an Fe-rich, radioactive vapor. This would explain the higher Pu concentrations in L_{Si} vs. L_{Fe}. The L_{Si} existing *ex situ* from the host melt could be caused by mechanical separation from the host melt or re-evaporation from the host melt. If the emulsification hypothesis holds true, is unclear whether the chemical fractionation of L_{Si} from the bulk melt would have occurred prior or after emulsification.

The preferential distribution of Ca into L_{Si} can also be interpreted as evidence for emulsification. This is because in most Fe-rich silicate immiscibility systems, Ca preferentially partitions in the L_{Fe} during decomposition [87]. Because Ca would be primarily associated with the bulk melt as a result of local minerals (vs. anthropogenic sourced Fe), emulsification would preserve the presence of Ca in the L_{Si} versus the L_{Fe}. However, complex melt interactions could also explain the Ca behavior under a decomposition hypothesis. The partitioning of Ca in silicate immiscibility systems varies according to the complex role of Al^{3+} and other 1^+ cations in the melt. Al^{3+} can act as a network former in these systems and partition into L_{Si} given sufficient 1^+ ions (such as Na^+ and K^+) are present to charge balance. It has been shown that higher Al/(Na+K) ratios in melts increases the partitioning of Ca into L_{Si}, as Ca^{2+} acts to partially charge balance Al^{3+} in the alkali-poor melt [61]. Most studies have been conducted with an Al/(Na+K)=1, whereas amoeboid compositions were $\sim$1.6. It is possible that compositional complexities of the melt result in the observed Ca partitioning within a decomposition framework. A more systematic exploration of the thermodynamics and kinetics of Ca in silicate immiscible systems would better inform the two amoeboid formation hypotheses.

The different amoeboid hypotheses offer different interpretations of the variable correlations of Pu with Ca and Fe observed within immiscible regions. While auto-radiography suggests a Fe/Pu correlation (and NanoSIMS data R1-R6 weakly supports this correlation), the reversal of this trend in immiscibility regions can be interpreted in different ways depending on the formation mechanism.

For a decomposition hypothesis, Pu is more strongly partitioned into the L_{Si} during phase separation, which is unexpected behavior considering most species besides network formers (and species that charge balance them) are expected to partition into the L_{Fe}. This partitioning behavior may be provide insight into understanding complex Pu chemistry within silicate melts.

If amoeboids formed via emulsification, the strange Pu-Ca-Fe trends can be used to infer complex mixing behavior since each liquid more closely reflects precursor compositions. In this case each liquid reflects the presence of a different precursor: (1) a Pu-poor, Fe-rich precursor (represented by the L_{Fe}) that is distinct from a (2) Pu-rich, Fe-poor source (represented by the L_{Si}). The first would be a more pure Fe source that was not intimately mixed with the radioactive vapor term. This may be due to later time entrainment of local Fe, or because the initial Fe in the fireball is not fully vaporized, and continually contributes Fe melt or vapor over the timescale of fireball cooling. In this case, late time melting/vaporization of Fe could occur at temperatures above its boiling point of 2862 °C after Pu has condensed (boiling point of 3232 °C).

The conflicting evidence for each formation hypothesis motivates a deeper investigation into amoeboid formation mechanisms. Given the complex nature of fireball dynamics, it is possible that both of these processes are significant. The first step is to establish whether compositions reflect equilibrium processes, which is explored in Chapter 4. Given the evidence presented for non-equilibrium compositions in Chapter 4, it then becomes important to investigate the kinetics of formation. Chapter 5 explores whether decomposition can explain the diversity of observed amoeboid morphologies through modeling the kinetics of phase separation and coarsening over time. The emulsification hypothesis is explored in Chapter 6 by investigating estimates of precursor compositions using the host melt compositions to determine if they match compositions of L_{Fe} and L_{Si}.

Chapter 4

Liquid Immiscibility Compositional Stability

The previous Chapter documented a variety of microstructures present in iron-rich nuclear fallout, some of which likely formed as a result of iron-silicate liquid immiscibility, a process that is sensitive to variety of parameters of interest such as temperature, oxygen fugacity (fO_2), and vapor composition. If compositions reach two-liquid equilibrium during some or all of their cooling through the miscibility gap, their compositions could provide a probe equilibrium conditions in the high temperature vapor. Whether amoeboid compositions reflect equilibrium conditions is difficult to determine because of the complexity of high temperature multi-component silicate melts and poor knowledge of amoeboid kinetics. It is more likely that amoeboids may reach equilibrium at higher temperatures due to faster kinetics. At lower temperatures the kinetics of phase separation may be sluggish. While the presence of glass in amoeboids is evidence of non-equilibrium behavior, it is possible that amoeboid compositions preserve a record of earlier processes. If so, amoeboids would provide unique insight into early fireball conditions. The focus of this Chapter is to establish whether amoeboid compositions preserve equilibrium conditions from these earlier processes.

The kinetics of and the range of thermodynamically stable silicate immiscibility regions in multi-component systems has been investigated. Such data are limited to a few systems (i.e., magmatic systems and meteorite impacts), making extrapolation to a compositionally and thermally distinct system like a nuclear fireball difficult. If amoeboids are formed via decomposition or emulsification, it is possible their two liquid compositions may reach equilibrium at some point in their evolution. Thus, as a first step in understanding amoeboid formation, it is important to understand whether their compositions reflect thermodynamically stable immiscibility. This would be evidence of an equilibrium process during a portion of fireball cooling, and would enable us to use amoeboids compositions to draw conclusions about early time vapor environments. If amoeboid compositions are not indicative of equilibrium conditions, a better understanding of the kinetics of the each theory of amoeboid formation (decomposition and emulsification) is needed.

In this Chapter, the evidence for equilibrium or non-equilibrium liquid immiscibility is investigated. First, a brief review of silicate immiscibility is presented. Second, the calculation of phase diagrams (CALPHAD) method is used to investigate general sensitivity of silicate immiscibility to a few parameters such as system composition and fO_2 and predicted two-phase compositions are compared to amoeboid compositions measured in Chapter 3. Finally, compositions are compared with literature data from similar silicate melt systems, and the presence of equilibrium conditions during amoeboid formation are evaluated. Some of this work is summarized in Genda *et al* [30] and Moore *et al* (in prep) [59].

4.1 Silicate Liquid Immiscibility

Silicate liquid immiscibility is a phenomenon that has been well documented in the literature. As excellent review of the topic exists [87], an in depth review of the literature is not offered here. Below is a brief description of the theory of liquid immiscibility in silicate systems.

The spontaneous separation of systems into distinct chemical phases is known as immiscibility and is due to a lower overall energy of the separated phases vs. when mixed together. In silicate (SiO_2) melt systems immiscible liquid phases can be stable for a range of compositions and temperatures which depend on the complex properties and compositions of the silicate melt. At temperatures where SiO_2 is molten, the melt is polymerized into networks of O-Si-O, where Si is referred to as a 'network former'. The addition of other ions into the melt do not polymerize as easily, serving to modify the silicate networks, and are known as 'network modifiers'. Network formers and network modifiers compete for non-bridging oxygen (oxygen that is not between two network forming ions). This results in the evolution of two compositionally distinct liquids, one which is highly polymerized (rich in SiO_2) and a second liquid that is less polymerized (depleted in SiO_2). The effect of different ions on silicate immiscibility is function of their charge, radius, and crystal field stabilization energies. Ions which are too large to enter tetrahedral sites act only as network modifiers and cannot act as network-formers (such as alakalis and alkine earths). Some ions can act as network-formers or as modifiers depending on the overall melt composition. One example of this behavior is Al^{3+} which alone acts as a network modifier, but in the presence of other 1+ ions, can act as a network former the 1+ ions charge balance the aluminum in the silicate network.

While liquid immiscibility has been studied in a variety of binary systems, the complex interactions of multi-component melts makes predictions of immiscibility in ternary, quaternary, and higher orders systems difficult. The interactions between network formers and modifiers result in immiscibility fields of varying compositional and temperature ranges. In a FeO-SiO_2 system (see Figure 4.X), a stable two-liquid field exists at T>1685°C between 55-100 mol% SiO_2 with this compositional range expanding as a metastable liquid immiscibility field at sub-liquidus temperatures. The solvus (the boundary between the two-liquid field and homogeneous liquid field) can extend to temperatures >2000°C, and the two liquids separate into FeO-rich and FeO-poor liquids. The difference in FeO content is smaller at higher temperatures. The addition of other ions in the system such as Aluminum suppresses the solvus of the immiscibility region, resulting in less difference in FeO between the two liquids. If sufficient Al is added to the system ($\sim$5 mol%), the stable immiscibility region is suppressed below the solidus such that only sub-solidus, metastable immiscibility is present in the system. However, in some cases (such as the leucite-fayalite-silica system), some species (such as Al) serve to reduce the solvus of the miscibility gap, while other species (alkalis like Na and K) simultaneously reduce the solidus. Because of these competing influences, some ratios of aluminum and alkalis (such as 1:1 present in leucite) result in the emergence of a second, lower temperature immiscibliity region for higher aluminum and alkali content. At high oxygen content, these two immiscibility regions merge into a single region of wide compositional and temperature ranges. The competitive nature of different ions in multicomponent silicate melts make predicting the extent of these regions of immiscibility complicated.

Because of complex mixing relationships between natural and anthropogenic precursors, single fallout glass samples can exist with a wide range of compositions. One example of this range is shown by sample F24 in Figure 4.1B. Here, an SEM-EDS mosaic map for Si, Fe, and Al of the exposed cross section is shown. Compositions range from Si-rich (primarily a quartz precursor), to Fe-rich (anthropogenic metal) and Al-rich (feldspathic precursor). As such, during formation of fallout glass, condensation, agglomeration, and mixing behavior can result in some regions with immiscible phase textures (Figure 4.1C) without (Figure 4.1D). It is uncertain to what extent the presence/non-presence of immiscibility is driven by composition vs. temperature history. Understanding conditions under which immiscibility regions are stable can better allow us to interpret the presence of such regions and predict to what extent immiscibility will be significant in a given system.

4.2 Prediction of Stable Compositions in the FeO-SiO_2-Al_2O_3-CaO-MgO System

One approach for identifying temperature ranges, oxygen partial pressures, and multicomponent melt compositions such as those documented in Chapter 3 is to apply a CALPHAD approach [40, 76, 86]. CALPHAD modeling is based on a set of adjustable parameters to represent Gibbs energy functions for a given phase as a function of composition, temperature and pressure. The model parameters are optimized by fitting inputs of critically selected thermochemical and constitutive data from the literature, including experiment and ab initio calculations. The assessed functions are compiled in a database for use in computational thermodynamic predictions across multicomponent materials. This permits the association of observed compositional phases with defined physical conditions. In the case that phase formation in fallout occurred in the brief period between ejection from the fireball and deposition on the ground, such fallout will record a snapshot of the historic fireball conditions.

In this work two sub-lattices are conceptualized for each phase, one which describes the

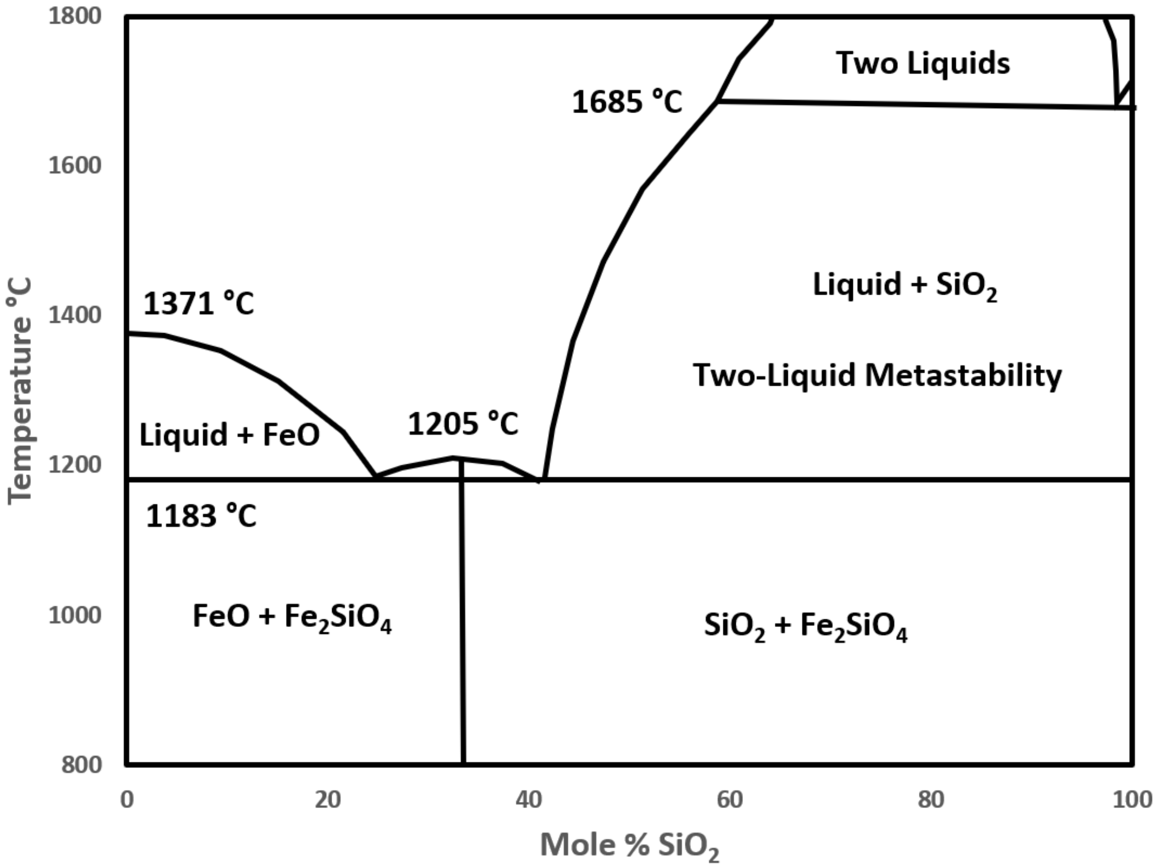

Figure 4.1: The FeO-SiO2 binary phase diagram, reproduced from [51]. The two liquid region represents the immiscibility region, with a solvus that is not well characterized at high temperatures. This diagram is altered when different Fe valence states are present (such as magnetite and hematite). The addition of other ions into the melt significantly alters the compositional and temperature extent of the two liquid region.

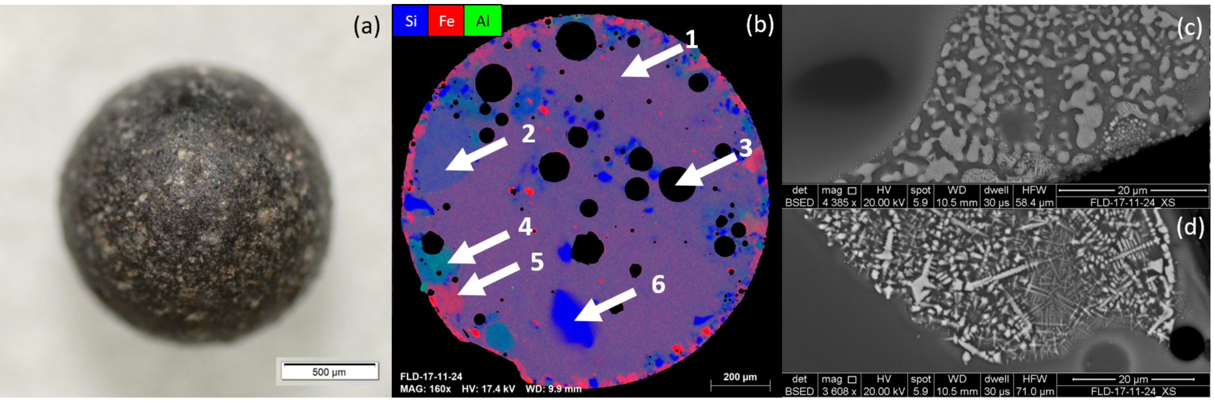

Figure 4.2: Sample F27 showing compositional heterogeneity and with some regions of silicate immiscibility. (a) Optical image with partially melted or unmelted grains across the surface. (b) An energy dispersive X-ray spectroscopy mosaic map showing the relative abundances of Si, Fe and Al from a cross section of the sample reveals compositional heterogeneities throughout the particle and highlights the Fe-rich sample rim. In this sample the interior preserves a relatively homogeneous melt composition (arrow 1) with Fe-poor melt regions (arrow 2), vesicles (arrow 3), Al-rich melts (arrow 4), Fe-rich melts (arrow 5), and partially melted entrained quartz grains (arrow 6). The Fe-rich regions of the sample often exhibit distinctive textures as illustrated by the lighter grey areas seen in backscatter electron images (c and d). Examples include (c) rounded, often interconnected textures hypothesized to be caused by liquid immiscibility, and (d) dendritic textures.

distribution of cations and the other for anions, neutral species, and vacancies, allowing distributions of each species to vary between the two liquid phases. The neutral species are introduced to help describe non-metallic liquids. For a given temperature and using assessed and extrapolated parameters for the Gibbs energy from lower order binaries and ternaries, the distribution of species between the two liquid phases is optimized to find the minimum Gibbs energy. The thermodynamic description of the Si-Fe-Al-Ca-Mg-O system used for this work is taken from the Thermodynamics of Advanced Fuels-International Database (TAF-ID)[67] and includes the Gibbs energy parameters of Fe-Si-O [78], Al-Si-O [53], Al-Fe-O [68], Al-Ca-O [54],and Al-Mg-O [54]. Using commercially available ThermoCalc software, calculations were preformed to predict a variety of phase diagrams and two-phase compositions.

First, this CALPHAD method is used to predict phase diagrams for a range of compositions relevant to fallout observations in order to investigate general temperature and compositional sensitivity to composition. Second, phase diagrams for two fO_2 were calculated in order to investigate general sensitivity to oxygen environments. Predictions are compared to amoeboid compositions in a later section of this Chapter, though there are significant limitations to this comparison due the TAF-ID database does not contain assessments of alkalis, which are known to have have a significant impact on the extent and range of immiscibility in silicate systems.

Immiscibility Sensitivity to Amoeboid Composition

To determine general sensitivity of liquid immisicbility to composition, a solvus for the stable liquid immiscibility region was calculated for the FeO-SiO_2 system, and then compared to gaps calculated with the addition of 5 wt% Al_2O_3, 5 wt% Al_2O_3 plus 1 wt% CaO, 5 wt% Al_2O_3 plus 2 wt% CaO, and 5 wt% Al_2O_3 plus 2 wt% CaO and 1 wt% MgO. Results of these calculations (Figure 4.2) demonstrate how the compositional variation results in changes to the temperature compositional range of the solvus. The simple FeO-SiO_2 system has a maximum predicted temperature of immiscibility at 1950 °C at compositions of 24 wt% FeO, and indicate a wide range of stability fo the 2-phase liquid domain across compositions between 5-67 wt. % FeO and a temperature range of 1620-1950 °C. With the addition of 5 wt% Al_2O_3, 2% CaO, and 1% MgO, this temperature is suppressed by more than 160 °C to 1790 °C and the compositional range of stable two-liquid immiscibility contracts to $\sim$10-60 wt% FeO. This behavior is consistent with studies by Roedder [74] where addition of these components suppress the solvus.

Sensitivities to minor species can result in the reduction or disappearance of a stable region of immiscibility. Plotted in Figure 4.2 are the average bulk compositions for the L_{Fe}-dispersed and L_{Si}-dispersed amoeboids for comparison, where the range in compositions represent the differences in the SEM-EDS and TEM-EDS averages. In this case the L_{Si}-dispersed amoeboid compositions would fail to experience stable phase separation with the addition of 5 wt% Al_2O_3, 2% CaO, and 1% MgO.

The limitations of modeling the miscibility gaps without the presence of alkali oxides (which significantly alters the miscibility gap shape, temperature, and compositional range) make drawing quantitative conclusions challenging. If amoeboids are formed via the decomposition hypothesis, CALPHAD predictions would expect both amoeboid morphologies to be L_{Si}-dispersed. We expect the L_{Fe}-dispersed and L_{Si}-dispersed amoeboid compositions to lie on opposite sides of the miscibility gap than their dispersed phase. Since the midpoint of the miscibility gaps (Figure 4.2) are roughly 30 wt% FeO, the L_{Fe}-dispersed amoeboid are predicted to be <30 wt% FeO, and the L_{Si}-dispersed amoeboids >30 wt%. Both amoeboid morphologies are >40 wt% FeO. These calculations demonstrate immiscibility sensitivity to overall composition, with consistent trends which validate the general approach. The omission of alkalis in this model means the decomposition hypothesis cannot be ruled out.

Immiscibility Sensitivity to Oxygen Fugacity

Recent studies suggest that oxygen fugacity can vary in nuclear fireball systems [70, 8]. Here the extent of fO_2 on immiscibility in fallout systems is explored. In Figure 4.3, the deviation in SiO_2 is plotted as a function of temperature for two different oxygen partial pressures, and for a range of Al_2O_3 mol%. In high oxygen environments where $p(O_2) = 1$ atm (Figure 4.3a), the two-phase liquid miscibility gap extends across a temperature range of

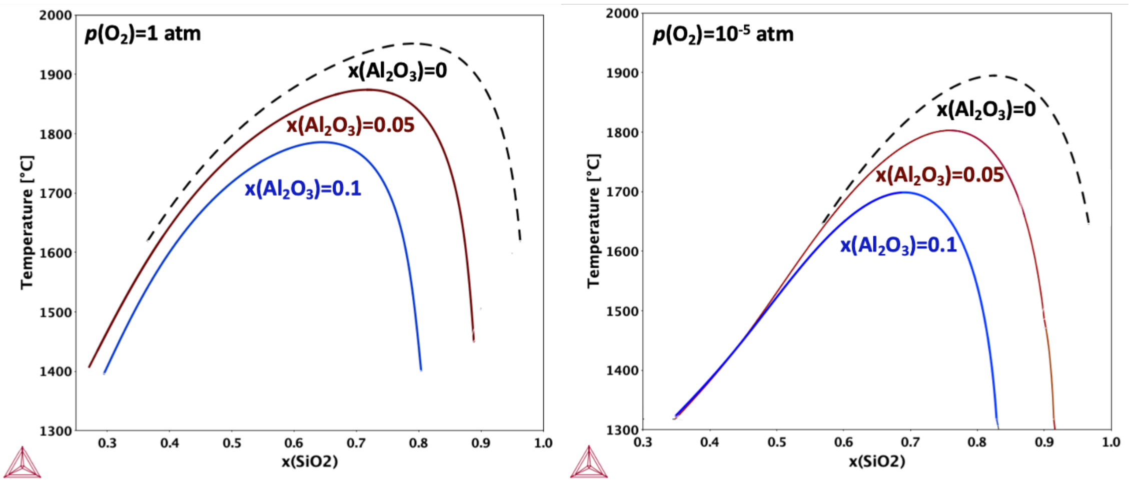

Figure 4.3: CALPHAD-predicted sensitivity to fO_2 in the FeO-SiO_2-Al_2O_3 system. Solvi are shown for the FeO-SiO_2 pseudobinary phase diagrams with variable contributions of Al_2O_3 for two oxygen partial pressures (a) $p(O_2) = 1$ atm and (b) $p(O_2) = 10^{-5}$ atm. The black dashed line shows the liquid miscibility gap in the absence of Al_2O_3, the red line illustrates the system including 5 mol% Al_2O_3, and blue line illustrates 10 mol% Al_2O_3. These calculations demonstrate sensitivity to both Al composition and fO_2.

from 1620 - 1950 °C without Al_2O_3 and exists between silicate compositions of approximately 35-95 mol% SiO_2. The addition of Al_2O_3 alters the stability of the two-phase liquid domain, decreasing the maximum temperature of the two-liquid region by 77 and 167 °C for 5 and 10 mol% Al_2O_3, respectively, but extending the stability range to lower temperatures. The presence of Al_2O_3 also shifts the phase boundaries towards enrichment in FeO (depletion in SiO_2). Similar trends are observed in Figure 4.3b for lower oxygen content system ($p(O_2) = 10^{-5}$ atm), where the maximum temperature of the liquid miscibility gap decreases with higher Al_2O_3 content and the phase boundaries are shifted towards a more Fe-rich, Si-depleted portion of the phase diagram. In the absence of Al_2O_3 (black dotted lines), a noticeable contraction of the miscibility gap at lower oxygen pressures is predicted, such that the two-phase domain is stable across a smaller composition range. The presence of Al_2O_3 (a comparison of the blue lines) causes an overall shift in the phase boundary for both higher and lower oxygen systems but results a similar range of compositions. The Al-containing systems at lower partial pressures stabilize the two-phase liquid domain to a lower temperature compared to atmospheric pressures, $p(O_2)$ =1 atm. These results demonstrates the contraction of the immiscibility field at lower oxygen partial pressures, consistent with general behavior in multicomponent systems of varying compositions [61].

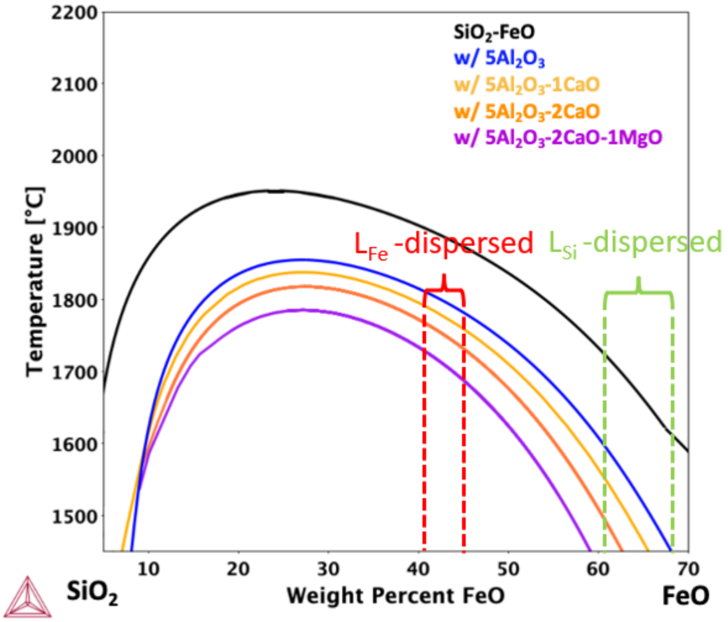

Figure 4.4: CALPHAD-predicted sensitivity to FeO, SiO_2, Al_2O_3, CaO, and MgO). The black line shows the predicted solvus for the FeO-SiO_2 system, with the other lines showing the effect of substituting varying levels of Al_2O_3, CaO, and MgO on the temperature and compositional range of stable high temperature liquid immiscibility. The dashed lines represent the range of average bulk composition of L_{Fe}-dispersed and L_{Si}-dispersed from both SEM and TEM-EDS measurements. While both morphologies have compositions that would experience high temperature liquid immiscibility for a simple FeO-SiO_2 system, the addition of other components suppresses the temperature range such that the temperature range of L_{Si}-dispersed compositions is significantly suppressed.

Table 4.1: Bulk composition of Amoeboids as measured by SEM and TEM in oxide weight percent. Low concentration elements measured but not modeled in this work (Na, K, Mn, Ti) are excluded and oxide sums are normalized to 100%

	Type 2(L_{Fe}-Dispersed)		**Type 1(L_{Si}-Dispersed)**	
Component	SEM	TEM	SEM	TEM
SiO_2	50.2	44.6	32.5	25.2
FeO	41.4	45.2	61	67.1
Al_2O_3	5.9	6.8	4.6	4.8
CaO	1	1.3	0.6	1.8
MgO	1.5	2.1	1.3	1.2

CALPHAD Predictions of Two-Liquid Compositions

The previous section explored overall sensitivities of liquid immisciiblity to composition and oxygen fugacity. In this section, we model compositions matching L_{Fe}-dispersed and L_{Si}-dispersed amoeoboids across a range of temperatures. TEM-EDS measurements of L_{Fe}-dispersed and L_{Si}-dispersed amoeoboids were used to calculate stable two-liquid compositions over a range of temperatures and compared to average L_{Fe} and L_{Si} compositions. Because the TAF-ID database used for these calculations does not include K, Na, Ti, or Mn (present in concentrations of 2-3 wt%, see Chapter 3), these elements were neglected and the balance was normalized to 100%. Two-liquid compositions were calculated (Figure 4.4). L_{Fe}-dispersed amoeboids are expected to have stable 2-liquid compositions >1400 °C, whereas the L_{Si}-dispersed amoeboids are expected to have stable 2-liquid compositions >1120 °C. CALPHAD calculations either overestimate or underestimate compositions of each liquid across the range of stable compositions, and thus each oxide concentration represents a different equilibrium temperature. This data can also be represented as Nernst distribution coefficients (Figure 4.5) which ratios the oxide wt% in the L_{Fe} phase to that in the L_{Si} phase. The Nernst coefficients for MgO, FeO, and CaO are most sensitive to temperature, each of which provide different apparent equilibrium temperature estimations. For instance, in L_{Fe}-dispersed amoeboids, measured FeO compositions imply T<1400 °C, whereas MgO implies T∼1500 °C. CaO is not consistent with predicted composition, but would imply higher temperatures (>1600 °C). Because the lack of alkali in the CALPHAD modeling efforts, it is difficult to say whether the mismatch between modeled and measured Nernst distribution coefficients is due to non-equilibrium conditions or a function of incompletely modeling of all species.

CALPHAD calculations demonstrate the utility of the approach in understanding fallout sensitivities to a range of parameters (composition, oxygen partial pressure, temperature) and the potential for these types of models to place quantitative constraints on phase formation thereby independently constraining the physical parameters attending fallout formation. Modeled two-phase compositions predicted varying equilibrium temperatures for measured amoeboid compositions, suggesting either non-equilibrium conditions and/or model limitations. Inclusion of alkalis and other minor components will improve equilibrium compositional estimates.

4.3 Comparison of Amoeboid Compositions to Literature Data

The development of the CALPHAD approach offers a flexible approach to investigating the range of compositions in fallout. However, until alkalis are incorporated into this approach, calculations cannot be used to reliably constrain equilibrium behavior. Accordingly, it is useful to compare amoeboid immiscible compositions to the closest stable two-liquid compositions that have been observed in the literature. In this section, amoeboid SEM

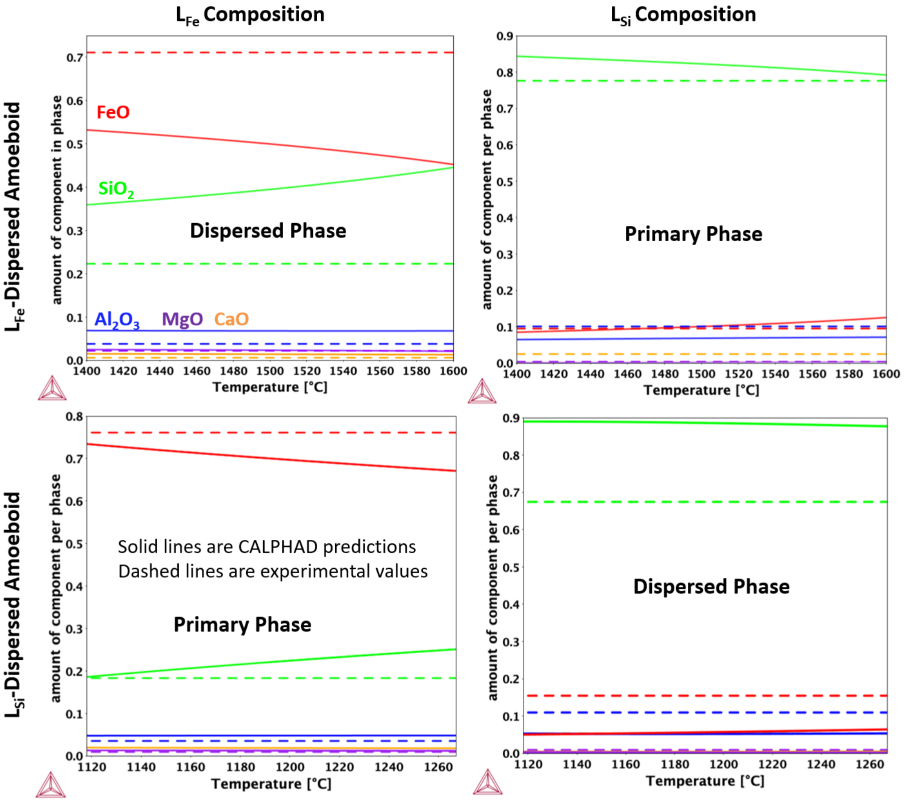

Figure 4.5: CALPHAD two-liquid compositions compared to average composition for each element as calculated by TEM-EDS (see Chapter 3). Top row shows the L_{Fe} and L_{Si} phase compositions for the L_{Fe}-dispersed amoeboid morphology. Bottom row shows phase compositions for L_{Si}-dispersed amoeboid morphology. Solid lines represent the predicted temperature dependent compositions of each liquid, and dashed lines represent the measured TEM 2-phase compositions. Where dashed and solid lines intersect represent temperatures where modeled compositions are in agreement with the average measured composition. Modeled and measured compositions vary in agreement.

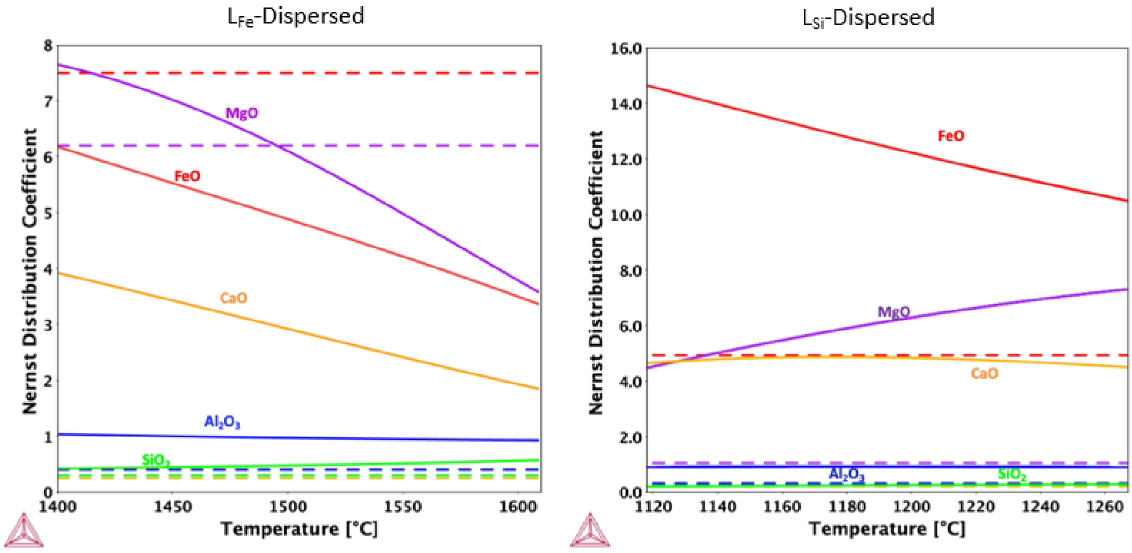

Figure 4.6: CALPHAD Nernst partitioning coefficient predictions. This figure is another way to express the data plotted in Figure 4.4. Nernst coefficients represent the wt% of each oxide species in the L_{Fe} divided by the wt% in the L_{Si}. Inconsistent agreement of Nernst coefficients with experimental measurements suggest that either amoeboid reflect non-equilibrium behavior or, if they represent equilibrium behavior, incorporation of alkali behavior (Na and K oxides) is necessary to use CALPHAD efforts to constrain equilibrium formation conditions.

and TEM-EDS compositions are compared to fO_2-dependent data for the $KAlSi_3O_8$-FeO-Fe_2O_3-SiO_2 system published by Naslund [61]. Compositions are then compared to a metric established by Borisov and Veksler [6] that empirically correlates compositions to equilibrium temperatures.

Comparison to Naslund Oxygen Fugacity Data

In traditional fallout models, we assume the after initial heating, reduction, and vaporization, the fireball increases in fO_2 over time due to oxygen entrainment and decreases in temperature due to radiative cooling and environmental entrainment. Both an increase in fO_2 and cooling would result in a broadening of the immiscibility gap. Even considering kinetic limitations caused by rapid quenching, any measured compositional contrast between phases represents a lower bound of the local fO_2. Amoeboid compositions are similar in major element composition to the $KAlSi_3O_8$-FeO-Fe_2O_3-SiO_2 system liquid immiscibility experiments [61], with similar two-liquid compositions. Naslund showed that the average wt% differences between the two immiscible liquids increases with fO_2, with average wt% difference of FeO at T_{Liq} of 66, 53, 39, and 25 wt% for fO_2 of $10^{-0.7}$, 10^{-5}, 10^{-9} and 10^{-12}, respectively. While amoeboids do also include minor amounts of Na_2O, CaO, MgO, and TiO_2, we expect Na_2O to behave chemically similarly to K_2O because of similar alkali role in the melt [87], and Naslund showed that CaO, MgO and TiO_2 effects are minor for concentrations <1.5 wt%.

The 2-phase compositions of all amoeboids characterized using SEM-EDS (Figure 4.6) are projected onto a pseudo-ternary diagram to compare their compositions to the fields of immiscibilty in the Naslund study. There is significant compositional range within measured L_{Fe} and L_{Si} compositions. This is either due variations in the extent of stable immiscibility (due to variations in bulk amoeboid composition and/or fO_2 conditions) or is due to the spatial resolution limitations of the SEM-EDS technique. Average FeO wt% difference of the two-phases present measured by SEM is 40 wt% for F34 amoeboids and 49 wt% for F28 amoeboids, which falls between a fO_2 values of 10^{-5} and 10^{-9}. Thus, amoeboid compositions qualitatively reflect $fO_2 > 10^{-9}$.

TEM-EDS measurements have submicron resolution and better reflect two-phase compositions (Figure 4.6). As was described in Chapter 3, a variety of ROIs were defined to take multiple measurements of L_{Fe} and L_{Si}. ROIs with the most contrasting compositions (highest Fe content for L_{Fe} and highest Si content for L_{Si}) are plotted. These data points represent the widest extent of the miscibility gap which exists at the most oxygenated systems and lowest temperatures. Intermediate compositions present in some core-shell structures that do not match well with L_{Fe} or L_{Si} phases are plotted.

Average difference in FeO wt% of the two-phases present measured by TEM captures more contrast than that of the SEM measurements (75 wt%). This FeO wt% difference between the two-phases is larger than reported in the Naslund experiments. This observation can be interpreted in several ways. Subliquidus metastable immiscibility (with greater compositional contrast) may continue to play a role at lower temperatures. Sluggish kinetics and rapid quench at lower temperatures makes this explanation unlikely. Alternatively, compositional differences in the Naslund experiments and this system (such as different alumina/alkali ratios) result in wider stable immiscibility fields. If amoeboids do not reflect equilibrium conditions, each amoeboid formation hypothesis would predict different compositional behavior, as discussed in Chapter 3. For a decomposition hypothesis, compositions would be less contrasting than expected. For an emulsification hypothesis, compositions would be more contrasting than expected. If amoeboids reflect non-equilibrium behavior their large compositional difference supports an emulsification hypothesis.

Amoeboid Compositional Comparison to Kamenetsky Temperature Data

L_{Fe} and L_{Si} compositions are also likely sensitive to their thermal histories due to the temperature-dependent width of the immiscibility solvus. Lower equilibrium temperatures will result in more contrasting compositions. Uncertainties in the shape of multi-component silicate miscibility gaps and in the kinetics of decomposition make quantitative constraints

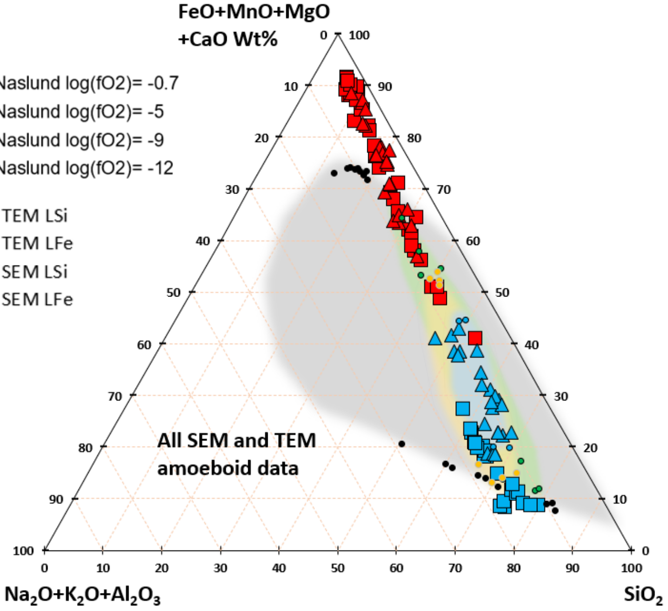

Figure 4.7: Amoeboid compositional comparison to Naslund fO_2 data. Two-phase compositions for amoeboids using SEM and TEM EDS data compared to measured fields of immiscibility for different fO_2 in multicomponent systems from Naslund[61]. The spread of data may represent spatial-resolution compositional limitations rather than real variation.

difficult to distinguish from fO_2 effects. If we assume amoeboids experienced similar fO_2 environments during decomposition, however, variations in amoeboid composition will reflect different apparent equilibrium temperatures (T_{AE}). Kamenetsky [39] developed an empirical connection for liquid immiscibility in a tholeiitic gabbro system to T_{AE} using the distribution coefficient D of SiO_2 between L_{Fe} and L_{Si} phases. Both SEM-EDS and TEM-EDS data for L_{Fe} phases correspond well with the Kamenetsky fit (Figure 4.7).

Distribution coefficients between amoeboids for SEM-EDS and TEM-EDS data vary from 0.07 to 0.58 (Fig. 4.7), corresponding to differences in T_{AE} of 180 °C in the Kamenetsky system. It is possible that, if fO_2 remains constant during decomposition, this variation in T_{AE} is related to variations in quench rates between amoeboids. While decomposition may rapidly result in stable liquid compositions at temperatures far above the liquidus, as amoeboids approach T_{Liq}, achievement of equilibrium may be kinetically limited and fail to reach the most contrasting equilibrium two liquid compositions. Such limitations would result in compositions that reflect a T_{AE}, where $T_{AE} > T_{Liq}$. In this case, T_{AE} is a geospeedometry metric, where a higher T_{AE} reflects a faster quench rate for amoeboids of similar composition [96]. Important differences exist in the Kamenetsky system (which contains significant amounts of P_2O_5) that preclude quantitative T_{AE} in amoeboids, but the

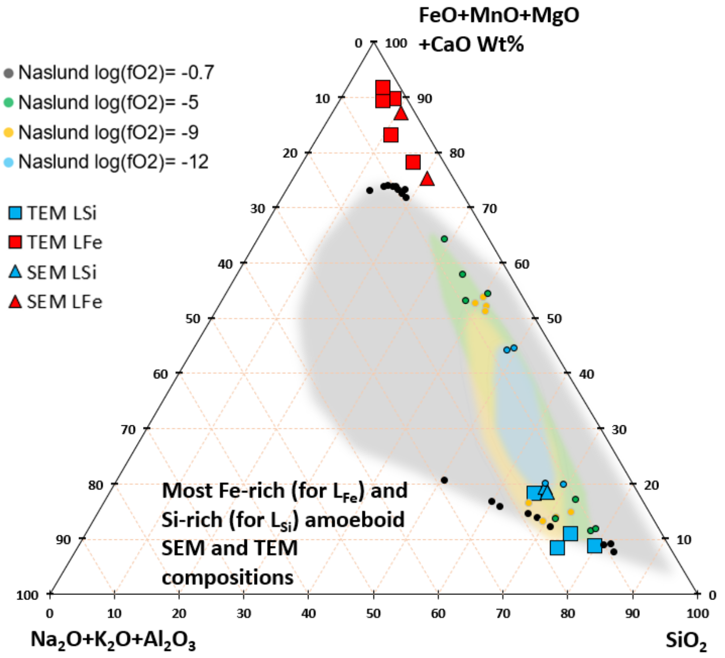

Figure 4.8: Amoeboid compositional estimates of most contrasting composition comparison to Naslund fO_2 data. This data is subset of the data from Figure 4.6 that show estimates for real L_{Fe} and L_{Si} compositions by using the most contrasting compositions (i.e. most Fe-rich for L_{Fe} and most Si-rich for L_{Si}. L_{Si} compositions are consistent with a range of Naslund immiscibility fields, but L_{Fe} compositions are not.

variation in this metric shows that decomposition compositional variations of amoeboids preserved in fallout may be sensitive to fireball thermal histories.

Amoeboid Comparison to Borisov and Veksler Equilibrium Metric

Inconsistencies with CALPHAD predictions and measured Naslund and Kamenetsky data in the previous sections suggest amoeboids may represent non-equilibrium behavior. It is difficult to determine if inconsistencies are due to non-equilibrium, analytical error, or differences in the compositional extent of stable immiscibility fields due to differences in overall system composition. Recent work by Borisov and Veksler [6] developed a metric to determine equilibrium behavior for immiscible liquids that is insensitive to systematic errors of microprobe analysis, temperature, pressure, and oxygen fugacity. Borisov and Veksler define a distribution coefficient as:

$$K_d^{K/Fe} = \left(X_K^s / X_K^f\right) / \left(X_{Fe}^s / X_{Fe}^f\right) \tag{4.1}$$

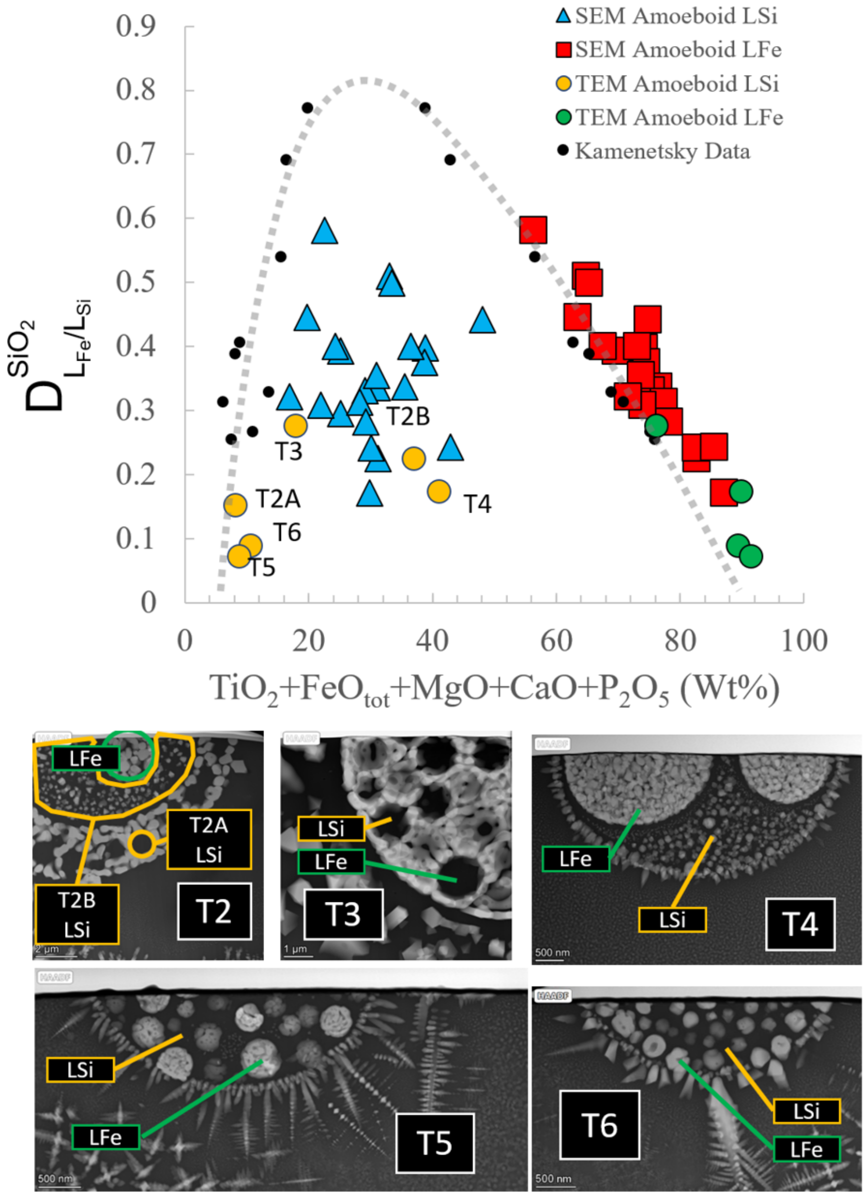

Figure 4.9: Amoeboid compositional comparison to Kamenetsky temperature data. Kamenetsky [39] uses the Nernst distribution coefficient D, defined as the ratio of SiO_2 in L_{Fe} with that in L_{Si}, and plots it as a function of the sum of network modifying oxides in each phase. D has been empirically correlated to equilibrium temperatures, with higher values corresponding to higher temperatures. Kamenetsky data are shown in black, and compared to SEM data (blue and red) and TEM data (yellow and green). L_{Fe} SEM and TEM data are in good agreement. L_{Si} data show more spread, likely due to spatial resolution limitations, amoeboid bulk compositional variation, and non-equilibrium behavior.

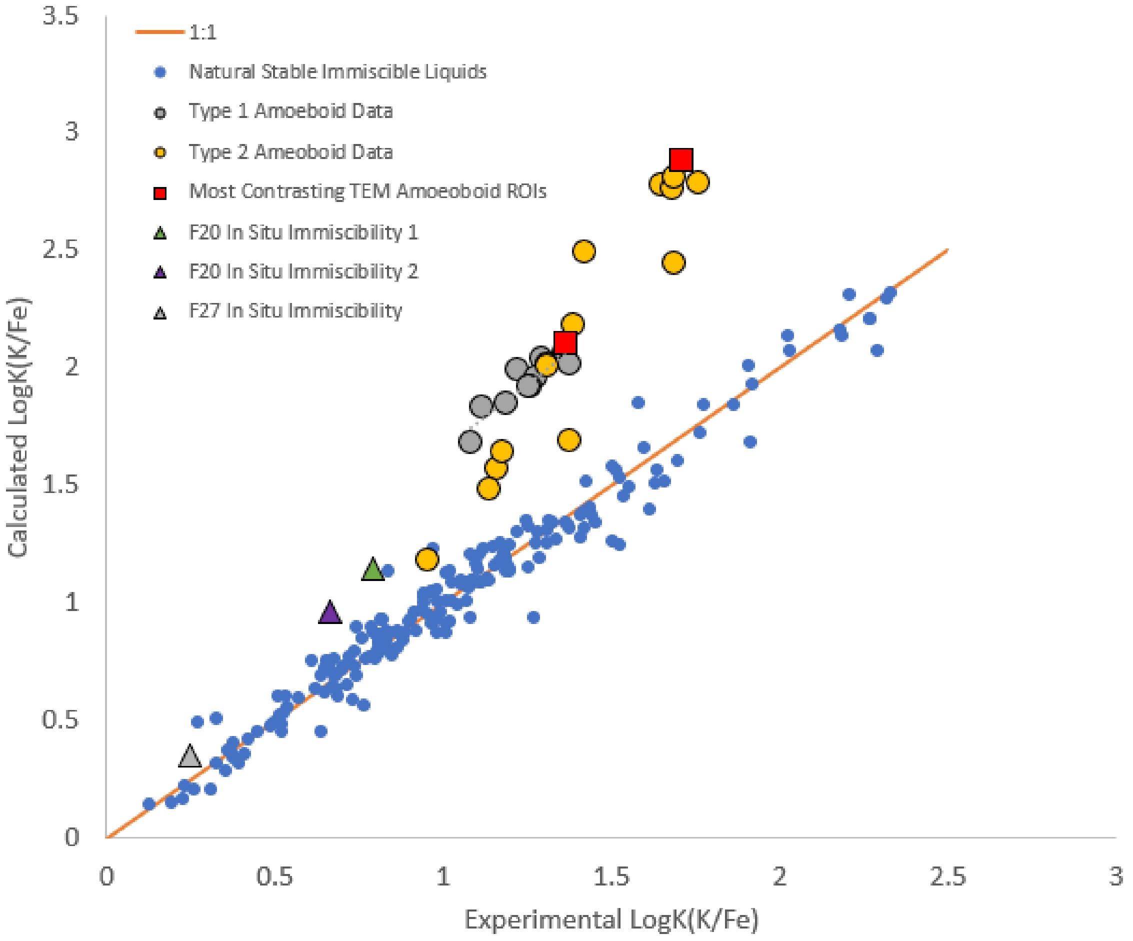

Figure 4.10: Borisov-Veksler equilibrium metric for TEM-measured compositions. Circles represent metric calculations for SEM measured ameoboids. Squares represent the most contrasting compositional measurements in TEM data. Triangles represent measurements of large *in situ* bands of immiscibility observed in F20 and F27 (Figure 3.18F for F20).

where X_K^s is the mole fraction of K in the silica-rich liquid (L_{Si}), X_K^f is the mole fraction of K in the Fe-rich liquid (L_{Fe}), X_{Fe}^s is the mole fraction of Fe in the silica-rich liquid (L_{Si}), and X_{Fe}^f is the mole fraction of Fe in the Fe-rich liquid (L_{Fe}). This metric is empirically fit to the mole fractions of network forming oxides that is thermodynamically derived:

$$logK_d^{K/Fe} = 3.796\Delta X_{sf}^{SiO_2} + 4.85\Delta X_{sf}^{Al_2O_3} + 7.235\Delta X_{sf}^{P_2)_5} \tag{4.2}$$

where ΔX_{sf}^i is the difference of the mole fractions of a component i between the L_{Si} and L_{Fe} phases. Compositions that deviate from this trend represent non-equilibrium conditions.

To test our data, TEM-EDS data from amoeboids described in Chapter 3, and plotted according to this metric (Figure 4.8), compared to the experimental datasets used to validate the Borisov and Veksler model. Results demonstrate that all amoeboid compositions deviate from this line and thus reflect non-equilibrium conditions. A data point from a region of *in situ* immiscibility observed within sample F20 s closer to equilibrium conditions than *ex situ* amoeboid compositions. This region of immiscibility has larger domain scale lengths for the two phases, which may reflect a longer time for coarsening than smaller amoeboid phases experienced, thus more time to reach compositional equilibrium.

4.4 Evidence for Non-Equilibrium Compositions

Understanding the thermodynamics of the multi-component system was explored using a CALPHAD approach to predict the stability of the liquid immiscibility regions in order to understand the composition and temperature experienced by the high temperature melt. This work showed that constraints on the miscibility gap as a function of temperature, composition, and oxygen content can be calculated using the CALPHAD method and can be used as a guide to predict the conditions attending phase formation in historic nuclear fallout. The development of CALPHAD predictions [30] of phase stability and the ability to use such predictions alongside characterization of historic fallout provides a new, interpretative tool, with such textures in fallout providing a snapshot in time of fireball conditions immediately prior to fallout quench. Further development of this approach could provide new data constraining fireball evolution and fallout formation in addition to advancing models of fallout formation and radioactivity distributions for compositionally complex, near surface nuclear explosions.

However, preliminary CALPHAD predictions, while consistent with general trends observed in the silicate immiscibility literature, do not match well with measured amoeboid compositions. This is either due analytical artifacts, the influence of alkalis which are not considered in the initial CALPHAD work, or because of non-equilibrium behavior. Comparison to similar silicate immiscible systems in work by Naslund and Kamenetsky showed varying degrees of agreement with stable compositions, making it difficult to distinguish between equilibrium or non-equilibrium compositions. A recent metric developed by Borisov and Veksler determines with good accuracy whether compositions reflect non-equilibrium compositions. Comparison of data in this work with this metric suggests that amoeboid data do not reflect equilibrium compositions and is very good evidence of non-equilibrium conditions. In conclusion, future studies using compositions to constrain amoeboid formation conditions (and by extension, fireball vapor conditions) should not only use liquid immiscibility equilibrium compositions, but also take into account the kinetics of phase separation and/or emulsification.

Chapter 5

Decomposition an Explanation for Amoeboid Morphology

During and after amoeboid formation, observations suggest Fe-rich (L_{Fe}) and Si-rich (L_{Si}) phases coarsen and evolve into a variety of morphologies. Immiscible textures in fallout are striking and warrant explanation, as their compositions and morphology reflect different information depending on their formation condition. If amoeboids are formed via emulsification, compositions may better reflect individual precursor compositions and record complex mixing and entrainment behavior. If amoeboids are formed via decomposition, such textures capture a 'snapshot' reflecting incomplete phase separation and highlight the significance of kinetics to understanding fallout formation.

In this chapter, the decomposition hypothesis is investigated by using a phase field method approach to investigate morphological dependence on a range of parameters. The goal is to determine whether decomposition can recreate the variety of amoeboid morphologies that have been observed. Our results show that amoeboid morphologies are consistent with a decomposition formation mechanism. An overview of each characteristic L_{Fe} and L_{Si} amoeboid morphology is reviewed. Next, motivation for the phase field methodology (PFM) and it's use in modeling amoeboid microstructures is described, and results of the simulations are reviewed. We also investigate the possibility of Marangoni migration as a possible contributing factor to core-shell amoeboids via decomposition or emulsification. Finally, the overall evidence for decomposition as the formation mechanism is summarized.

5.1 Amoeboid Morphologies Observed in Iron-Rich Fallout

Amoeboids have a variety of morphological arrangements of an iron-rich liquid phase (L_{Fe}) and silica-rich phase (L_{Si}). While L_{Fe} and L_{Si} solidify into some mixture of iron oxide crystals and silicate glass, we presume the original compositions of each phase prior to solidification is preserved within the micro-scale compositional boundaries. The approximate

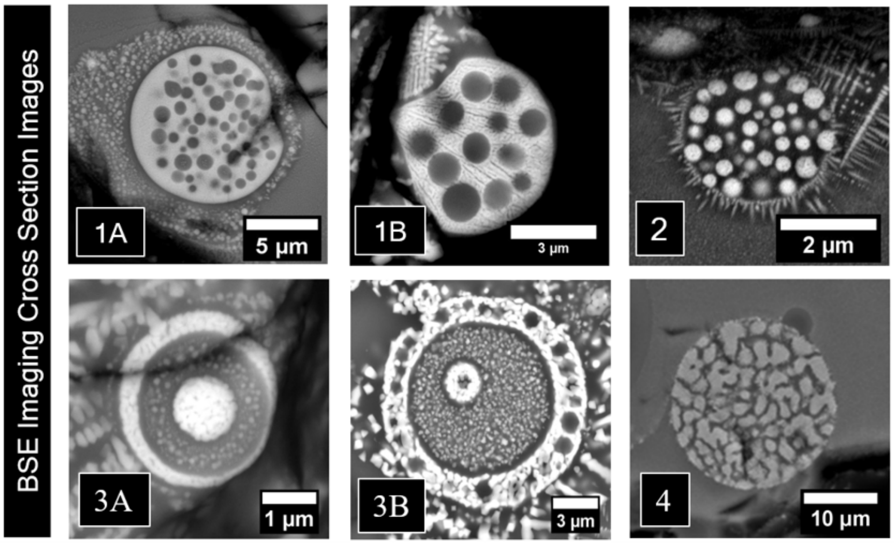

Figure 5.1: Overview of primary amoeboid morphology categories. Amoeboids take on a variety of morphologies shown as backscatter electron (BSE) images , where brighter regions represent the solidified iron-rich liquid (L_{Fe}) and darker regions represent the solidified silicate-rich liquid (L_{Si}). L_{Fe} regions generally solidify to Fe-oxide crystalline grains dispersed in silicate glass, and L_{Si} regions solidify to glass or Fe-oxide crystalline grains dispersed in silicate glass. Morphologies generally fall into four categories: (1) L_{Si}-dispersed amoeboids (A,B), (2) L_{Fe}-dispersed amoeboids (C), (3) Core-shell amoeboids (D,E), or (4) Interconnected amoeboids (F).

compositions of these amoeboids and their two phases are described in chapter 3 and in the appendix. Amoeboids generally fall into four morphological categories, shown in Figure 1: (1) L_{Si}-dispersed, (2) L_{Fe}-dispersed, (3) Core Shell, and (4) Interconnected. Type 1 L_{Si}-dispersed morphologies can be subdivided into Type (1A) which exhibit an L_{Si} rim and (1B) those without an L_{Si} rim. Nano-scale dispersions of Fe-rich phase is sometimes observed within the dispersed L_{Si} phase but is always observed in L_{Si} rims. Type 3 core-shell morphologies can also be subdivided into (3A) those with no L_{Si} dispersed within the L_{Fe} core and rim, and (3B) those with an L_{Si} phase dispersed within the L_{Fe} phases. The majority of amoeboids exhibit Type 1 and 2 morphologies (on the order of 100s of amoeboids in the exposed cross sections of 10 aerodynamic glass fallout samples), whereas Type 3 or more rare (10-20 amoeboids), and Type 4 was very rare (3 amoeboids).

Development of a modeling framework can support whether decomposition can reasonably explain the diversity of amoeboid morphologies that have been documented. Although there are a range of modeling methodologies that could be adapted for our spatial domain of interest, a widely used method today for mesoscale microstructure modeling is the phase field method (PFM).

5.2 Phase Field Methodology

The PFM is μm length-scale approach well suited for dealing with complex interface morphologies. This approach has the advantage of being computationally straightforward and can incorporate the basic thermodynamics and kinetics of phase transformations. The PFM treats the interface as a diffuse boundary and allows a single (or multiple) order parameter(s) to define the entire system continuously, where certain space and time-dependent values define each phase, and regions where the order parameter varies defines interfaces between phases. These phase field(s) could be as simple as the concentration of a minority solute, or other phase definitions for microstructure coarsening in solids. This method allows us to set boundary conditions where we deem necessary but does not require boundary conditions at each interface. With the evolution of phase field(s), the interface evolution can be tracked over time in an *ad hoc* manner, though choosing parameters is difficult in order to quantitatively describe the kinetics of a given system.

A quantitative model is not attempted here due to the complexities and uncertainties in melt thermodynamics, physical parameters, and kinetics, and instead choose a simplified model to explore morphological sensitivity. In general, there are two PFM equations that govern the evolution of different classes of field variables: The Allen-Cahn equation for non-conserved field variables, and the Cahn-Hilliard equation (CHE) for conserved field variables [4]. Silicate immiscibility can be modeled using two-liquid phase separation involving concentration changes of some solute. The CHE is used to evolve a phase field that represents the concentration of Fe-oxide or Si-oxide numerically over time. Although each component in a complex melt will have different diffusivities, a simplified approach is applied that utilizes a single field variable ϕ which represents the stable iron-rich liquid composition at ϕ=-1 and the stable silicate-rich liquid composition at ϕ=+1.

The CHE is derived by taking the continuity equation, which describes the time dependent behavior of a conserved variable ϕ representing the concentration of an atomic species within the melt:

$$\frac{\partial \phi(\bar{r},t)}{\partial t} = -\nabla \bullet \overrightarrow{J}(\bar{r},t) \tag{5.1}$$

Where J is the atomic flux of atoms, and is defined as:

$$\overrightarrow{J}(\bar{r},t) = -M\nabla \bullet \mu(\bar{r},t) \tag{5.2}$$

Where M is the atomic mobility and ψ is the chemical potential. The chemical potential ψ is defined as the functional derivative of the free energy functional with respect to the spatially dependent concentration function:

$$\mu(\bar{r},t) = \frac{\delta F[\phi(\bar{r})]}{\delta \phi(\bar{r})} \tag{5.3}$$

This free energy functional F can be designed to accurately represent the energy of our system. The term functional means that F is dependent not just on a variable, but an entire function, which in this case is the position dependent phase field $\phi(\mathrm{r})$. The functional formation of the total free energy is important because it allows energy terms to be defined not only as a function of local compositions but also in relation to compositional variations throughout the system (i.e., energy formed from interfaces between phases). Combining equations (1.1 – 1.3), we arrive at the general form of the CHE:

$$\frac{\partial \phi}{\partial t} = \nabla M \nabla \frac{\delta F}{\delta \phi} \tag{5.4}$$

If the relevant energy terms are assumed in our system rely on bulk thermodynamic energy and the energy from the interfacial energy between phases, we can define the total free energy as:

$$F\left(\phi\right) = \int_V \left[f\left(\phi\right) + \kappa (\nabla \phi)^2\right] dv \tag{5.5}$$

Where the first term f is the bulk free energy density of the system given by local concentration only (usually expressed as the Gibbs free energy), and the second term depends on the concentration gradient, which describes the energy added to the system by interfacial tension. With this energy definition and the algebraic rules of functional derivatives, we can arrive at a term for the chemical potential as:

$$\psi\left(\overline{r}, t\right) = \frac{\delta F\left[\phi\left(\overline{r}\right)\right]}{\delta \phi\left(\overline{r}\right)} = \frac{\partial f}{\partial \phi} - \kappa \nabla^2 \phi \tag{5.6}$$

Which allows us to arrive at a CHE of the form:

$$\frac{\partial \phi}{\partial t} = \nabla M \nabla \left(\frac{\partial f}{\partial \phi} - \kappa \nabla^2 \phi\right) \tag{5.7}$$

To model the system, f, M and κ are defined to appropriately reflect the thermodynamics and kinetics of the system. In this work, these parameters are qualitatively defined to investigate parameter sensitivity in a computationally simple manner. The f is defined as a symmetric double-well form to represent the Gibbs energy of a liquid immiscible system such that its minimums are at ϕ=±1 representing the L_{Fe} phase ϕ=-1 and the L_{Si} phase ϕ=+1:

$$f\left(\phi\right) = A\left(\frac{\phi^4}{4} - \frac{\phi^2}{2}\right) \tag{5.8}$$

Any double-well function would work for a qualitative model. This functional form is chosen for convenience, since it's derivative (the forcing function) in the CHE is simple and computationally straightforward:

$$\frac{\partial f}{\partial \phi} = A\phi\left(\phi^2 - 1\right) \tag{5.9}$$

In this case, A defines the height of the Gibbs energy barrier between the two stable phases. Because f is not well characterized for complex systems, A is arbitrarily set to

1 for computational simplicity. If f is well characterized or A is known, then these two parameters can be related to a measured interfacial energy per unit area derived by Chen [10], but requires an adaptation of the value of κ as well:

$$\sigma = \frac{4\sqrt{2}}{3}\sqrt{\kappa A} \tag{5.10}$$

While there has been one study that has measured liquid-liquid inter-facial energies (σ) in the system K_2O-FeO-Fe_2O_3-Al_2O_3-SiO_2 at atmospheric oxygen fugacity at T=1500°C and 1550°C (16.4 mN/m and 7.8 mN/m, respectively), insufficient knowledge of the Gibbs energy curve for complex systems with evolving compositions precludes us from setting A and κ in any semi-quantitative manner. Thus, with A=1, κ is related to some characteristic width of the interface between the two liquid phases. The interfacial coefficient is defined as $\kappa = \epsilon^2$ where ϵ is the characteristic width of the interface such that decomposition interfaces are created and evolve on the length scale of our simulation. For amoeboids of 5 μm, the interfacial width is defined to be 0.1 μm. The mobility is defined to be on the order of the self-diffusivity of Fe in the FeO-SiO_2 system [79] to be 8×10^{-9} m^2/s. Because these parameters are set arbitrarily to observe decomposition on the length scale of the amoeboids, results are qualitative and sensitive to boundary conditions.

To compute the evolution of ϕ in equation 1.7, the 4^{th} order differential equation is split up into two coupled 2^{nd} order differential equations for computational simplicity and solved simultaneously:

$$\frac{\partial \phi}{\partial t} = \nabla M \nabla \psi \tag{5.11}$$

$$\psi = \frac{\partial f}{\partial \phi} - \kappa \nabla^2 \phi \tag{5.12}$$

A wetting boundary condition is defined on the surface of the droplet (see Figure 5.2) such that θ defines the wetting angle between the two liquids and **n** is the vector normal to the surface of the droplet:

$$n \cdot \kappa \bigtriangledown \phi = \kappa cos(\theta) \left|\bigtriangledown \phi\right| \tag{5.13}$$

The wetting angle θ is related to the interfacial energies of the system:

$$\cos\theta \; = \frac{\gamma_{L1} - \gamma_{L2}}{\sigma} \tag{5.14}$$

Where σ is the interfacial tension between the two liquids and γ_{L1} and γ_{L2} are the interfacial tensions between each liquid and air. Since we lack a good understanding of these interfacial energies especially for non-equilibrium systems, θ is defined explicitly in these simulations.

In order to solve the system, the finite element method is used available in the commercially available COMSOL software. Equations 5.11 and 5.12 are implemented using a coefficient form PDE option within the software. The boundary conditions applied in 5.13 is available as a boundary condition within the software and is applied to the surface of the

2D cross section of the amoeboid, with κ and θ being defined by the user. The simulations were run with an extra fine mesh and a Lagrange function for discretization. Simulations were performed over a timescale of 1 ms with 1 μs time steps, with the exception of the cooling behavior study (section 5.3), which was extended to 10 ms. Some 3D simulations were also performed with the only observed difference to the 2D model being a slightly more rapid coarsening effect during and after decomposition. However, because the current model is not quantitative, this effect is neglected and 2D simulation results are shown in this work.

5.3 PFM Results and Discussion

Morphology can be visualized by calculating the phase fraction of L_{Fe}, where regions of L_{Si} phase have a phase fraction of 0, and regions of L_{Fe} have a phase fraction of 1. Simulation results are also visualized in the cooling behavior study by plotting ϕ directly. Many simulations were preformed to demonstrate how morphology evolution depends on each parameter. Morphological sensitivities were systematically explored to (1) initial amoeboid composition, (2) wetting angle, (3) cooling behavior, and (4) atomic mobility and interfacial energy. The following sections discuss sensitivity to these parameters.

Compositional Sensitivity

It is expected that for a miscibility gap with two components A and B, a liquid enriched in component A will first nucleate component B resulting in a dispersed B phase in a matrix A phase, and a liquid enriched in some component B will first nucleate component A, resulting in a dispersed A phase in a matrix B phase. At intermediate compositions, interconnected spinodal decomposition textures can also develop. It is expected that amoeboids more enriched in FeO (ϕ=-1) will have the SiO_2-rich phase (ϕ=+1) dispersed within the interior and those less enriched in Fe-oxide will have the Fe-oxide rich phase dispersed within the interior.

PFM simulations were performed across a range of initial compositions that are within the spinodal of the Gibbs energy curve using a phase field parameter of -0.5 to +0.5 in 0.1 increments. Inside the spinodal, phase separation occurs spontaneously from any fluctuation in the melt, and so we restrict our study to spinodal decomposition for simplicity. More extreme compositions outside the spinodal exist in a region called the binodal, where phase separation can also occur. However, in the binodal, modeling phase separation requires incorporating nucleation theory which will result in a number of nucleated phases determined by the temperature-dependent thermal compositional fluctuations such that a random formation of a cluster of a nucleated phase must be sufficiently large to overcome the energy of creating the interface to grow stably over time.

For this study, the wetting angle is set to $\theta = 2\pi/5$ radians to approximate the wetting angle measured from one partially wetted L_{Fe} droplet on the surface of one amoeboid using

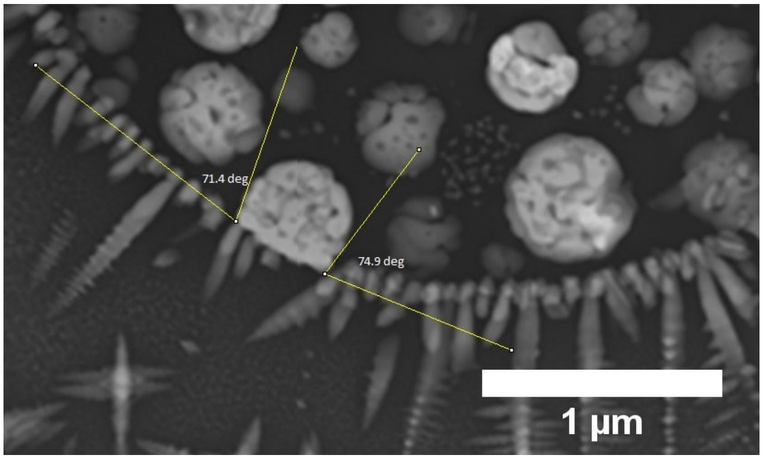

Figure 5.2: TEM HAADF image evidence of wetting behavior. Here, the L_{Fe} phase is dispersed (bright spherical regions) and one can be seen wetting the interior surface of the amoeboid at approximately 71-79°. A value of 72° ($2\pi/5$ radians) is used.

TEM imaging techniques (Figure 5.2), κ=$10^{-14}m^2$, M=$8\times10^{-9}m^2/s$, and an initial ϕ thermal fluctuation of 0.1. We ran the simulations for 1 ms using 1 μs timesteps.

Final amoeboid morphologies are displayed for a subset of simulations in Figure 5.3. As expected, high positive ϕ_0 values result in a Type 2 morphology with partially wetted droplets, and intermediate ϕ_0 values resulted in Type 4 morphologies. However, setting wetting angle to match that observed in Type 2 morphologies precluded negative ϕ_0 values of evolving into Type 1 or Type 3 morphologies. Wetting behavior of the L_{Si} phases are not observed on the surface of Type 1 amoeboids, suggesting that composition is not the only parameter that amoeboid morphologies are sensitive to.

Wetting Angle Sensitivity

Varying initial composition is insufficient to explain the diversity of morphologies. Variations in wetting angle must also be invoked. The wetting angle is a function of the surface energies of each liquid and the interfacial energy between the two liquids, as defined in equation 5.14. However, there is insufficient data on these parameters for this system, and so the wetting angle is defined explicitly. Morphology variation was explored over 3 different wetting angles ($\theta = 0$, $\pi/2$, and π) for 3 different compositions (ϕ_0 = -0.3, 0, and +0.3).

With a wetting angle of 0 rad, variations in composition can recreate Type 1B and Type 3A morphologies, but is inconsistent with the other Types. In Figure 5.4C the Type 3A morphology has not yet developed, but for longer simulation times the dispersed phases in the interior coarsen into a single phase (Type 3A in Figure 1) and given sufficient time, eventually the interior dispersed phase completely disappears as the wetted surface phase grows

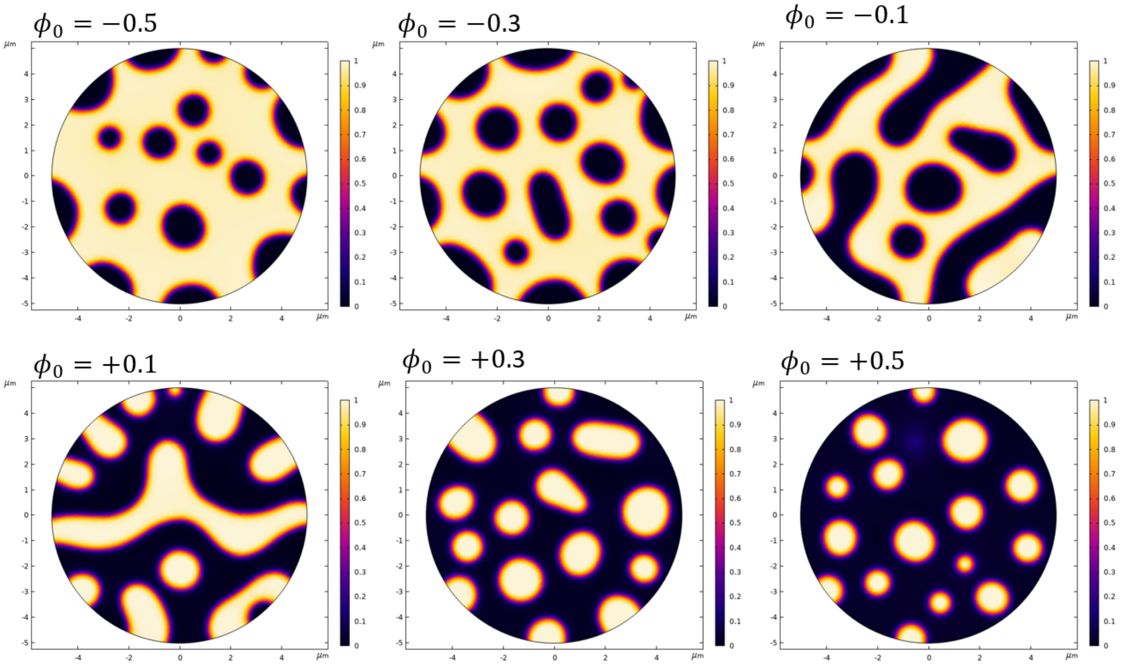

Figure 5.3: Decomposition sensitivity to amoeboid composition with initial compositions spanning the compositional space of the spinodal from ϕ_0=-0.5 to +0.5. Holding the wetting angle constant, and only changing the composition results in the observed morphologies, which match Type 2 and Type 4, but not Type 1 and Type 3 morphologies. The color scale legend represents the phase fraction of the L_{Fe}, from 0 to 1, where 0 represents the L_{Si}.

in thickness. With a wetting angle of $\pi/2$, intermediate compositions are consistent with Type 4 morphologies. Finally, with a wetting angle of π rad, variations in composition result in morphologies consistent with 1A, and 2 but is not consistent with the other morphology Types. While it is expected that wetting angles will depend on each liquid composition, a total reversal of wetting behavior is unexpected (Type 1A vs Type 1B), since some studies [89] suggest that the more polymerized L_{Si} phase should preferentially wet the surface. It is possible that the kinetics of decomposition in a non-equilibrium system, contributes to variations in wetting behavior, that there are unknown surface-interfacial energy dependencies on composition, temperature, and (fO_2), or that other mechanisms of formation are occurring during decomposition.

Cooling Behavior Sensitivity

Wetting angle and compositional variation can explain the majority of amoeboid morphology. One exception is that of the complex core-shell morphology (Type 3B, Figure 5.1). We hypothesize that this morphology can be a result of decomposition, but requires at least

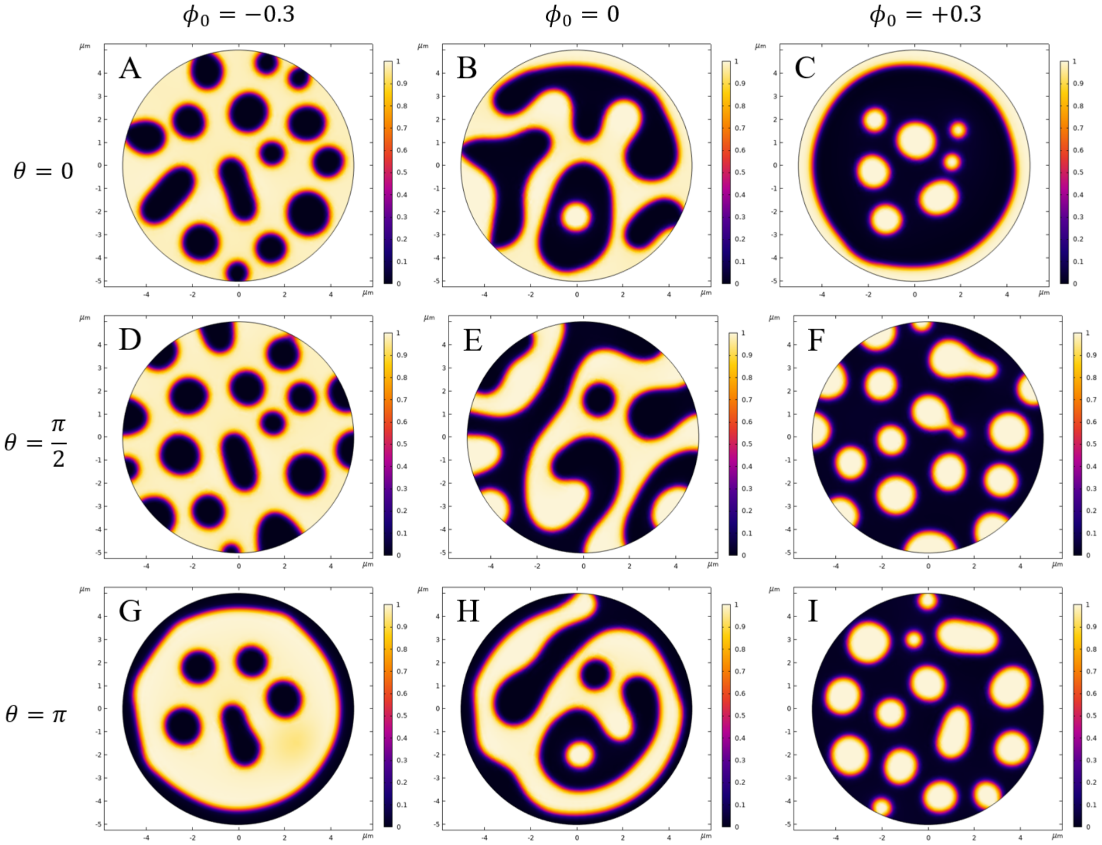

Figure 5.4: Amoeboid sensitivity to wetting angle. Final morphology for simulations across three different wetting angles and three different initial phase field values. Across the range of compositions and wetting angles studied, morphologies that are consistent with all observed amoeboid morphologies are modeled with the exception of 3B.

two-stage process. First, primary decomposition occurs and the amoeboid coarsens into a multi-layer core-shell morphology (Type 3A). Then, as the amoeboid cools or becomes more oxygenated, the miscibility gap widens, and secondary phase separation occurs into even more compositionally contrasted phases. A simplified model is developed to approximate this behavior by instantaneously adjusting parameters at 7.5 ms into a simulation of 10ms. The Gibbs energy curve is adjusted from one where the stable phases exist at ϕ=+1 and -1 (function t1 in Figure 5.5A) in equation 1.8 to one where stable phases exist at $\phi = \pm\sqrt{(10)}$ (function t2 in Figure 5.5A):

$$f(\phi) = \left(\frac{\phi^4}{40} - \frac{\phi^2}{2}\right) \tag{5.15}$$

At the same time, M is lowered from $8 \times 10^{-9} m^2/s$ to $4 \times 10^{-9} m^2/s$ to represent decreased atomic mobility at lower temperatures. The same interfacial energy is maintained according to equation 1.10 by decreasing κ from $\times 10^{-14} m^2$ to $1 \times 10^{-15} m^2$ to counter the increase in barrier height between the two stable phases in equation 1.15. These parameter changes approximate an instantaneous quench, but if this model is advanced to be more quantitative, it could account for temperature dependent parameter changes that shift according to timescales of fireball cooling. Figure 5.5 shows the results of this instantaneous quench. Primary phase separation occurs and coarsens into a 3-layer core-shell structure of Type 3A morphology by 7.1 ms. At t=7.5 ms, we simulate an instantaneous quench by adjusting our parameters, and secondary phase separation and coarsening begins. Eventually the morphology evolves towards the primary phase separation morphology (but with new compositions) and eventually a 2-layer core-shell structure at later times (>10ms). At intermediate times (t=7.9 ms), we are left with an L_{Si} dispersed phase within the initial decomposition L_{Fe} rim and L_{Fe} core. However, this model also results in dispersions of L_{Fe} in the initial decomposition L_{Si} layer, which is not observed in our Type 3B morphologies. It is possible the dispersed crystals in the interior L_{Si} region of Type 3B amoeboids are a result of secondary phase separation, but were sufficiently small that crystallization behavior erased the record of the original spherical morphology that would be expected from decomposition. If this is true, their smaller size compared to the dispersed L_{Si} preserved in the rim may be because the widening Gibbs energy curve upon cooling (t2) is not symmetrical as we have modeled, or because of differences in the kinetics of decomposition in the primary decomposition L_{Fe} and L_{Si} phases. However, this model qualitatively shows how cooling behavior can result in the more complex Type 3B morphologies that cool fast enough to preserve their morphologies at intermediate simulation time.

Mobility and Interfacial Energy Sensitivity

Most amoeboids (with the exception of Type 4) result in one phase that preferentially wets the surface. For any amoeboid with a wetted surface, given sufficient time, it will eventually coarsen into a 2-layer core-shell structure. Amoeboids with >2 layers or with interior dispersed phases represent intermediate times of coarsening due to rapid cooling. While constraining cooling timescales using quenched preserved morphologies will require a more quantitative model, a qualitative investigation of parameters influencing coarsening behavior. We chose a composition and wetting angle from the model for Figure 5.4C, and then alternatively varied M and κ. For a given simulation time, increasing M serves to rapid coarsening, and thus decreasing the timescale of evolution towards a final, stable 2-phase morphology. Increasing κ represents a higher interfacial energy, and because Ostwald coarsening time is proportional to the interfacial energy this also quickens coarsening. Figure 5.6 shows the results for the same simulation timeframe for lower M-intermediate κ (left), intermediate M-intermediate κ (center), and intermediate M-high κ (right). Note that reduced coarsening on the same simulation timescale is present for lower M and for lower κ. During the cooling of the melt, we expect M to decrease, and for κ to increase. Thus, during cooling, coarsening slows due to lower M, it also quickens due to increased κ. These two parameters

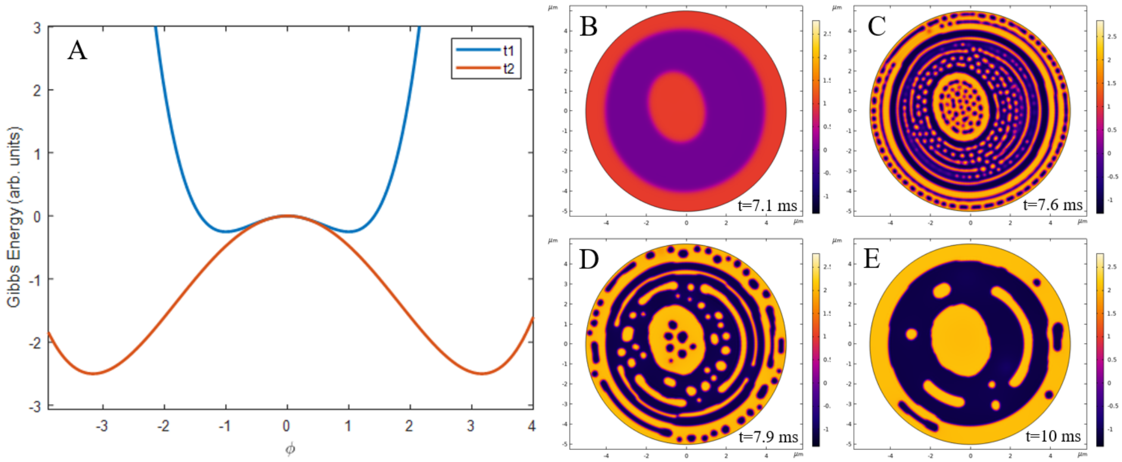

Figure 5.5: Amoeboid sensitivity to cooling behavior. Type 3B amoeboid morphologies can be recreated by adjusting parameters to simulate an instantaneous quench and secondary phase separation. (A) Curve t_1 represents the initial Gibbs energy for decomposition at a higher temperature, where curve t_2 represents the Gibbs energy for secondary decomposition at a lower temperature. (B) Amoeboids first experience decomposition and evolve to Type 3A morphologies by t=7 ms. At t=7.5 ms, the Gibbs energy curve, M, and κ are changed, resulting in secondary phase separation and coarsening (C-E).

compete, but we have poor knowledge of their compositional and temperature dependence. Thus, any quantitative constraints on cooling timescales from morphology are not realistic until a better understanding of complex multi-component silic

5.4 Marangoni Migration

A mechanism that has been shown to contribute to the evolution of core-shell structures in some immiscible systems is that of Marangoni migration [80]. Marangoni migration is a phenomenon in which a liquid will flow towards a region with higher surface tension. In the case of two-liquid immiscible systems, a dispersed liquid phase can migrate due to gradients in surface tension caused by temperature gradients [80] or compositional gradients [58]. Temperature gradients caused by cooling result in a surface tension gradient, and cause dispersed droplets to migrate more rapidly into core-shell structures. In this study, calculations were performed using empirical fireball cooling rates to determine if Marangoni migration may have played a significant role in the coarsening behavior of amoeboids. To do this, commercially available COMSOL software was used to calculate the expected temperature gradients for amoeboids, and an explicit time stepping method was used to calculate the total possible migration distance for a dispersed droplet within an amoeboid over the timescale of fireball

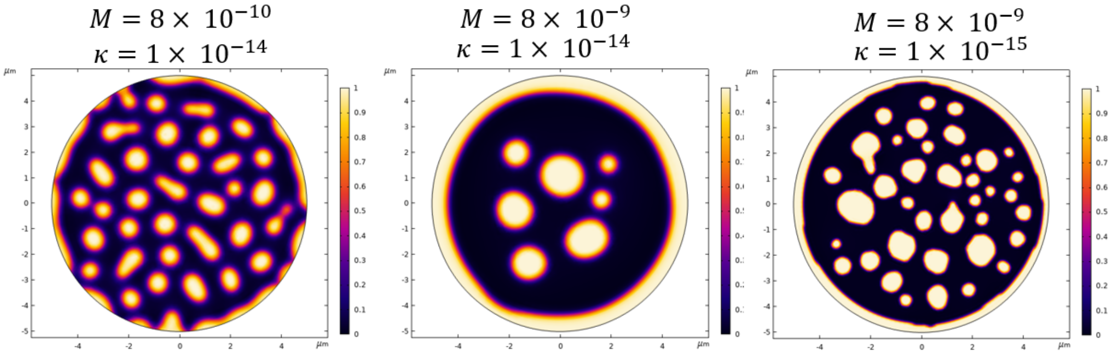

Figure 5.6: Amoeboid sensitivity to chemical mobility. Rapid quench of amoeboids preserve intermediate morphologies. Ostwald coarsening competes with the quench rate to determine final preserved morphology. The rate of coarsening is governed by the mobility (M) and the interfacial energy coefficient (κ). For a given M and κ (center), lowering the mobility (left) or lowering the κ (right) both result in less coarsened morphologies for a given timescale. However, since cooling the amoeboids will generally result in lower M but higher κ, these parameters compete with each other to determine coarsening rate, making quench time constraints based on morphology impossible at this time without a better understanding of multicomponent silicate melt kinetics.

cooling. The COMSOL model details and assumptions used are discussed below.

COMSOL Model of Temperature Gradients

To estimate the temperature gradient an amoeboid micro-structure may experience during fireball cooling, a model was constructed using the COMSOL multiphysics software. In this scenario, a sphere with 5 μm radius was built inside a 10 μm^3 cube. The sphere was defined as a standard rhyolite, with material parameters defined by [94] used, with a heat capacity of 1200 J/(kg K), a desnity of 2300 kg/m^3. The surrounding material was defined as standard air with associated temperature dependent heat capacity, density and thermal conductivity defined by COMSOL. We initialize the temperature of all domains at 2500 K. The air outside the sphere is forced to cool according to the Hillendahl cooling equation [24]. As the air cools, the sphere undergoes radiative cooling using surface-to-ambient radiation as a function of the temperature of the air and the temperature of the surface of the sphere. We perform a simulation for nuclear explosion yields of 0.1, 1, 5, 10, 20, 30, 40, 50, and 100 kT. For each simulation, time steps of 0.1 ms were used for a total of 10 seconds. For each time step, the temperature at the center of the sphere and at the surface was recorded. The small size of the sphere resulted in a relatively small temperature gradient of 10-15 mK, or 2-3 K/mm.

Thermal Gradients and Estimation of Marangoni Velocities

From Shi [80], the Marangoni migration velocity of a dispersed droplet of liquid within another liquid matrix can be analytically described as:

$$v_m = \frac{-2}{3(3\mu_d + 2\mu_m)} \frac{\partial \sigma}{\partial T} \cdot \bigtriangledown T \cdot r_d \tag{5.16}$$

Where μ_d is the viscosity of the dispersed droplet, μ_m is the viscosity of the matrix liquid, σ is the interfacial tension, T is the temperature, $\bigtriangledown T$ is the temperature gradient, and r_d is the radius of the droplet. Viscosity of the two liquids were calculated using Giordano's model [31]. Due to lack of experimental data, the temperature dependence of the interfacial energy ($\frac{\partial \sigma}{\partial T}$) is ill-constrained. However, one study [89] measured the interfacial tension between liquids of similar composition to be 16.4 mN/m and 7.8 mN/m at 1500 °C and 1550 °C. Using these two datapoints, a linear relationship is assumed and calculate a value of 0.000172 mN/(m sec).

To calculate an estimate of the total possible Marangoni migration distance, temperature profiles from the COMSOL radiative cooling model are used to calculate $\bigtriangledown T$. For each time step, v_m is calculated using temperature dependent Giordano viscosity and calculate the distance traveled over that time step. This is done for each time step and the total migration distance is summed over time. A variety of simulations are performed, over a range of droplet sizes from 100 nm to 1 μm, and for both an L_{Fe} droplet in a L_{Si} matrix, and an L_{Si} droplet in a L_{Fe} matrix. Calculating the migration distance for each time step, the total migration distance for L_{Fe} dispersed in L_{Si} and L_{Si} dispersed in L_{Fe} was summed over the duration of fireball cooling for a 10kT fireball cooling scenario. It was found that the highest migration distance was limited to approximately 0.8 μm for a 1 μm droplet of L_{Fe} in L_{Si}. This means the droplet would not migrate more than the length of its own radius over the timescale of fireball cooling, which is a statement that holds true across all droplet size that were calculated. Example migration distances for a range of fireball cooling curves for yields for 0.1 kT to 100 kT are shown in Figure 5.7. For this example, the viscosities of the liquids are sufficiently high that the Marangoni forces supplied from the very small temperature gradient are insufficient to cause significant droplet migration. Thus, Marangoni migration was likely not a significant process in the evolution of core-shell structures. Because the temperature dependence of the interfacial tension remains ill-constrained with only one relevant measurement in the literature [89], it is possible that if this dependence is more pronounced at higher temperatures that such an effect may play a role. It also remains possible that migration may have had effected the timescale of coalescence and coagulation of the dispersed phases.

5.5 Evidence for Liquid Decomposition

Phase field method simulations in this work, though qualitative in nature, suggest that decomposition is consistent with the range of amoeboid morphologies observed in aerody-

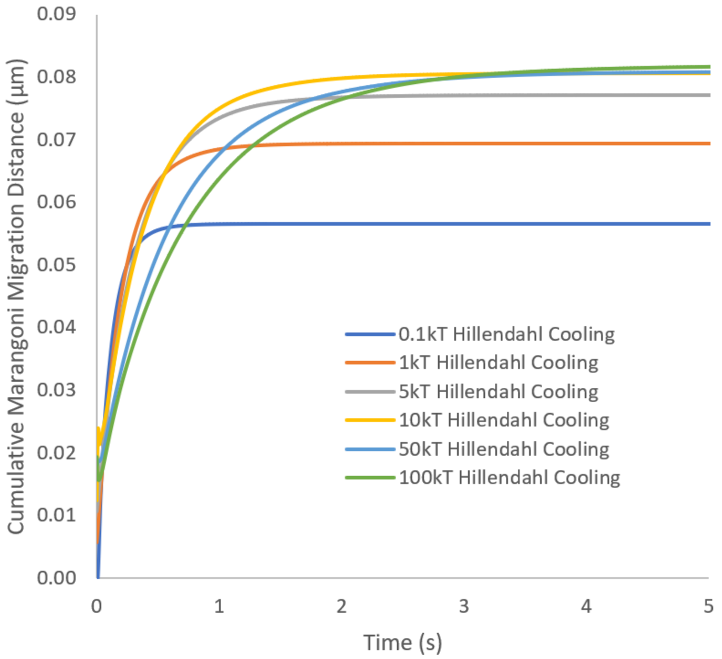

Figure 5.7: Estimation of Marangoni migration distances using relevant cooling timescales and melt properties. Cumulative Marangoni migration distance for a 100nm droplet using COMSOL temperature gradients in a matrix droplet with a radius of 5 μm using fireball Hillendahl cooling curves [24] for a range of explosive yields. Across the range of fireball cooling curves, Marangoni migration distances do not exceed the radii or the migrating droplet, and are not significant.

namic fallout glass sample to date (Figure 5.8). However, no single parameter can explain the variation in morphologies, and a variety of parameter variations must be invoked to explain the full range of amoeboid morphologies. Morphology variation depends most heavily on initial droplet composition, which determines which liquid phase is dispersed within a majority liquid phase prior to solidification. But the full range of observed morphology variation depends also on wetting angles driven by varying surface and interfacial energies of the two stable liquid composition, secondary phase separation driven by cooling rate, and speed of Ostwald coarsening [73] driven by competition between atomic mobility and interfacial energies in the two liquids. Also noted is that for morphologies where one phase wets the surface, morphologies all evolve into simple 2-layer core-shell arrangements given sufficient evolution time. The consistency of PFM results with observed amoeboid morphologies strengthens the textural evidence for the decomposition that was discussed in Section 3.6.

However, the qualitative nature of these simulations and the need to fine tune parameters to match observed morphologies cast doubt on decomposition processes explaining all immis-

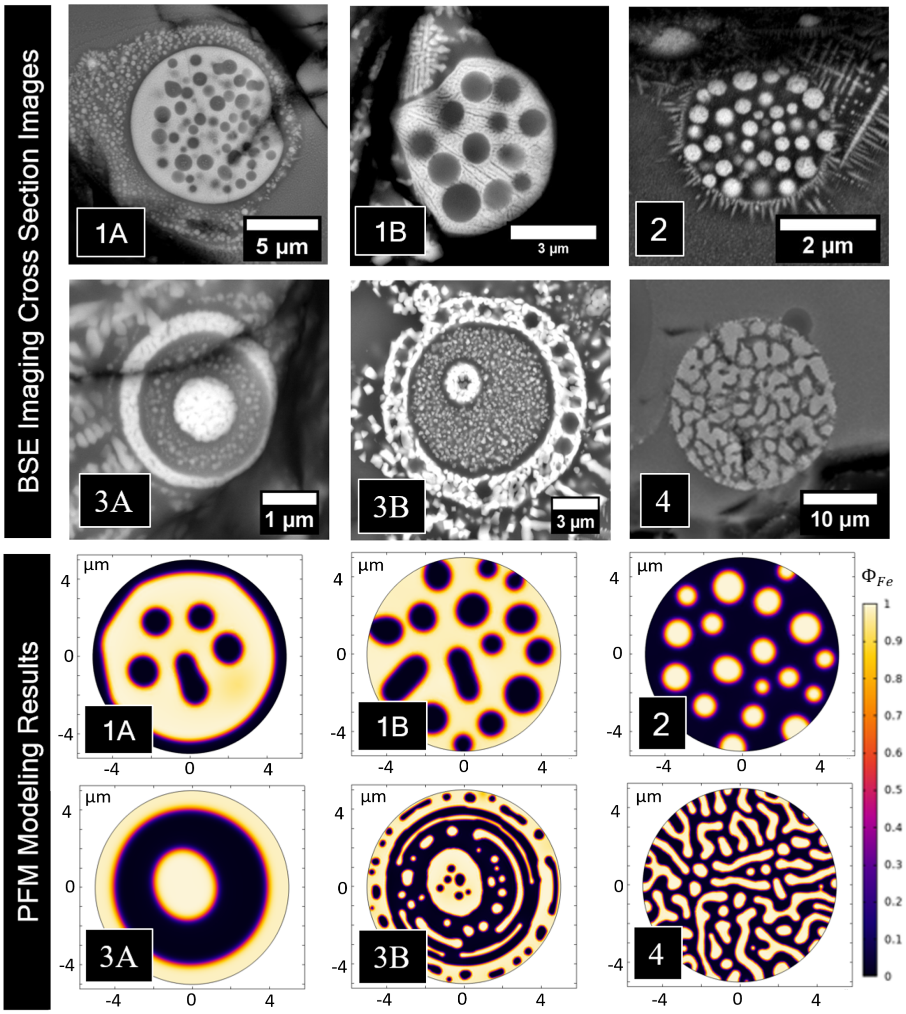

Figure 5.8: Comparison of amoeboid morphologies to PFM simulation results. Amoeboid morphologies from Figure 5.1 are shown compared to individual PFM simulations where parameters described in the previous sections were adjusted to match each morphology. The color bar represents the phase fraction of L_{Fe}.

cible textures in this work. Wetting behavior that conflicts with limited published interfacial energy data suggests that complex variations in multi-component silicate melt properties are necessary to explain the range of observed textures using decomposition alone. Additional work to understand these properties and the kinetics of phase separation may confirm decomposition as the primary formation mechanism of amoeboids. Alternatively, modeling and experiments of other formation mechanisms such as spontaneous emulsification should be explored. Multiple simultaneously formation mechanisms may also play a role, such as continuous condensation or agglomeration during phase separation.

Chapter 6

Precursor Relationships Using Spatially Resolved Chemical Data

This chapter applies a multivariate approach to semi-quantitative compositional data for 13 samples to estimate precursor compositions and their contributions resulting in compositional heterogeneity. A recent method has been developed and validated by Fitzgerald *et al* [20] using multivariate linear-least squares approaches to estimate precursor compositions in energetic melts such as those resulting in fallout glass. This method is used to investigate the emulsification hypothesis of amoeboid formation, and to investigate general fallout formation mechanisms. This investigation is done by posing two questions: First, do precursor compositions independently estimated from mm-scale fallout glass match micro-scale L_{Fe} and L_{Si} compositions described in Chapter 3? Second, what is the general relationship between radioactivity and each precursor?

The first question of whether precursors match L_{Fe} and L_{Si} compositions is intended to investigate the emulsification (vs. a decomposition) amoeboid formation hypothesis. If precursor estimation matches amoeboid 2-phase compositions, this would provide independent evidence for an emulsification hypothesis. Such a result would mean that amoeboids would offer a more immediate estimate of precursors, which would aid in understanding complex mixing processes in fallout without relying on complex un-mixing methods. Without a good match, emulsification may still be a valid hypothesis to explain amoeboids and immiscibility textures, but means that the two liquids are not sourced from pure precursors, but from already mixed precursors, and/or that some chemical equilibration occurs following emulsification. If amoeboids still form via emulsification, then precursor contributions to each liquid provides some insight into energetic mixing behavior prior to emulsfication. However, if amoeboids form via decomposition, precursor contributions do not provide much additional insight, as the decomposition process represents a non-ideal phase separation process rather than the ideal mixing behavior that MCR-ALS is designed to address.

Precursor compositional relationships also inform our understanding of general fallout formation processes in iron-rich environments. In particular, previous studies have shown correlations between bomb-derived radionuclides and a Fe-Ca-Mg-rich glass or interfaces

[5, 46, 47]. The mechanism of formation for this glass has been debated, and has been hypothesized to either represent a direct condensate [5], or a mixture of soil constituents [20]. Applying these precursor estimation techniques allows an investigation into the presence of and/or extent of this Fe-Ca-Mg/radioactivity relationship in Fe-rich fallout.

In this chapter the multi-variate precursor estimation technique that was applied to the semi-quantitative SEM-EDS data-set is described. Next, the estimated compositions and contributions from each precursor for each sample are presented, and interpretations are offered for each precursor. Next, a variety of micro-scale immiscible compositional measurements are projected onto the multi-variate model to understand precursor contributions for each immiscible phase. General precursor contribution maps are then presented to inform precursor spatial relationships, and autoradiography and nanoSIMS Pu data are also compared to precursor contribution data. Finally, Fe-rich fallout formation interpretations from applying this method are summarized, and some suggestions for further work are offered.

6.1 Multi-component Precursor Estimation Techniques

This work does not develop novel techniques for estimating precursor compositions or vapor compositions. Instead, a developed and validated method in the literature [20] is applied to the data in this study. A general methodology for this method is outlined below, but a more detailed description of the mathematics used for these techniques can be found in the Fitzgerald paper. This method uses the set of semi-quantitative SEM-EDS compositional measurements for 13 samples described in Chapter 3 and uses commercially available Eigen-Vector software [18] to apply Principal Component Analysis (PCA) and Multi-component Curve Resolution - Alternating Least Squares (MCR-ALS) [27] approaches to the data. PCA techniques are applied to pre-treated data using a mean-centering approach to investigate general compositional trends, and to estimate the number of principal components (and by extension, the number of precursors) that best explain observed compositional variability. When n principal components are used on pre-treated data, then there are n+1 precursors that best explain the variance in the data. Thus, after PCA approaches are applied and n principal components are determined, n+1 precursors are used in a multivariate curve resolution-alternating least squares (MCR-ALS) approach to estimate precursor compositions and contributions for each spatially resolved data-point. The MCR-ALS approach is used because precursor compositions can be constrained to non-negativity (as would be expected for real compositions), can be applied with limited or no *a prior* knowledge of precursor compositions, and can implement closure and 2-norm constraints. SEM-EDS data-sets from immiscible regions are then projected onto the MCR-ALS model calculated from the broader SEM-EDS data-set. This allows precursors estimated independently from the whole dataset to be used to estimate precursor contributions to each immiscible phase.

Principal Component Analysis (PCA)

The R-mode PCA method is a well-known technique used to understand relationships between variables in a data-set [42]. In this method, a series of principal component vectors are defined, each with some elemental concentration (i.e., 'loadings'), which serve as an orthonormal basis to project the data-set onto. The characteristic equation of PCA, with k principal component vectors is defined as:

$$\mathbf{X} = \mathbf{T}\mathbf{P}^T + \mathbf{E} \tag{6.1}$$

where **X** is an m x n matrix of the pre-treated SEM EDS data defined by m measurements and n chemical elements, **T** is contributions (or "scores") m x k matrix with m measurements and k principal component vectors, and **P** is the principal component compositions (loadings) n x k matrix with n chemical elements and k principal component vectors, and **E** is an m x n matrix of the residuals. The PCA approach decomposes **X** into **T** and **P** using some chosen number k of eigenvectors. One difficulty is determining the number of eigenvectors that are appropriate. If too many eigenvectors are used, the PCA model can describe variability in the data-set that doesn't describe actual compositional variation, but instead is due to random variation caused by measurement uncertainty. In this work, we use a quantitative approach proposed by Wold [95] and validated for fallout by Fitzgerald that compares a metric known as the root mean squared error of the calibration set (RMSEC) and of the cross-validation test set (RMSECV), the details of which are supplied in [95]. Another method is using the scree log test [9], which predicts similar numbers of precursors in this work. While choosing the number of PCs is somewhat subjective, in general, when these metrics are plotted vs. the number of PCs, when their values begin to deviate due to an inflection in the RMSECV, additional PCs are explaining variation due to noise rather than real compositional variation. That PC threshold can be used as an estimate of the appropriate number of PCs in the PCA model. The data can then be projected onto the PCs, and is typically visualized using bimodal plots of different combinations of the PCs.

In this work, 13 samples selected for semi-quantitative SEM EDS analysis were used, which span the range of radioactivity and represent both aerodynamic glassy samples and unmelted/partially melted samples. The method described in Chapter 2 was used to reject all pixels that don't represent the exposed sample surface. Each map contains >3 million pixels, which makes applying PCA and MCR-ALS computationally expensive. To reduce the computational burden, a random selection of 1000 downselected pixels from each sample was used. It is assumed that the low summation is due to insufficient counting time for low abundance species, rather than failure to account for significant major elements, and so all data is normalized to 100%. Per the Fitzgerald method, species that routinely have low concentrations and thus may introduce significant error into the model are ignored. For this data set Mn and Ti are ignored which have abundances <1%. In addition, oxygen is ignored because it exhibits minimal variance and because it's quantification is suspect due to significant low energy X-ray interference and susceptibility to surface defect effects [20]. The majority of Na and K in these samples come from K and Na-rich feldspars, which form

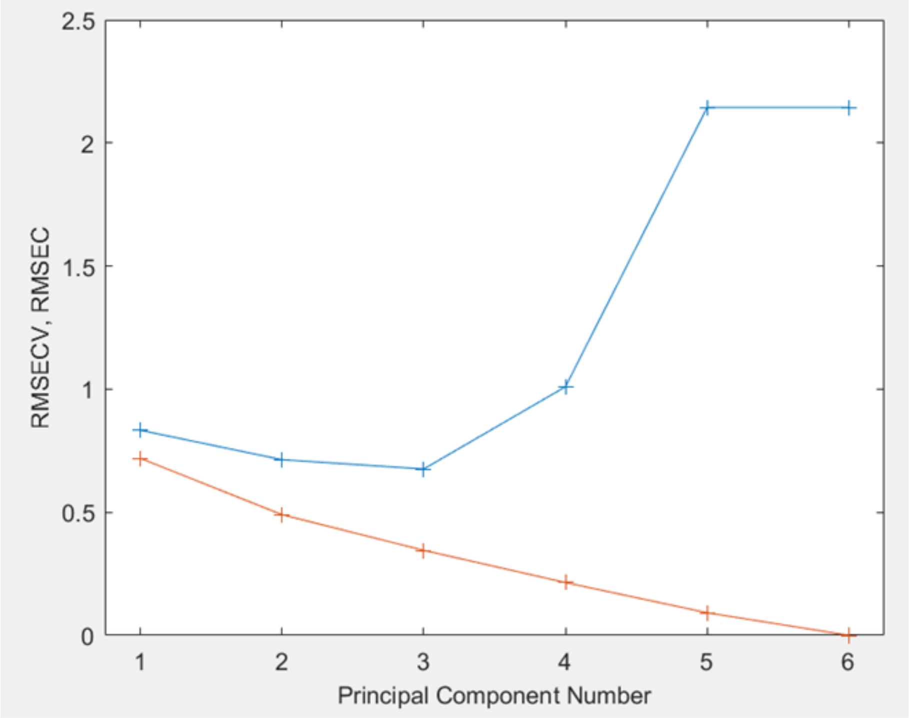

Figure 6.1: Cross-validation results used for determining the appropriate number of principal components in this study. The root mean squared error of the calibration set (RMSEC, red) and for the cross-validation set (RMSECV, blue) values begin to significantly deviate at PC3, suggesting that using >3 PCs explain variations in noise rather than compositional variation.

a natural solid solution. Thus, per the Fitzgerald method, alkali metals are summed to a total alkali concentration so that the model de-emphasizes natural heterogeneity between feldspars. Thus, the final PCA model investigates the relationship between Si, Al, Fe, Ca, Mg, and Na+K. Data is pre-treated using an autoscaling approach, which mean centers and scales the columns to unit variance, such that the PCs describe general relationships between elements but place equal emphasis on the variation of all elements that are investigated. Each PC does not directly reflect quantitative precursor compositions, which are later estimated using MCR-ALS techniques.

The RMSECV/RMSEC plot is shown in Figure 6.1. Because the RMSECV begins to deviate form the RMSEC from PC3 to PC4, it is inferred that 3-4 PCs best explain the variance in the selected data-set. The compositions of precursors calculated using MCR-ALS in the next section made the most physical sense using 3 PCs - in particular, the prediction of alkali feldspar with compositions that closely matched measured partially melted grains in sample F29. When >3PCs (and thus precursors P>4), the MCR-ALS model no longer

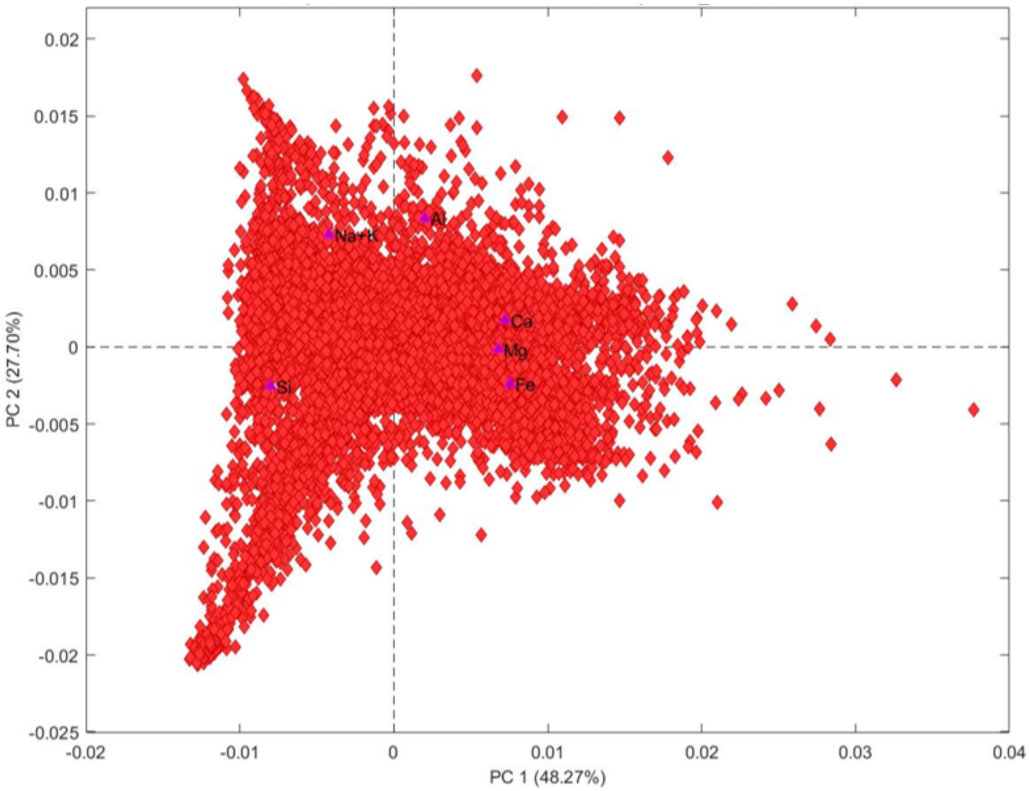

Figure 6.2: Model principal component 1 (PC1) vs. principal component 2 (PC2). Each element and all individual datapoints are projected onto PC1 vs PC2. PC1 primarily describes the anti-correlation between Si and Ca-Mg-Fe, and some variation between Na+K and Al, likely due to variation in feldspathic mineral compositions or variations in alkali content due to volatile loss and chemical fractionation. PC2 describes the anti-correlation between Si and Al, Na-K, likely distinguishing between quartz and feldspars. This figure can be interpreted as showing general mixing between three components: quartz, feldspar, and a Ca-Mg-Fe-rich source.

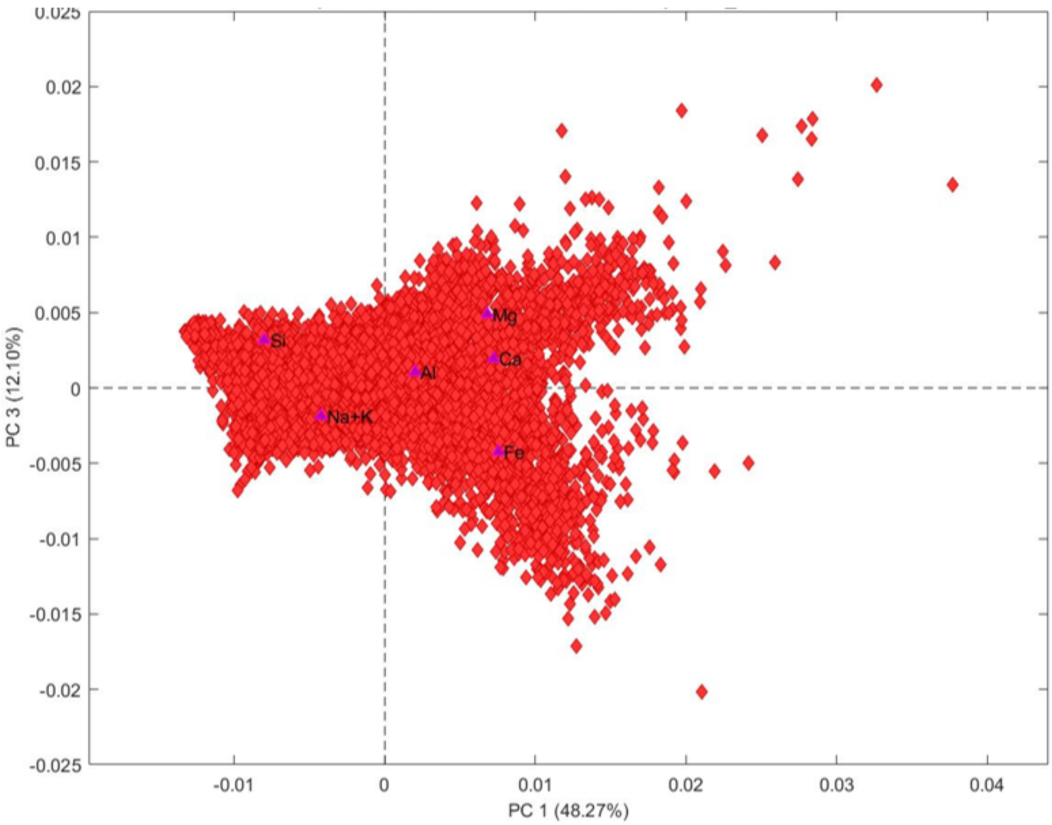

Figure 6.3: Model principal component 1 (PC1) vs. principal component 3 (PC3). Each element and all individual datapoints are projected onto PC1 vs PC3. PC1 primarily describes the anti-correlation between Si and Ca-Mg-Fe, and some variation between Na+K and Al, likely due to variation in feldspathic mineral compositions or variations in alkali content due to volatile loss and chemical fractionation. PC3 describes the anti-correlation between Fe, Ca, and Mg, as well as describing some minor variability between Si and Na+K (quartz vs. feldspar). Note how Mg-Ca exists in a distinct branch of the data projection from the Fe branch.

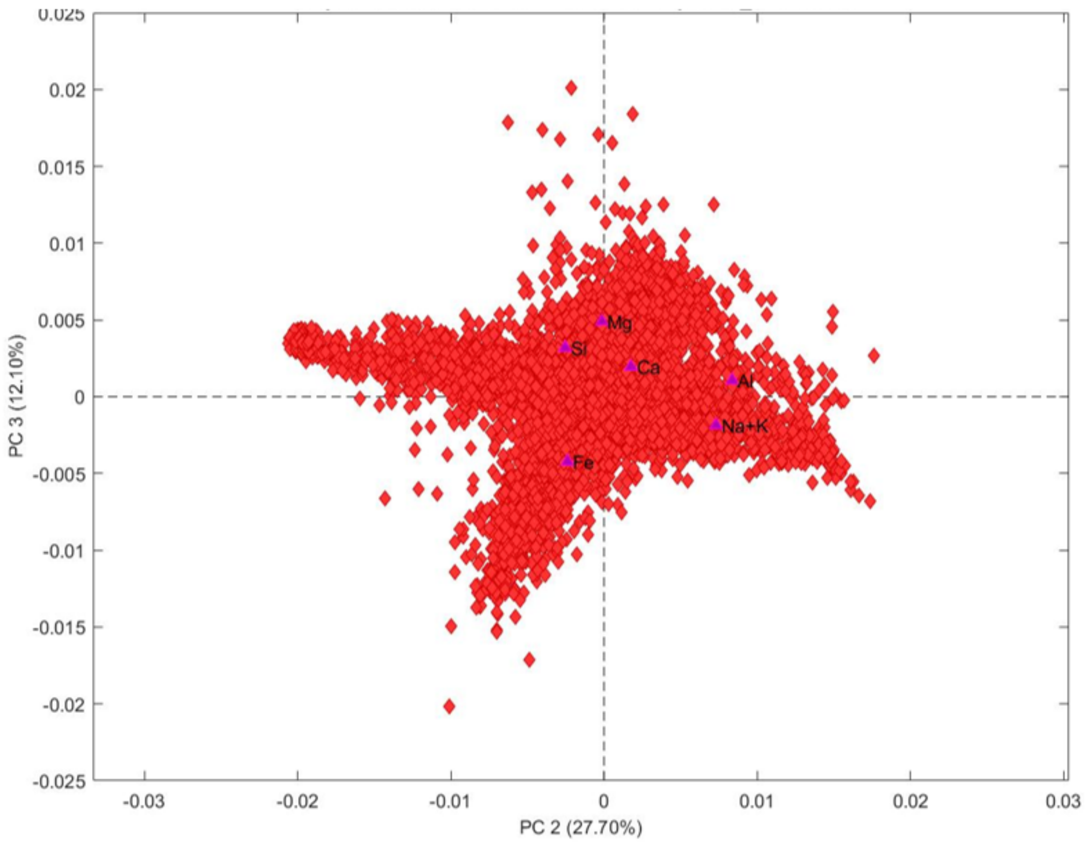

Figure 6.4: Model principal component 2 (PC2) vs. principal component 3 (PC3). Each element and all individual datapoints are projected onto PC2 vs PC3. PC2 describes the anti-correlation between Si and Al, Na-K, likely distinguishing between quartz and feldspars. PC3 describes the anti-correlation between Fe, Ca, and Mg, as well as describing some minor variability between Si and Na+K (quartz vs. feldspar). Note again, similar to Figure 6.3, the distinction between Fe as a distinct branch of the data vs. Mg-Ca. This projection of the data allows us to see the branches representing quartz and feldspars, similar to Figure 6.2.

predicted the alkali feldspar composition for one of the precursors. Thus, there is good confidence in the choice of n=3 PCs and P=n+1=4. Using 3 PCs explains a cumulative 88.1% of the variance in the data-set, with PC1 explaining 48.3%, PC2 explaining 27.7%, and PC3 explainng 12.1%. In Figures 6.2, 6.3, and 6.4, the full data-set is shown projected on the PC1 vs PC2, PC1 vs PC3, and PC2 vs PC3, respectively. Each element is also shown projected so that general relationships between elements can be observed in PC-space. This data represents all datapoints from all samples, though some samples span the space to varying degrees caused by variable amounts of each presumed precursor and mixing in each sample. However, this study doesn't look in detail at precursor mixing relations for each individual sample, so they are not shown here.

PC1 is the component with the maximum variability describing 48.27% of the variability in the data, and describes the anti-correlation between Si (sourced from quartz) and Ca-Mg-Fe glass. It also somewhat describes variation between Na+K and Al, which is likely due to variation in feldspathic mineral compositions or variations in alkali content as a result of volatile loss during heating.

PC2 (27.7% of the variation) describes the anticorrelation between Si (quartz) and Al and Na+K (feldspars), as well as some small distinction between Ca (more closely associated with feldspar), Mg (neutral), and Fe (more closely associated with Si).

PC3 (12.1% of variation) distinguishes Fe from the Mg-Ca-rich portions of the samples, with some added variability between quartz and feldspar. Thus, while Fe, Ca, and Mg are generally associated with each other (as seen in PC1), PC3 distinguishes between a more pure Fe source and the general Fe-Ca-Mg glass.

These PC plots (Figures 6.2-6.4) can generally be interpreted as representing a mixture between quartz, alkali feldspar, an Fe-Mg-Ca rich source, and an Fe source (Figure 6.2). A mixture of quartz, feldspar, and Fe-Mg-Ca source can be most easily visualized in the PC1 vs. PC2 plot. The other plots allow the fourth Fe source to be more easily visualized. The plot of PC2 vs. PC3 (Figure 6.4) in particular appears to represent mixing of a quartz, feldspar, and pure iron precursors. While there certainly is some sort of Fe-Ca-Mg relationship, these PCA results suggest that a separate, Fe-rich source is present that is not as closely associated with Mg and Ca.

Multivariate Curve Resolution - Alternating Least Squares (MCR-ALS)

The PCA approach gave us some compositional relationships from which to interpret predicted precursor compositions using the MCR-ALS approach. It established the likelihood of 3-4 PCs. This study uses 3 PCs on a normalized data-set, and thus the MCR-ALS approach uses n+1 = 4 precursors. This approach iteratively solves for precursor abundances and chemical compositions while applying constraints to the solution. The governing equation for MCR is:

$$\mathbf{X} = \mathbf{CS} + \mathbf{E} \tag{6.2}$$

where **X** is m x n matrix of the SEM EDS data defined by m measurements and n chemical element, **C** is contributions m x k matrix with m measurements and k precursors, and **S** is precursor compositions k x n matrix with k precursors and n chemical elements, and **E** is an m x n matrix of the residuals. In this case, **C** and **S** are iteratively solved using the alternating least squares (ALS) method, with constraints applied for each iteration. Each iteration estimates either **C** or **S** by minimizing the residual sum of squares, and while applying chosen constraints. This iteration proceeds until convergence is reached. In this work, 4 precursors are utilized (i.e. k=4), the ALS routine is solved using the FNNLS (faster non-negative least squares) algorithm, and a constraint of closure for each iteration is applied which ensures the sum of elements for each precursor (i.e. the sum of each row in **S**) equals 1. Equality constraints can also be applied, which sets a precursor composition based on some *a prior* knowledge. The constraint can be applied as a hard constraint (that forces a precursor to a defined composition) or a soft constraint, which weights the ALS routine to find precursor compositions that are similar to the equality constraint.

One issue that arises in MCR-ALS is the non-uniqueness of solutions. Rather than a single, unique solution, there sometimes exists a range of solutions due to the non-orthogonality of the precursor compositions (in contrast to PCA). This non-uniqueness is one source of error in this approach and is referred to as 'rotational ambiguity' [34]. Some ways that rotational ambiguity can be decreased is by implementing appropriate equality constraints or initializing precursor compositions close to their true (though unknown) values. This work attempts to reduce rotational ambiguity by applying constraints. While some efforts have been made to quantify rotational ambiguity for a given system [69, 72], such efforts are reserved for future work.

6.2 Precursor Compositions and Contributions

An advantage of the MCR-ALS approach is that a variety of constraints (such as non-negativity, closure, and equality constraints) can be applied to the ALS method. However, justifying these constraints can be somewhat subjective and depends on the certainty of *a priori* knowledge of the system. In this work, closure was always applied to ensure all precursor compositions sum to 1 for each spatially-resolved data point. Because there is uncertainty in the magnitude of the effect of these constraints on final compositions/contributions, the final MCR-ALS results that are used for interpretation in this work uses closure, but applies no equality constraints. However, to understand general sensitivity of precursor compositions to constraints, a variety of hard constraints were applied using a variety of likely precursor compositions. The observed sensitivities are used in assessing the confidence in the final predicted precursor compositions and results. All EDS data was normalized to 1, but no additional pre-treatment of the data was applied to emphasize the overall magnitude of variation for each element.

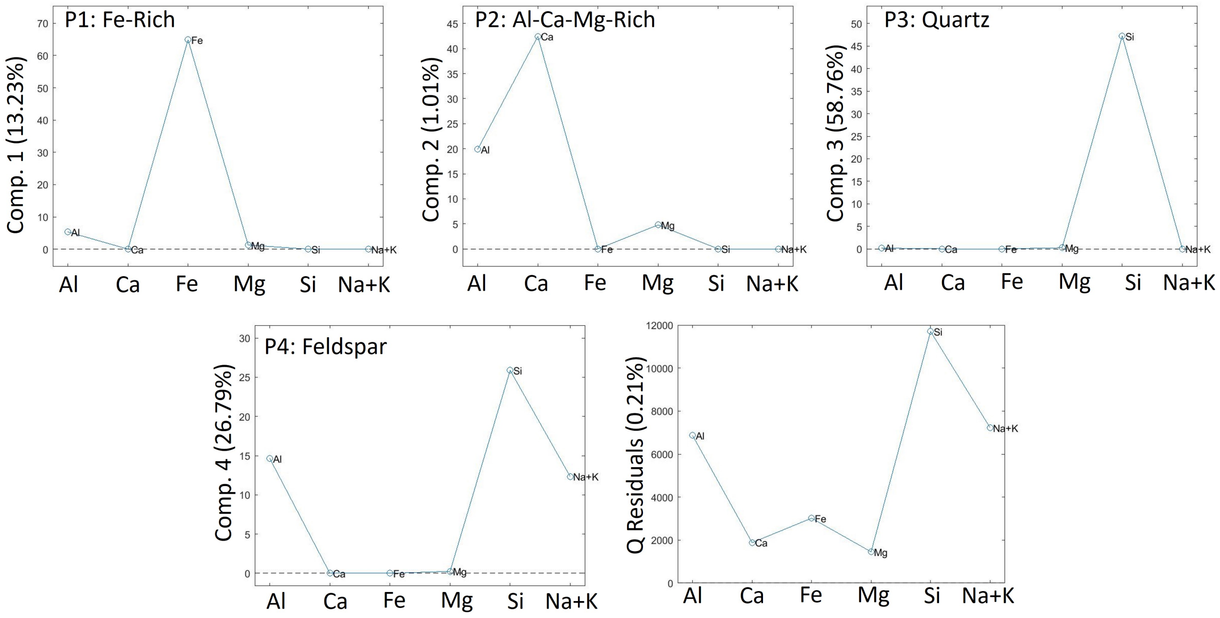

Figure 6.5: MCR-ALS 4 Component Compositions. This model applied a closure constraint but no equality constraints on individual precursurs. P1 is referred to as an iron oxide composition/precursor. P2 is referred to as a Al-Ca-Mg composition/precursor. P3 is referred to as a quartz composition/precursor. P4 is referred to as a feldspathic composition/precursor. P2 composition is sensitive to added equality constraints on the model. Q residuals are highest in the model for Si, followed by alkalis and Al, and finally for Fe, Ca, and Mg.

Precursor Compositions

Using a 4 precursor MCR-ALS model with closure enforced on each iteration, but no equality constraints, 99.8% of the variation in the data-set was explained. These precursor compositions are shown in Figure 6.5 as wt%. While compositions are normalized to 100%, the mass difference in the graphs is due to oxygen and minor elements that were ignored in the model (Ti and Mn). Because of the variability in precursor compositions under different constraints or with different samples, each precursor is referred to as P1, P2, P3, or P4 to avoid confusion. In general, however, P1 refers to a very Fe-rich oxide precursor, P2 refers to an aluminous Ca-Mg-Fe-rich precursor with significant variability, P3 refers to a quartz precursor, and P4 refers to a feldspathic precursor.

For the MCR-ALS model using all sample data, the composition of precursor 1 (P1) was 5.3 wt% Al, 64.9 wt% Fe, and 1.3 wt%Mg. Due to the high Fe content, P1 is referred to as the Fe-rich precursor. Applying stoichiometric conversions using Al_2O_3, MgO, and each Fe oxide of FeO, Fe_3O_4, and Fe_2O_3, results in mass sums of 96%, 102%, and 105%, respectively. The best summation in oxide content (closest to 100%) with Fe_3O_4 is consistent with TEM measurements of Fe oxide structure in Chapter 3. This precursor likely represents an anthropogenic Fe source such as structural material. The minor presence of Al could be due to multiplicative rotational ambiguities in the model [20], could be anthropogenic and associated with the Fe, or could be sourced from the soil and becomes more closely associated with P1 due to non-ideal chemical fractionation processes.

The composition of precursor 2 (P2) is 19.9 wt% Al, 42.4 wt% Ca, and 4.8 wt% Mg. P2 is referred to as the AlCaMg-rich precursor. Conversion to oxides results in a sum of 105%. This composition does not match any real mineral composition, and any significant minerals bearing these elements would be expected to have some Si as well. It's assumed this precursor is either a combination of accessory minerals and/or anthropogenic material, or melt that has experienced some level of chemical fractionation. This fractionation could be as simple as volatile loss, or could represent to some degree condensation from a vapor term. Although P2 lacks Fe, it is assumed this precursor is similar to the traditional radioactivity-bearing Fe-Ca-Mg-rich glass observed in fallout. The lack of Fe in this estimation could be due to rotational ambiguities in the model, which assigns all Fe to the nearly pure-Fe precursor P1.

The composition of precursor 3 (P3) is 0.2 wt%Al, 0.3 wt%Mg, 47.2 wt% Si. We refer to P3 as the quartz precursor, and oxide conversion sum is 102%. Minor contributions from Al and Mg may represent trace species in quartz or (more likely) rotational ambiguities. P3 is not surprising, as quartz grains are common and routinely observed in fallout glass since they have a higher melting point than many other local minerals that fallout glass is sourced from.

Finally, the composition of precursor 4 (P4) is 14.6 wt% Al, 0.25 wt% Mg, 25.9 wt% Si, and 12.32 wt% Na+K. This composition closely matches alkali feldspars and is consistent with sanidine grains characterized in sample F29 (Chapter 3). Thus, P4 is referred to as a feldspar precursor. Oxide conversion sum is 99% (using an average of Na and K conversion factors for the Na+K composition). The composition of P4 is also not surprising, as feldspar is another common mineral, and is consistent with general element trends seen in the PCA model.

The only result inconsistent withe PCA model is that the composition of P2 does not contain Fe, as might be expected from the cluster of Fe-Mg-Ca in the data (Figure 6.2). While there is clearly some association of Fe with Ca and Mg in the samples, it could be that P1 being so strongly Fe-rich causes a rotational ambiguity where all Fe associated with P2 is assigned to P1. Adding constraints to the model does not significantly alter the compositions of P3 and P4, but does alter that of P2. For instance, adding a hard sanidine or hard quartz compositional constraint to P3 or P4 respectively causes some Si to be present in P2.

Hard equality constraints were applied to anchor compositions that are either easily observable in these samples (quartz, feldspar) or hypothesized (Fe, Fe_3O_4, L_{Si}, L_{Fe}). Calculations were performed using each of these single equality constraints, and with two constraints (quartz and sanidine) and three constraints (quartz, sanidine, and Fe_3O_4). These constraints offered higher overall Q residuals (and thus a poorer fit), but allowed observations of general compositional sensitivity for each precursor. Quartz (P3) and feldspar (P4) precursor

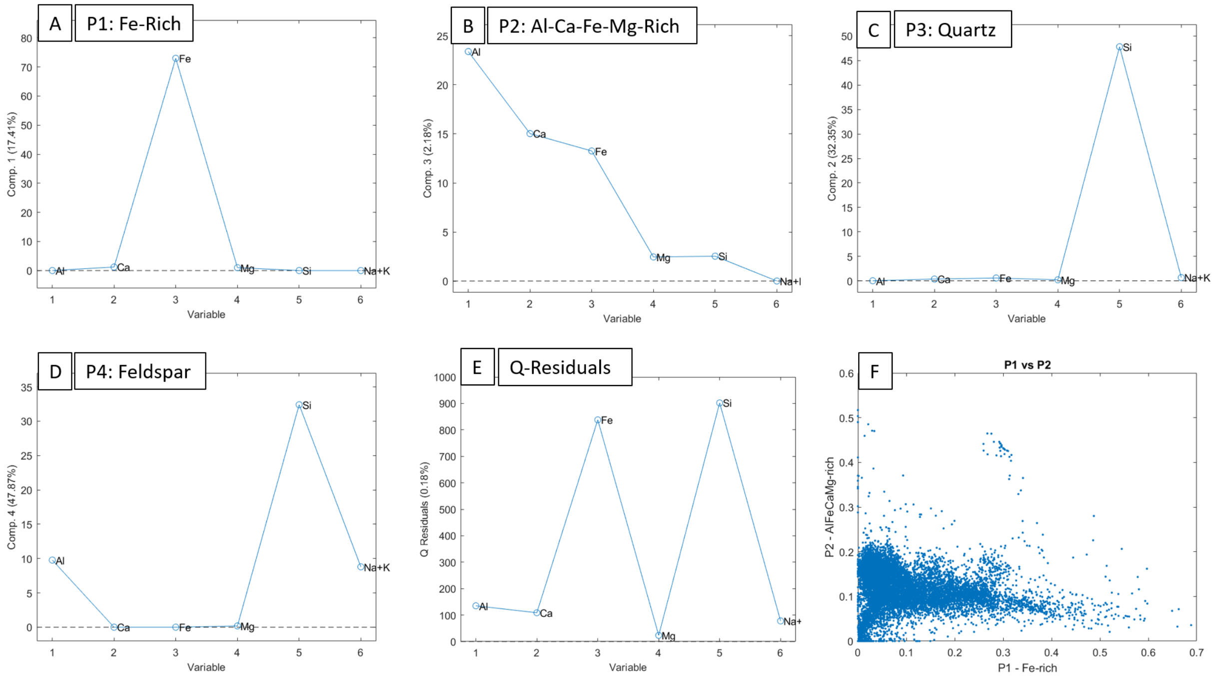

Figure 6.6: MCR-ALS 4-component compositions for a single sample (F27). The same MCR-ALS approach was applied as shown in Figure 6.5, but for a single sample. The primary difference in precursor compositions (A-D) is that for F27, both P1 and P2 contain significant quantities of Fe. (E) The greatest Q residuals are in Fe and Si. (F) Plotting contributions for each pixel for P1 and P2 show some positive correlation for low contributions but disappears for high P1 contributions. Additional discussion of this trend is in section 6.5 (and Figure 6.13).

compositions were insensitive to constraints. The iron oxide (P1) precursor showed some compositional sensitivity, with variation in Al and Si content, but in every case primarily composed of Fe. The Al-Ca-Mg (P2) precursor showed the most compositional sensitivity. P2 was always rich in Al (19-35 wt%), Ca (2-15 wt%), and Mg (1-4 wt%), but some constraints resulted in both Si (0-15 wt%) and Fe (0-22 wt%) components. Because there is not high confidence in applying these constraints and because compositional variability in precursors did not significantly alter precursor spatial distributions and relationships, final analysis was conducted using an MCR-ALS model with closure, but no equality constraints. However, P2 compositional sensitivity to constraints should be considered when interpreting conclusions made using the MCR-ALS approach.

In this study, all samples with semi-quantitative SEM EDS data was combined into a a singular data-set for the MCR-ALS model with the assumption that all samples represent mixing of the same set of precursors. Rotational ambiguity could be made worse by combining samples that represent different mixing behavior or that reflect precursors of different compositions. This can be seen in the differences in MCR-ALS model results when the method is applied to a single sample. The same method was applied to sample F27 (Figure 6.6), which resulted in Fe being significantly associated with both P1 and P2. A comparison of the contribution of P1 to P2 for each datapoint shows that for high contributions of P1, there is no significant positive correlation (likely representing the Fe-rich rim), whereas for low contributions of P1, there is a positive correlation between P1 and P2 (likely representing an earlier mixture of P1 and P2). Additional discussion of this trend is in section 6.5 Applying the MCR-ALS model to other individual samples resulted in significant variation in the composition of P2 from sample to sample but did not significantly alter the spatial distribution of each precursor. A systematic study of individual sample MCR-ALS models and how each sample influences the overall MCR-ALS model provide some insight on the source and behavior of P1 and P2.

Precursor Contributions

The contributions (i.e. scores, or C matrix) from each precursor for each down-selected pixel is solved for iteratively as the composition matrix **S** is solved using the ALS algorithm. To assess the total contribution of each precursor to each sample, the total scores were summed for all pixels and the total percentage of each precursor present in a given sample was calculated (Table 6.1). All samples were primarily composed of the quartz (P3) and feldspar (P4) precursors, with minor contributions from the iron oxide (P1) and Al-Ca-Mg (P2) precursors. P1 contributions ranged from 2% (for partially molten sample F29) to 16% for F9. P2 contributions ranged from 1% (F20) to 8% (F34). P3 contributions ranged from 37% (F34) to 54% (F13). P4 contributions ranged from 36% (F24) to 54% (F29).

Since each sample uses only 1k data-points in the MCR-ALS model, the calculated **C** matrix does not have good resolution for visualizing precursor spatial relationships. For visualization, quantitative maps prior to down-selection to 1k pixels were projected onto the MCR-ALS model, and resulting **C** matrix was mapped. Examples of these plots are shown in Figures 6.7, 6.8, and 6.9, with the remainder of the maps in the appendix. In general, P3 and P4 show varying levels of mixing throughout each sample with evidence of un-melted and incompletely mixed quartz and feldspar.

P1 and P2 are of particular interest due to their anthropogenic source and/or likely association with radioactivity, and experience a range of behaviors in different samples. The range of behavior observed with P1 and P2 is exemplified in the study of three samples: F27, F20, and F34.

In sample F20 (Figure 6.7), P1 is well correlated to P2 on the rim of the sample. Rim structures are observed for both P1 and P2, which are largely correlated. P3 map shows the presence of unmelted (or melted but unmixed) quartz grains within the bulk glass, which still has significant contributions from quartz. P4 shows the distribution of feldspathic contributions within the melt with regions of higher concentration representing incompletely mixed feldspar melt.

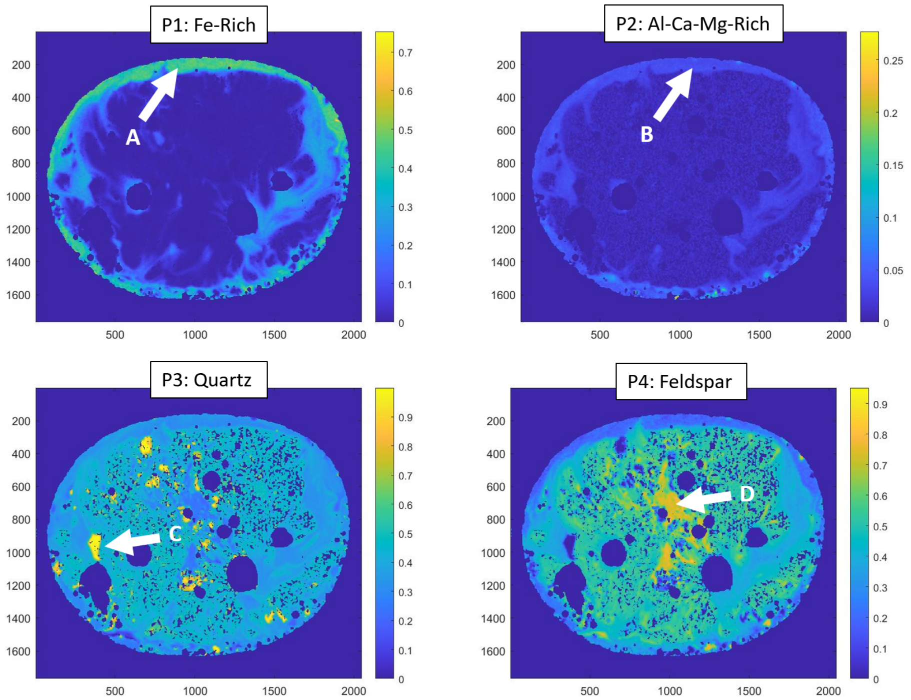

Figure 6.7: F20 Precursor Maps. Rim structures are observed for both P1 and P2, which are largely correlated. P3 map shows the presence of unmelted (or melted but unmixed) quartz grains within the bulk glass, which still has significant contributions from quartz. P4 shows the distribution of feldspathic contributions within the melt with regions of higher concentration representing incompletely mixed feldspar melt.

In sample F27 (Figure 6.8), there is a similar P1 enrichment on the rim, but no consistent correlation exists between P1 and P2. Some agglomerates have high contributions from both P1 and P2. Rim structures are observed for P1. In contrast to sample F20 (Figure 6.6), no rim structure is observed for P2, though there are some agglomerates that are enriched in P2. The P3 map shows the presence of unmelted (or melted but unmixed) quartz grains within the bulk glass, which still has significant contributions from quartz. P4 shows the distribution of feldspathic contributions within the melt with regions of higher concentration representing incompletely mixed feldspar melt.

Finally, sample F34 (Figure 6.9) have both characteristics, with the outermost rim being enriched in P1, but no correlation between P1 and P2, but an inner rim with both P1 and P2 contributions. Rim structures are observed for both P1 and P2. However, the correlation between these precursors is not as strong as in sample F20 (Figure 6.6) and thus likely represent intermediate behavior between that observed in F20 anf F27. The P3 map shows the presence of unmelted (or melted but unmixed) quartz grains within the bulk glass,

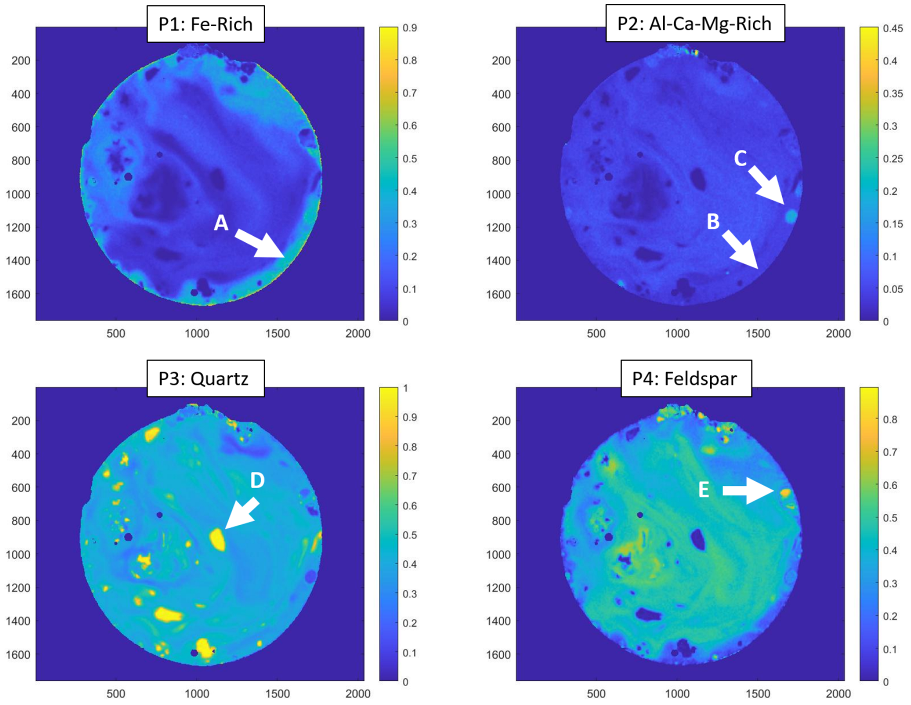

Figure 6.8: F27 Precursor Maps. Rim structures are observed for P1. In contrast to sample F20 (Figure 6.6), no rim structure is observed for P2, though there are some agglomerates that are enriched in P2. The P3 map shows the presence of unmelted (or melted but unmixed) quartz grains within the bulk glass, which still has significant contributions from quartz. P4 shows the distribution of feldspathic contributions within the melt with regions of higher concentration representing incompletely mixed feldspar melt.

which still has significant contributions from quartz. P4 shows the distribution of feldspathic contributions within the melt with regions of higher concentration representing incompletely mixed feldspar melt. This sample shows less mixing of P4 (feldspar) in the interior of the sample.

6.3 Immiscible Compositional Projection onto the MCR-ALS Model

Precursor compositions do not directly match amoeboid L_{Fe} and L_{Si} compositions (Table 6.2) and so do not offer evidence of immiscibility textures representing the direct emulsification of precursors. Each immiscible phase is also composed of some mixture of precursors. To estimate the relative contribution of each precursor to each immiscible phase, the overall

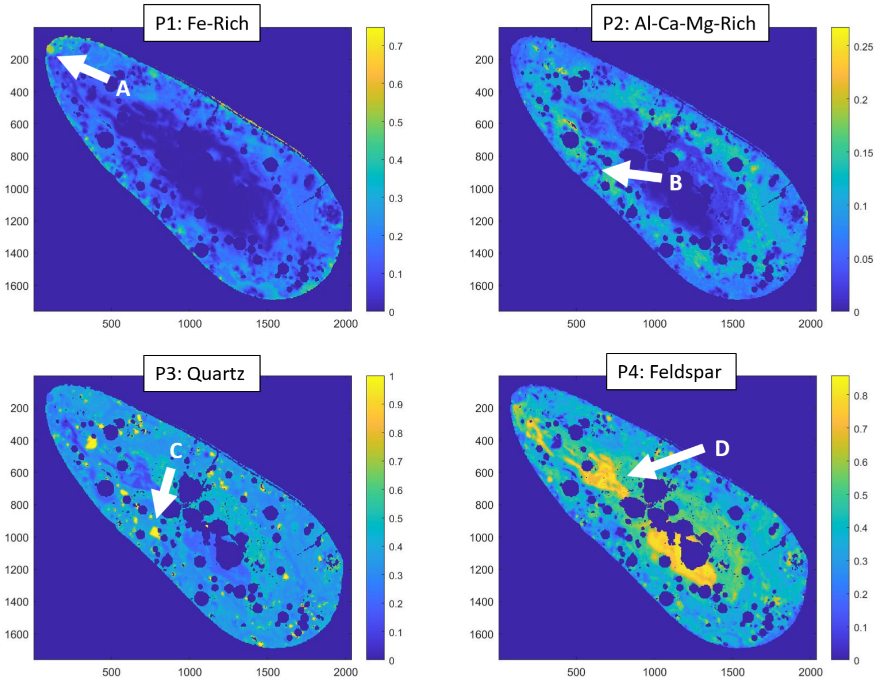

Figure 6.9: F34 Precursor Maps. Rim structures are observed for both P1 and P2. However, the correlation between these precursors is not as strong as in sample F20 (Figure 6.6) and thus likely represent intermediate behavior between that observed in F20 anf F27. The P3 map shows the presence of unmelted (or melted but unmixed) quartz grains within the bulk glass, which still has significant contributions from quartz. P4 shows the distribution of feldspathic contributions within the melt with regions of higher concentration representing incompletely mixed feldspar melt. This sample shows less mixing of P4 (feldspar) in the interior of the sample.

SEM-EDS dataset is amended with a matrix of data containing a variety of additional TEM-EDS data, to include all measured L_{Fe} and L_{Si} compositions and R1-R6 glass compositions. This matrix is projected onto the model using the calculated **S** matrix. After projection, average contributions for L_{Si} and L_{Fe} are calculated. L_{Si} is estimated to be 19% P1 (Fe-Rich), 4% P2 (AlCaMg-Rich), 52% P3 (Quartz), and 25% P4 (Feldspar). L_{Fe} is estimated to be 83% P1 (Fe-rich), 0.05% P2 (AlCaMg-rich), 16% P3 (Quartz) and 0.9% P4 (Feldspar). Thus the L_{Si} represents a more even distribution of all precursors (i.e. a mixed melt) while L_{Fe} represents primarily P1 and P3.

Table 6.1: Total precursor contribution by sample. Columns are the total percent contribution to each sample (rows) from each precursor (P1-P4) from the pixels used in the MCR-ALS model. P1 is the iron oxide precursor, P2 is the Al-Ca-Mg precursor, P3 is the quartz precursor, and P4 is the feldspar precursor.

	%P1 (Fe-rich)	**%P2 (AlCaMg-rich)**	**%P3 (Quartz)**	**%P4 (Feldspar)**
F9	16	4	40	40
F11	12	4	42	42
F13	8	2	54	36
F14	11	5	40	44
F18	12	6	40	42
F20	11	1	41	47
F24	16	7	41	36
F25	10	4	44	42
F27	15	5	42	38
F28	8	3	43	45
F29	2	2	41	54
F34	14	8	37	41
F35	11	6	47	36

Table 6.2: L_{Si} and L_{Fe} TEM EDS average compositions compared to MCR-ALS estimations of precursors

TEM EDS Wt %	**O**	**Na+K**	**Mg**	**Al**	**Si**	**Ca**	**Fe**
L_{Si}	43.82	3.50	0.62	5.07	30.19	1.84	14.42
L_{Fe}	31.58	1.30	0.97	1.89	8.97	0.47	53.53
MCR-ALS Compositions							
P1 Fe-Rich	28.51	–	1.27	5.34	–	–	64.88
P2 AlCaMg-Rich	32.90	–	4.78	19.89	–	42.43	–
P3 Quartz	52.34	–	0.25	0.17	47.24	–	–
P4 Feldspar	46.92	12.32	0.25	14.63	25.87	–	–

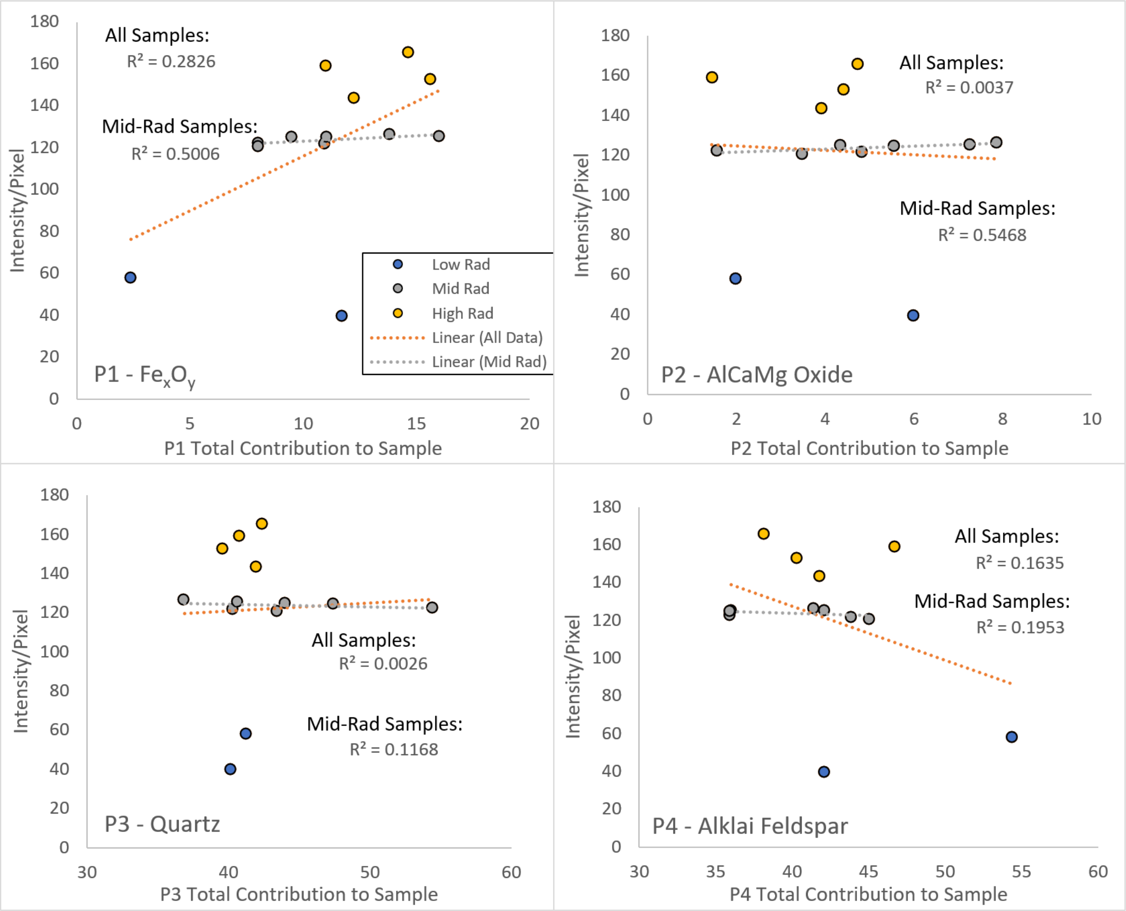

Figure 6.10: Total correlation between radiograph pixel density and total sample precursor contributions. R^2 values for trends for each precursor are low (<0.2) and likely not significant. Using a subset of the mid-rad samples increases the correlations ($R^2 = 0.2 - 0.5$). There exists for mid-rad samples a positive correlation in radioactivity for both P1 and P2 and a negative correlation for P3 and P4.

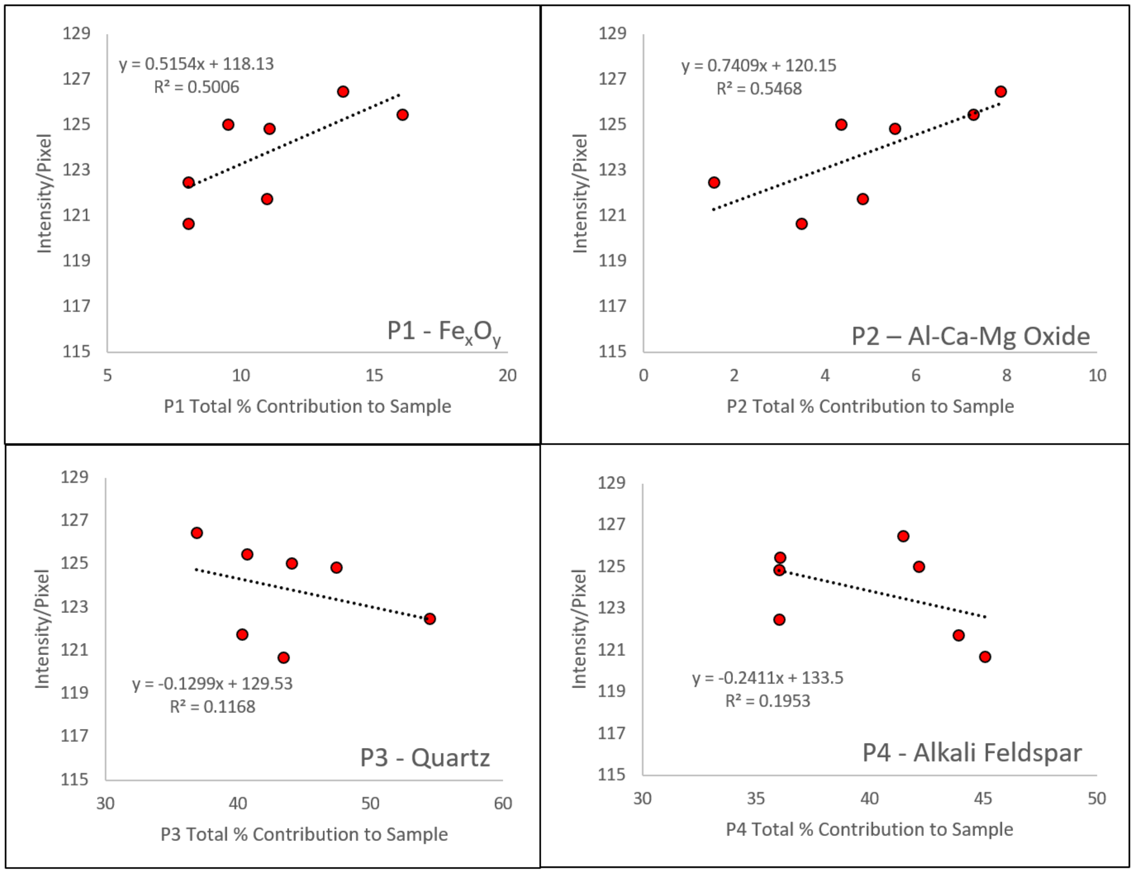

Figure 6.11: Correlation between radiograph pixel density and total sample precursor contributions for mid-radioactivity samples only. There exists for mid-rad samples a positive correlation in radioactivity for both P1 and P2 and a negative correlation for P3 and P4.

6.4 Radioactivity Correlation to Precursors

Measures of radioactivity (auto-radiography measures of total radioactivity and NanoSIMS measurements of ^{239}Pu) were correlated to precursor contributions. Autoradiography pixel density (Chapter 3) is plotted vs. each sample precursor contribution (Table 6.1). Overall data is scattered (Figure 6.11) and do not show clear precursor correlations to total radioactivity across all samples. When autoradiography pixel values outside 1-σ of the mean are excluded to form a 'mid-rad' subset of the samples, a correlation becomes much stronger, with a positive correlation of radioactivity with both P1 and P2 (R^2=0.50, 0.55) and a weak negative correlation with P3 (R^2=0.12) and P4 (R^2=0.19). NanoSIMS ^{239}Pu cps in non-immiscible glass (R1-R6) values compared to precursor fractions (Figure 6.12) have similar correlations, but with weaker trends.

Deviations in immiscible regions from Pu/Fe and Pu/Ca trends observed in the NanoSIMS

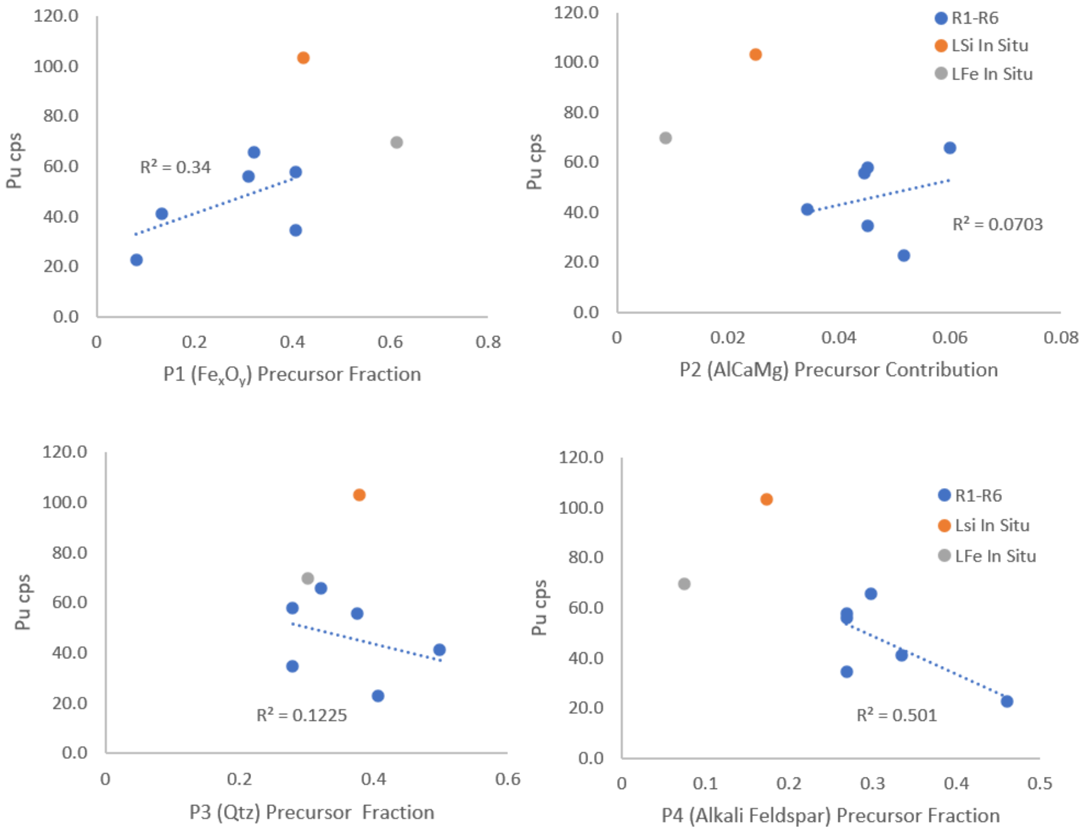

Figure 6.12: Relationship between ^{239}Pu concentration and estimation of precursor fractions in R1-R6 and *in situ* immiscible phases. Weak positive correlations are seen between ^{239}Pu and P1 (FexOy) and P2(AlCaMg), and weak negative correlations are seen between ^{239}Pu and P3 (quartz) and P4 (feldspar). While NanoSIMS data has significant spread, these trends are consistent with the overall sample correlations in Figure 6.10. Immiscible regions exhibit some deviations from these trends, consistent with observed elemental trends in Chapter 3.

data (Chapter 3) were thought to be either due to unexpected decomposition elemental partitioning, and/or because Pu was associated with an individual emulsified precursors that made up different portions of each phase. If the latter was true, projecting immiscible compositions into their precursor contribution might correct for this effect and result in L_{Fe} and L_{Si} precursor fractions that are consistent with general Pu/Precursor trends in non-immiscible regions. After applying the MCR-ALS approach, immiscible regions precursor/Pu relations still deviate from general trends. This projection of immiscible compositions onto the MCR-ALS model does not offer additional support for an emulsification hypothesis.

6.5 Summary of Precursor Relationships in Iron-Rich Fallout

This work applied the MCR-ALS approach to 13 samples to estimate precursor compositions and their contributions to sample heterogeneity. The precursor compositions, relationships, and correlations with radioactivity allow some key interpretations to be made about the formation of fallout in iron-rich environments.

The compositions of P3 (quartz) and P4 (alkali feldspar) are not surprising given that unmelted and partially melted grains are present in the interiors of many samples, and are similar in composition to the feldspathic and Si-rich precursors calculated using the MCR-ALS approach by Fitzgerald *et al* [20]. The iron oxide composition of P1 is primarily due to anthropogenic iron that is either vaporized and re-condensed from intitial heating, or is entrained at later times and experiences varying levels of melting and/or vaporization. The presence of Al in P1 (and occasionally Si for some constrained models) may be due to anthropogenic aluminum associated with the Fe, or is due to rotational ambiguities in the model. One source of these ambiguities could be the presence of accessory minerals in the soil that are not significant enough for PCA or the MCR-ALS model to distinguish. The lack of Al in P1 for the single sample (F27) MCR-ALS model (Figure 6.6) suggests that the presence of Al is likely a result of rotational ambiguities rather than anthropogenic Al.

The composition of P2 (AlCaMg-rich) is more difficult to interpret given it's sensitivity to constraints and sensitivity to what samples are included in the model. While the overall sample model does not include any Fe in P2, there is significant Fe in the single sample (F27) MCR-ALS model. One interpretation is that P2 represents the same refractory CaMgFe-rich glass observed in the fallout glass literature. While Bonamici [5] interprets this glass to be caused by bomb vapor condensation or a mixing of soil constituents [15, 20]. It is possible that in this case, P2 represents mixing of other minor soil constituents. Alternatively, P2 could represent a chemically fractionated melt that has experienced significant heating to volatilize species with lower boiling points such as K_2O (350 °C), Na_2O (1950 °C), SiO_2 (2230 °C), resulting in a melt enriched in more refractory species such as Al_2O_3 (2977 °C), MgO (3600 °C), °CaO (2850°C) and FeO (3414 °C). The sensitivity of P2 composition to constraints and sample inclusion may be because P2 represents a chemically fractionated term, which may introduce rotational ambiguity into the model. This is in contrast to Fitzgerald's assumption [20] that an ideal mixture can be assumed and that chemical fractionation is negligible.

The MCR-ALS approach failed to independently predict precursor compositions that matched well with L_{Fe} and L_{Si} compositions. This method did not provide smoking gun evidence for an emulsification hypothesis. If amoeboids formed via emulsification of two distinct liquids, each liquid represents some mixture of precursors, or diffusive exchange altered the composition of each liquid after emulsification. TEM-EDS measurements (Figure 3.27) of L_{Si} have compositions that fall neatly along the edge of SEM-EDS compositional data points on the pseudo-ternary projection, with compositions that are alkali-poor compared to the average bulk sample composition. Volatile depletion in L_{Si} suggests some level of chemical fractionation and more significant heating. This evidence suggests that, while amoeboids don't represent emulsification of two individual precursors, they may represent an emulsification of the more signficantly heated, chemically fractionated bulk melt (a mixture of P1-P4) with P1 (Fe-rich).

For most of the samples in this study (where radioactivity is within 1-sigma of the mean radioactivity), radioactivity is positively associated with two precursors: an iron-rich precursor (P1) and a Al-Ca-Mg-rich precursor (P2). This claim is primarily supported by correlations in the summed precursor contributions over all data-points used in the model with total auto-radiography pixel density (Figure 6.11). Weak correlations in the NanoSIMS Pu data (Figure 6.12) add additional support for this claim. These correlations can be explained either by co-condensation of the radioactive vapor with refractory elements in P1 and P2, rapid incorporation of condensates in lower viscosity melts that have experiences volatile loss, or a combination of both.

Inclusion of low and high radioactivity samples weakens this correlation, suggesting that these trends are dependent on specific time-temperature histories which do not hold for outlier (low radioactivity and high radioactivity) samples . Low radioactivity samples are morphologically distinct, with non-aerodynamic and incompletely melted features, and thus exhibit clear evidence of lower time-temperature histories, either due to late term entrainment or early ejection/fallout from the fireball and/or mushroom cloud. A deviation from precursor contribution/radioactivity trends is not surprising given the presence of incompletely melted features which cannot rapidly incorporate radioactive condensates. However, high radioactivity samples are not consistent with precursor contribution trends, but are not morphologically distinct from mid-rad samples. All high radioactivity samples (F9, F11, F20, F27) have radioactive Fe-rich rims, and one sample (F20) has a rim also enriched in Ca. The failure of trends to follow across all samples highlights the importance of understanding entrainment and time-temperature histories of different sample types in understanding the resulting distribution of radioactivity in fallout samples.

Another observed trend that highlights the variability in precursor behavior in different samples is that of the relationship between P1 and P2 in individual samples. Plots of P1 vs. P2 for two high radioactivity samples (F20 and F27) are shown in Figure 6.13. In F20, the Ca enrichment in the Fe-rich rim can be seen in a clear positive correlation (noted by the ellipse A) between P1 (Fe-rich) and P2 (AlCaMg-rich). In F27 no such Ca enrichment was noted in

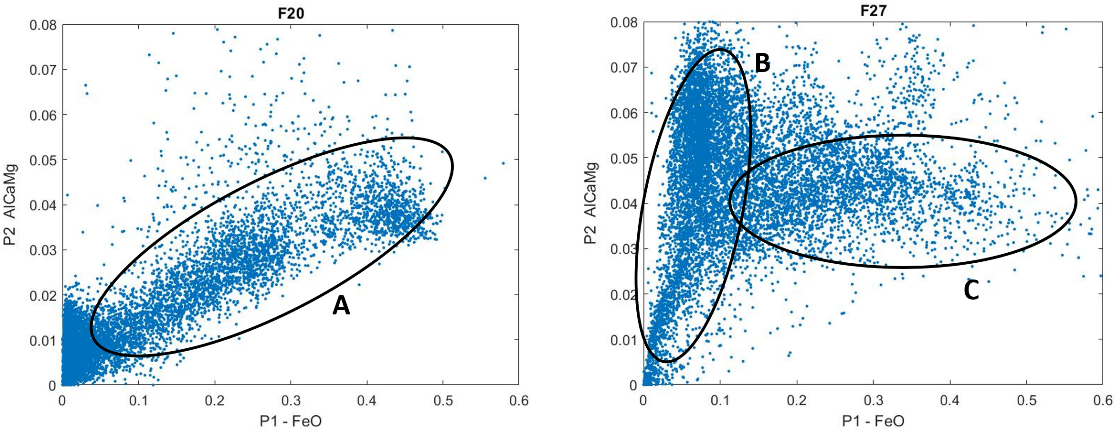

Figure 6.13: Variable relationships between precursors correlated to radioactivity. Sample F20 shows good correlation between P1 and P2 (ellipse A), consistent with quantitative maps that showed a rim enriched in both Fe and Ca. Sample F27 shows some correlation between P1 and P2 (ellipse B) which is not present at high Fe concentrations (ellipse C), consistent with quantitative maps that showed rims enriched in Fe but not in Ca.

the Fe-rich rim. The interior of the sample has some correlation between P1 and P2 (ellipse B), but the lack of Ca-enrichment in the Fe-rich rim can be seen for high P1 contributions. This adds support for the theory that some iron is well mixed with the P2 term (likely early vaporized/entrained Fe) adn some is not well mixed (likely late vaporized/entrained Fe).

6.6 Multi-Component Mixing Interpretation

This MCR-ALS model offers a way to investigate mixing relationships in Fe-rich fallout. The 4-precursor model used in this work showed correlations of radioactivity with two precursors, one nearly pure Fe-oxide (P1) and one Al-Ca-Mg-rich (P2). The composition of P2 is variable depending on constraints and which samples are used in the model, and likely represents a chemically fractionated melt, which the MCR-ALS model has some difficulties modeling, introducing rotational ambiguity. Variable relationships between P1 and P2 can be explained by the time-varying incorporation of an Fe source. Early Fe is well mixed with a heated and chemically fractionated melt (represented by P2), whereas late Fe is not well mixed with P2. The current MCR-ALS approach failed to conclusively support the immiscibility hypothesis of emulsification of pure precursors. However, projection of immiscibility compositions onto the model showed that L_{Si} is representative of a mixture of all precursors, supporting the theory that, if amoeboids represent an emulsification process, they are an emulsification of late entry Fe-oxide (P1) and a melt mixture (P1-P4) that has experienced some level of chemical fractionation.

The P1 contribution to L_{Si} and the chemically fractionated melt may represent initially vaporized and condensed iron, whereas the P1 contribution to L_{Fe} represents Fe that is mixed into the samples at later times, either due to late entrainment or continual melting/vaporization during fireball evolution. The interpretations gleaned from the work in this chapter will balanced against evidence and observations of other chapters and be incorporated into overall key observations and interpretations in Chapter 7.

Chapter 7

Iron-Rich Fallout Behavior

The goal of this work is to investigate how iron influences nuclear fallout formation. This chapter highlights a few key features that were discovered and studied in this work that have not been documented in studies of iron-poor fallout [3, 5, 21, 46, 52, 93], . These observations highlight processes that are unique to fallout formed in Fe-rich silicate environments, though some findings may be relevant to all Fe-rich environments. For example, while constraints of fO_2 caused by buffering behavior of Fe using FeO-SiO_2 immiscibility are possible only in fallout where immiscibility is present (such as in this study), if these constraints are primarily governed by Fe buffering behavior, such constraints would be applicable to other events with similar quantities of Fe. These findings highlight processes that will be instrumental in developing fallout formation models that incorporate the complex behavior of fallout formation and which do not rely on empirical relationships to predict radiochemical fractionation. The key findings in this work include variable Fe relationships to other refractory species (such as Ca, Mg, and Pu), liquid immiscibility, iron oxide crystallization, and evidence of intermediate oxygen environments, each of which are discussed below. Following discussion of each, a brief description of fallout formation in Fe-rich silicate environments is presented, and suggestions for future work are offered.

7.1 Key Findings

Inconsistent Fe-Ca-Pu Relationships

The first key feature is the variable relationship between Fe and other refractory species (such as Ca, Mg, and Pu) that have been noted in other fallout studies. The high levels of Fe in these samples are not surprising given that these samples were selected for their formation from a nuclear explosion with significant iron. Radiography measurements showing a correlation between Fe and alpha/beta radioactivity was also not surprising since this trend has been previously observed in the form of CaMgFe-rich surface depositions layers bearing evidence of bomb vapor [93] and CaMgFe-rich glass with radioactivity [5]. This work deviates from these observations with many radioactive Fe-rich rims lacking the expected Ca and Mg enrichment. Distinguishing individual elemental enrichment can be difficult in complex systems, but multi-component un-mixing models using PCA and MCR-ALS explored in Chapter 6 confirm that that such variability between samples represents real variations in precursor mixing and/or melt fractionation. The Fe in these samples is primarily associated with an Fe oxide precursor (labeled P1 in Chapter 6), while the Ca and Mg is primarily associated with an AlCaMg-rich precursor (labeled P2 in Chapter 6). The relationship between precursor contributions (which were calculated for each spatially-resolved compositional measurement) revealed bi-modal behavior, with some datapoints demonstrating a positive correlation, and some demonstrating a primarily P1 (Fe oxide precursor) contribution without the associated P2 (AlCaMg-rich precursor) contribution. Both of these precursors were weakly correlated to radioactivity for the majority of precursors, but this trend varied for low-radioactivity and high-radioactivity samples.

The inconsistent relationship between Fe and other refractory species was also observed on smaller length scales. Micro-scale studies of Pu concentrations in samples demonstrated variable relationships between Pu, Fe, and Ca. NanoSIMS data (R1-R6) demonstrated that one region in F27 exhibited correlations between Pu, Ca, and Fe (consistent with previous studies of CaMgFe-rich regions of fallout), but data in other regions of F27 (IM1) or in other samples (IM2, IM3) did not fall on this trendline. This means this correlation is not universal across all samples, with variations stemming from sample-to-sample variations in the mixing relationships of two precursors associated with the bomb vapor. In addition, positive correlations between Pu and Fe were reversed in regions of liquid immiscibility, and some Fe-rich regions were identified in sample F29 with no detectable Pu. If these immiscibility trends are due to emulsification of distinct liquids (as opposed to decomposition from a single liquid), then this supports the theory that variable relationships between Fe, Ca, and Pu are due to variations in timing of Fe mixing exhibited in different samples. Early vaporized or entrained Fe is well mixed with the refractive radioactive bomb vapor which becomes more rapidly associated with the refractory chemically fractionated melt (P2), whereas late vaporization or melting of entrained Fe results in less radioactive (or non-radioactive) Fe oxide that is emulsified with the fractionated melt. The complexity of entrainment processes results in variations in this behavior from sample to sample that does not seem to follow any easily identifiable trend using the limited dataset in this work.

Liquid Immiscibility

A second key feature is the widespread presence of liquid immiscibility textures in Fe-rich silicate fallout. This feature is unique to environments with overall average compositions which when mixed together may result in melt compositions that fall within stable immiscibility fields. Previous studies of mm-scale trinitite glass formed in the first nuclear explosion have noted the presence of metal or metal oxide species and limited textural evidence of liquid immiscibility [7, 16, 3]. However, such observations and interpretations have remained sparse, likely because thermodynamically stable immiscible liquids only exist for a limited range of compositions, oxygen environments, and temperatures. These textures are more widespread in these samples than previously reported. In particular, *ex situ* amoeboid immiscibility has not been reported in the fallout literature, and some morphologies have not been reported in any immiscibility literature. Immiscibility may be significant to fallout formation models for at least two reasons: (1) micro-scale phases may partition radionuclides in ways that effect both chemical mobility or chemical fractionation processes and (2) liquid immiscibility sensitivity to fireball parameters of interest such as temperature and oxygen fugacity.

If amoeboids formed via decomposition form a single miscible condensed phase, this process alters the initial chemistry and physical distribution of species within the particle while in the liquid state, including trace element partitioning between two immiscible silicate liquids [88]. In early times after a nuclear detonation, a significant portion of hazardous radioactivity is emitted from fission products which exist in trace concentrations within fallout glass. Decomposition may affect the distribution of hazardous radioactive species in the particle interiors (i.e., radioactive ^{137}Cs will partition into L_{Si} and ^{140}Ba will partition into L_{Fe} [91]). Radionuclides which partition into the less chemically durable L_{Fe} phase may have higher environmental mobility for fallout where such textures are present. In addition, liquid phase separation affects nearly all the properties of glass, and tends to decrease the chemical durability of the glass in general, which may result in increased radionuclide mobility in glasses where this process is significant [92]. Limited nanoSIMS data in sample F27 suggests that amoeboids can contain Pu concentrations that are roughly 4 times higher than Pu concentrations in the radionuclide-rich rim of their host samples, highlighting the importance of understanding this partitioning behavior. There is uncertainty in the magnitude of such an effect due to the limited nanoSIMS data and since amoeboids preserved in mm-scale fallout glass are not a representative sampling of all radionuclide-bearing condensate particles formed in the fireball.

Decomposition processes may have implications for better understanding radiochemical fractionation processes historically observed in fallout, depending on what timeframe decomposition occurred during fireball cooling. Current models used for prediction of nuclear fallout formation [65] treat radiochemical fractionation semi-empirically and assume that all trace radioactive oxide species that condense prior to the solidification of the carrier material are distributed volumetrically throughout the μm-scale particles, and species that condense after solidification are distributed on the surface [23, 57]. Other models attempt to account for kinetic condensation, diffusion, and re-evaporation effects, but suffer from a lack of experimental data [64]. If decomposition occurs while fission product mass chains are still condensing, the evolving composition of the amoeboid surface liquid may influence condensation processes if there are kinetic limitations to condensation (i.e., liquid-vapor surface sticking coefficients [64] or diffusion limitations [94]) and thus perturb particle size-dependent radiochemical fractionation patterns in μm-scale fallout particles. Studies of the temperature range of the stable liquid immiscibility region explored in Chapter 4 suggest this process may be significant in the range of 1620-1950 °C, temperatures at which many fission product oxides are still condensing.

There is also uncertainty on how agglomeration processes influence radiochemical fractionation patterns in fallout particles [25, 84]. The immiscible nature of amoeboids reported here offer a new means to distinguish *in situ* vs. *ex situ* processes, which may increase our understanding of how agglomeration plays a role in fallout formation and radiochemical fractionation. While the effect of decomposition is limited to environments with compositions conducive to liquid immiscibility (i.e., iron-silicate), it warrants consideration in physics-based radiochemical fractionation and fallout contamination models that can be applied to a range of explosion geologies and environments.

Liquid immiscibility sensitivity to fireball parameters of interest such as temperature and oxygen fugacity also highlight the importance of these discoveries in developing fallout formation models. As discussed in Chapter 1, volatility-driven chemical fractionation can be influenced by (1) changes in fireball cooling because it determines what chemical form each fission product mass chain is at time of condensation and (2) changes in oxygen fugacity which influences condensation behaviors for mass chains. For example, the A=140 mass chain contains ^{140}La, an important refractory fission product. Elemental lanthanum has a boiling point of 3464 °C, but La_2O_3 has a boiling point of 4200 C, thus the oxidation of Lanthanum will determine the timescale of condensation during fireball cooling, as well as the quantity of the 140 mass chain that exists as La (as the mass chain decays from it's more volatile precursors ^{140}Xe, $t_{1/2}$=13.6 sec and ^{140}Cs, $t_{1/2}$=1.1 min) at each of those temperatures. Estimating temperatures in the fireball has historically been done using luminosity measurements and doesn't account for temperature heterogeneity within the fireball. Furthermore, the fireball is assumed to be fully oxygenated at times of condensation, an assumption that has been questioned in recent work. Thus novel probes of both temperature and oxygen may be useful in adding constraints to fireball temperature and oxygen histories during fallout formation in complex environments. Liquid immiscibility compositions in this work are sensitive to both of these parameters and thus may be important in constraining future models of fallout. In particular, the *ex situ* formation of amoeboids and their micro-scale size suggest they can more rapidly reach thermal and chemical equilibrium with the fireball vapor for at least a portion of their history than *in situ* immiscibility, and thus are of primary interest in probing fireball conditions.

Providing such temperature and oxygen constraints using amoeboids, however, is made difficult by (1) the complex dependence of the stable immiscibility fields on multi-component melt composition, and (2) poor knowledge of the kinetics of silicate liquid immiscibility. Immiscible liquids generally have the potential to be present for some melt compositions and temperatures in glass-forming iron-rich aluminosilicate systems, where varying structural roles of cation species in the melt result in stable silicate-rich liquids (L_{Si}) and iron-rich liquids (L_{Fe}) [87, 37]. These complex melt interactions result in variations in the compositional and temperature range of this field that is not fully understood, and which is also significantly sensitive to the oxygen fugacity (fO_2) of the system [61]. Even with a good knowledge of the compositional and temperature range of stable immiscibility for a given oxygen environment, evidence presented in Chapter 4 shows that amoeboid likely reflect non-equilibrium compositions. While this result is not surprising given the rapid cooling behavior of nuclear fireballs, some fallout models assume that some level of equilibrium can be achieved, and the transition between equilibrium and kinetically limited behavior is not clear. A further complication is uncertainty in the role that meta-stable immiscibility may continue to play a role in melt partitioning as the melt cools below the liquidus. While amoeboids cannot provide robust constraints at this time due to incomplete knowledge of the thermodynamics and kinetics of silicate liquid immiscibility, their non-equilibrium behavior shows that that 3-20 micron size particles do not achieve chemical equilibrium during the rapid cooling through the temperatures at which liquid immiscibility is a significant formation process (1620-1950 °C).

The non-equilibrium compositions of *ex situ* amoeboids means that understanding their kinetics of formation is important to using them for vapor inferences. The kinetics of formation will differ depending on the mechanism of formation. While knowledge of the kinetics of decomposition and emulsification in this system preclude quantitative interpretation at this time, determining the formation process of amoeboids is an important first step. In this work, two potential formation mechanisms were explored (Figure 3.34): decomposition and emulsification. A summary of how different processes result in similar compositional partitioning is shown in Figure 7.1. While each process may result in similar elemental partitioning, the mechanism of formation results in different interpretation and insights into the history of the fireball and fallout formation. In the case of kinetically limited decomposition (Figure 7.1A), distribution of species between two phases may offer an estimate of cooling rates that amoeboids experienced, a metric that was investigated in Chapter 4 (Figure 4.7). In the case of kinetically limited emulsification (Figure 7.1B), the composition of the two phases reflect distinct compositions prior to emulsification, assuming diffusive exchange between phases after emulsification is not significant. The evidence for each hypothesis is summarized below.

The evidence for decomposition (Figure 7.1A) is primarily textural, with evidence of interconnected morphologies and continuous gradients in the size of L_{Fe} spheres within the host melt, as discussed in Section 3.6, and which have been interpreted to result from decomposition from a miscible melt in similar systems such as terrestrial and lunar impact melts and terrestrial magmatic systems. The phase field method approach explored in Chapter 5 strengthened the argument for this theory by showing that decomposition processes are consistent with the range of amoeboid morphologies observed in these samples. However, to reproduce all observed morphologies, variable wetting behavior that conflicts with limited published data on the physical properties of silicate immiscible melts casts doubt as to whether decomposition alone can explain amoeboid formation. This model is qualitative and a quantitative model would allow better exploration of the timescales of formation for amoeboid decomposition.

The evidence for emulsification (Figure 7.1B) is primarily compositional, as was also discussed in Section 3.6. TEM EDS compositions of L_{Si} that coincide with the most alkali-poor region of the overall sample (Figure 3.27) is unlikely to occur via a decomposition process. While the MCR-ALS approach explored in Chapter 6 did not demonstrate that each phase primarily represent a single environmental precursor, it did show that L_{Si} is a mixture of all four precursors, one of which (P2) represents a chemically fractionated melt. This suggests that amoeboids represent the emulsification of an already well-mixed melt with an Fe-rich precursor (P1). The rim location of amoeboids suggest a late-time formation and agglomeration after early condensed radioactive vapor has been incorporated into the rim of the mm-scale sample. Emulsification occurred *ex situ*, so the compositional similarity of L_{Si} to chemically fractionated boundary region of the well-mixed host melt suggests that *ex situ* L_{Si} globules formed after initial mixing of entrained precursors and bomb vapor. This may have occurred via a variety of mechanisms. One possibility is that mechanical separation of the melt may have occurred during turbulent mixing in the fireball, resulting in micro-scale droplets of L_{Si} that were emulsified with late entry Fe (L_{Fe}). Alternatively, L_{Si} could represent direct vapor condensate particles that at earlier times agglomerate or directly condense onto the mm-scale host melt, and at late times if not already scavenged by mm-scale aerodynamic melt, grow larger and emulsify with Fe that enters the fireball at late time.

While radioactivity is associated with Fe in all samples, the reversal of this trend in near-surface immiscibility textures and the presence of non-radioactive Fe in non-aerodynamic samples (F17 and F18, Figure 3.21) is consistent with a late time amoeboid formation hypothesis via emulsification of non-radioactive iron with a well-mixed melt that contains condensed radioactive bomb vapor. This late-time iron could be due to late time entrainment of proximate Fe material or due to incompletely vaporized iron within the fireball that continues to melt and vaporize throughout the duration of fireball cooling.

The compositional evidence for an emulsification hypothesis (Figure 7.1B) is the most convincing, as one has to use multiple caveats or explanation to explain compositional data using a decomposition hypothesis (Figure 7.1A). However, the textural and morphological evidence of decomposition cannot be ignored, and it is clear that, especially in some *in situ* textures, decomposition did occur. It is likely that both mechanisms play a role in these samples, and that continual condensation/evaporation, elemental diffusive exchange, and phase coarsening obscure the record of each process. This work does not definitively determine a single mechanism of formation, but highlights the conflicting evidence and suggest immiscibility may influence fundamental formation mechanisms or be used to probe fireball parameters in the future, if a method to reliably distinguish between these processes can be developed.

Crystallization

A third key feature is the abundant presence of crystalline growth in Fe-rich fallout, both as nano-scale crystals (euhedral and non-euhedral) and as dendritic crystalline growth. Fallout formed in silicate environments generally results in samples that quench to a glass which has been documented in numerous fallout studies, but the addition of significant quantities of iron permits the development of iron oxide crystallization within the glass, a feature unique to such environments. Dendritic growth has been observed in some localized regions of trinitite glass [16, 7], magnetite rims have recently been reported in some aerodynamic glassy

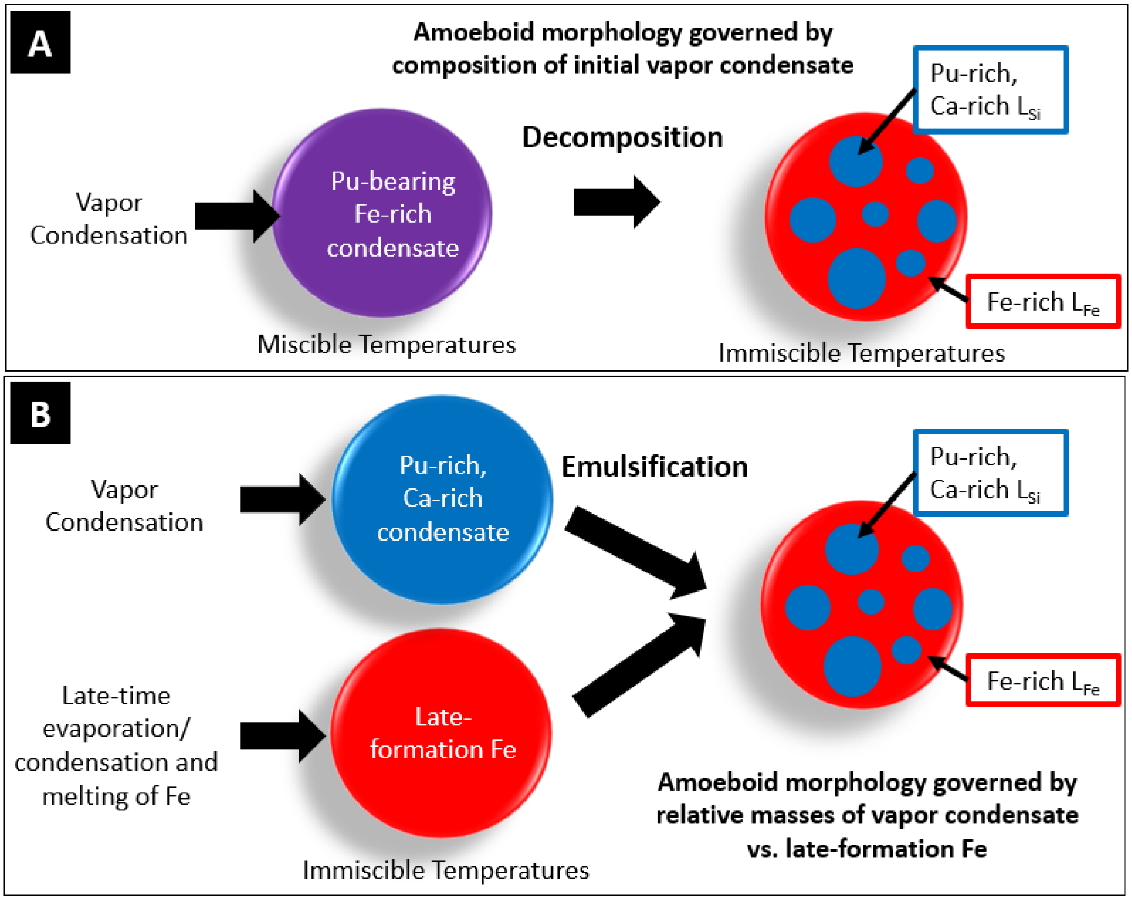

Figure 7.1: Overview of kinetically-limited competing formation mechanisms for amoeboids with liquid immiscibility textures. (A) The decomposition hypothesis posits that an initial droplet is formed via vapor condensation at miscible temperatures and then as the fireball and droplet cool to compositionally-dependent immiscible temperatures, the droplet experiences phase separation and the phases continue to coarsen into their final observed morphology. (B) the emulsification hypothesis posits that the initial vapor condensation is more consistent with only the composition of the L_{Si} phase in amoeboids and is emulsified with Fe which forms later. This late-formation Fe may be due to continual evaporation/melting of Fe that was not initially vaporized.

fallout [49], and iron oxide fallout particles were historically reported [2], but crystalline growth in mm-scale fallout samples is relatively rare. Devitrification has been suggested as the genesis of magnetite structures recently reported by Lukashenko [49], but no evidence for devitrification [48] is observed in the current sample suite. This work supports previous interpretations that non-equilibrium dendritic growth is the cause of magnetite rims in fallout [7] rather than devitrification of iron-rich glass after formation. Crystallization in a melt can affect the distribution of trace species between the melt and crystals which would include trace radionuclides. This effect is supported by compositional heterogeneity at the terminus of dendrite growth (Figure 3.23). However, dendrite growth in these samples is typically limited to <50 μm, and so may not significantly affect the spatial distribution of radionuclides in mm-scale glass. While crystallization occurs after radionuclides have condensed and are unlikely to affect overall chemical fractionation patterns, the high levels of crystallization in the radionuclide-rich rim may may alter the environmental mobility of radionuclides. While crystallization of fallout in Fe-rich environments is not important for predicting radiochemical fractionation, it may be more important for understanding environmental contamination in a post-detonation scenario.

Buffering of the Oxygen Environment

A third key feature is the evidence variable redox conditions within the fireball. This work did not provide the conclusive evidence that Fe may buffer the oxygen environment of the fireball as theorized and suggested by Cassata *et al* [8]. TEM SADP analysis of amoeboids only identified cubic crystals that matched magnetite, but did not identify Fe oxides with other oxidation states (such as wustite or hematite) which would have supported a buffering hypothesis. However, in other samples (F17 and F18) metallic (i.e., reduced) iron was observed. These features were in non-aerodynamic samples that likely represent late entrainment or early ejection from the fireball, and were not proximate to Fe oxide crystals, and so do not support a hypothesis of buffering behavior. Even though no conclusive evidence is offered for Fe buffering behavior, this evidence still supports the presence of varying oxidation environments in different samples or at different timescales of formation. This is consistent with recent evidence of behavior, but no evidence was found that shows this to be unique to Fe-rich fallout.

7.2 Conceptual Overview of Iron-Rich Silicate Fallout Formation

This characterization work has identified many features that are unique and highlight the influence that Fe has on fallout formation. These unique processes may influence radiochemical fractionation and radionuclide environmental mobility. Immiscible textures unique to Fe-rich silicate fallout and representing higher temperature liquid interactions (versus

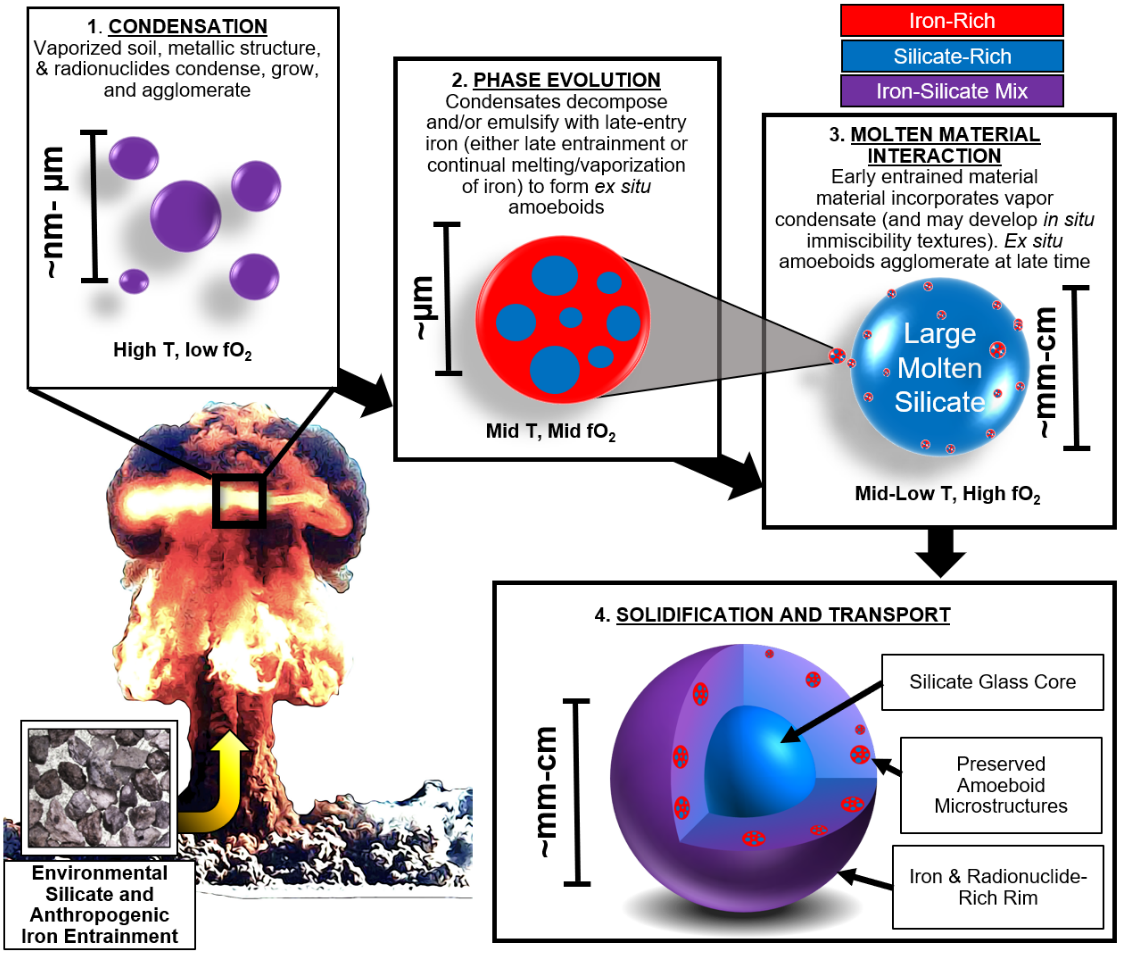

Figure 7.2: Overview of fallout formation in Fe-rich silicate environments

crystallization textures) are more likely to influence chemical fractionation processes processes. Unique *ex situ* amoeboid micro-structures also offer a unique probe of the fireball vapor environment. Their interpretation depends on their exact mechanism of formation. If they formed from the decomposition of a single phase, they offer measures of oxygen fugacity and quench rates. If they formed from the emulsification of distinct liquids, they provide additional insight into complex mixing processes and agglomeration within the fireball. However, quantitative interpretation for both of these hypotheses and amoeboid compositional sensitivity to parameters of interest is hampered by incomplete thermodynamic and kinetic knowledge for Fe-rich silicate systems.

Given the data and modeling done in this work, a conceptual overview for fallout formed in Fe-rich silicate environments is offered in Figure 7.2. In the first phase, the vaporized material condenses into particles that are a mixture of the initially vaporized material, which includes the radionuclide inventory and may include varying levels of soil, metallic structure, and other proximate material depending on the height of burst and energetic yield of the explosion. As the fireball begins to cool, more refractory elements condense and result in an association between Fe, Ca, Mg, and Pu that has been observed in other fallout studies and in non-immiscible glass in this work. In the second phase, the fireball continues to cool and the condensed droplets respond to the evolving vapor environment, decomposing into two immiscible phases and/or emulsifying with iron that enters the fireball at late times. This late-entry iron either is iron that is entrained at late times during turbulent mixing and/or is iron that continually melts/evaporates during the timeframe of fireball cooling. In the third phase, these condensate particles are incorporated into the mm-scale aerodynamic melt that is some variable mixture of entrained material. During heating of the entrained material, the melt composition evolves to represent some degree of chemical fractionation via volatile loss and/or due to the addition of chemically fractionated vapor condensate. Earlier incorporation of condensate at higher miscible temperatures (¿ 1950°C) results in the iron-rich, radionuclide-rich rims which also exhibit Ca, Mg, and Pu enrichment (Sample F20, Figure 3.9). As these melts cool, *in situ* immiscibility textures may also develop within the mm-scale aerodynamic melt. At later times, amoeboids are deposited on or near the surface and experience limited dissolution and/or incorporation into the interior prior to solidification. Late entry iron that is not associated with Ca, Mg, or Pu may also be deposited on sample surfaces at this time (Sample F27, Figure 3.6), explaining the deviations from traditional CaMgFe-rich glass patterns seen in Fe-poor fallout. In the final phase, the melt glass solidifies, preserving the amoeboid microstructures and iron and radionuclide rich rims. During solidification, dendritic iron grows within regions of the melt that are sufficiently rich in iron, which may be exaccerbated in regions of decomposition that result in a more Fe-rich phase than the original, miscible melt.

7.3 Implications for Fallout Research

This study of fallout formed in relatively iron-rich conditions has highlighted a variety of formation mechanisms and behavior that are unique to such environments. Variable correlations between Fe and other species that have been associated with Fe in other fallout work (such as Ca, Pu, and Mg) were highlighted using MCR ALS methods. This variable behavior supports a theory that in Fe present in fallout from Fe-rich environments is not solely due to vapor condensation, and that the time-varying entry of Fe into the fireball due to entrainment or continual melting/vaporization should be further investigated.

Studies of immiscible silicate oxide systems allow inference of conditions during and following high-temperature decomposition not previously explored in nuclear fallout. In particular, *ex situ* amoeboid compositions sensitive to oxygen fugacity and quench rates provide a new means to understand high-temperature melts enriched in iron, with implications for radionuclide condensation, as well as expanding the compositional range of rapidly quenched silicate immiscibility systems observed in the meteorite impact melt and fulgurite literature. Crystallization of L_{Fe} regions offer further evidence for incompletely oxidized formation conditions and appear minimally complicated by potential weathering and low-temperature redox interactions in the decades since sample formation. Iron-rich amoeboid micro-structures observed in nuclear debris provide a new record of complex fireball system evolution with implications for incorporation of silicate immiscibility in future fallout fractionation and environmental contamination models.

However, the use of these textures and amoeboid microstructures to inform formation conditions is hindered by an incomplete knowledge of the thermodynamics and kinetics of complex multi-component silicate immiscibility. Due to the non-equilibrium nature of amoeboid formation, work that distinguishes between either decomposition or emulsification will be key to using these observations to constrain future fallout formation models. Future work should focus on developing quantitative phase field method models (or other microstructure modeling methods) for both decomposition (which was initially explored in this work) and emulsification (which was not explored in this work). In order to develop a quantitative phase field method model, measurements of interfacial tensions and viscosity of silicate melts with similar compositions and across a range of relevant temperatures (1200-2000 °C) is necessary. This data would also enable better interpretation of the range of amoeboid morphologies and constrain wetting behavior in future microstructure models. In addition, experiments measuring stable two-liquid compositions for compositions and temperatures that are closer in composition to fallout in this study (and which include trace quantities of Pu or Pu surrogates) would validate whether unexpected Pu and Ca partitioning behavior represents decomposition or emulsification.

Bibliography

[1] C.E. Adams, N.H. Farlow, and W.R. Schell. “The compositions, structures and origins of radioactive fall-out particles”. In: *Geochimica et Cosmochimica Acta* 18.1 (1960), pp. 42–56. ISSN: 0016-7037. DOI: `https://doi.org/10.1016/0016-7037(60)90016-8`. URL: `http://www.sciencedirect.com/science/article/pii/0016703760900168`.

[2] CE Adams. *The Nature of Individual Radioactive Particles: fallout particles from a tower shot, Operation Redwing. vi.* Vol. 208. US Naval Radiological Defense Laboratory, 1957.

[3] Jeremy Bellucci and Antonio Simonetti. “Nuclear forensics: searching for nuclear device debris in trinitite-hosted inclusions”. In: *Journal of Radioanalytical and Nuclear Chemistry* 293.1 (2012), pp. 313–319.

[4] S Bulent Biner et al. *Programming phase-field modeling.* Springer, 2017.

[5] Chloë E Bonamici et al. “A geochemical approach to constraining the formation of glassy fallout debris from nuclear tests”. In: *Contributions to Mineralogy and Petrology* 172.1 (2017), p. 2.

[6] Alexander Borisov and Ilya V Veksler. “Immiscible silicate liquids: K and Fe distribution as a test for chemical equilibrium and insight into the kinetics of magma unmixing”. In: *Contributions to Mineralogy and Petrology* 176.6 (2021), pp. 1–11.

[7] Ted E Bunch et al. “Very high-temperature impact melt products as evidence for cosmic airbursts and impacts 12,900 years ago”. In: *Proceedings of the National Academy of Sciences* 109.28 (2012), E1903–E1912.

[8] WS Cassata et al. “When the dust settles: stable xenon isotope constraints on the formation of nuclear fallout”. In: *Journal of environmental radioactivity* 137 (2014), pp. 88–95.

[9] Raymond B Cattell. “The scree test for the number of factors”. In: *Multivariate behavioral research* 1.2 (1966), pp. 245–276.

[10] Long-Qing Chen. “Phase-field models for microstructure evolution”. In: *Annual review of materials research* 32.1 (2002), pp. 113–140.

[11] G. Cliff and G. W. Lorimer. "The quantitative analysis of thin specimens". In: *Journal of Microscopy* 103.2 (1975), pp. 203–207. DOI: `https://doi.org/10.1111/j.1365-2818.1975.tb03895.x`. eprint: `https://onlinelibrary.wiley.com/doi/pdf/10.1111/j.1365-2818.1975.tb03895.x`. URL: `https://onlinelibrary.wiley.com/doi/abs/10.1111/j.1365-2818.1975.tb03895.x`.

[12] National Research Council et al. "A review of the dose reconstruction program of the Defense Threat Reduction Agency". In: (2003).

[13] Glenn R Crocker, Joseph D O'Connor, and Edward C Freiling. *Physical and radiochemical properties of fallout particles*. Tech. rep. Naval Radiological Defense Lab., San Francisco, Calif., 1965.

[14] Y. Dardnne, W. Parker, and K Knight. "Chemical fractionation is not a constant: revisiting bomb vapor chemistry". In: *Combating Weapons of Mass Destruction Journal* 21 (2020), pp. 59–71.

[15] Patrick H Donohue et al. "Nuclear forensic applications involving high spatial resolution analysis of Trinitite cross-sections". In: *Journal of Radioanalytical and Nuclear Chemistry* 306.2 (2015), pp. 457–467.

[16] G Nelson Eby et al. "Trinitite redux: Mineralogy and petrology". In: *American Mineralogist* 100.2-3 (2015), pp. 427–441.

[17] Ray F. Egerton. *Physical principles of electron microscopy*. Springer, 2005. URL: `http://link.springer.com/content/pdf/10.1007/978-3-319-39877-8.pdf` (visited on 09/06/2017).

[18] *Eigenvector Research Incorporated*. `https://eigenvector.com/software/`. Accessed: 2022-06-02.

[19] NH Farlow and WR Schell. *Physical, Chemical, and Radiological Properties of Slurry Particulate Fallout Collected During Operation Redwing*. Tech. rep. Naval Radiological Defense Lab., San Francisco, 1957.

[20] Marc A Fitzgerald et al. "Interpreting mixing relationships in energetic melts to estimate vapor contribution and composition". In: *Chemical Geology* 507 (2019), pp. 96–119.

[21] Marc Alan Fitzgerald. "Mechanisms for the Incorporation and Distribution of Radionuclides in Near-Surface Fallout". PhD thesis. University of Nevada, Las Vegas, 2018.

[22] ME Fleet. "The structure of magnetite". In: *Acta Crystallographica Section B: Structural Crystallography and Crystal Chemistry* 37.4 (1981), pp. 917–920.

[23] E. C. Freiling. "Radionuclide Fractionation in Bomb Debris". In: *Science* 133.3469 (1961), pp. 1991–1998. ISSN: 0036-8075. DOI: `10.1126/science.133.3469.1991`. eprint: `https://science.sciencemag.org/content/133/3469/1991.full.pdf`. URL: `https://science.sciencemag.org/content/133/3469/1991`.

[24] EDWARD C Freiling, GLENN R Crocker, and CHARLES E Adams. “Nuclear debris formation”. In: *Radioactive fallout from nuclear weapons tests. Proceedings of an USAEC Conference. Washington, DC: US Atomic Energy Commission.* 1965, pp. 1–41.

[25] Edward C Freiling and Michael A Kay. “Radionuclide fractionation in air-burst debris”. In: *Nature* 209.5020 (1966), pp. 236–238.

[26] Christopher A Fry. “3D laser imaging and modeling of iron meteorites and tektites”. PhD thesis. Carleton University, 2013.

[27] Neal B Gallagher et al. “Curve resolution for multivariate images with applications to TOF-SIMS and Raman”. In: *Chemometrics and intelligent laboratory systems* 73.1 (2004), pp. 105–117.

[28] Raynald Gauvin. “A universal equation for the emission range of X rays from bulk specimens”. In: *Microscopy and Microanalysis* 13.5 (2007), pp. 354–357.

[29] Tim Genda et al. “Iron-rich microstructure records of high temperature multi-component silicate melt behavior in nuclear fallout”. In: *Journal of Environmental Radioactivity* 237 (2021), p. 106700. ISSN: 0265-931X. DOI: `https://doi.org/10.1016/j.jenvrad.2021.106700`. URL: `https://www.sciencedirect.com/science/article/pii/S0265931X21001727`.

[30] TP Genda et al. *Phase Formation in Nuclear Fallout.* Tech. rep. Lawrence Livermore National Lab.(LLNL), Livermore, CA (United States), 2020.

[31] Daniele Giordano, James K Russell, and Donald B Dingwell. “Viscosity of magmatic liquids: a model”. In: *Earth and Planetary Science Letters* 271.1-4 (2008), pp. 123–134.

[32] BP Glass et al. “Atomic bomb glass beads: Tektite and microtektite analogs”. In: *Proceedings of the Second International Conference on Natural Glasses.* Charles University Prague. 1987, pp. 361–369.

[33] Samuel Glasstone, Philip J Dolan, et al. *The effects of nuclear weapons.* Vol. 50. 3. US Department of Defense, 1977.

[34] Azadeh Golshan et al. “A review of recent methods for the determination of ranges of feasible solutions resulting from soft modelling analyses of multivariate data”. In: *Analytica Chimica Acta* 911 (2016), pp. 1–13.

[35] Christopher Hamann et al. “Silicate liquid immiscibility in impact melts”. In: *Meteoritics & Planetary Science* 53.8 (2018), pp. 1594–1632.

[36] Robert E Heft. “The Characterization of Radioactive Particles from Nuclear Weapons Tests”. In: ACS Publications, 1970.

[37] Pierre Hudon and Don R Baker. “The nature of phase separation in binary oxide melts and glasses. I. Silicate systems”. In: *Journal of Non-Crystalline Solids* 303.3 (2002), pp. 299–345.

[38] Yuri A Izrael. *Radioactive fallout after nuclear explosions and accidents.* Elsevier, 2002.

[39] Vadim S Kamenetsky et al. "Magma chamber–scale liquid immiscibility in the Siberian Traps represented by melt pools in native iron". In: *Geology* 41.10 (2013), pp. 1091–1094.

[40] Larry Kaufman and Harold Bernstein. "Computer calculation of phase diagrams. With special reference to refractory metals". In: (1970).

[41] AB Kersting et al. "Migration of plutonium in ground water at the Nevada Test Site". In: *Nature* 397.6714 (1999), pp. 56–59.

[42] JE Klovan and AT Miesch. "Extended CABFAC and QMODEL computer programs for Q-mode factor analysis of compositional data". In: *Computers & Geosciences* 1.3 (1976), pp. 161–178.

[43] Kim Knight. *Fallout bulk chemistry dissolution data, personal communication.*

[44] Batikan Koroglu et al. "Gas phase chemical evolution of uranium, aluminum, and iron oxides". In: *Scientific reports* 8.1 (2018), pp. 1–15.

[45] Henry Lehmann. "Investigation of the matrix effect of Mg, Si, Ca, Sc, Fe, Y, La and Lu in pyroxene composition synthetic silicate glasses by ion microprobe". In: *Geostandards Newsletter* 27.1 (2003), pp. 99–117.

[46] LA Lewis et al. "Spatially-resolved analyses of aerodynamic fallout from a uranium-fueled nuclear test". In: *Journal of environmental radioactivity* 148 (2015), pp. 183–195.

[47] Laurence Lewis. "The origin of agglomerates and their role in forming near-surface glassy fallout". PhD thesis. University of California, Berkeley, 2018.

[48] Gary Lofgren. "Experimentally produced devitrification textures in natural rhyolitic glass". In: *Geological Society of America Bulletin* 82.1 (1971), pp. 111–124.

[49] S. Lukashenko et al. "Radioactive particles released from different sources in the Semipalatinsk Test Site". In: *Journal of Environmental Radioactivity* 216 (2020), p. 106160. ISSN: 0265-931X. DOI: `https://doi.org/10.1016/j.jenvrad.2020.106160`. URL: `http://www.sciencedirect.com/science/article/pii/S0265931X19304588`.

[50] BC Luo, XR Liu, and B Wei. "Macroscopic liquid phase separation of Fe–Sn immiscible alloy investigated by both experiment and simulation". In: *Journal of Applied Physics* 106.5 (2009), p. 053523.

[51] Yanhong Luo et al. "Coproduction of DRI powder and semi-coke from siderite ore and low rank coal by excessive coal-based direct reduction in rotary kiln". In: *ISIJ International* (2015), ISIJINT–2015.

[52] Aaron J Lussier et al. "Nuclear-blast induced nanotextures in quartz and zircon within Trinitite". In: *American Mineralogist* 102.2 (2017), pp. 445–460.

[53] Huahai Mao and Malin Selleby. "Thermodynamic reassessment of the Si3N4–AlN–Al2O3–SiO2 system—Modeling of the SiAlON and liquid phases". In: *Calphad* 31.2 (2007), pp. 269–280.

[54] Huahai Mao, Malin Selleby, and Bo Sundman. "A re-evaluation of the liquid phases in the CaO–Al2O3 and MgO–Al2O3 systems". In: *Calphad* 28.3 (2004), pp. 307–312.

[55] Charles R Martin. *Fallout fractionation in silicate soils.* Tech. rep. AIR FORCE INST OF TECH WRIGHT-PATTERSONAFB OH SCHOOL OF ENGINEERING, 1983.

[56] Joachim Mayer et al. "TEM Sample Preparation and FIB-Induced Damage". In: *Mrs Bulletin* 32 (2007), pp. 400–407.

[57] CF Miller. *A theory of formation of fallout from land-surface nuclear detonations and decay of the fission products.* Tech. rep. NAVAL RADIOLOGICAL DEFENSE LAB SAN FRANCISCO CA, 1960.

[58] Pepijn G Moerman et al. "Emulsion patterns in the wake of a liquid–liquid phase separation front". In: *Proceedings of the National Academy of Sciences* 115.14 (2018), pp. 3599–3604.

[59] Emily Moore et al. "Thermodynamic study of liquid immiscibility in iron-silicate melt systems: a study of nuclear fallout glass". In: *in prep* (2022).

[60] J t Myers and HP Eugster. "The system Fe-Si-O: Oxygen buffer calibrations to 1,500 K". In: *Contributions to Mineralogy and Petrology* 82.1 (1983), pp. 75–90.

[61] HR Naslund. "The effect of oxygen fugacity on liquid immiscibility in iron-bearing silicate melts". In: *American Journal of Science* 283.10 (1983), pp. 1034–1059.

[62] M. W. Nathans et al. "Particle size distribution in clouds from nuclear airbursts". In: *Journal of Geophysical Research (1896-1977)* 75.36 (1970), pp. 7559–7572. DOI: `https://doi.org/10.1029/JC075i036p07559`. URL: `https://agupubs.onlinelibrary.wiley.com/doi/abs/10.1029/JC075i036p07559`.

[63] J. Norman et al. *Radionuclides in the Environment.* Ed. by E. Freiling. Vol. 93. American Chemical Society, 1970.

[64] John H Norman and Perrin Winchell. *Cloud chemistry of fallout formation.* Tech. rep. GENERAL DYNAMICS SAN DIEGO CA GENERAL ATOMIC DIV, 1967.

[65] Hillyer G Norment. *DELFIC: Department of Defense Fallout Prediction System. Volume I-Fundamentals.* Tech. rep. ATMOSPHERIC SCIENCE ASSOCIATES BEDFORD MA, 1979.

[66] Jamie Nunez et al. "NanoSIMS for biological applications: current practices and analyses". In: *Biointerphases* 13.3 (2018), 03B301.

[67] NEA OECD. *NSC: Thermodynamics of Advanced Fuels- International Database (TAF-ID).*

[68] NEA OECD. *unpublished Al-Fe-O assessment.*

[69] Alejandro C Olivieri. “A down-to-earth analyst view of rotational ambiguity in second-order calibration with multivariate curve resolution- a tutorial”. In: *Analytica Chimica Acta* 1156 (2021), p. 338206.

[70] JI Pacold et al. “Chemical speciation of U, Fe, and Pu in melt glass from nuclear weapons testing”. In: *Journal of Applied Physics* 119.19 (2016), p. 195102.

[71] Tashi Parsons-Davis et al. “Application of modern autoradiography to nuclear forensic analysis”. In: *Forensic science international* 286 (2018), pp. 223–232.

[72] Rocío B Pellegrino Vidal and Alejandro C Olivieri. “A new parameter for measuring the prediction uncertainty produced by rotational ambiguity in second-order calibration with multivariate curve resolution”. In: *Analytical Chemistry* 92.13 (2020), pp. 9118–9123.

[73] Lorenz Ratke and Peter W Voorhees. *Growth and coarsening: Ostwald ripening in material processing*. Springer Science & Business Media, 2002.

[74] Edwin Roedder. “Silicate liquid immiscibility in magmas and in the system K2O-FeO-AI2O3-SiO2: an example of serendipity”. In: *Geochimica et Cosmochimica Acta* 42.11 (1978), pp. 1597–1617.

[75] Edwin Roedder and Paul W Weiblen. “Silicate liquid immiscibility in lunar magmas, evidenced by melt inclusions in lunar rocks”. In: *Science* 167.3918 (1970), pp. 641–644.

[76] Nigel Saunders and A Peter Miodownik. *CALPHAD (calculation of phase diagrams): a comprehensive guide*. Elsevier, 1998.

[77] Caroline A Schneider, Wayne S Rasband, and Kevin W Eliceiri. “NIH Image to ImageJ: 25 years of image analysis”. In: *Nature methods* 9.7 (2012), pp. 671–675.

[78] Malin Selleby. “An assessment of the Ca-Fe-O-Si system”. In: *Metallurgical and Materials Transactions B* 28.4 (1997), pp. 577–596.

[79] Won-Gap Seo and Fumitaka Tsukihashi. “Thermodynamic and structural properties for the FeO–SiO2 system by using molecular dynamics calculation”. In: *Materials transactions* 46.6 (2005), pp. 1240–1247.

[80] RP Shi et al. “Formation mechanisms of self-organized core/shell and core/shell/corona microstructures in liquid droplets of immiscible alloys”. In: *Acta materialia* 61.4 (2013), pp. 1229–1243.

[81] Conxita Solans, Daniel Morales, and Maria Homs. “Spontaneous emulsification”. In: *Current Opinion in Colloid and Interface Science* 22 (2016), pp. 88–93. ISSN: 1359-0294. DOI: `https://doi.org/10.1016/j.cocis.2016.03.002`. URL: `https://www.sciencedirect.com/science/article/pii/S1359029416300309`.

[82] Gregory D Spriggs et al. *Fallout Cloud Regimes*. Tech. rep. Lawrence Livermore National Lab.(LLNL), Livermore, CA (United States), 2020.

[83] K Stewart. “The condensation of a vapour to an assembly of droplets or particles”. In: *Transactions of the Faraday Society* 52 (1956), pp. 161–173.

[84] Per B Storebo. “Formation of radioactivity size distributions in nuclear bomb debris”. In: *Journal of Aerosol Science* 5.6 (1974), pp. 557–577.

[85] Per B. Storebö. “Meteorological Fractionation of Nuclear Bomb Debris”. In: *Tellus* 12.3 (1960), pp. 293–297. DOI: `10.3402/tellusa.v12i3.9400`. URL: `https://doi.org/10.3402/tellusa.v12i3.9400`.

[86] Bo Sundman, HL Lukas, and SG Fries. *Computational thermodynamics: the Calphad method*. Cambridge university press Cambridge, 2007.

[87] Alan B Thompson, Maarten Aerts, and Alistair C Hack. “Liquid immiscibility in silicate melts and related systems”. In: *Reviews in Mineralogy and Geochemistry* 65.1 (2007), pp. 99–127.

[88] Finn Ulff-Moller. “Effects of liquid immiscibility on trace element fractionation in magmatic iron meteorites: A case study of group IIIAB”. In: *Meteoritics & Planetary Science* 33.2 (1998), pp. 207–220.

[89] Ilya V Veksler et al. “Interfacial tension between immiscible liquids in the system K2O-FeO-Fe2O3-Al2O3-SiO2 and implications for the kinetics of silicate melt unmixing”. In: *American Mineralogist* 95.11-12 (2010), pp. 1679–1685.

[90] CP Wang et al. “Formation of core-type macroscopic morphologies in Cu-Fe base alloys with liquid miscibility gap”. In: *Metallurgical and Materials Transactions A* 35.4 (2004), pp. 1243–1253.

[91] E Bruce Watson. “Two-liquid partition coefficients: experimental data and geochemical implications”. In: *Contributions to Mineralogy and Petrology* 56.1 (1976), pp. 119–134.

[92] William J Weber et al. “Radiation effects in glasses used for immobilization of high-level waste and plutonium disposition”. In: *Journal of Materials Research* 12.8 (1997), pp. 1946–1978.

[93] David Weisz. “Mass Transport of Condensed Species in Aerodynamic Fallout Glass from a Near-Surface Nuclear Test”. PhD thesis. University of California, Berkeley, 2016.

[94] David G Weisz et al. “Diffusive mass transport in agglomerated glassy fallout from a near-surface nuclear test”. In: *Geochimica et Cosmochimica Acta* 223 (2018), pp. 377–388.

[95] Svante Wold. “Cross-validatory estimation of the number of components in factor and principal components models”. In: *Technometrics* 20.4 (1978), pp. 397–405.

[96] Youxue Zhang, Juleen Jenkins, and Zhengjiu Xu. “Kinetics of the reaction H2O+ O$\rightarrow$ 2 2OH in rhyolitic glasses upon cooling: Geospeedometry and comparison with glass transition”. In: *Geochimica et Cosmochimica Acta* 61.11 (1997), pp. 2167–2173.

Appendix A

Sample Optical and SEM Images

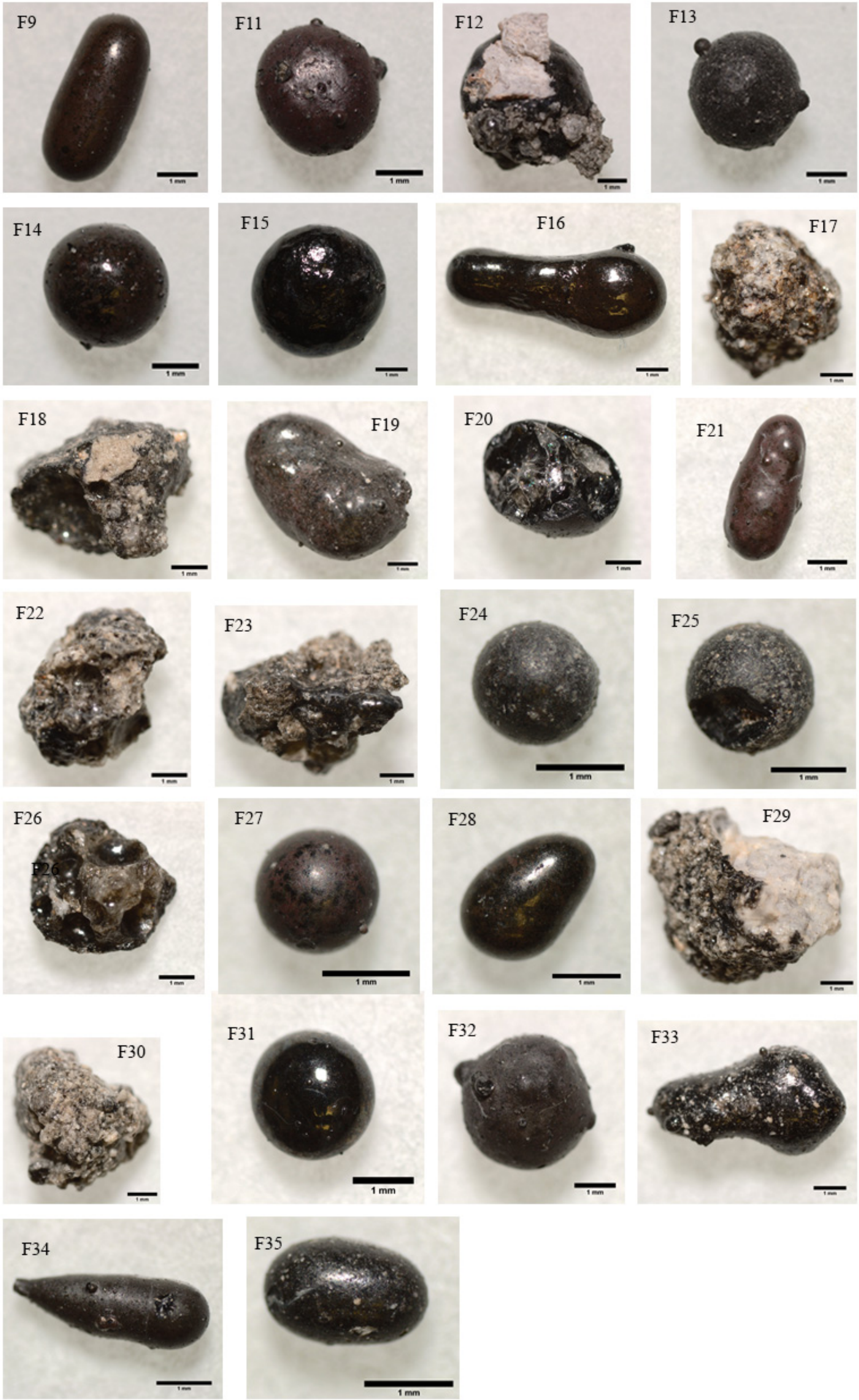

Figure A.1: Optical images of all samples in this study

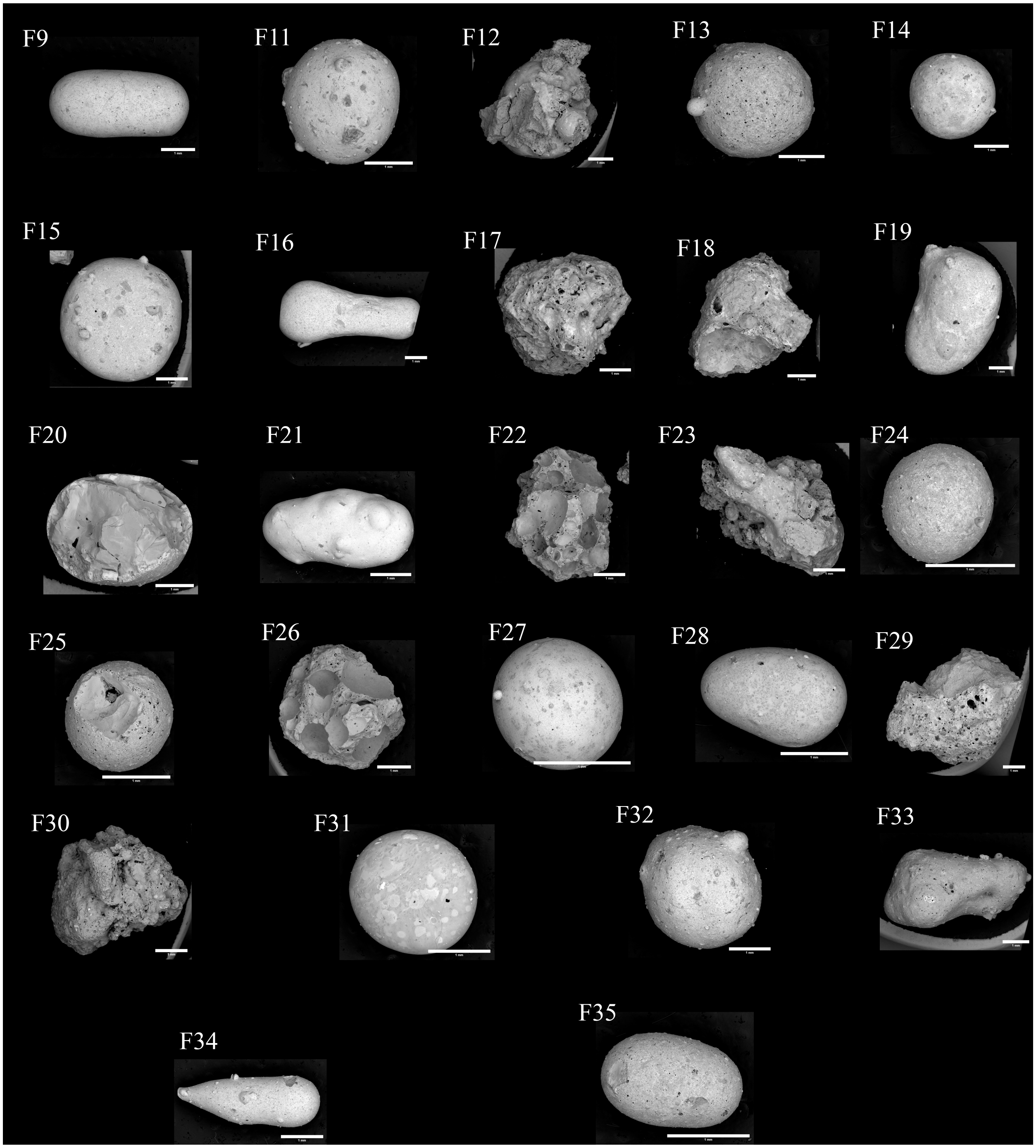

Figure A.2: BSE images of all samples mounted on sticky tape. Each image is scaled for contrast, so contrast is not comparable between different images.

Appendix B

Qualitative SEM EDS Maps

The figures below are qualitative SEM EDS maps each collected using 1 hour rasters over the exposed cross sections of samples. Element images only reflect relative distribution of each element within a sample since they are not scaled to each other. A subset of these samples were selected for longer semi-quantitative 12 hour maps which are shown in Appendix C.

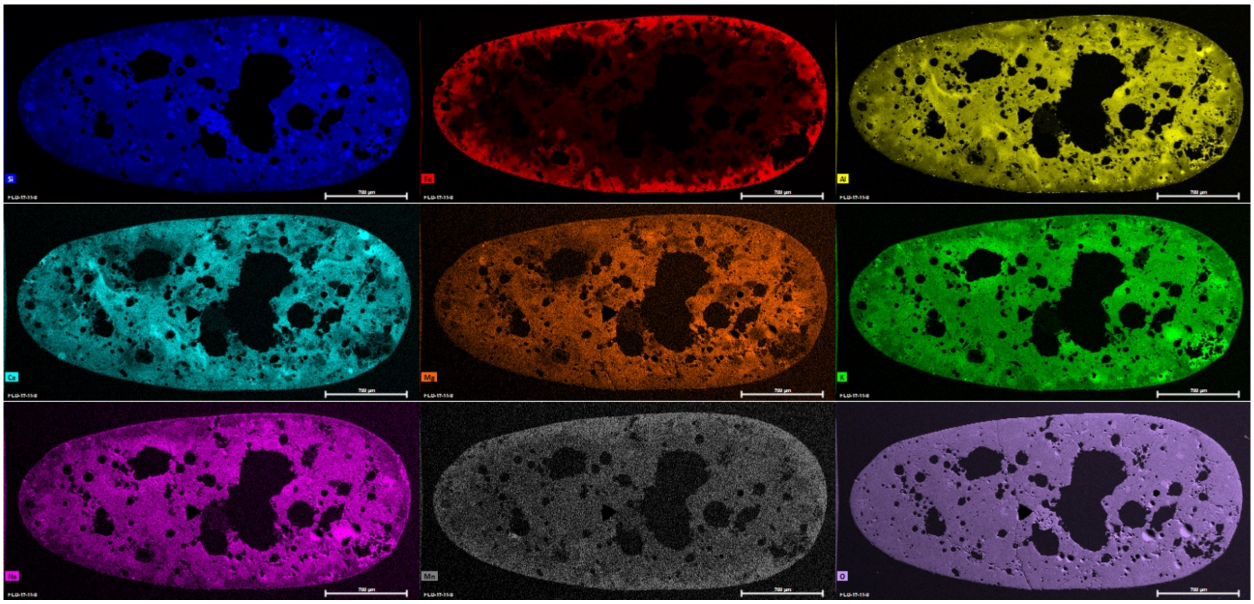

Figure B.1: Sample F9 EDS Maps

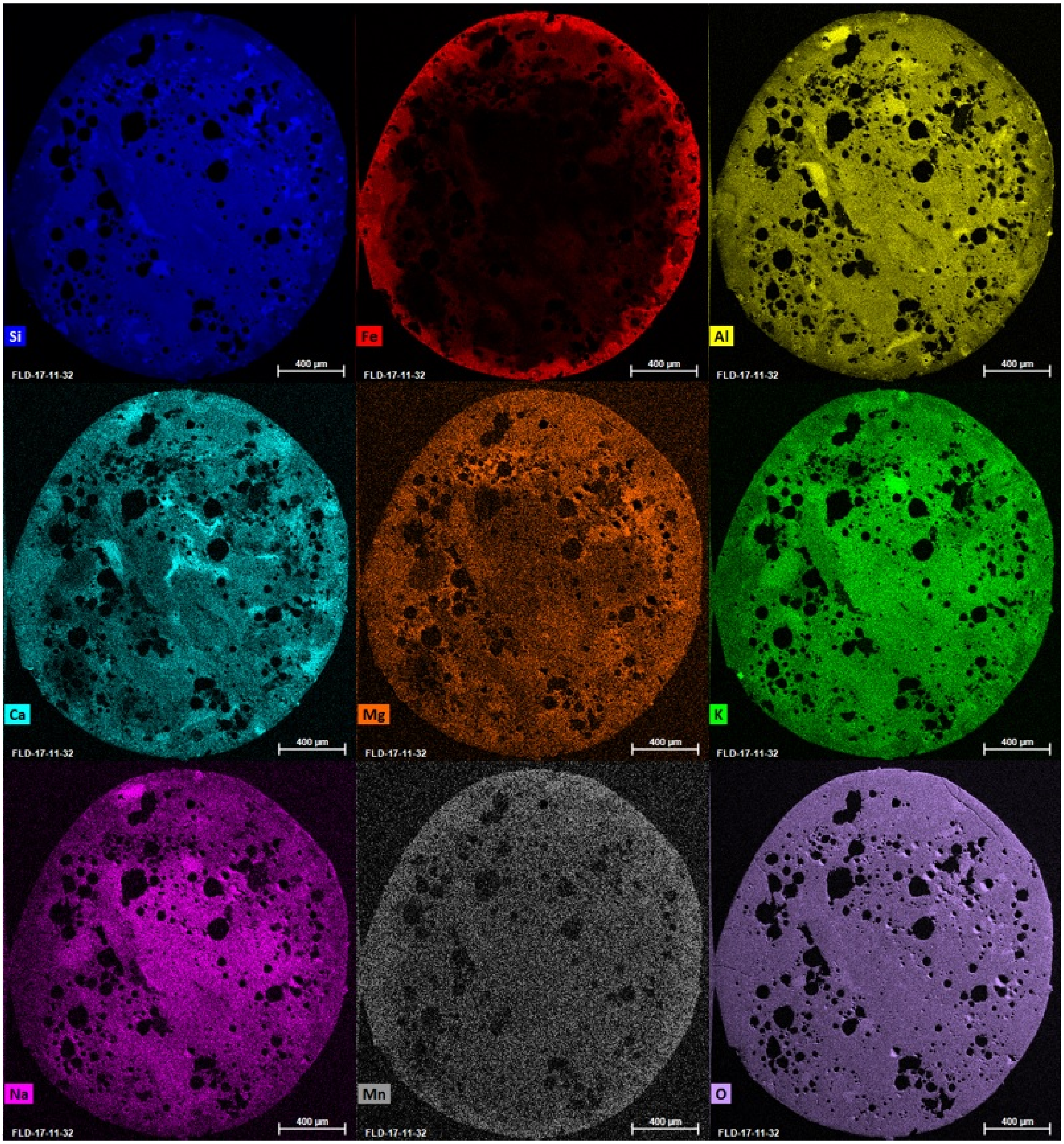

Figure B.2: Sample F11 EDS Maps

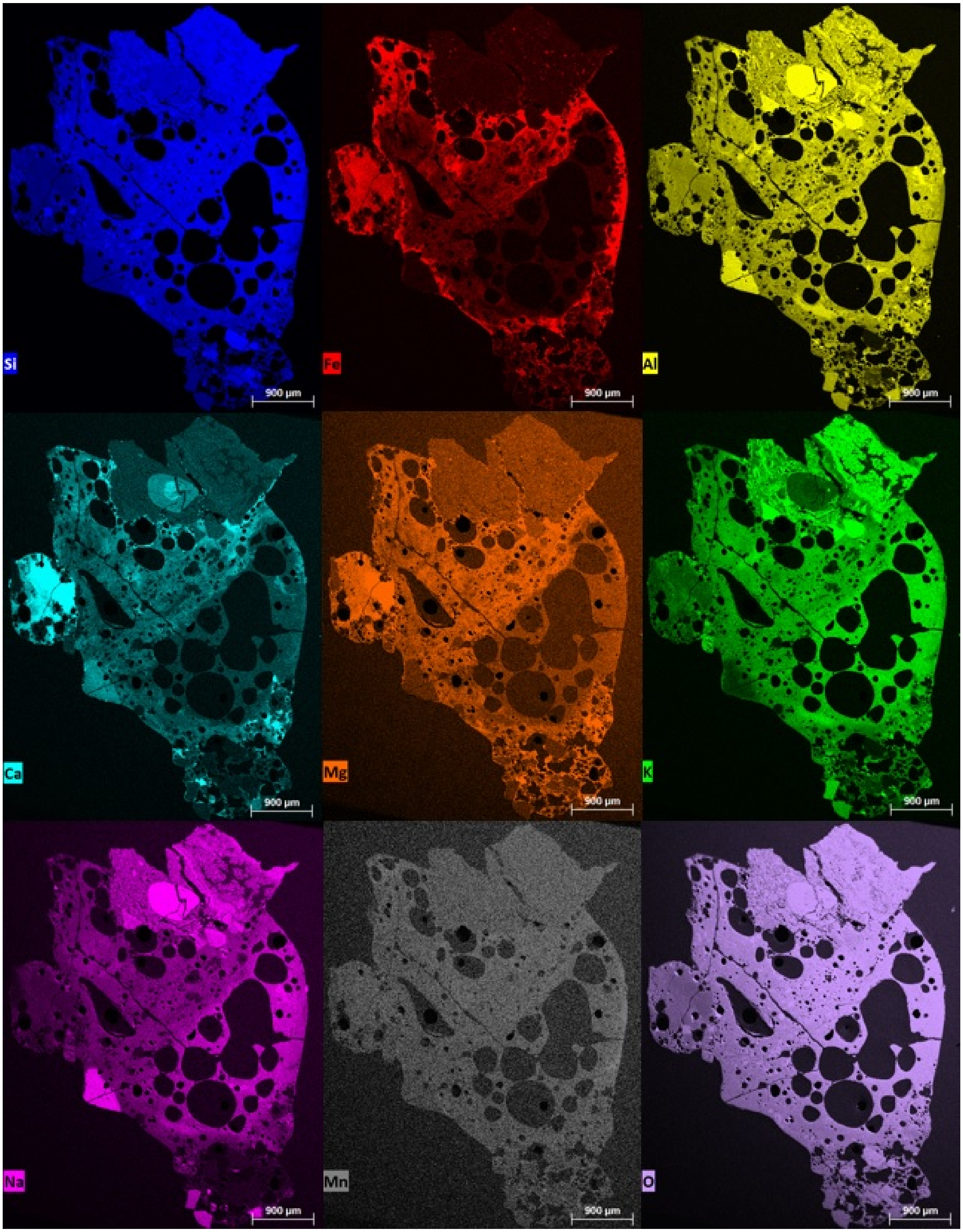

Figure B.3: Sample F12 EDS Maps

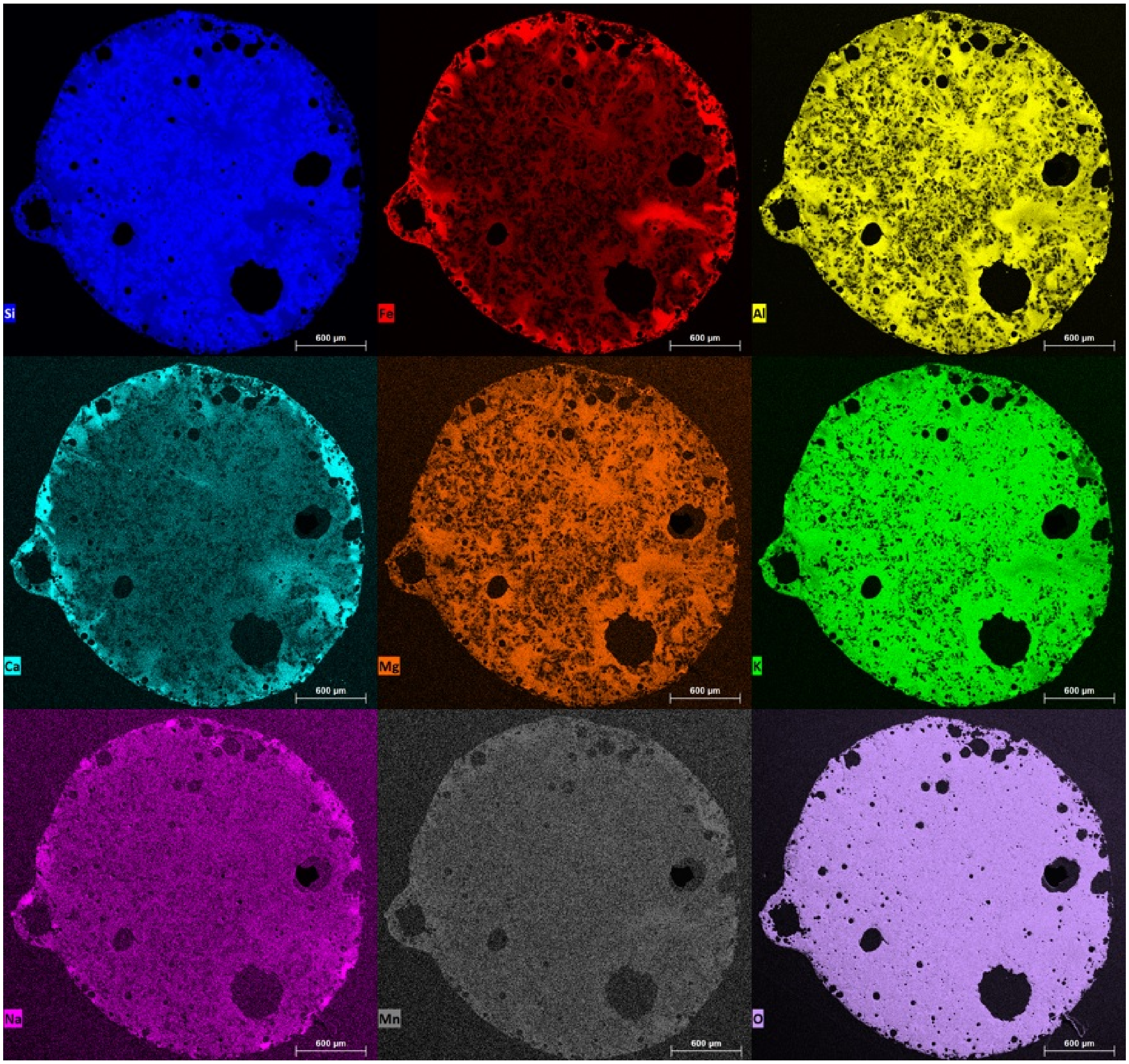

Figure B.4: Sample F13 EDS Maps

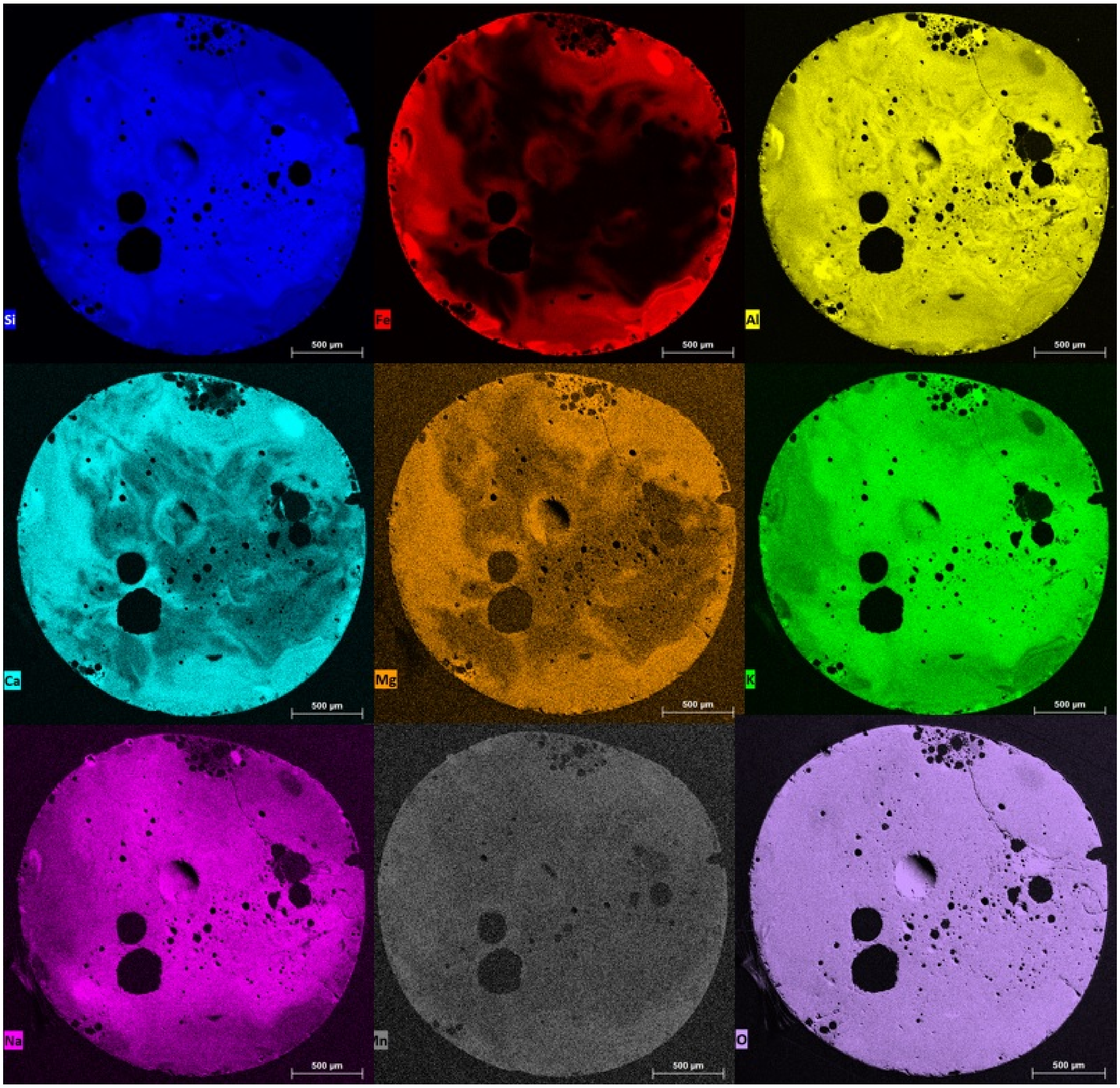

Figure B.5: Sample F14 EDS Maps

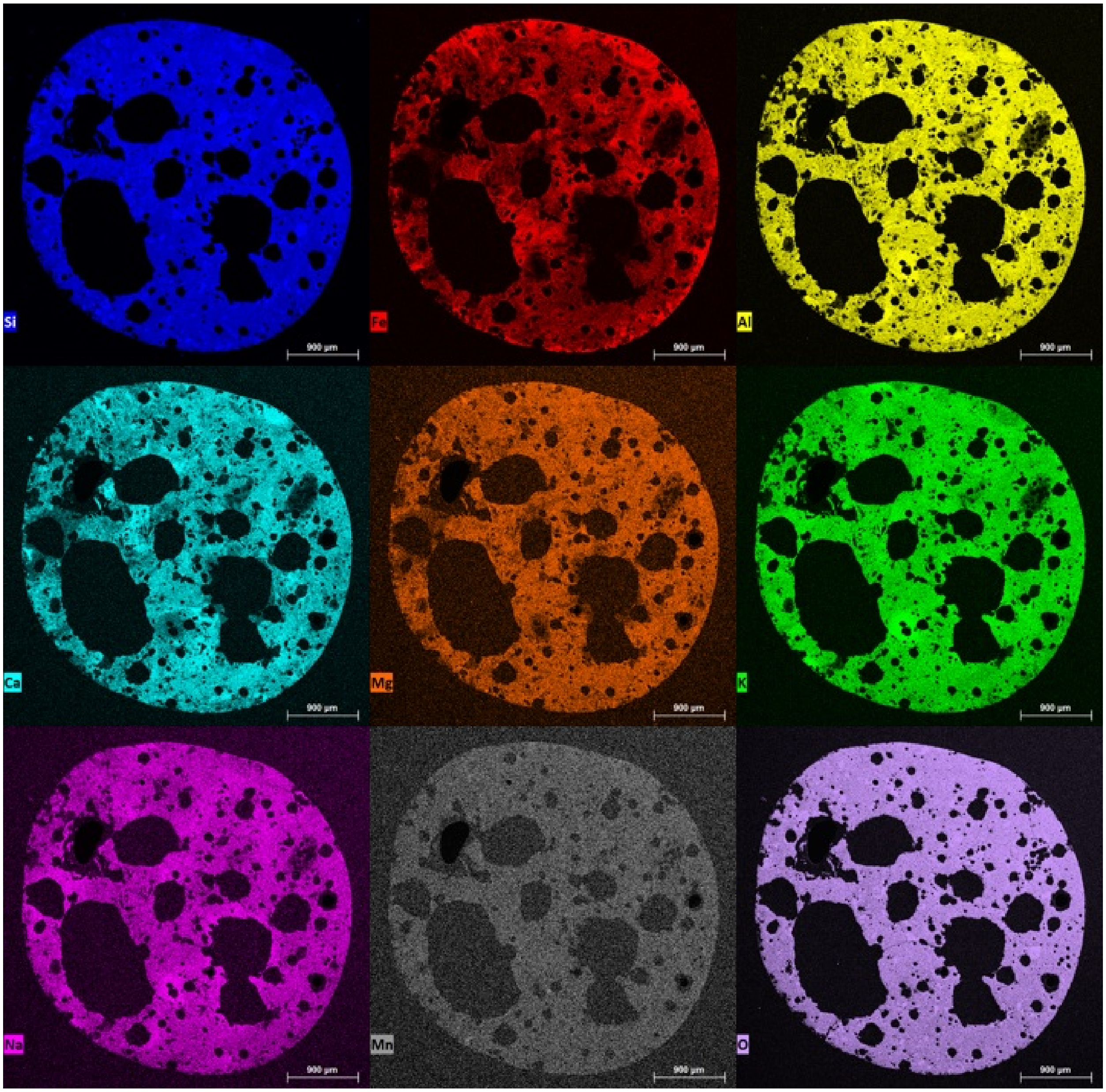

Figure B.6: Sample F15 EDS Maps

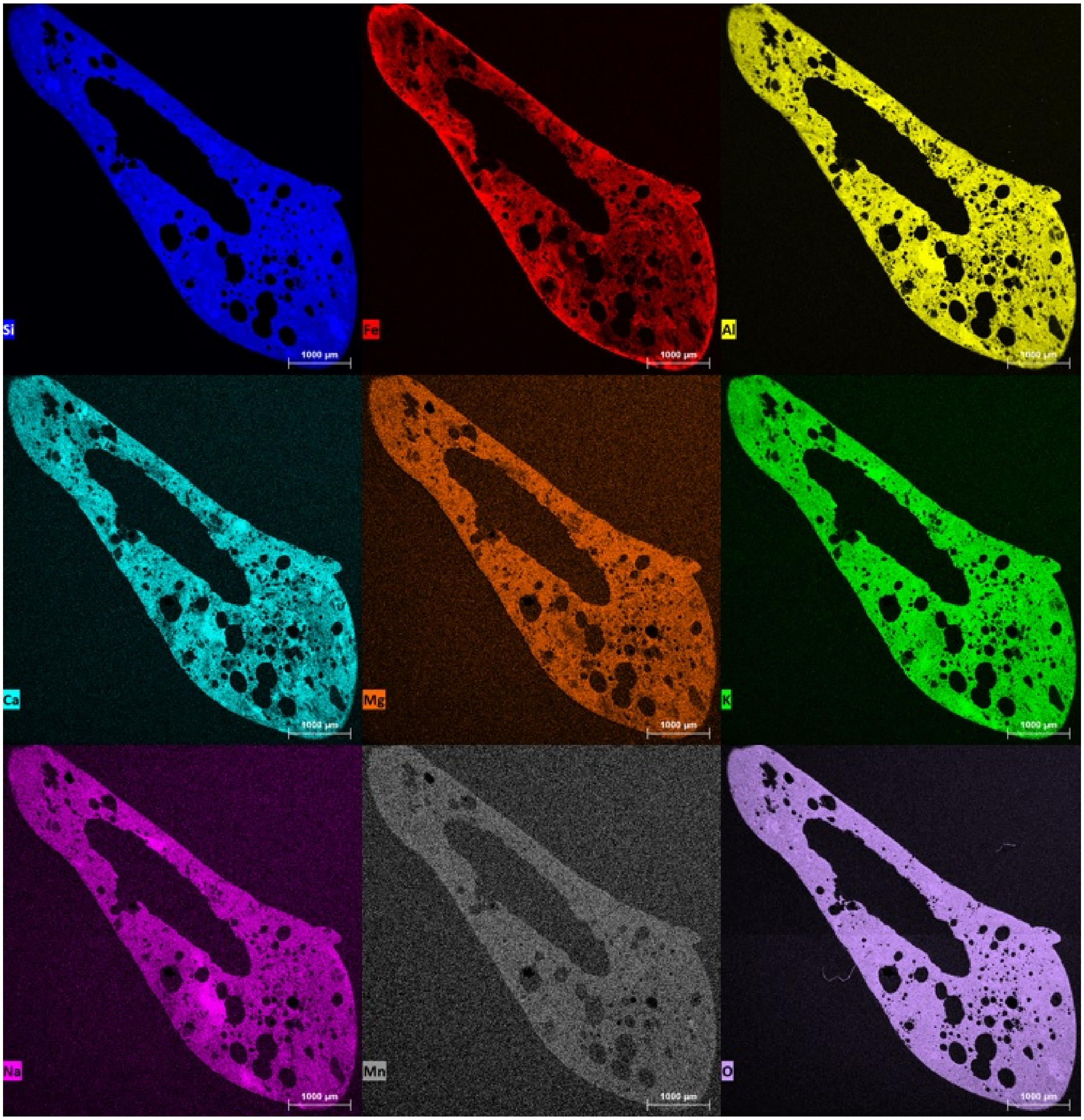

Figure B.7: Sample F16 EDS Maps

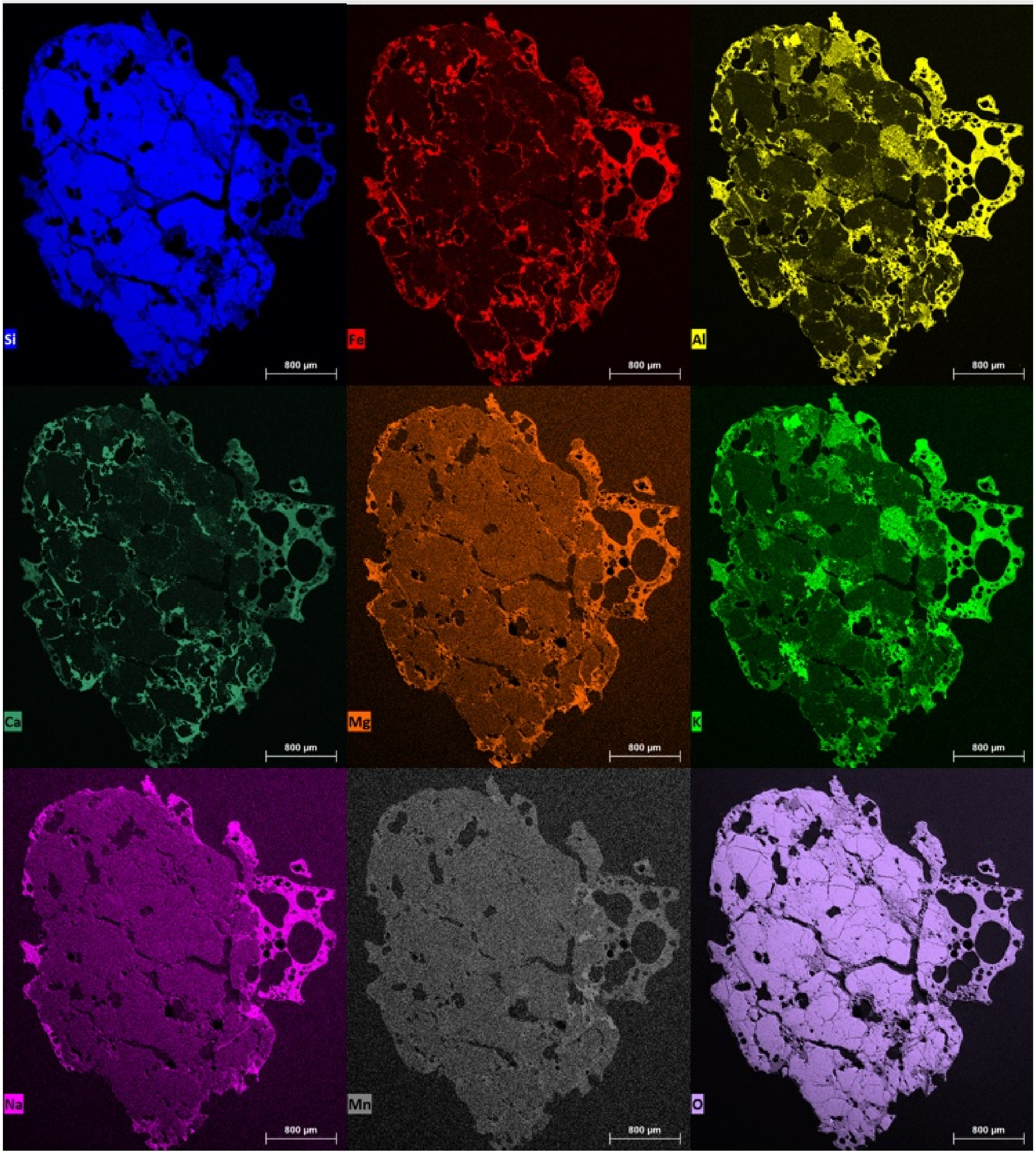

Figure B.8: Sample F17 EDS Maps

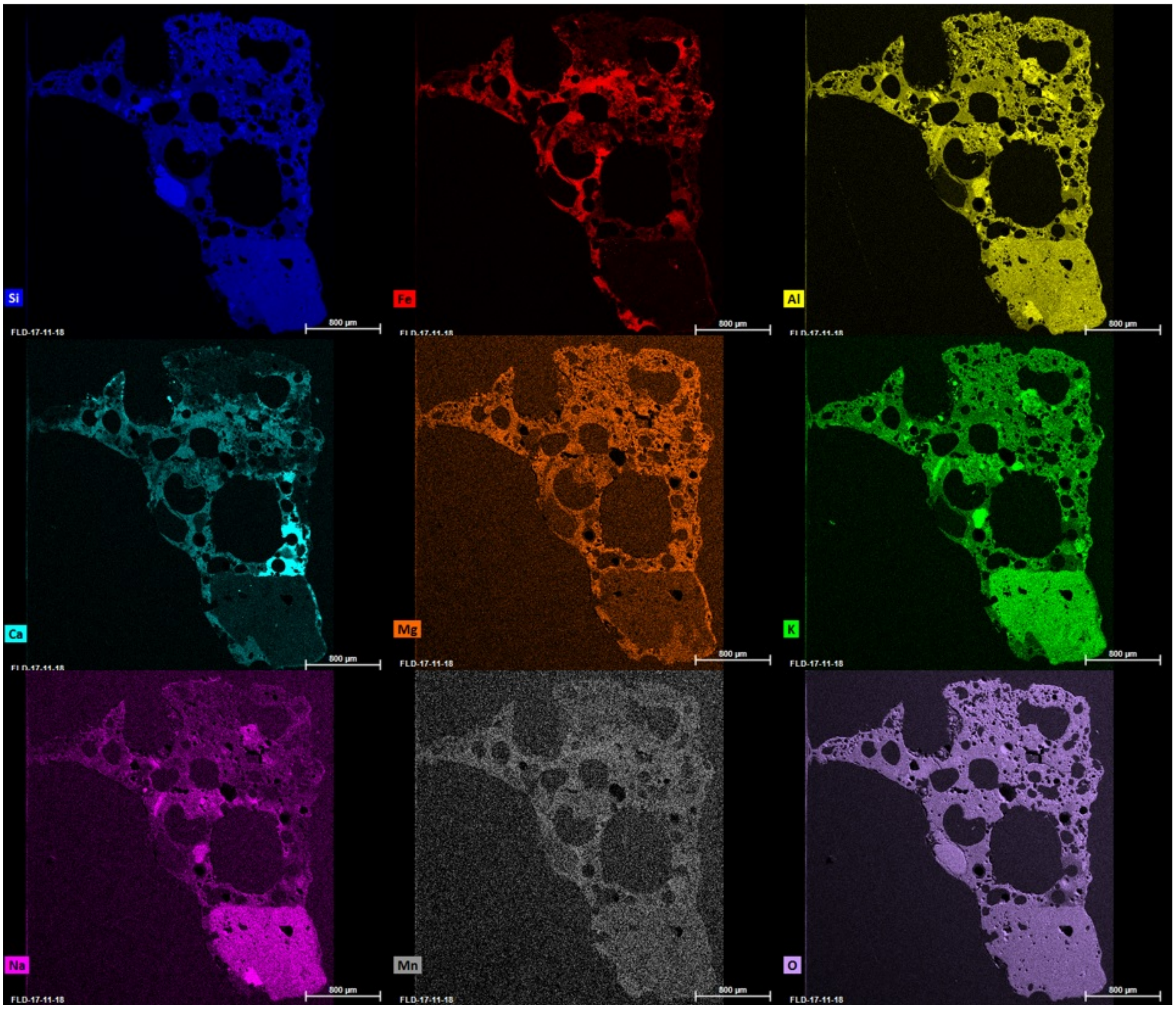

Figure B.9: Sample F18 EDS Maps

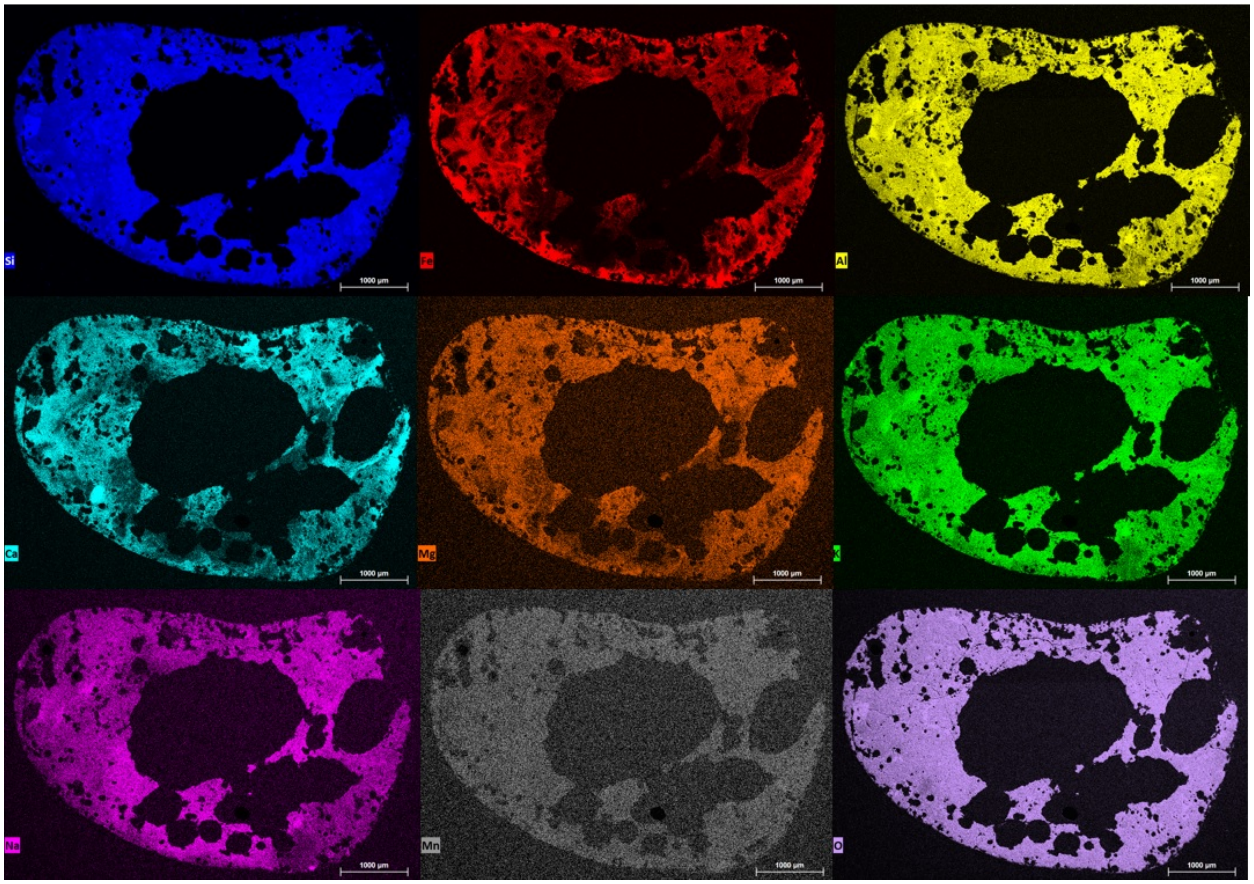

Figure B.10: Sample F19 EDS Maps

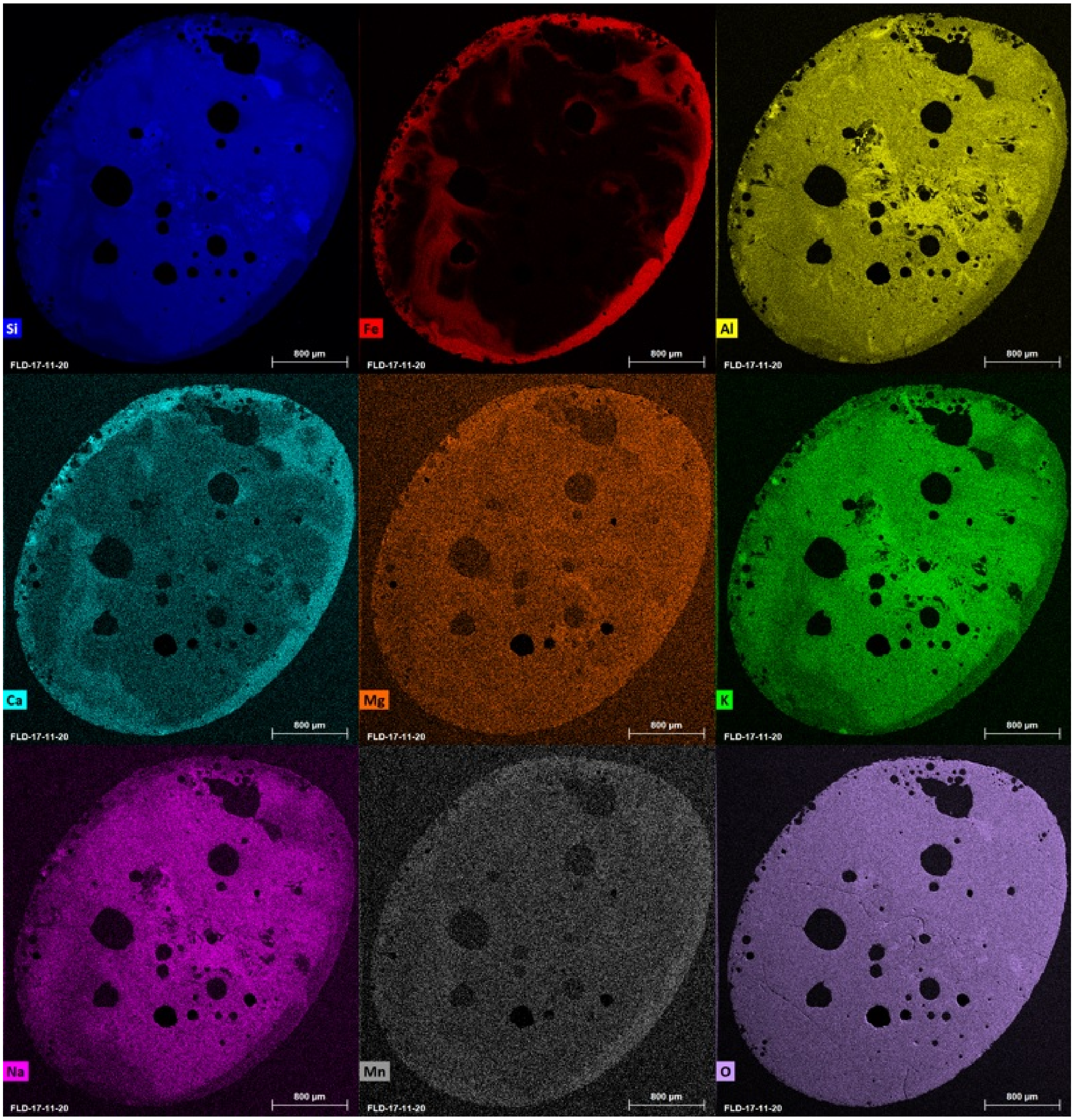

Figure B.11: Sample F20 EDS Maps

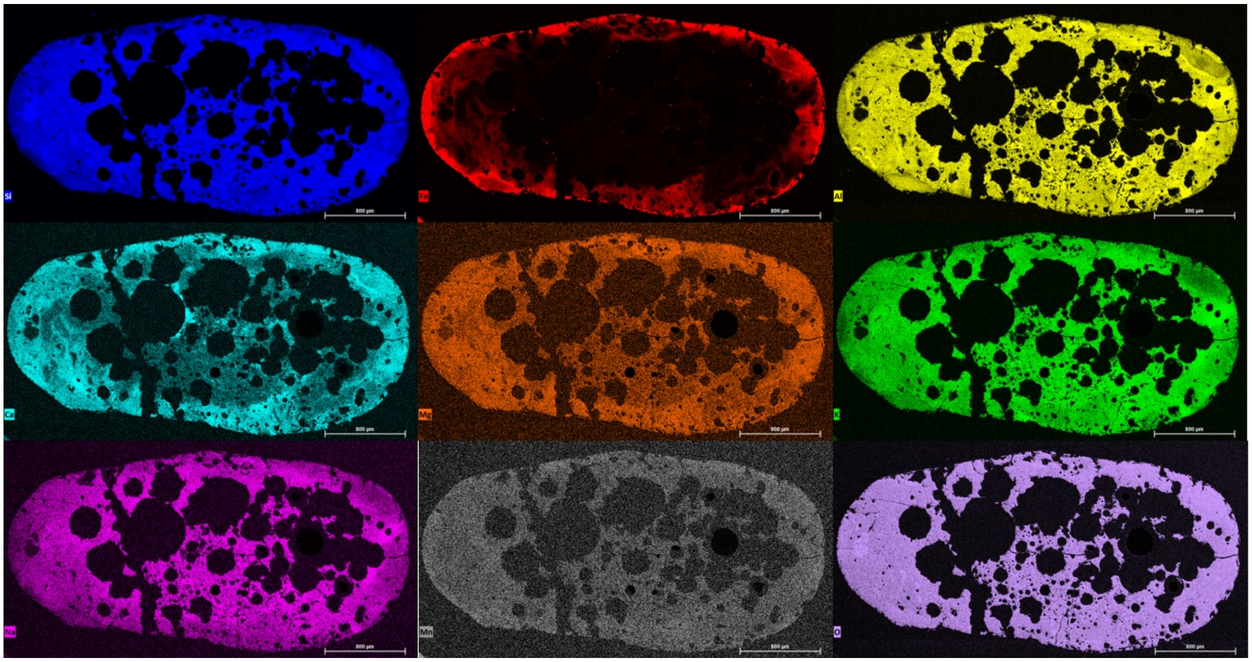

Figure B.12: Sample F21 EDS Maps

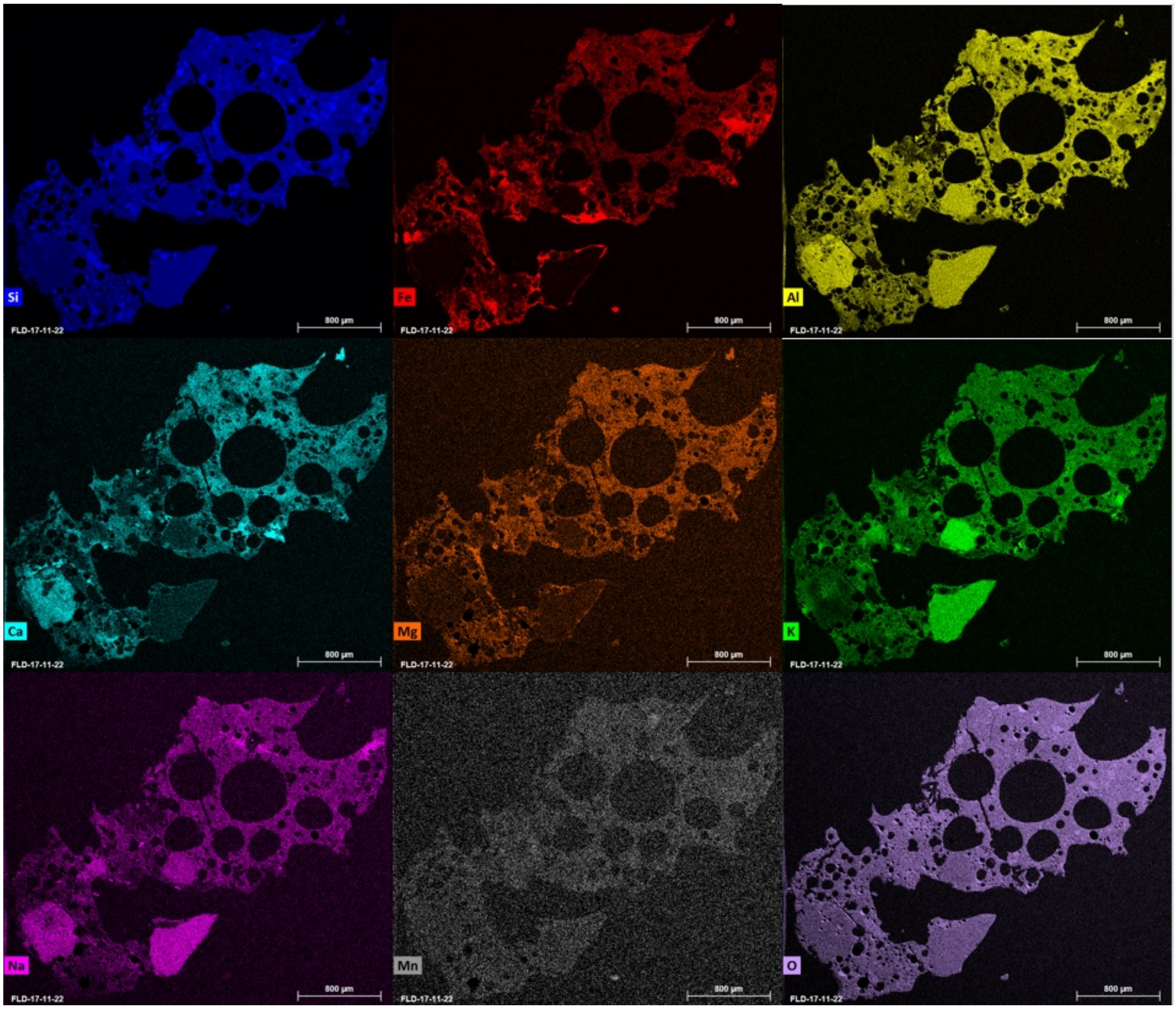

Figure B.13: Sample F22 EDS Maps

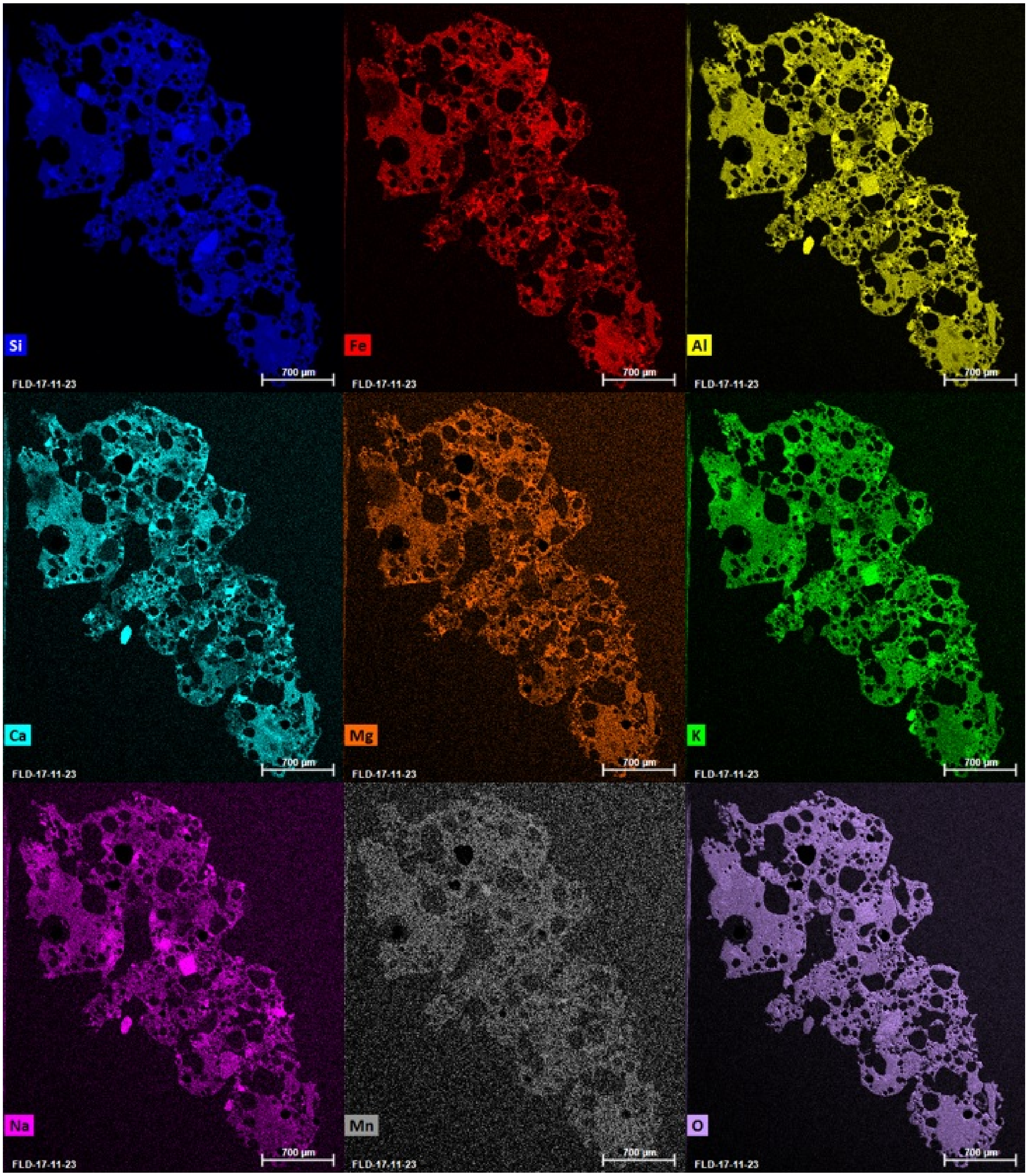

Figure B.14: Sample F23 EDS Maps

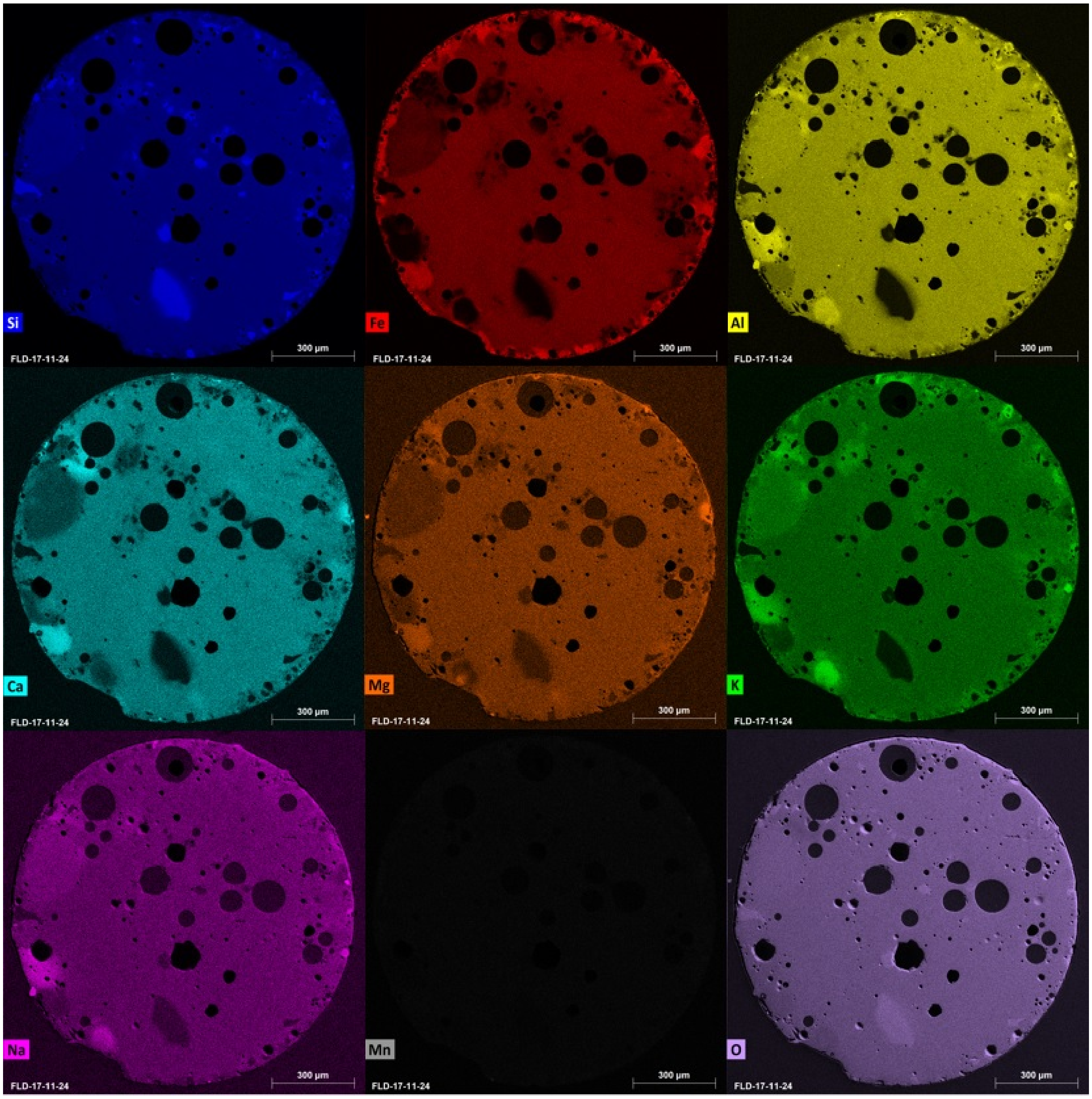

Figure B.15: Sample F24 EDS Maps

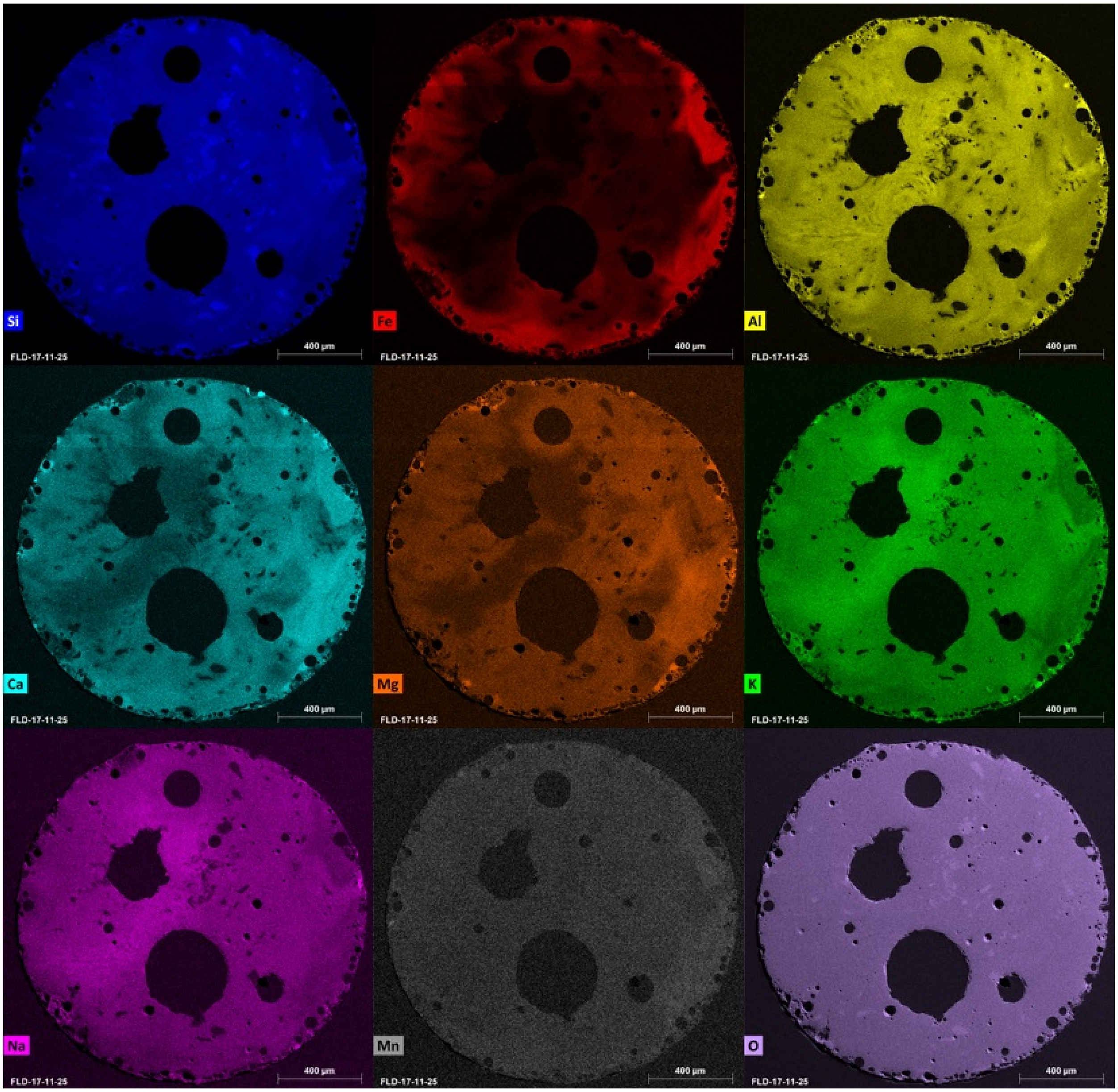

Figure B.16: Sample F25 EDS Maps

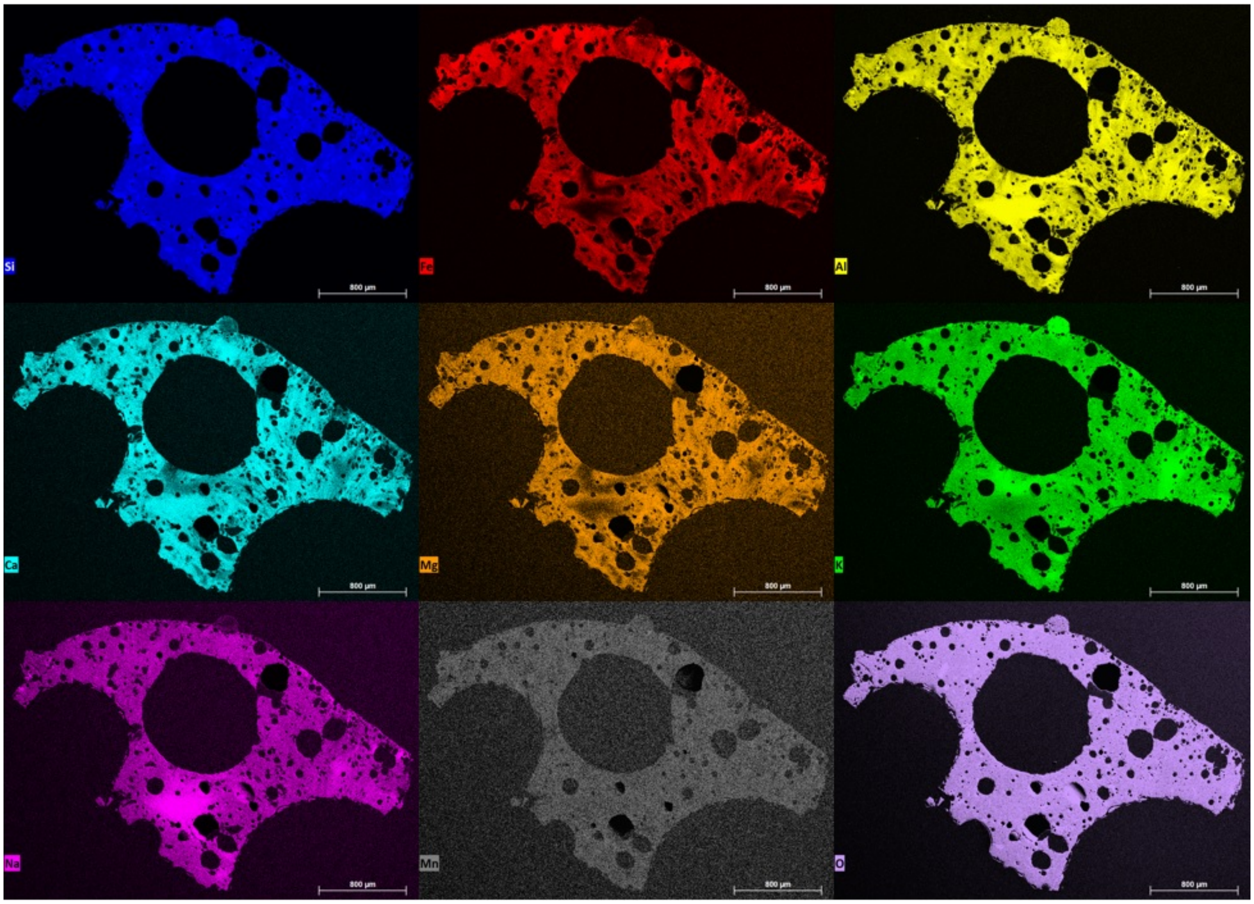

Figure B.17: Sample F26 EDS Maps

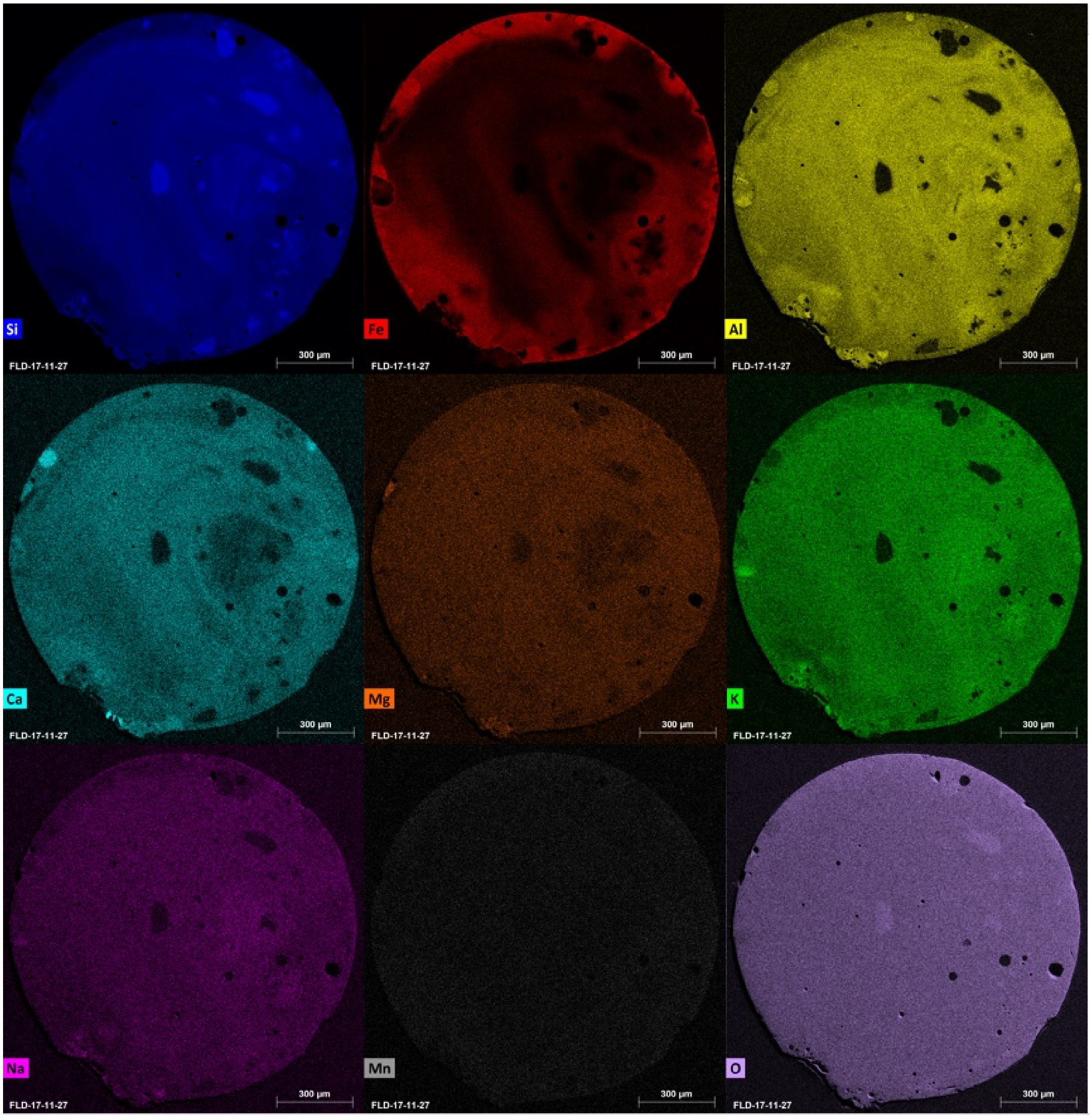

Figure B.18: Sample F27 EDS Maps

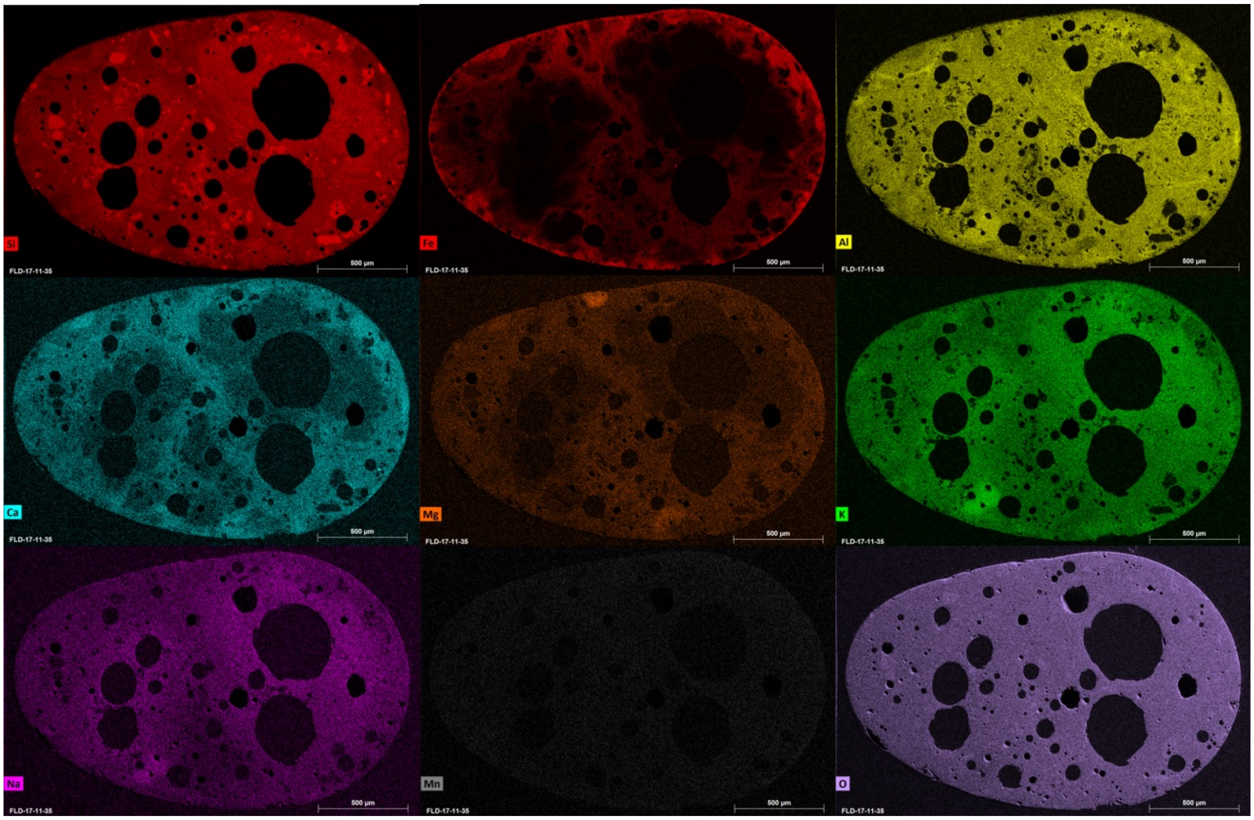

Figure B.19: Sample F28 EDS Maps

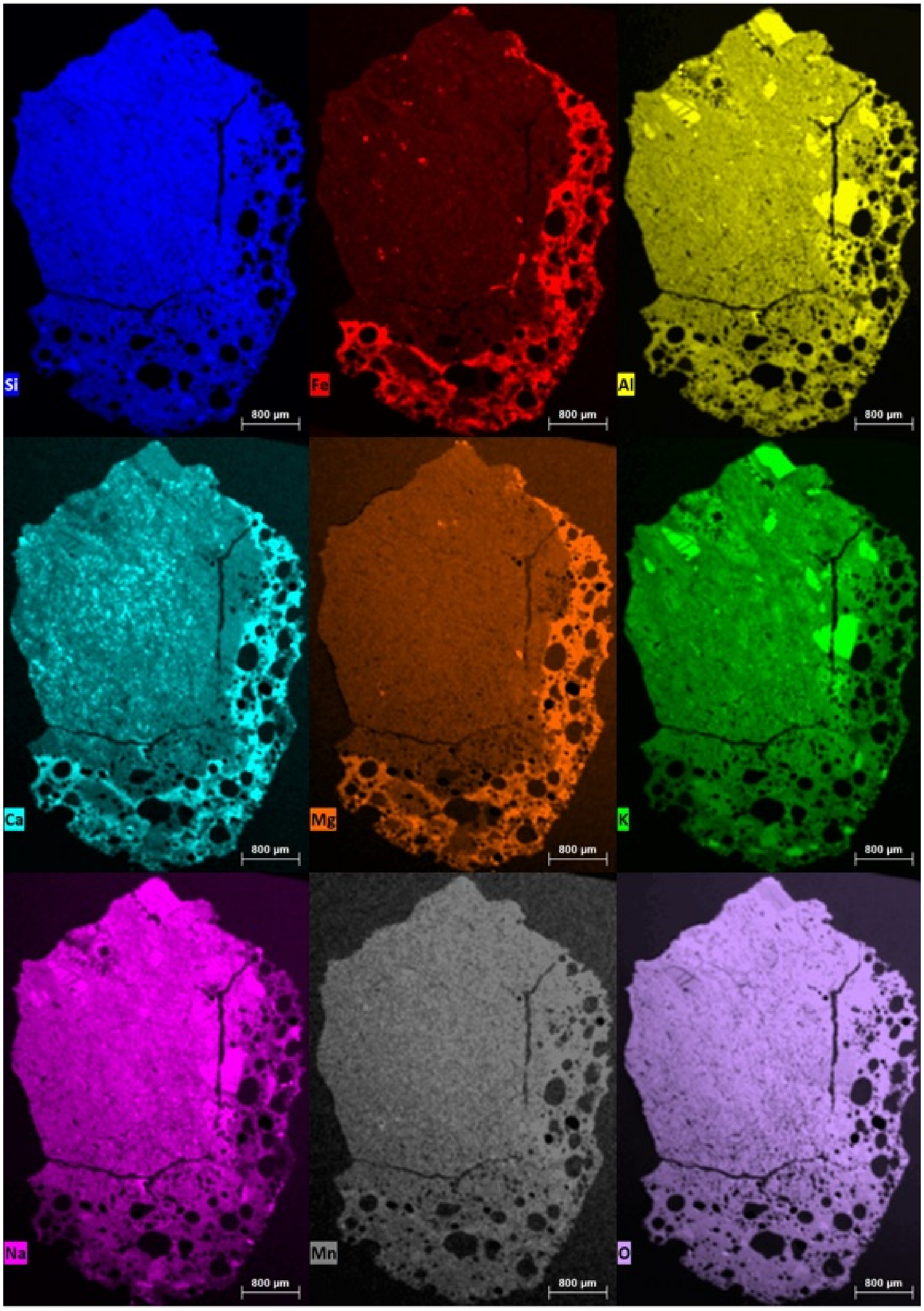

Figure B.20: Sample F29 EDS Maps

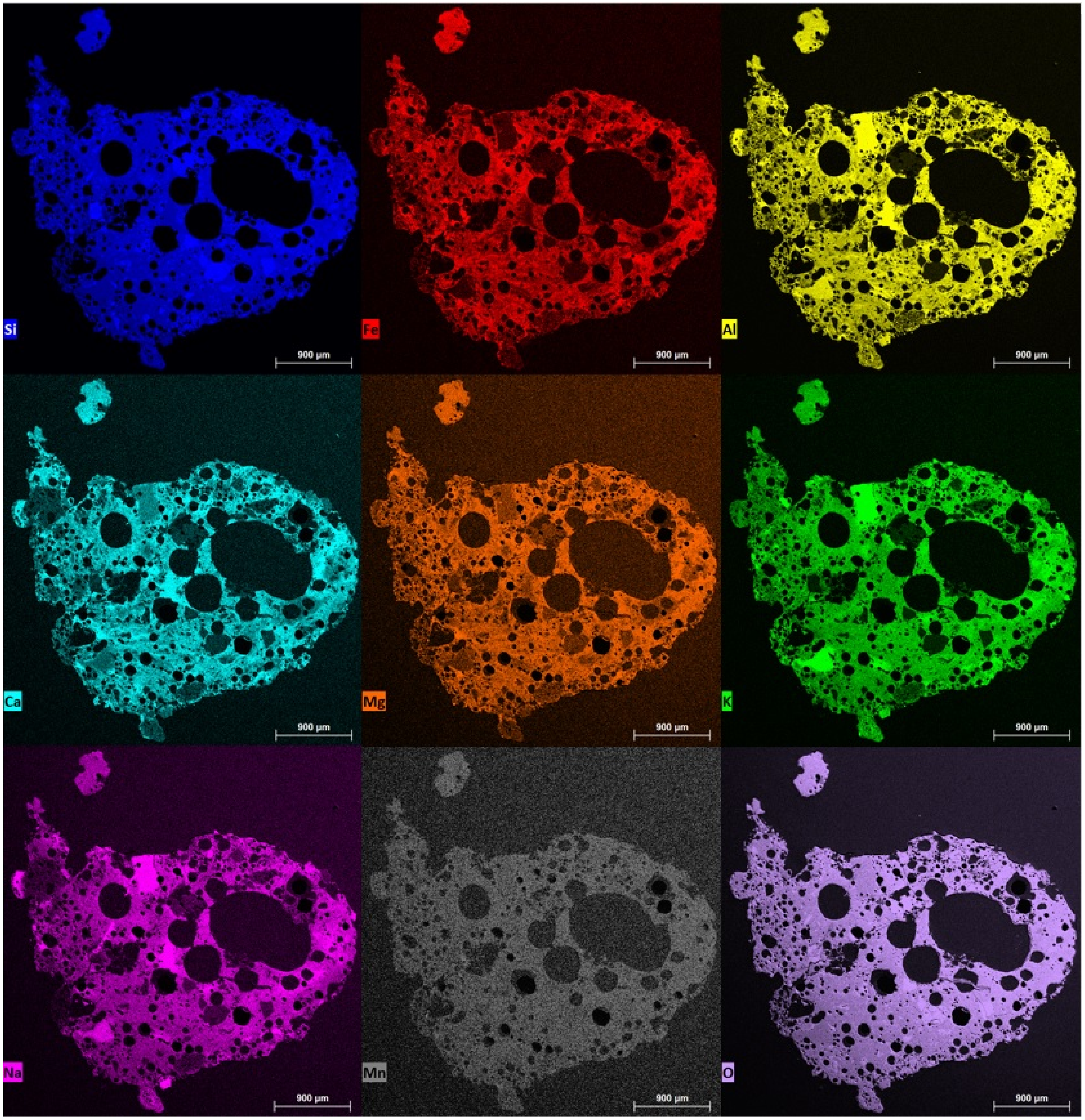

Figure B.21: Sample F30 EDS Maps

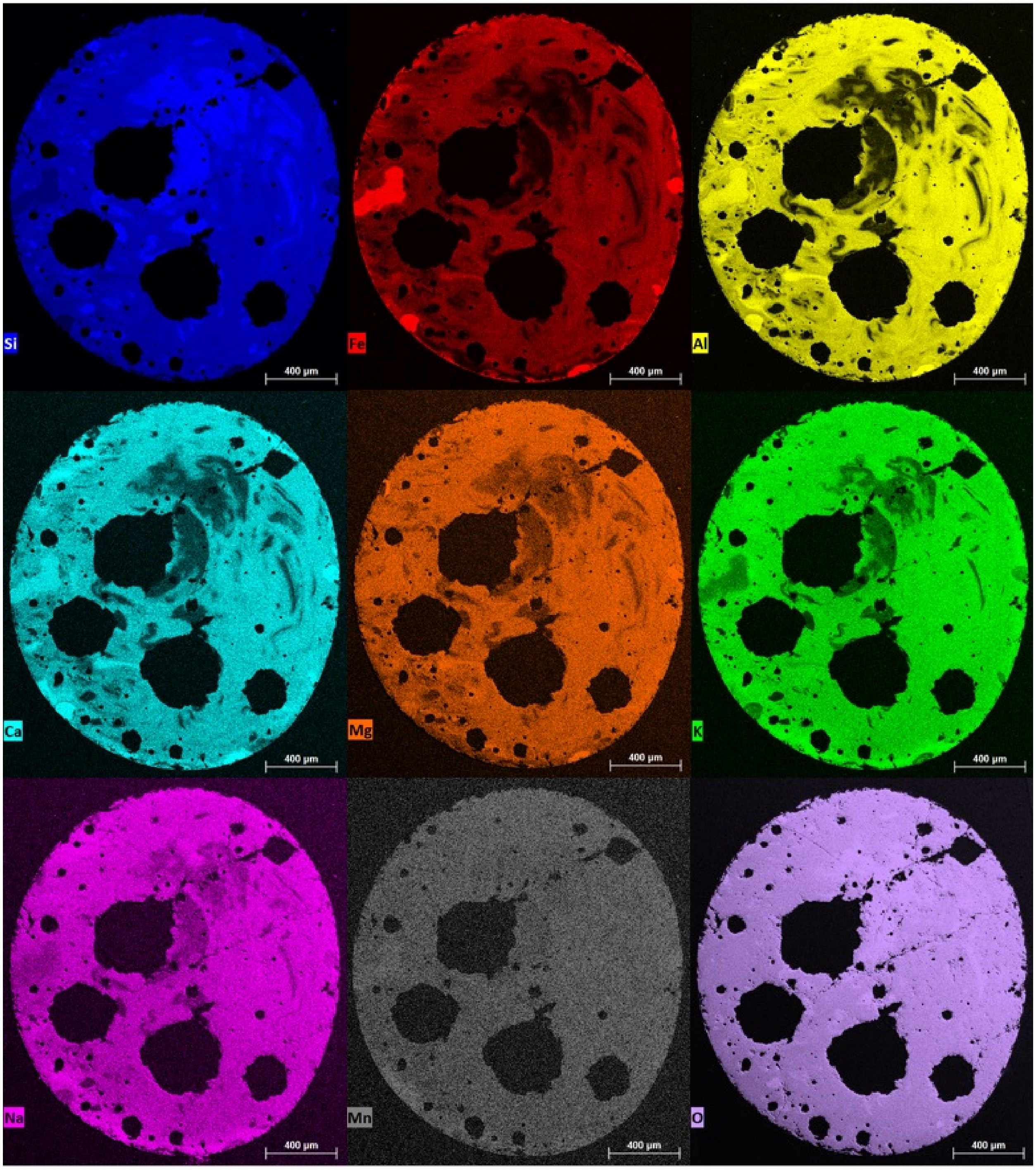

Figure B.22: Sample F31 EDS Maps

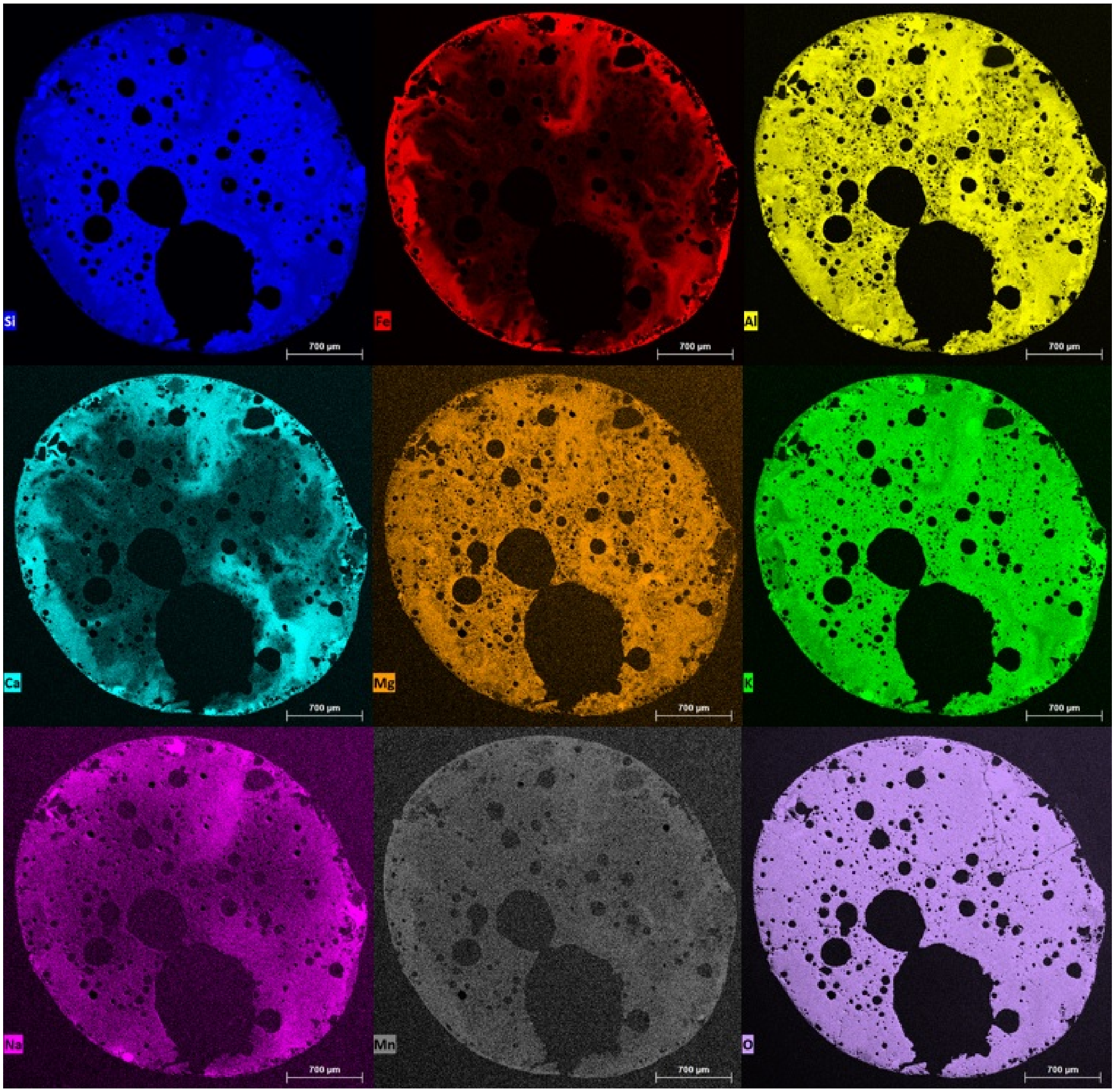

Figure B.23: Sample F32 EDS Maps

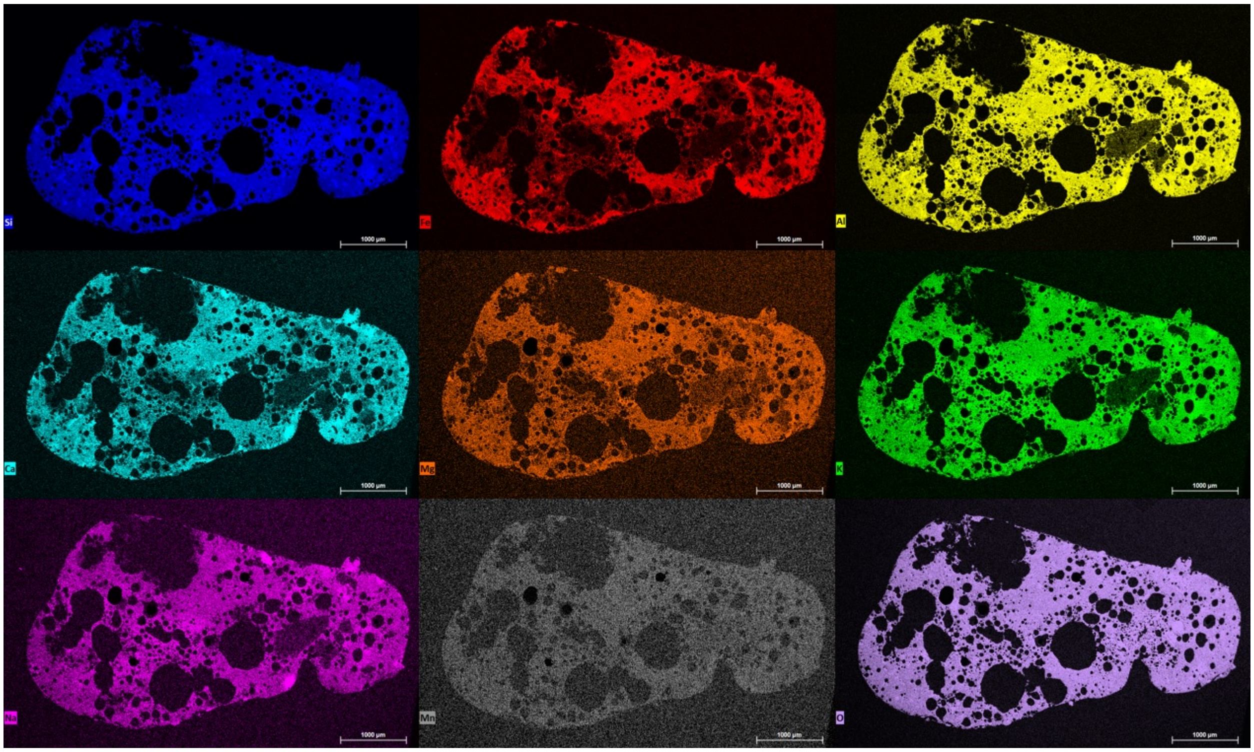

Figure B.24: Sample F33 EDS Maps

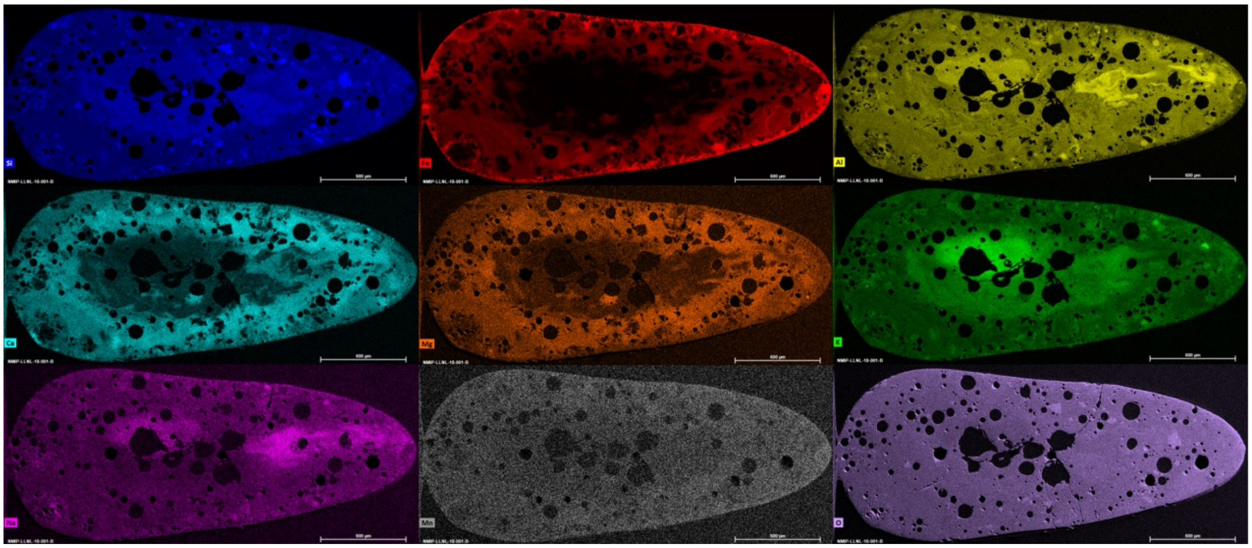

Figure B.25: Sample F34 EDS Maps

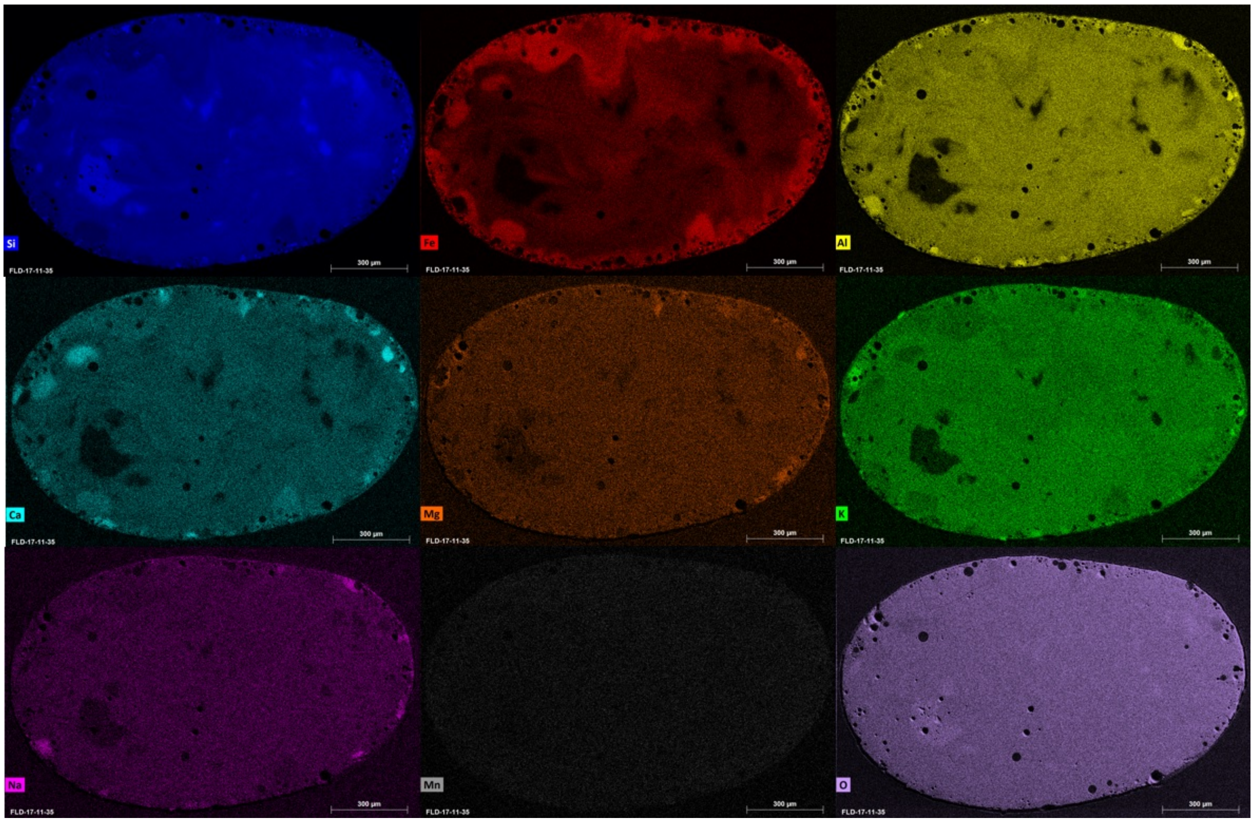

Figure B.26: Sample F35 EDS Maps

Appendix C

Semi-Quantitative SEM EDS Maps

Figures below are a subset of samples in Appendix B selected for longer semi-quantitative maps (12 hours). Each scale bar is scaled differently, and so quantitative interpretations should pay close attention to scale bars. Estimates less than approximately 1% are not reliable (such as the case with Mn and Ti).

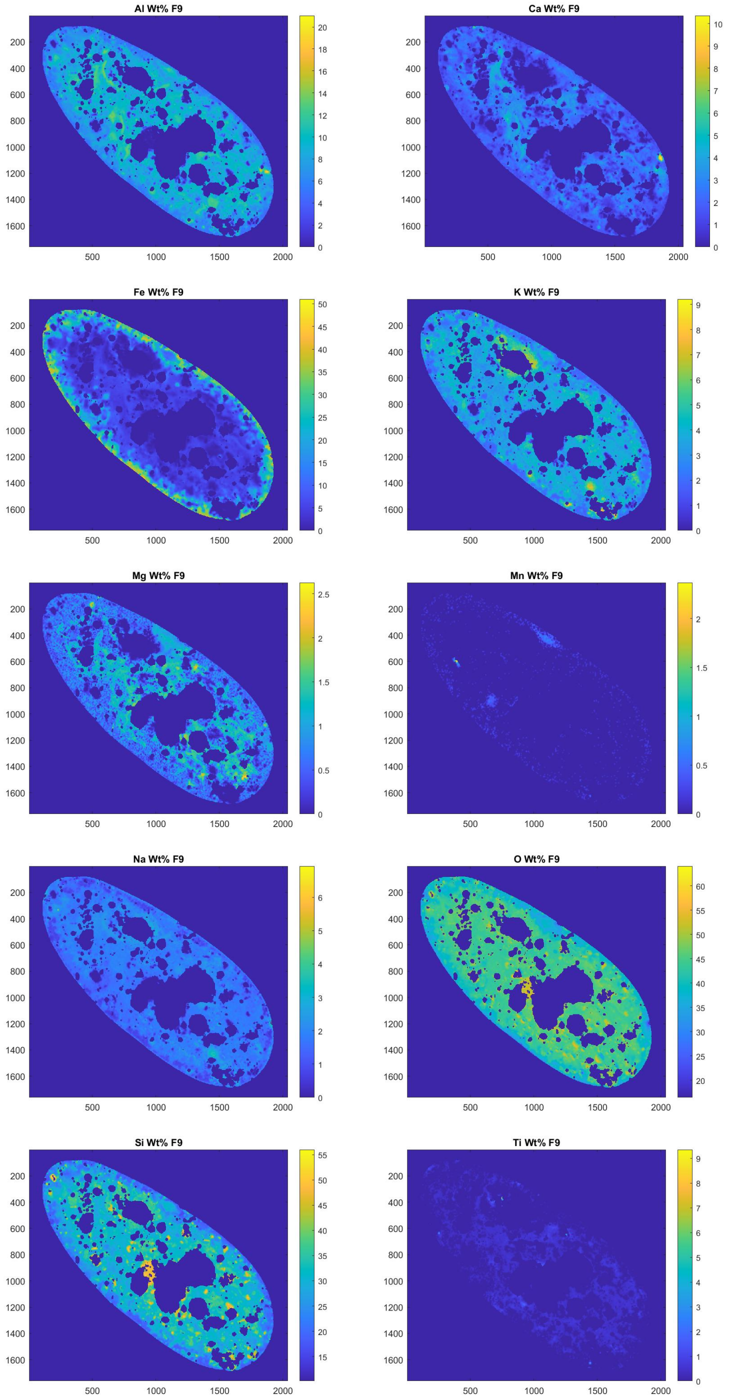

Figure C.1: Sample F9 Quantitative EDS Maps

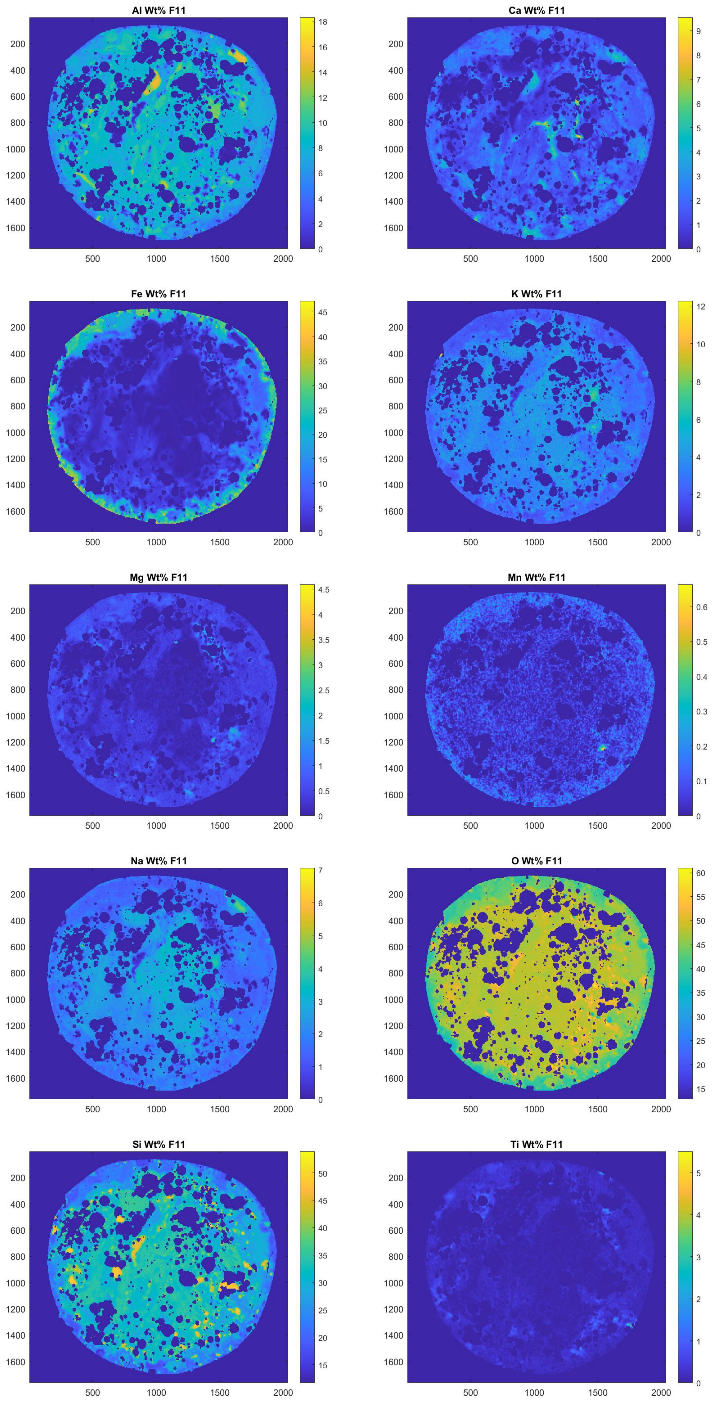

Figure C.2: Sample F11 Quantitative EDS Maps

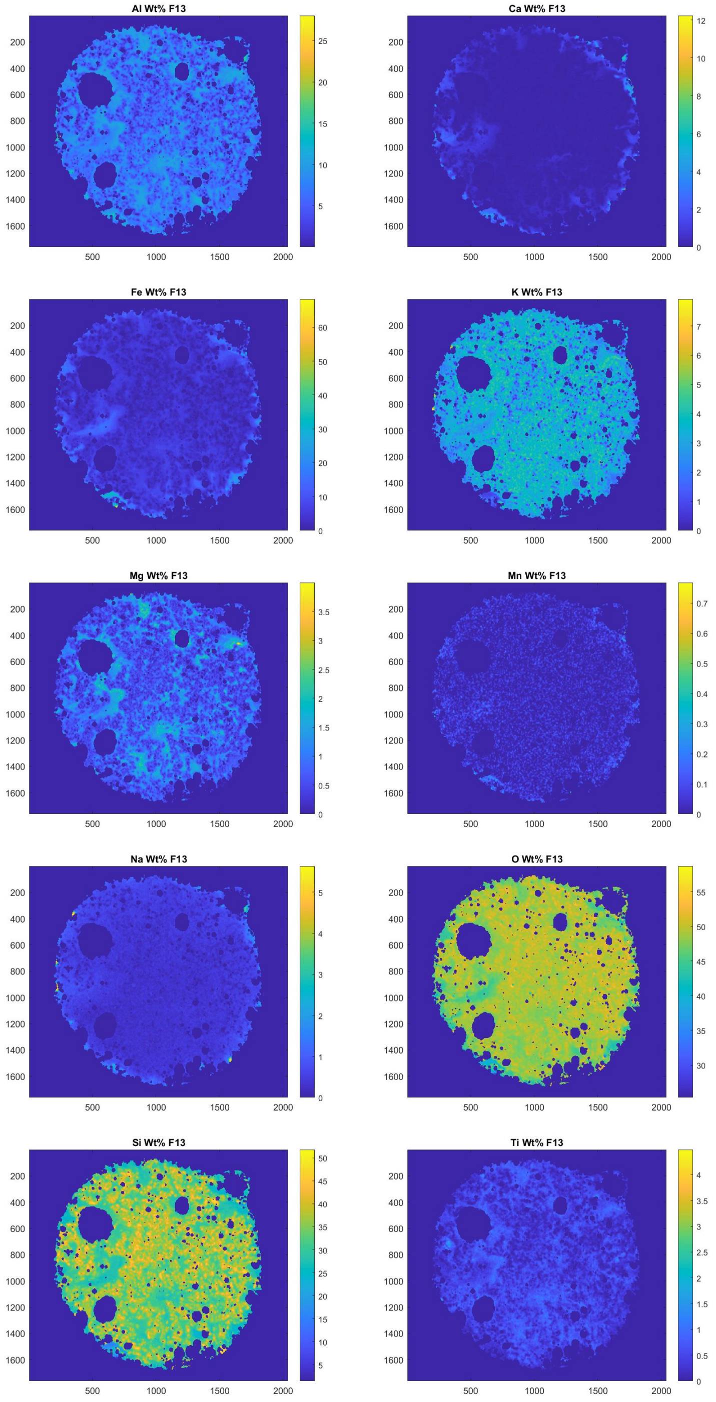

Figure C.3: Sample F13 Quantitative EDS Maps

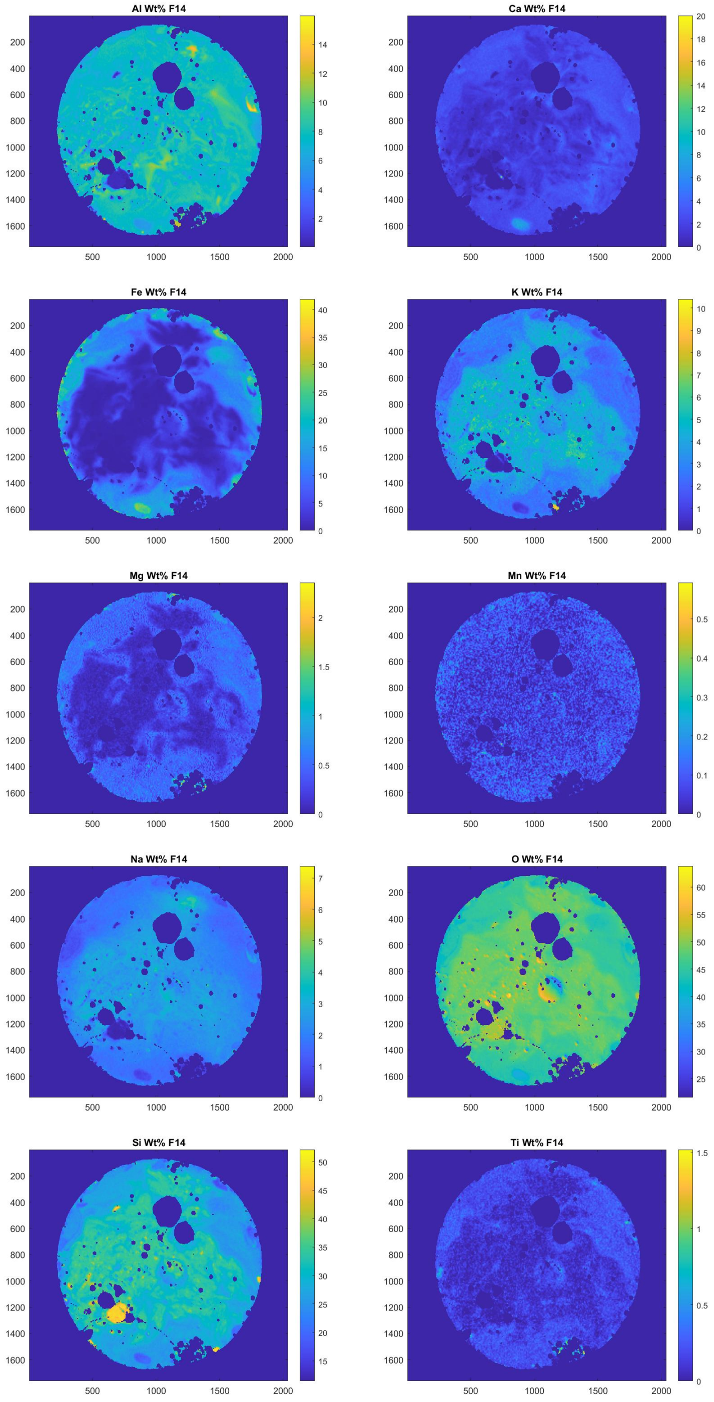

Figure C.4: Sample F14 Quantitative EDS Maps

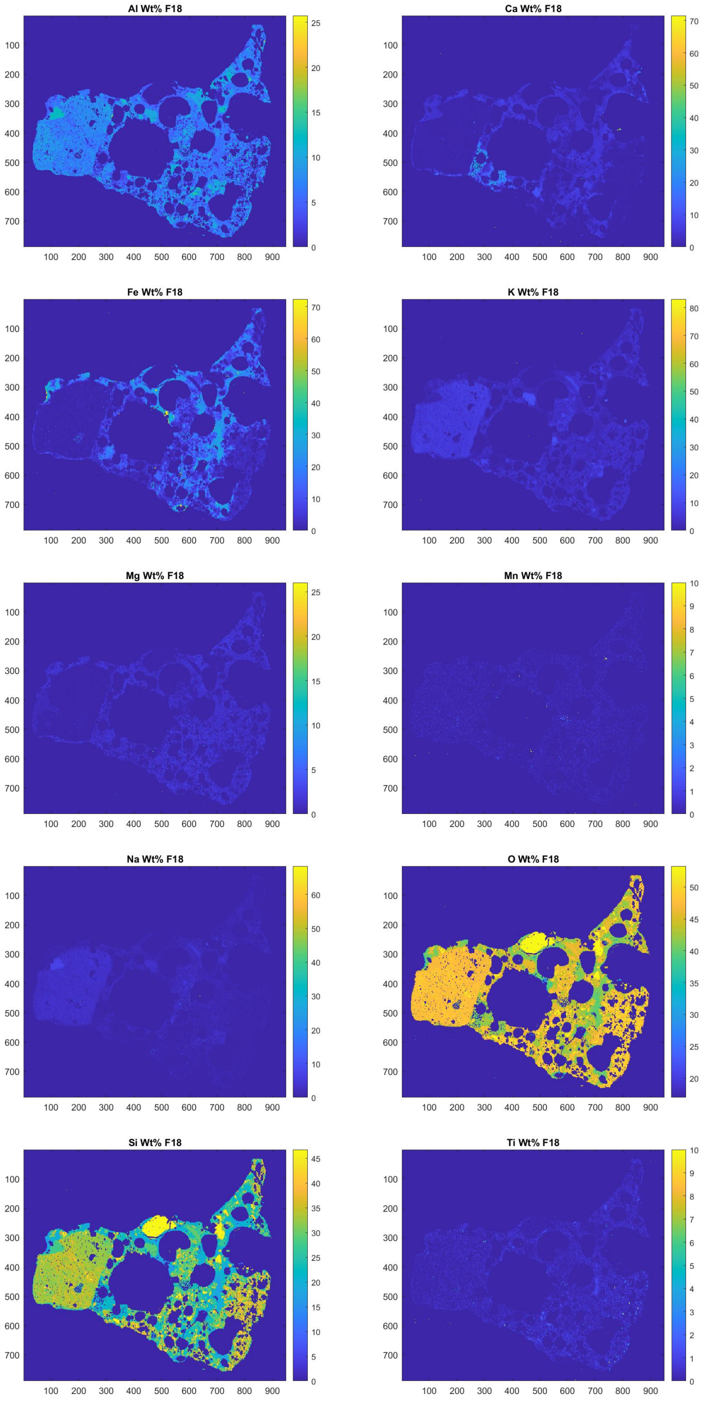

Figure C.5: Sample F18 Quantitative EDS Maps

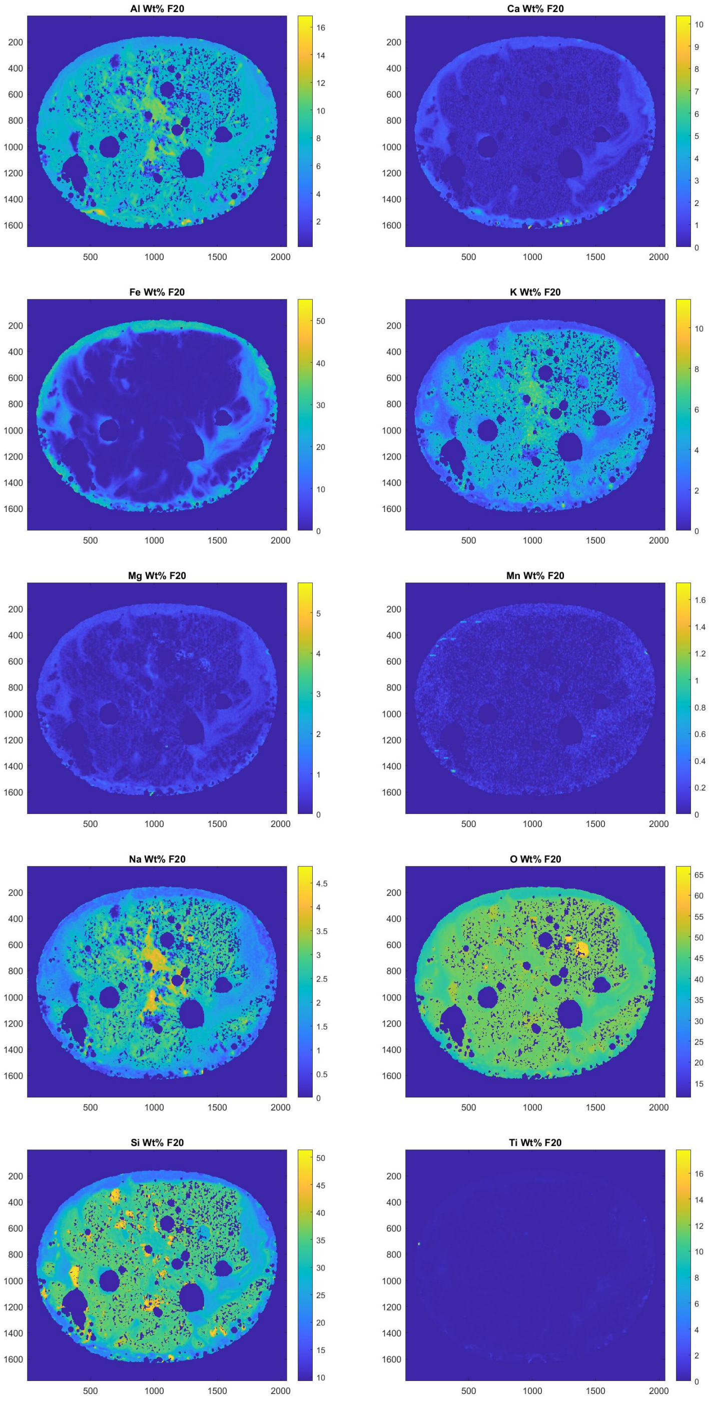

Figure C.6: Sample F20 Quantitative EDS Maps

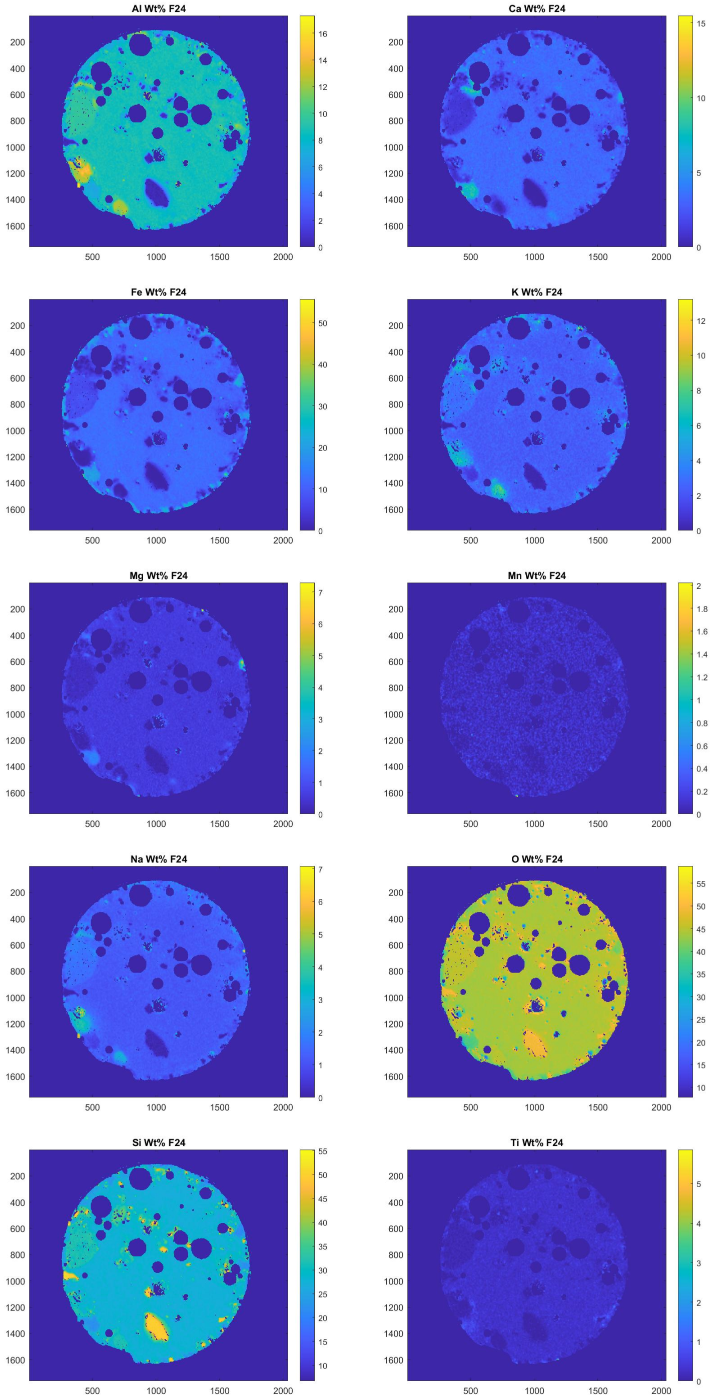

Figure C.7: Sample F24 Quantitative EDS Maps

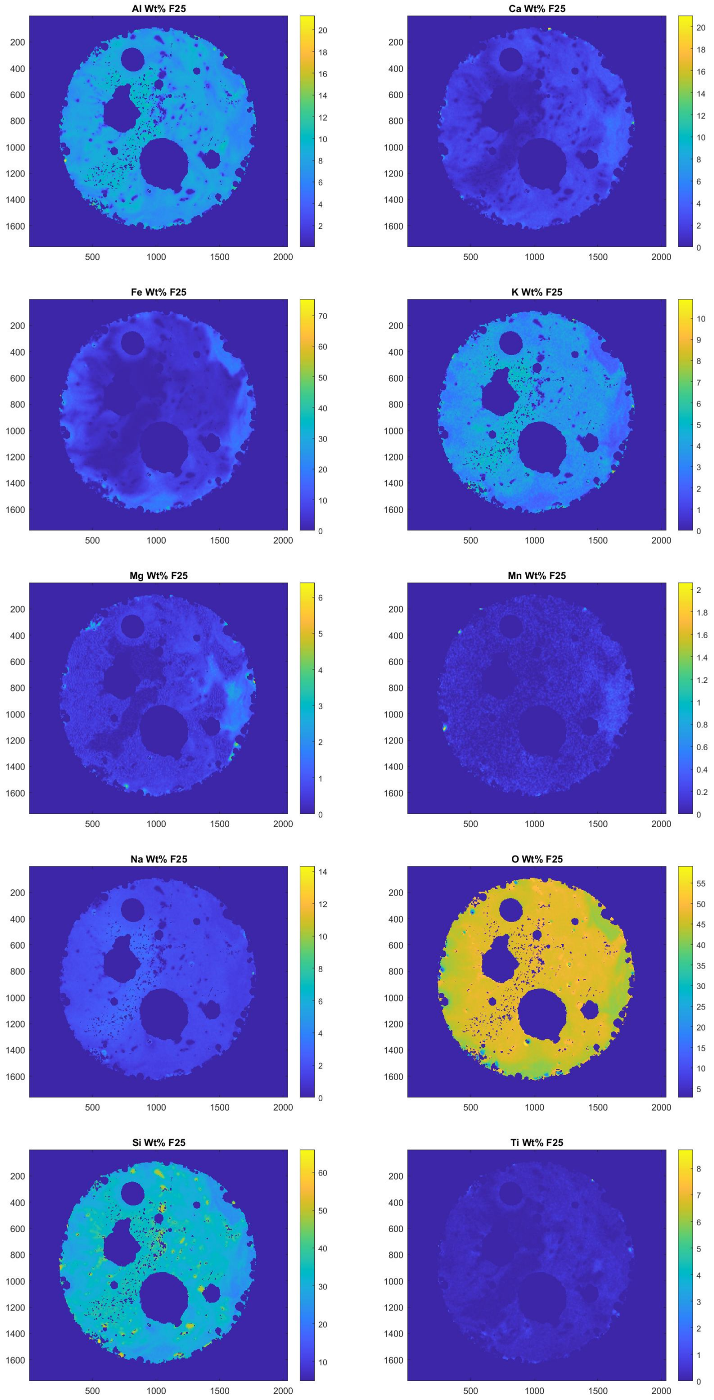

Figure C.8: Sample F25 Quantitative EDS Maps

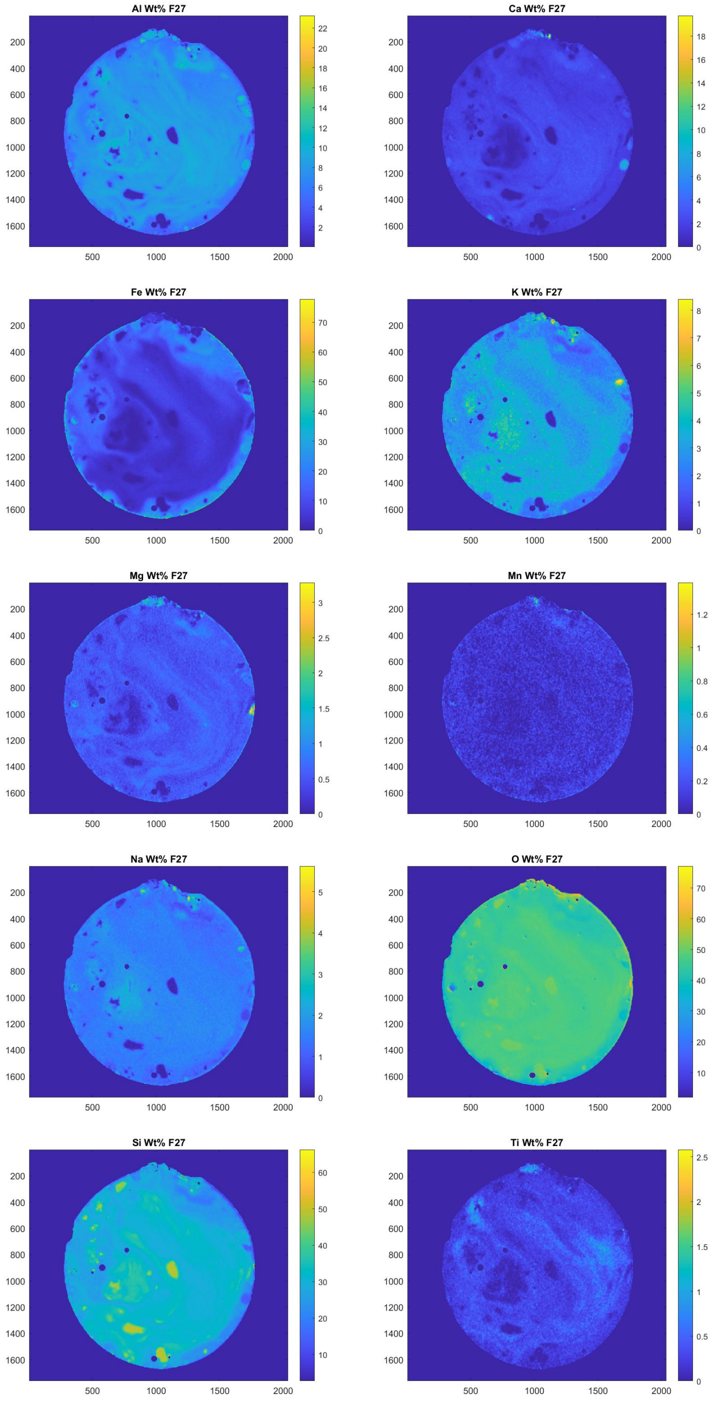

Figure C.9: Sample F27 Quantitative EDS Maps

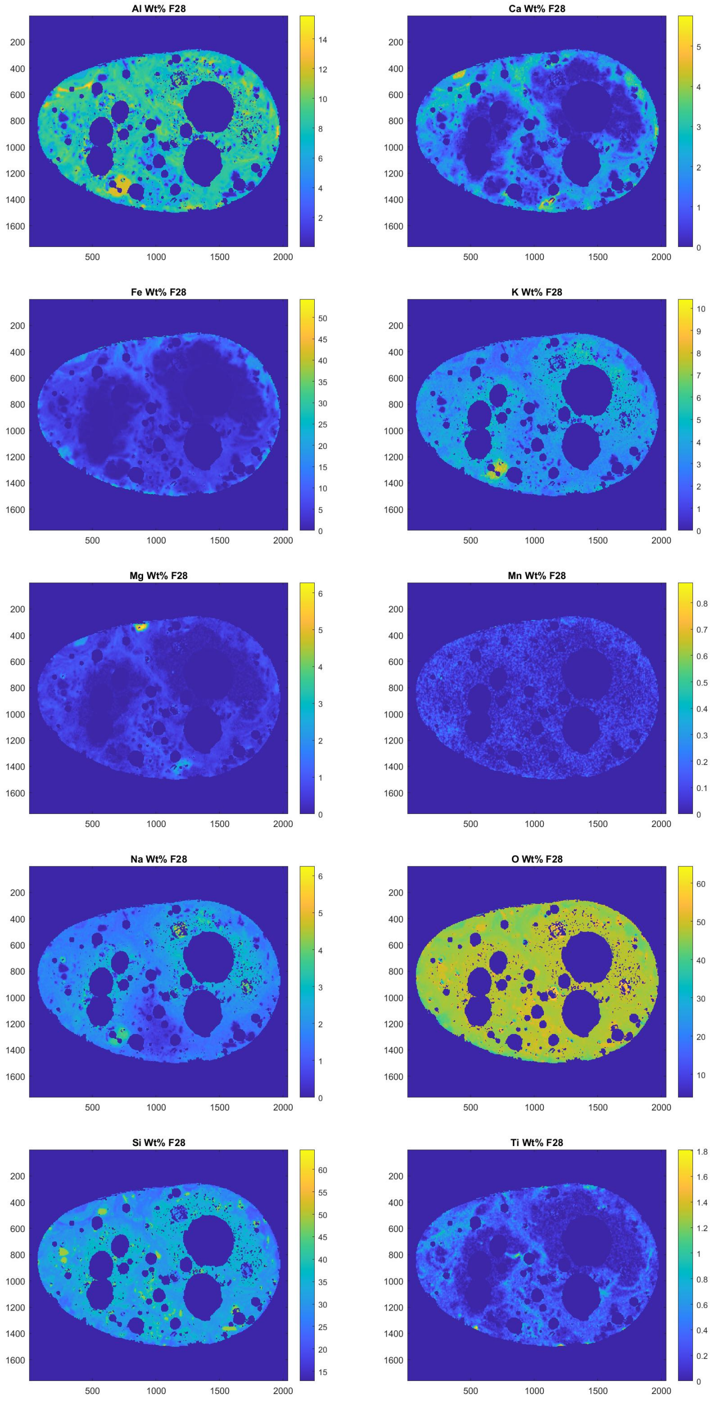

Figure C.10: Sample F28 Quantitative EDS Maps

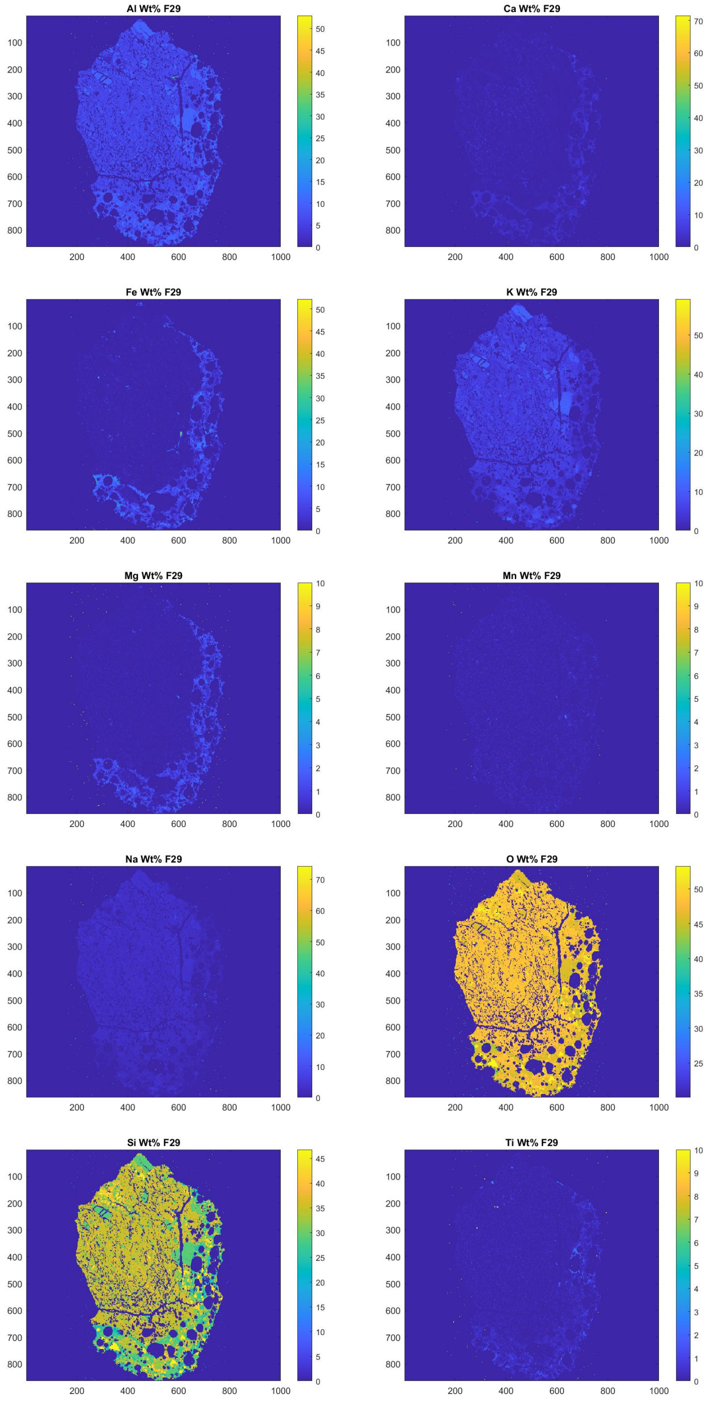

Figure C.11: Sample F29 Quantitative EDS Maps

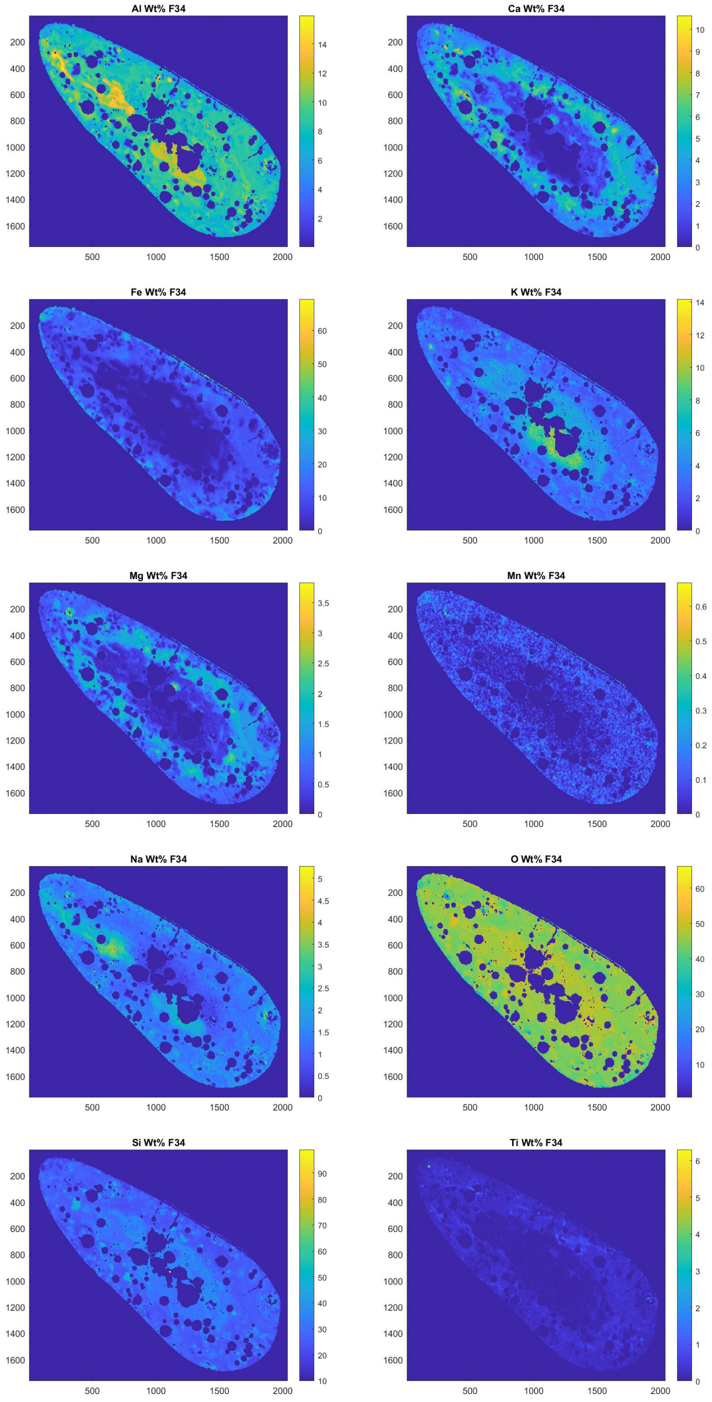

Figure C.12: Sample F34 Quantitative EDS Maps

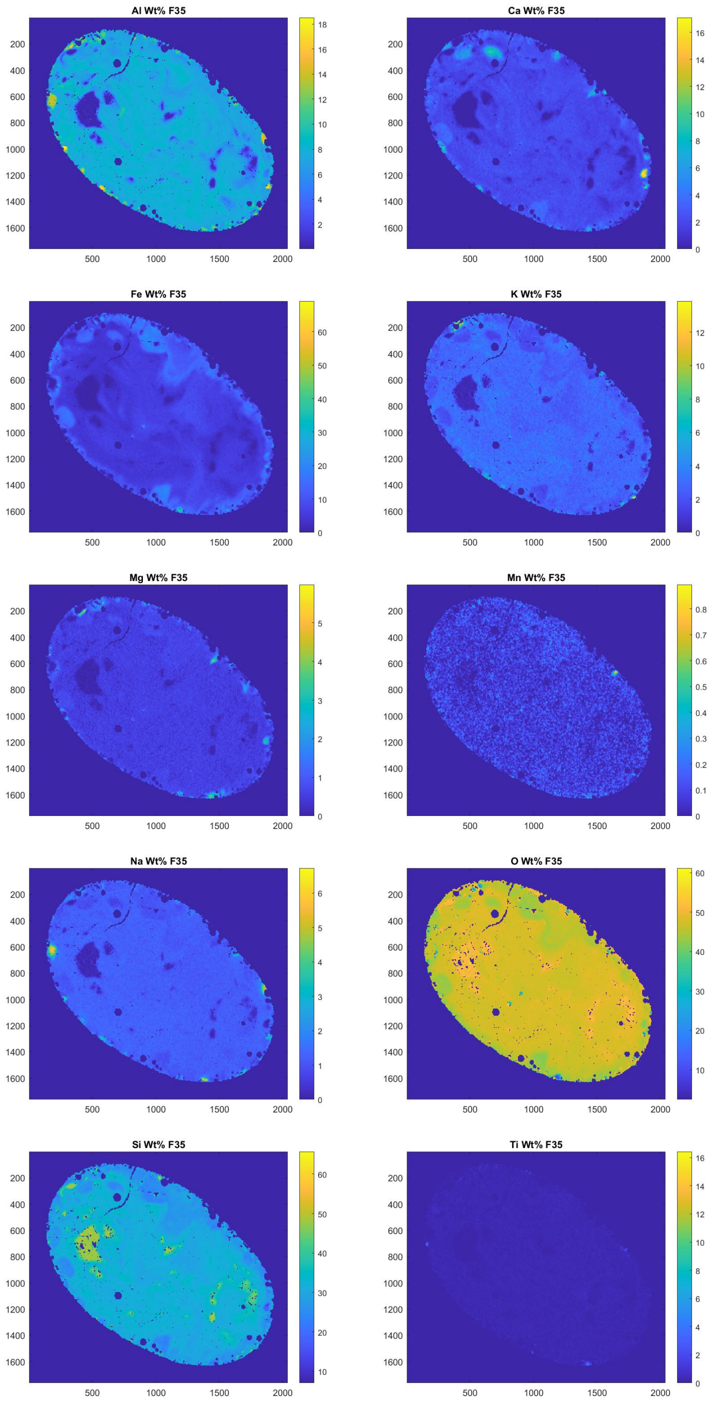

Figure C.13: Sample F35 Quantitative EDS Maps

Appendix D

Precursor Estimation Maps

Figures below show the projection of semi-quantitative SEM-EDS data from Appendix C onto the MCR-ALS model developed in Chapter 6 using a subset of data from each sample (1000 pixel measurements). Precursor 1 is the Fe-rich precursor. Precursor 2 is an AlCaMg-rich precursor that is interpreted to represent the chemically fractionated melt (either due to heating or vapor condensation) and which is partially correlated to precursor 1 in some samples. Precursor 3 is a quartz precursor and precursor 4 is an alkali feldspar precursor both of which are from local soil minerals.

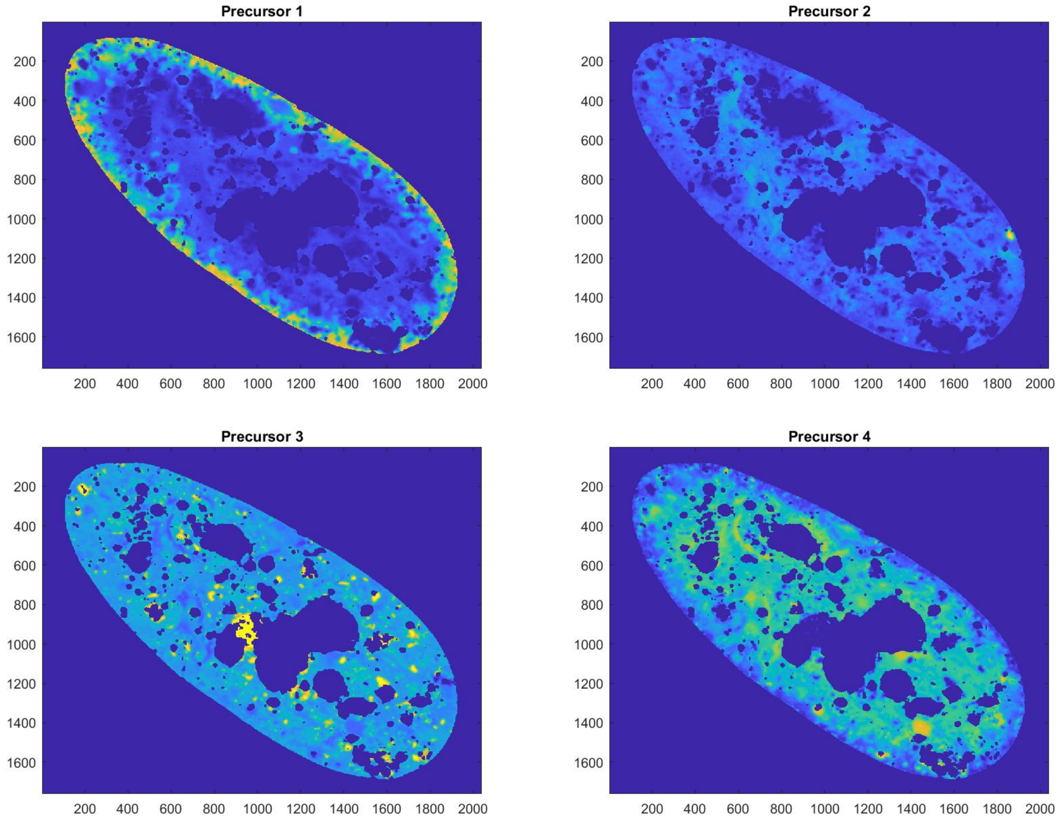

Figure D.1: Sample F9 Precursor Maps

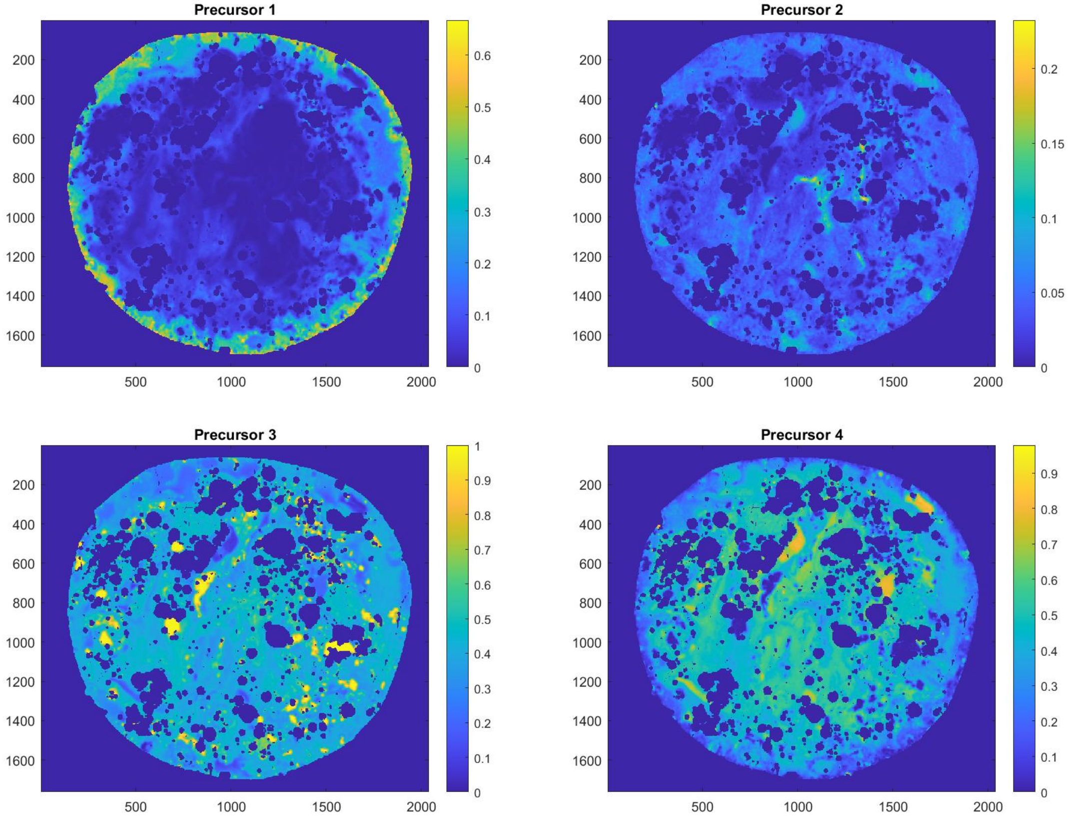

Figure D.2: Sample F11 Precursor Maps

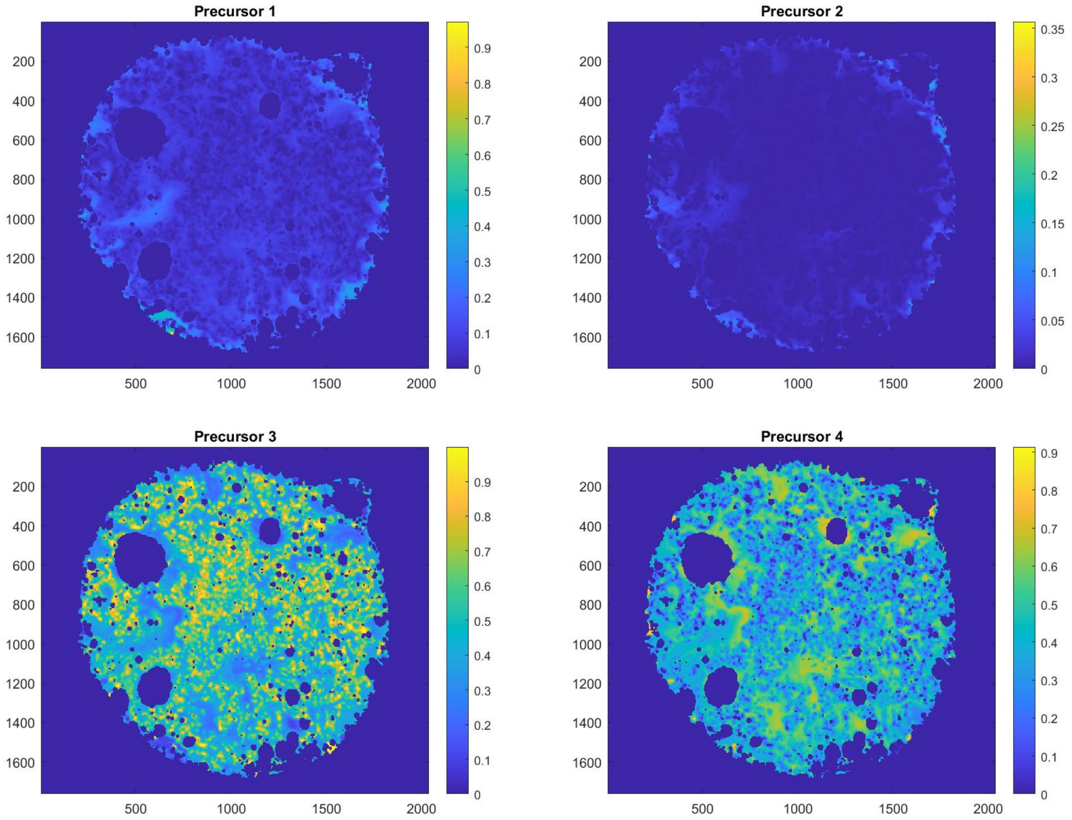

Figure D.3: Sample F13 Precursor Maps

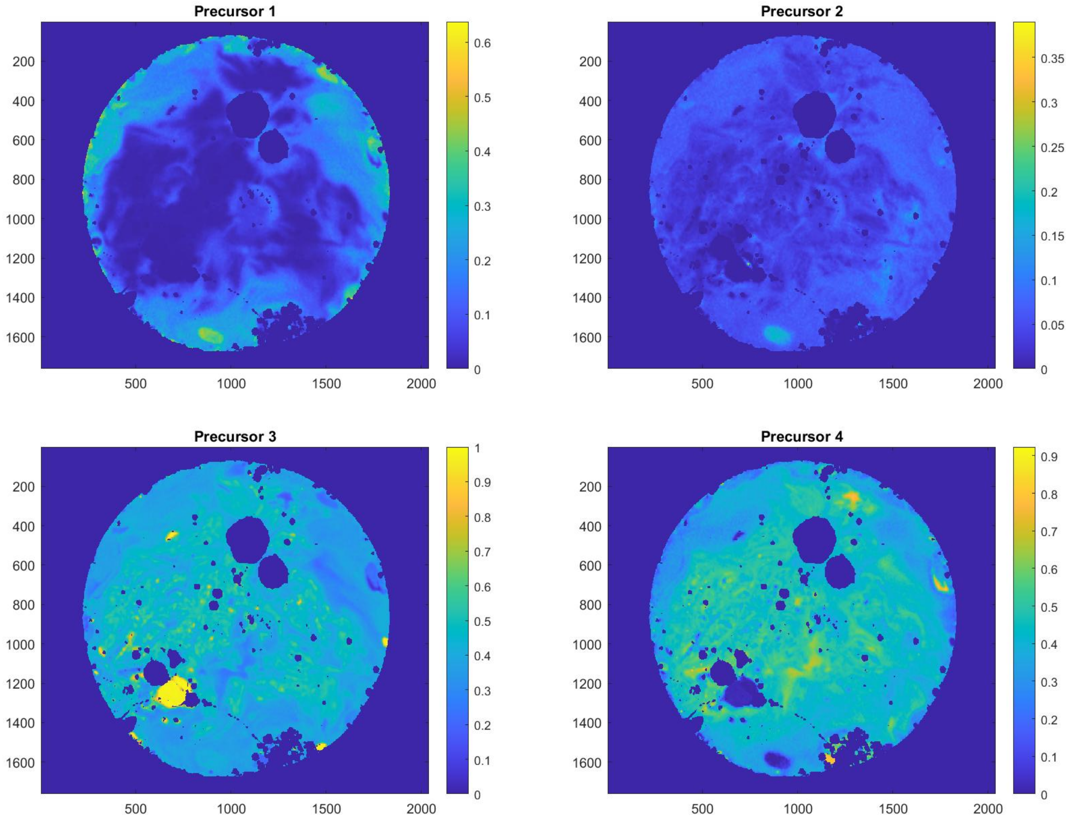

Precursor 1

Precursor 2

Precursor 3

Precursor 4

Figure D.4: Sample F14 Precursor Maps

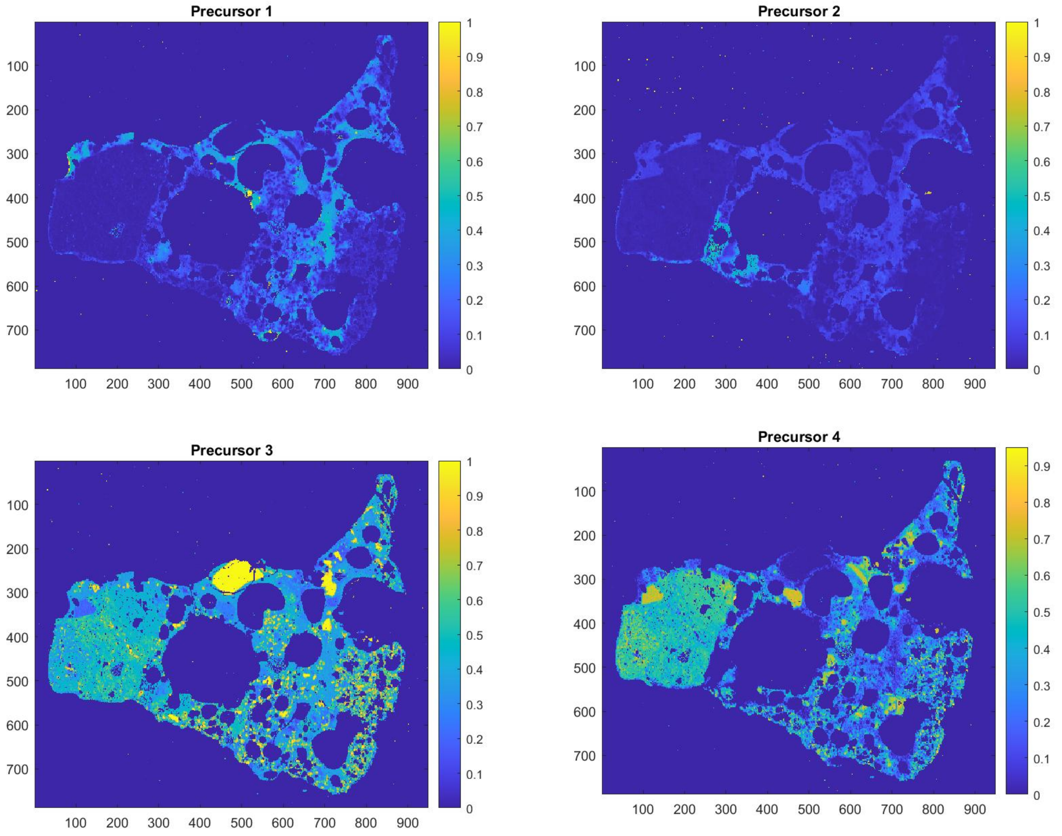

Figure D.5: Sample F18 Precursor Maps

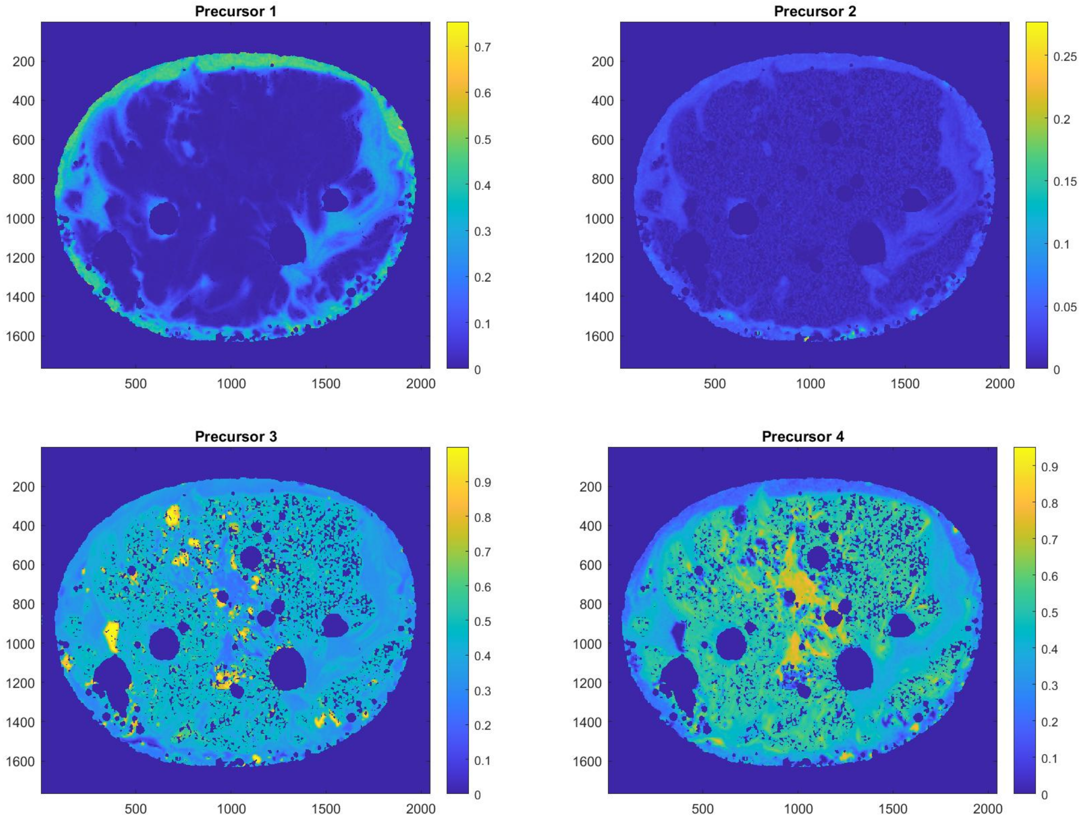

Figure D.6: Sample F20 Precursor Maps

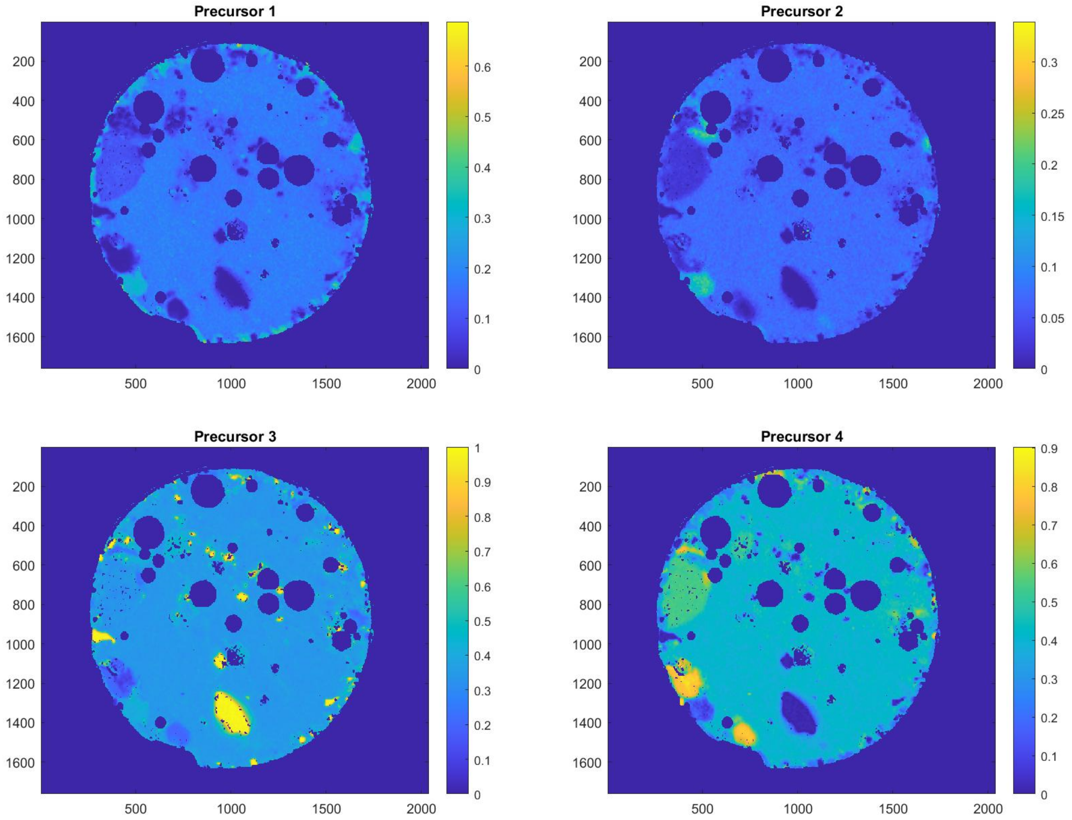

Figure D.7: Sample F24 Precursor Maps

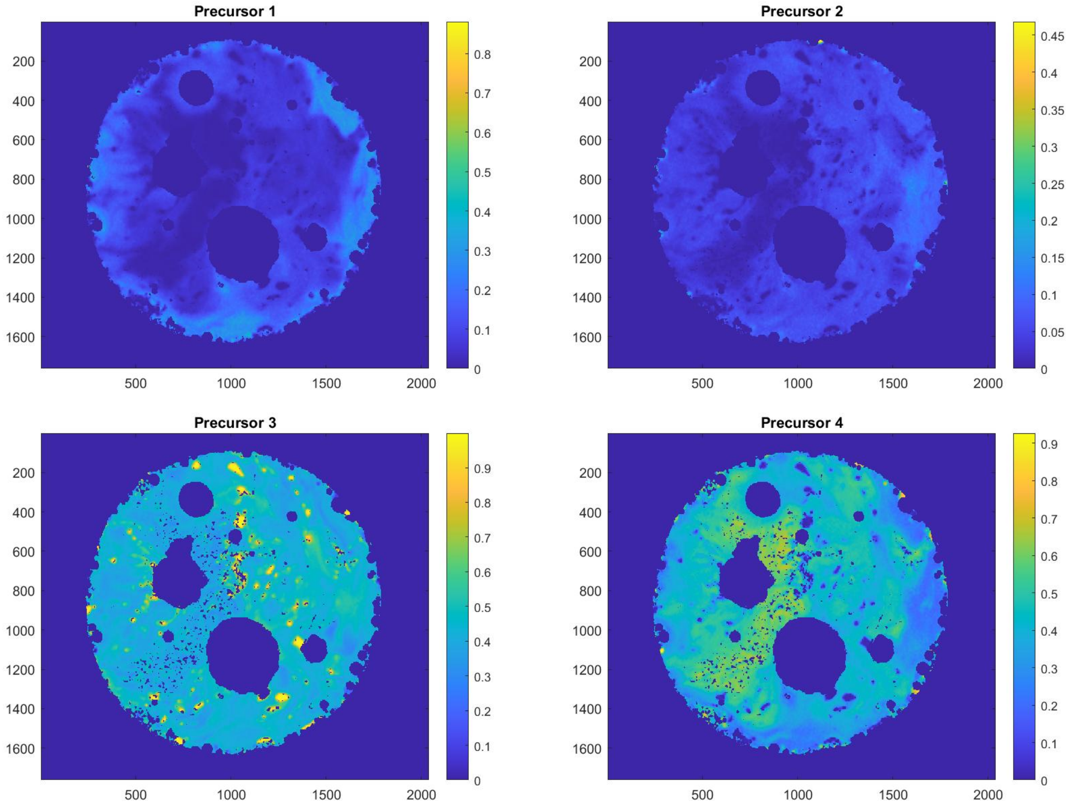

Figure D.8: Sample F25 Precursor Maps

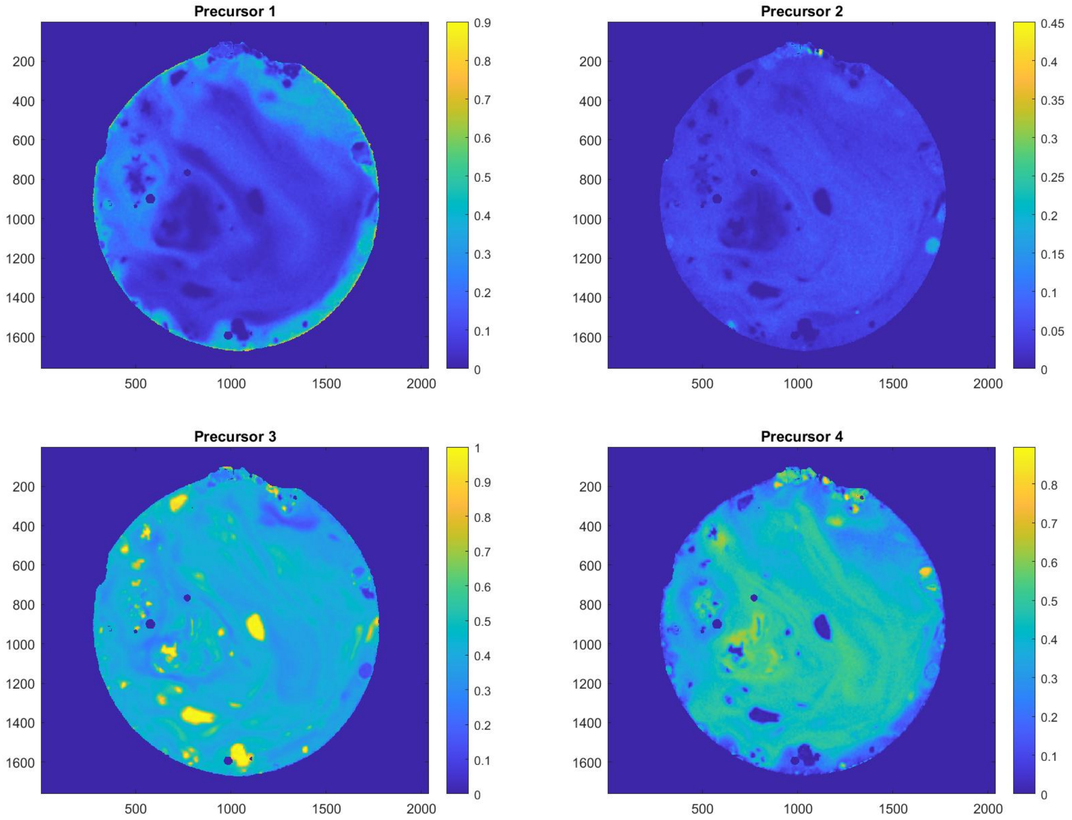

Figure D.9: Sample F27 Precursor Maps

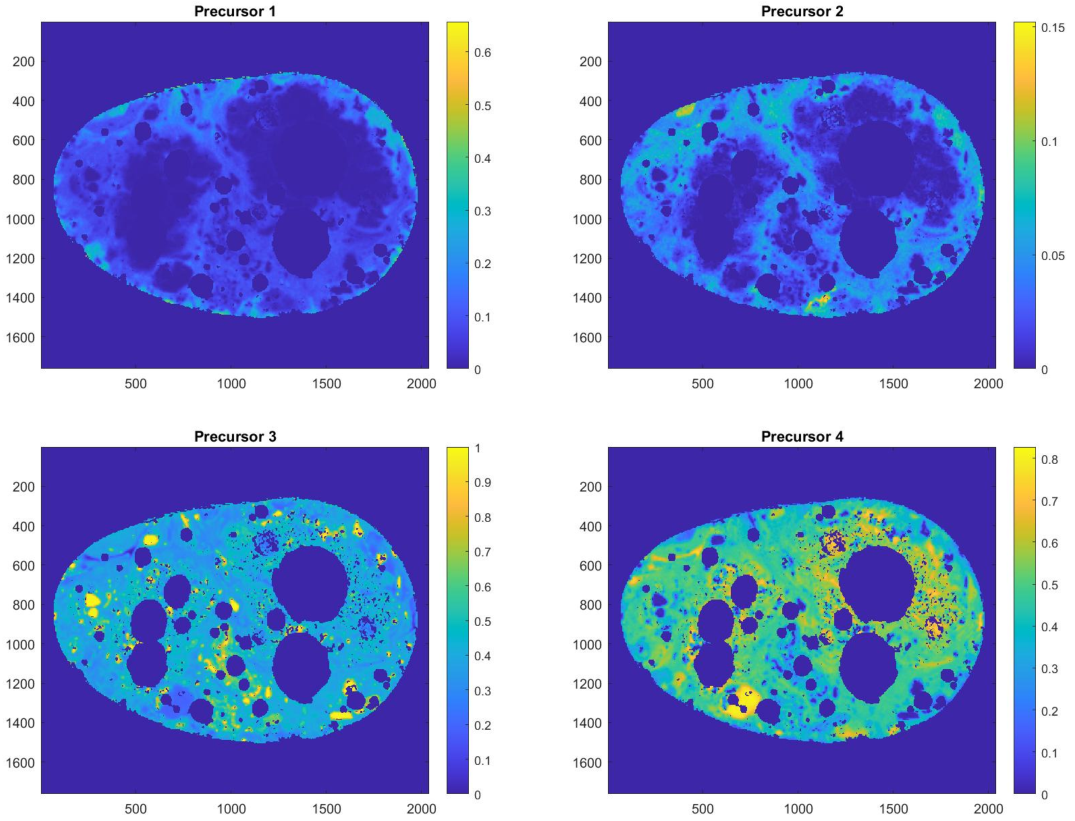

Figure D.10: Sample F28 Precursor Maps

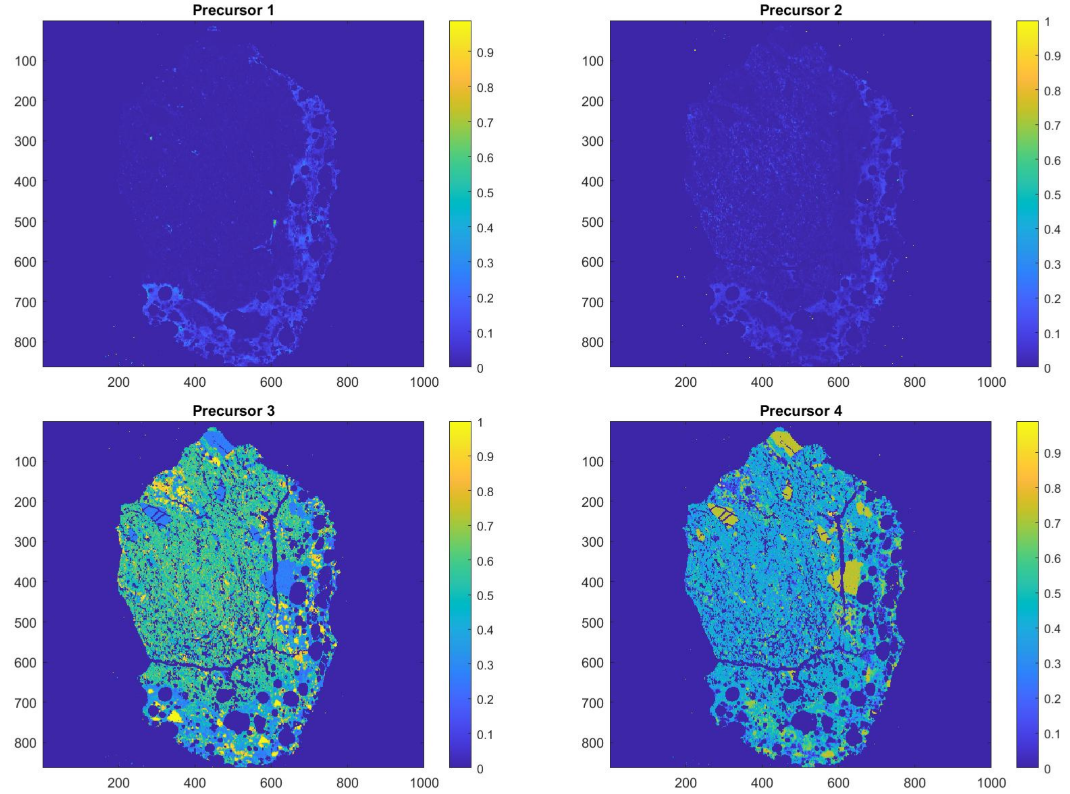
Precursor 1

Precursor 2

Precursor 3

Precursor 4

Figure D.11: Sample F29 Precursor Maps

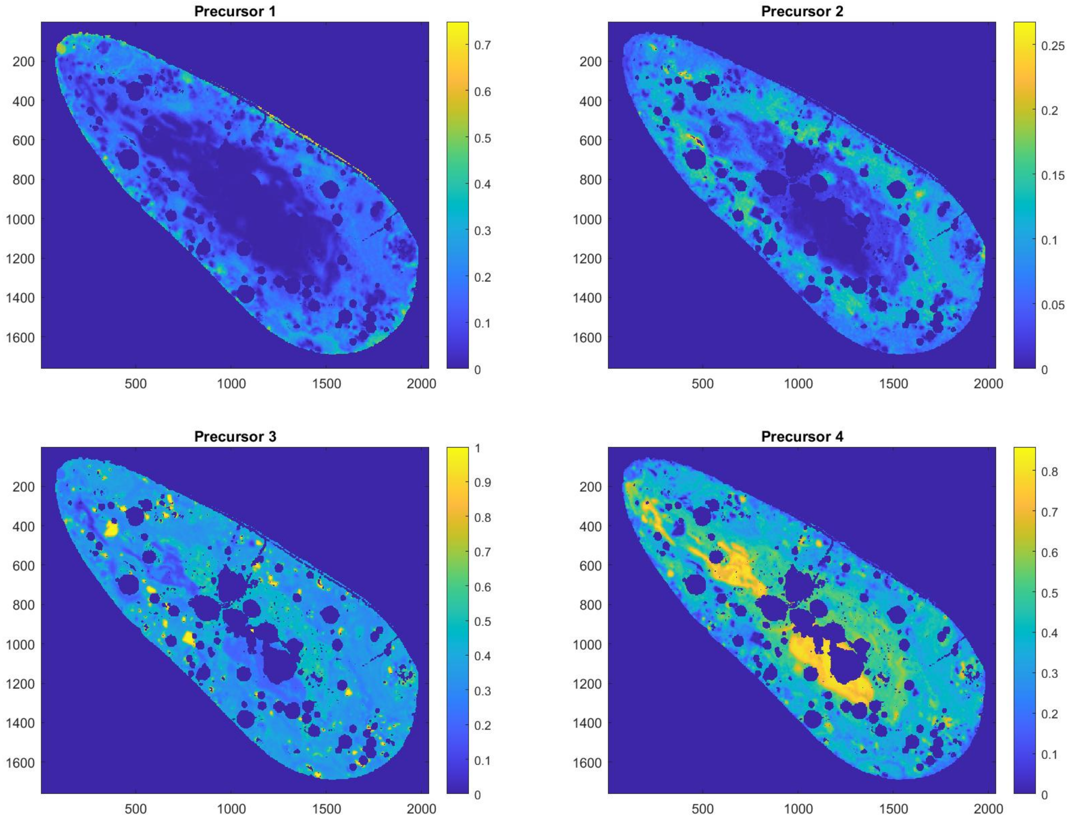

Figure D.12: Sample F34 Precursor Maps

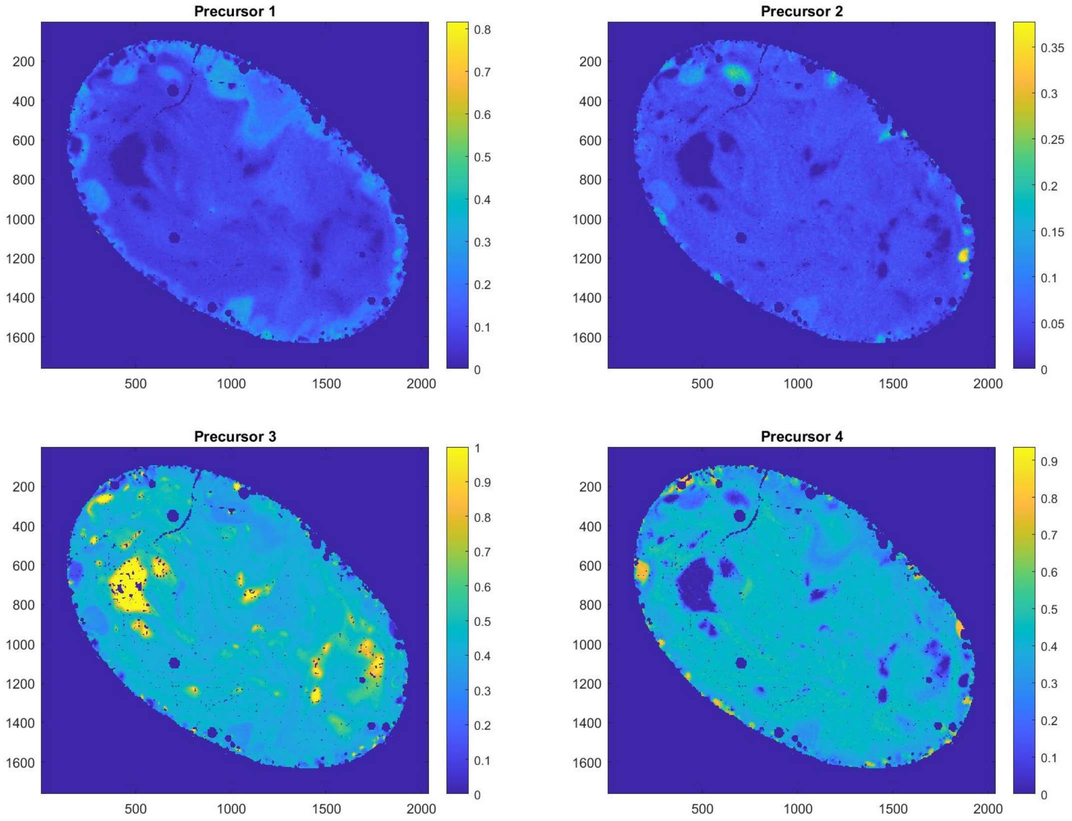

Precursor 1

Precursor 2

Precursor 3

Precursor 4

Figure D.13: Sample F35 Precursor Maps

Appendix E

SEM and TEM Ameoboid Compositions

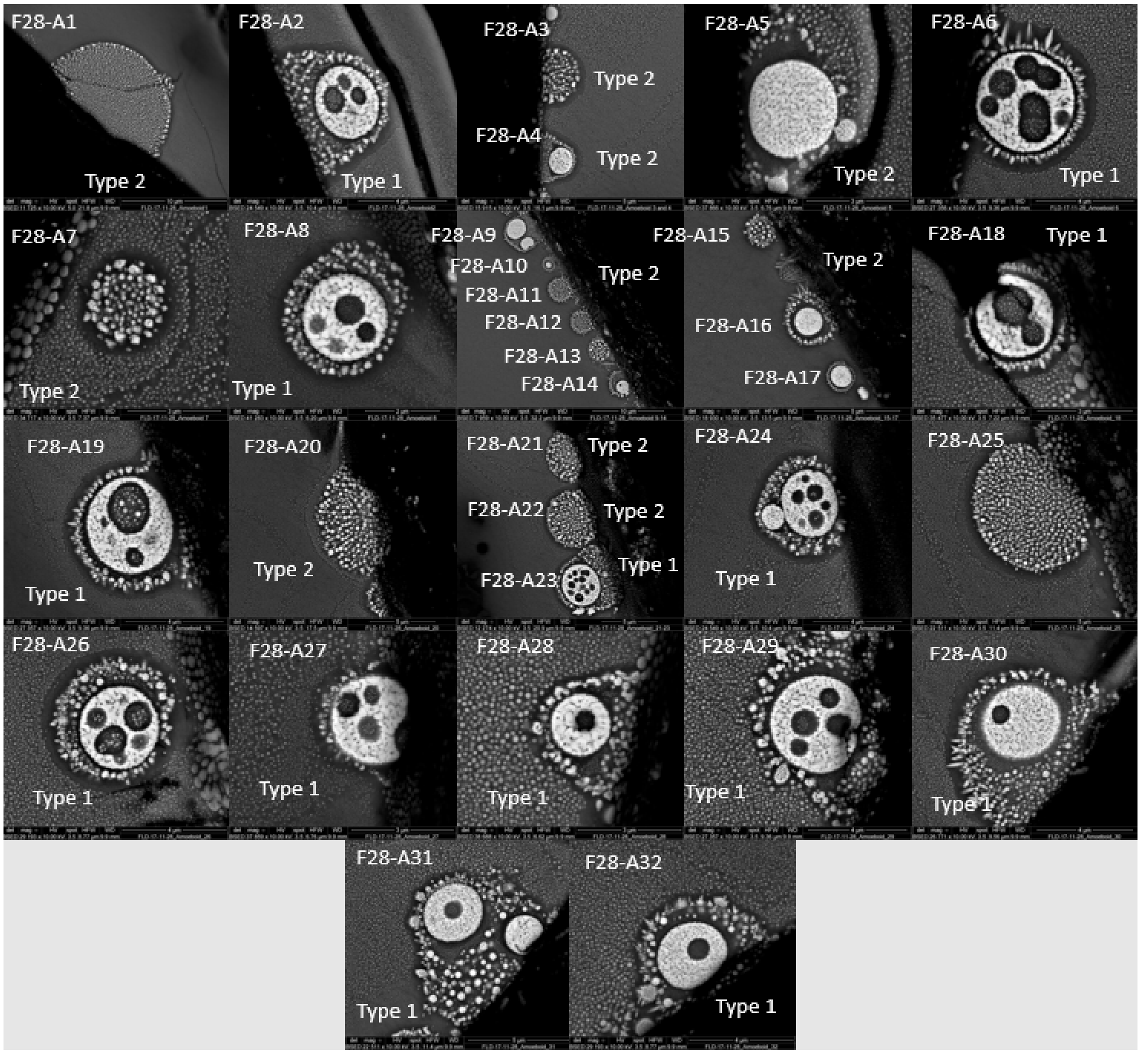

Figure E.1: Images of each F28 amoeboid used for SEM-EDS analysis

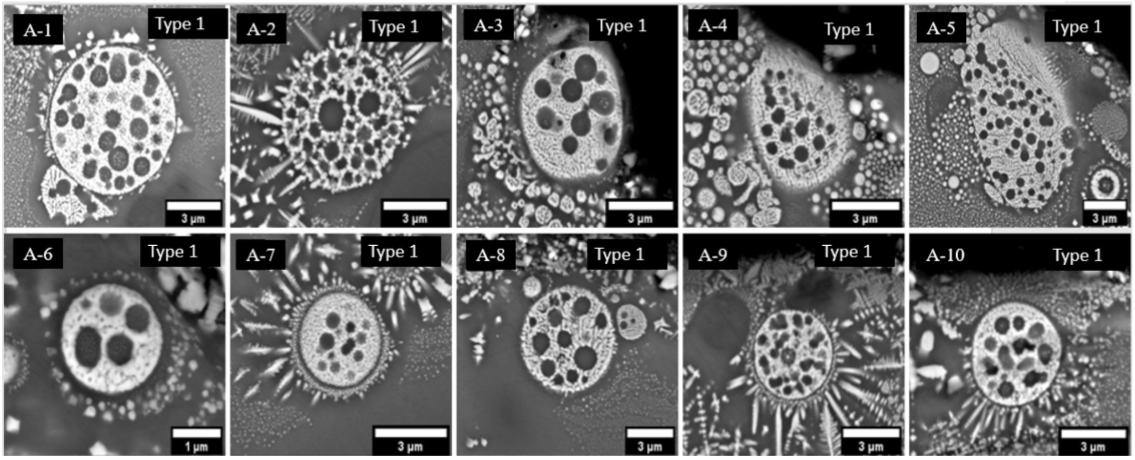

Figure E.2: Images of each F34 amoeboid used for SEM-EDS analysis

Table E.1: SEM EDS amoeboid semi-quantitative compositions. Type 1 are amoeboids where the L_{Si} phase is dispersed within a L_{Fe} phase. Type 2 are amoeboids where the L_{Fe} phase is dispersed within a L_{Si} phase. Type 2 amoeboids had L_{Fe} phases too small to estimate compositions using SEM EDS and so each phase composition is not reported. SEM BSE images of each amoeboid are shown in Figures E.1 and E.2

ID	**Description**	**O**	**Na**	**Mg**	**Al**	**Si**	**K**	**Ca**	**Fe**	**SUM**
F28-A1	Type 2 Amoeboid	43.32	0.68	0.45	3.85	25.79	2.34	0.37	32.63	109.44
	L_{Fe}	NM	NM	NM	NM	NM	NM	NM	NM	
	L_{Si}	NM	NM	NM	NM	NM	NM	NM	NM	
F28-A2	Type 1 Amoeboid	33.14	0.54	0.62	1.94	14.68	0.95	0.24	48.18	100.29
	L_{Fe}	29.79	0.29	0.80	1.40	9.59	0.62	0.20	58.57	101.26
	L_{Si}	42.02	0.59	0.36	2.89	27.97	1.78	0.56	22.87	99.04
F28-A3	Type 2 Amoeboid	25.51	0.08	0.58	1.03	7.41	0.37	0.06	54.58	89.62
	L_{Fe}	NM	NM	NM	NM	NM	NM	NM	NM	
	L_{Si}	NM	NM	NM	NM	NM	NM	NM	NM	
F28-A4	Type 2 Amoeboid	47.86	0.75	0.49	2.52	30.52	2.03	0.41	33.82	118.40
	L_{Fe}	NM	NM	NM	NM	NM	NM	NM	NM	
	L_{Si}	NM	NM	NM	NM	NM	NM	NM	NM	
F28-A5	Type 2 Amoeboid	26.77	0.27	0.78	0.54	4.77	0.29	0.36	69.99	103.76
	L_{Fe}	NM	NM	NM	NM	NM	NM	NM	NM	
	L_{Si}	NM	NM	NM	NM	NM	NM	NM	NM	
F28-A6	Type 1 Amoeboid	36.52	0.79	0.56	2.73	19.06	1.56	0.55	38.30	100.08
	L_{Fe}	30.37	0.33	0.88	1.92	11.33	0.94	0.43	50.77	96.95
	L_{Si}	44.67	1.03	0.29	3.66	30.28	2.56	0.98	18.46	101.93
F28-A7	Type 2 Amoeboid	45.21	1.57	0.88	5.18	25.81	2.56	0.77	32.26	114.23
	L_{Fe}	NM	NM	NM	NM	NM	NM	NM	NM	
	L_{Si}	NM	NM	NM	NM	NM	NM	NM	NM	
F28-A8	Type 1 Amoeboid	30.51	0.78	0.72	1.53	13.03	0.79	0.16	46.55	94.07
	L_{Fe}	27.81	0.74	0.85	1.23	9.39	0.50	0.09	52.57	93.18

	L_{Si}	31.87	0.50	0.35	1.75	20.09	1.28	0.41	23.00	79.25
F28-A9	Type 2 Amoeboid	29.22	0.74	1.18	1.70	10.01	0.78	0.54	51.18	95.36
	L_{Fe}	NM	NM	NM	NM	NM	NM	NM	NM	
	L_{Si}	NM	NM	NM	NM	NM	NM	NM	NM	
F28-A10	Type 2 Amoeboid	32.25	0.91	1.15	2.04	13.31	1.03	0.58	47.23	98.49
	L_{Fe}	NM	NM	NM	NM	NM	NM	NM	NM	
	L_{Si}	NM	NM	NM	NM	NM	NM	NM	NM	
F28-A11	Type 2 Amoeboid	42.89	1.28	1.34	3.20	25.74	1.87	0.97	29.67	106.96
	L_{Fe}	NM	NM	NM	NM	NM	NM	NM	NM	
	L_{Si}	NM	NM	NM	NM	NM	NM	NM	NM	
F28-A12	Type 2 Amoeboid	39.15	1.07	1.33	2.79	23.92	1.57	0.89	25.48	96.20
	L_{Fe}	NM	NM	NM	NM	NM	NM	NM	NM	
	L_{Si}	NM	NM	NM	NM	NM	NM	NM	NM	
F28-A13	Type 2 Amoeboid	37.79	1.05	1.10	3.13	22.20	1.50	1.20	27.04	95.01
	L_{Fe}	NM	NM	NM	NM	NM	NM	NM	NM	
	L_{Si}	NM	NM	NM	NM	NM	NM	NM	NM	
F28-A14	Type 2 Amoeboid	30.23	0.86	2.03	1.99	11.45	0.90	0.48	45.96	93.90
	L_{Fe}	NM	NM	NM	NM	NM	NM	NM	NM	
	L_{Si}	NM	NM	NM	NM	NM	NM	NM	NM	
F28-A15	Type 2 Amoeboid	47.31	1.59	1.75	4.50	28.23	2.03	1.25	29.76	116.42
	L_{Fe}	NM	NM	NM	NM	NM	NM	NM	NM	
	L_{Si}	NM	NM	NM	NM	NM	NM	NM	NM	
F28-A16	Type 2 Amoeboid	25.64	0.09	0.78	0.86	6.38	0.34	0.16	57.04	91.30
	L_{Fe}	NM	NM	NM	NM	NM	NM	NM	NM	
	L_{Si}	NM	NM	NM	NM	NM	NM	NM	NM	
F28-A17	Type 2 Amoeboid	33.41	0.94	1.69	2.38	12.98	0.96	0.50	50.21	103.07
	L_{Fe}	NM	NM	NM	NM	NM	NM	NM	NM	
	L_{Si}	NM	NM	NM	NM	NM	NM	NM	NM	
F28-A18	Type 1 Amoeboid	36.08	1.03	0.93	2.32	18.70	1.14	0.36	39.68	100.23
	L_{Fe}	55.30	1.84	1.13	5.86	37.12	2.33	1.73	18.30	123.60
	L_{Si}	37.77	0.80	1.24	2.33	18.70	1.04	0.29	44.94	107.10
F28-A19	Type 1 Amoeboid	34.25	0.90	1.02	1.94	16.44	1.11	0.36	43.42	99.43
	L_{Fe}	36.04	0.80	1.73	1.57	11.05	0.69	0.26	70.87	123.01
	L_{Si}	43.53	1.08	0.61	3.15	30.02	1.91	0.71	17.74	98.74
F28-A20	Type 2 Amoeboid	43.97	1.77	0.51	3.20	26.91	2.10	0.61	30.85	109.94
	L_{Fe}	NM	NM	NM	NM	NM	NM	NM	NM	
	L_{Si}	NM	NM	NM	NM	NM	NM	NM	NM	
F28-A21	Type 2 Amoeboid	38.39	1.33	0.60	2.57	23.97	1.68	0.47	25.85	94.87
	L_{Fe}	NM	NM	NM	NM	NM	NM	NM	NM	
	L_{Si}	NM	NM	NM	NM	NM	NM	NM	NM	
F28-A22	Type 2 Amoeboid	35.88	0.88	0.65	2.07	21.61	1.56	0.44	28.57	91.67
	L_{Fe}	NM	NM	NM	NM	NM	NM	NM	NM	
	L_{Si}	NM	NM	NM	NM	NM	NM	NM	NM	
F28-A23	Type 1 Amoeboid	29.54	0.93	0.73	1.85	13.48	0.95	0.22	39.96	87.66
	L_{Fe}	32.21	0.85	0.74	1.68	13.78	0.90	0.23	48.69	99.08
	L_{Si}	34.87	0.69	0.31	2.27	22.79	1.63	0.61	20.45	83.62
F28-A24	Type 1 Amoeboid	28.84	1.03	1.21	2.36	11.76	0.95	0.32	41.43	87.90
	L_{Fe}	28.74	0.98	1.67	2.11	8.64	0.59	0.15	53.73	96.61
	L_{Si}	29.59	0.67	0.77	2.70	17.59	1.31	0.66	20.53	73.82
F28-A25	Type 2 Amoeboid	44.16	1.41	0.65	3.33	27.16	2.02	0.61	30.31	109.65
	L_{Fe}	NM	NM	NM	NM	NM	NM	NM	NM	
	L_{Si}	NM	NM	NM	NM	NM	NM	NM	NM	
F28-A26	Type 1 Amoeboid	31.89	1.06	0.84	2.53	14.72	1.19	0.32	40.41	92.96

	L_{Fe}	30.29	0.55	1.40	1.89	6.63	0.49	0.12	69.12	110.48
	L_{Si}	41.50	1.29	0.51	3.72	26.46	2.35	0.68	22.72	99.22
F28-A27	Type 1 Amoeboid	30.24	1.13	0.65	2.05	13.16	1.19	0.37	42.66	91.45
	L_{Fe}	32.79	1.26	0.98	1.79	9.67	0.67	0.18	65.94	113.29
	L_{Si}	40.50	1.18	0.32	3.22	25.23	2.13	0.70	26.35	99.63
F28-A28	Type 1 Amoeboid	30.34	0.87	0.80	1.35	11.67	0.80	0.17	51.58	97.57
	L_{Fe}	35.95	0.99	1.15	1.41	11.85	0.57	0.16	69.50	121.59
	L_{Si}	32.28	0.53	0.22	1.78	22.13	1.54	0.35	16.39	75.22
F28-A29	Type 1 Amoeboid	29.74	0.97	0.56	1.94	12.48	1.03	0.19	44.74	91.64
	L_{Fe}	30.92	0.21	0.78	1.50	7.40	0.58	0.12	71.19	112.70
	L_{Si}	33.93	1.19	0.25	2.93	21.93	1.97	0.36	18.21	80.77
F28-A30	Type 1 Amoeboid	25.77	0.30	0.53	1.15	7.72	0.54	0.18	53.44	89.63
	L_{Fe}	28.95	0.19	0.64	0.92	5.48	0.40	0.16	74.17	110.91
	L_{Si}	35.60	0.32	0.21	2.35	24.03	1.71	0.86	18.11	83.18
F28-A31	Type 1 Amoeboid	30.18	0.90	0.69	1.78	11.49	0.82	0.48	50.19	96.53
	L_{Fe}	26.90	0.10	0.87	1.05	5.61	0.34	0.21	65.65	100.73
	L_{Si}	32.90	0.71	0.32	2.23	19.45	1.23	0.73	27.03	84.60
F28-A32	Type 1 Amoeboid	30.04	0.24	0.43	1.27	11.12	0.69	0.38	54.36	98.54
	L_{Fe}	32.43	0.21	0.51	1.06	10.44	0.49	0.28	66.25	111.67
	L_{Si}	32.63	0.37	0.12	2.05	22.43	1.38	0.89	15.36	75.23
F34-A1	Type 1 Amoeboid	33.38	0.90	0.59	2.90	15.67	1.41	0.62	40.63	96.09
	L_{Fe}	30.01	0.87	0.63	2.19	9.48	0.70	0.34	56.27	100.49
	L_{Si}	36.49	1.05	0.27	3.56	23.13	1.96	0.96	19.49	86.92
F34-A2	Type 1 Amoeboid	35.52	0.88	0.76	2.83	18.36	1.46	0.70	37.11	97.62
	L_{Fe}	33.39	0.83	0.78	2.22	14.31	1.00	0.20	48.90	101.64
	L_{Si}	36.74	0.92	0.32	3.19	25.72	2.46	1.21	10.72	81.28
F34-A3	Type 1 Amoeboid	32.06	1.10	0.69	3.06	14.74	1.47	0.35	39.15	92.61
	L_{Fe}	26.86	0.80	0.83	2.18	8.16	0.70	0.09	50.88	90.50
	L_{Si}	37.99	1.54	0.27	4.15	25.20	2.80	0.78	13.56	86.28
F34-A5	Type 1 Amoeboid	32.68	1.00	0.67	3.48	14.79	1.46	0.40	39.86	94.34
	L_{Fe}	32.00	0.91	0.66	3.04	11.48	1.36	0.35	52.33	102.13
	L_{Si}	32.81	1.08	0.29	4.08	21.10	2.09	0.74	13.02	75.22
F34-A6	Type 1 Amoeboid	32.13	0.98	0.44	2.04	14.19	1.15	0.42	45.53	96.87
	L_{Fe}	26.51	1.06	0.41	1.35	8.87	0.64	0.02	49.66	88.54
	L_{Si}	31.73	0.82	0.29	2.21	19.73	1.99	0.52	21.38	78.66
F34-A7	Type 1 Amoeboid	31.20	0.84	1.01	3.41	11.82	1.41	0.55	45.99	96.22
	L_{Fe}	28.41	0.78	1.06	2.71	7.87	1.07	0.28	54.52	96.71
	L_{Si}	29.99	0.81	0.47	3.53	14.92	1.95	0.92	28.60	81.18
F34-A8	Type 1 Amoeboid	33.14	1.05	0.76	3.03	15.85	1.84	0.73	37.72	94.13
	L_{Fe}	29.42	0.88	0.92	2.24	9.78	0.95	0.26	52.31	96.75
	L_{Si}	38.14	1.26	0.23	4.14	26.29	3.10	1.63	8.94	83.72
F34-A9	Type 1 Amoeboid	33.42	1.06	0.92	2.43	16.22	1.53	0.60	39.01	95.19
	L_{Fe}	30.41	1.02	0.99	2.03	12.16	1.31	0.34	46.40	94.66
	L_{Si}	30.30	1.03	0.43	2.34	18.98	2.18	0.65	17.90	73.81
F34-A10	Type 1 Amoeboid	30.41	0.64	0.59	1.97	12.77	1.05	0.43	45.58	93.45
	L_{Fe}	26.98	0.71	0.65	1.58	7.50	0.43	0.16	56.43	94.45
	L_{Si}	33.05	0.64	0.22	2.52	21.81	2.15	0.67	16.63	77.68

Table E.2: SEM EDS amoeboid semi-quantitative composition uncertainties. Type 1 are amoeboids where the L_{Si} phase is dispersed within a L_{Fe} phase. Type 2 are amoeboids where the L_{Fe} phase is dispersed within a L_{Si} phase. Type 2 amoeboids had L_{Fe} phases too small to estimate compositions using SEM EDS and so each phase composition is not reported.

ID	**1-σ Method**	**O 1-σ**	**Na 1-σ**	**Mg 1-σ**	**Al 1-σ**	**Si 1-σ**	**K 1-σ**	**Ca 1-σ**	**Fe 1-σ**
F28-A1	SEOM	1.17	0.02	0.04	0.11	0.74	0.14	0.07	0.85
	NM	NM	NM	NM	NM	NM	NM	NM	NM
	NM	NM	NM	NM	NM	NM	NM	NM	NM
F28-A2	EDS Quant	3.86	0.06	0.06	0.12	0.63	0.07	0.04	2.22
	EDS Quant	3.47	0.05	0.07	0.09	0.42	0.05	0.04	2.67
	EDS Quant	4.90	0.07	0.05	0.16	1.17	0.10	0.06	1.13
F28-A3	EDS Quant	2.98	0.03	0.06	0.08	0.33	0.05	0.03	2.49
	NM	NM	NM	NM	NM	NM	NM	NM	NM
	NM	NM	NM	NM	NM	NM	NM	NM	NM
F28-A4	EDS Quant	5.60	0.08	0.06	0.15	1.28	0.11	0.05	1.61
	NM	NM	NM	NM	NM	NM	NM	NM	NM
	NM	NM	NM	NM	NM	NM	NM	NM	NM
F28-A5	SEOM	2.23	0.07	0.13	0.01	0.01	0.07	0.03	7.58
	NM	NM	NM	NM	NM	NM	NM	NM	NM
	NM	NM	NM	NM	NM	NM	NM	NM	NM
F28-A6	EDS Quant	4.26	0.08	0.06	0.15	0.81	0.09	0.06	1.79
	EDS Quant	3.53	0.05	0.08	0.12	0.49	0.07	0.05	2.32
	EDS Quant	5.20	0.09	0.05	0.20	1.26	0.12	0.07	0.94
F28-A7	EDS Quant	5.22	0.13	0.08	0.26	1.08	0.12	0.06	1.53
	NM	NM	NM	NM	NM	NM	NM	NM	NM
	NM	NM	NM	NM	NM	NM	NM	NM	NM
F28-A8	EDS Quant	3.48	0.08	0.07	0.10	0.56	0.06	0.04	2.14
	EDS Quant	3.18	0.08	0.07	0.09	0.41	0.05	0.03	2.39
	SEOM	1.27	0.06	0.04	0.08	0.57	0.15	0.04	2.11
F28-A9	EDS Quant	3.35	0.08	0.09	0.11	0.44	0.06	0.05	2.34
	NM	NM	NM	NM	NM	NM	NM	NM	NM
	NM	NM	NM	NM	NM	NM	NM	NM	NM
F28-A10	EDS Quant	3.69	0.09	0.09	0.12	0.57	0.07	0.05	2.17
	NM	NM	NM	NM	NM	NM	NM	NM	NM
	NM	NM	NM	NM	NM	NM	NM	NM	NM
F28-A11	EDS Quant	4.87	0.11	0.10	0.17	1.08	0.10	0.07	1.41
	NM	NM	NM	NM	NM	NM	NM	NM	NM
	NM	NM	NM	NM	NM	NM	NM	NM	NM
F28-A12	EDS Quant	4.45	0.10	0.10	0.16	1.00	0.09	0.07	1.22
	NM	NM	NM	NM	NM	NM	NM	NM	NM
	NM	NM	NM	NM	NM	NM	NM	NM	NM
F28-A13	EDS Quant	4.30	0.09	0.09	0.17	0.93	0.08	0.08	1.29
	NM	NM	NM	NM	NM	NM	NM	NM	NM
	NM	NM	NM	NM	NM	NM	NM	NM	NM
F28-A14	EDS Quant	3.45	0.08	0.13	0.12	0.50	0.06	0.05	2.11
	NM	NM	NM	NM	NM	NM	NM	NM	NM
	NM	NM	NM	NM	NM	NM	NM	NM	NM
F28-A15	EDS Quant	5.36	0.13	0.12	0.23	1.18	0.10	0.08	1.42
	NM	NM	NM	NM	NM	NM	NM	NM	NM
	NM	NM	NM	NM	NM	NM	NM	NM	NM

F28-A16	EDS Quant	2.93	0.04	0.07	0.07	0.29	0.04	0.04	2.59
	NM	NM	NM	NM	NM	NM	NM	NM	NM
	NM	NM	NM	NM	NM	NM	NM	NM	NM
F28-A17	EDS Quant	3.81	0.09	0.12	0.14	0.56	0.07	0.05	2.30
	NM	NM	NM	NM	NM	NM	NM	NM	NM
	NM	NM	NM	NM	NM	NM	NM	NM	NM
F28-A18	EDS Quant	4.10	0.09	0.08	0.14	0.79	0.07	0.05	1.85
	EDS Quant	6.27	0.14	0.09	0.29	1.54	0.12	0.10	0.93
	SEOM	4.15	0.05	0.84	0.47	11.05	0.68	0.22	29.46
F28-A19	EDS Quant	3.91	0.09	0.08	0.12	0.70	0.07	0.05	2.01
	SEOM	3.90	0.30	0.41	0.20	5.02	0.31	0.14	6.54
	SEOM	0.22	0.10	0.06	0.01	0.81	0.07	0.05	2.25
F28-A20	EDS Quant	5.00	0.14	0.06	0.17	1.13	0.11	0.06	1.47
	NM	NM	NM	NM	NM	NM	NM	NM	NM
	NM	NM	NM	NM	NM	NM	NM	NM	NM
F28-A21	EDS Quant	4.37	0.11	0.06	0.15	1.01	0.09	0.05	1.24
	NM	NM	NM	NM	NM	NM	NM	NM	NM
	NM	NM	NM	NM	NM	NM	NM	NM	NM
F28-A22	EDS Quant	4.08	0.08	0.06	0.12	0.91	0.09	0.05	1.36
	NM	NM	NM	NM	NM	NM	NM	NM	NM
	NM	NM	NM	NM	NM	NM	NM	NM	NM
F28-A23	EDS Quant	3.38	0.09	0.07	0.11	0.58	0.07	0.04	1.85
	EDS Quant	3.68	0.08	0.07	0.11	0.59	0.06	0.04	2.24
	SEOM	0.79	0.02	0.03	0.04	0.48	0.07	0.03	1.63
F28-A24	EDS Quant	3.30	0.09	0.09	0.14	0.51	0.07	0.04	1.91
	EDS Quant	3.29	0.09	0.12	0.13	0.38	0.05	0.04	2.45
	SEOM	1.23	0.09	0.11	0.10	0.91	0.07	0.06	3.65
F28-A25	EDS Quant	5.02	0.12	0.06	0.18	1.14	0.10	0.06	1.44
	NM	NM	NM	NM	NM	NM	NM	NM	NM
	NM	NM	NM	NM	NM	NM	NM	NM	NM
F28-A26	EDS Quant	3.65	0.09	0.07	0.14	0.63	0.07	0.04	1.87
	SEOM	1.79	0.22	0.06	0.12	0.97	0.06	0.01	4.47
	EDS Quant	4.74	0.11	0.06	0.20	1.11	0.11	0.06	1.11
F28-A27	EDS Quant	3.45	0.10	0.06	0.12	0.57	0.07	0.05	1.97
	SEOM	3.42	0.14	0.10	0.22	1.61	0.09	0.06	6.57
	SEOM	2.28	0.01	0.04	0.27	2.29	0.29	0.09	2.24
F28-A28	EDS Quant	3.48	0.08	0.07	0.09	0.51	0.06	0.04	2.36
	EDS Quant	4.12	0.09	0.09	0.10	0.52	0.05	0.04	3.16
	EDS Quant	3.69	0.06	0.04	0.11	0.93	0.09	0.05	0.83
F28-A29	EDS Quant	3.41	0.09	0.06	0.12	0.54	0.07	0.04	2.06
	SEOM	1.44	0.07	0.13	0.20	1.00	0.06	0.05	1.24
	SEOM	1.82	0.06	0.06	0.26	1.96	0.29	0.10	2.97
F28-A30	EDS Quant	2.98	0.05	0.06	0.08	0.35	0.05	0.04	2.44
	EDS Quant	3.35	0.04	0.07	0.07	0.26	0.05	0.04	3.36
	EDS Quant	4.12	0.05	0.04	0.14	1.01	0.09	0.07	0.92
F28-A31	EDS Quant	3.48	0.09	0.07	0.11	0.50	0.06	0.05	2.30
	SEOM	3.51	0.03	0.12	0.16	0.53	0.04	0.01	9.32
	EDS Quant	3.80	0.07	0.05	0.13	0.82	0.08	0.06	1.30
F28-A32	EDS Quant	3.50	0.05	0.05	0.09	0.49	0.06	0.05	2.49
	EDS Quant	3.78	0.04	0.06	0.08	0.46	0.05	0.04	3.02
	EDS Quant	3.81	0.05	0.03	0.12	0.94	0.08	0.07	0.78
F34-A1	EDS Quant	3.53	0.08	0.06	0.16	0.66	0.07	0.05	1.80
	SEOM	1.07	0.08	0.08	0.17	0.70	0.11	0.07	3.69

	SEOM	1.19	0.08	0.06	0.19	1.74	0.14	0.08	4.26
F34-A2	EDS Quant	3.74	0.08	0.06	0.15	0.77	0.07	0.05	1.64
	SEOM	0.71	0.15	0.03	0.05	0.93	0.19	0.11	1.69
	SEOM	4.31	0.25	0.07	0.49	3.73	0.33	0.24	1.93
F34-A3	EDS Quant	3.39	0.09	0.06	0.16	0.62	0.08	0.04	1.74
	SEOM	0.31	0.05	0.08	0.07	0.13	0.05	0.03	0.69
	SEOM	1.63	0.07	0.03	0.21	1.40	0.21	0.11	1.25
F34-A5	EDS Quant	3.45	0.08	0.06	0.18	0.63	0.07	0.04	1.77
	SEOM	1.43	0.11	0.09	0.08	0.70	0.04	0.08	2.39
	SEOM	2.78	0.25	0.08	0.51	2.38	0.22	0.12	1.89
F34-A6	EDS Quant	3.54	0.09	0.05	0.12	0.61	0.07	0.04	2.05
	SEOM	0.53	0.05	0.16	0.07	0.11	0.08	0.02	2.27
	SEOM	2.37	0.04	0.05	0.18	1.22	0.18	0.03	3.91
F34-A7	EDS Quant	3.33	0.08	0.08	0.18	0.51	0.07	0.05	2.04
	SEOM	1.03	0.06	0.01	0.14	0.84	0.22	0.08	1.54
	SEOM	1.87	0.14	0.01	0.13	1.33	0.09	0.13	5.33
F34-A8	EDS Quant	3.51	0.09	0.06	0.16	0.67	0.09	0.05	1.67
	SEOM	0.48	0.07	0.10	0.04	0.32	0.12	0.10	0.96
	SEOM	2.29	0.17	0.04	0.27	1.86	0.16	0.15	0.83
F34-A9	EDS Quant	3.59	0.09	0.07	0.14	0.69	0.08	0.05	1.74
	SEOM	1.77	0.13	0.08	0.20	1.25	0.22	0.10	1.52
	SEOM	1.06	0.08	0.05	0.20	0.89	0.26	0.12	2.24
F34-A10	EDS Quant	3.22	0.06	0.06	0.11	0.54	0.06	0.04	2.01
	SEOM	0.80	0.06	0.02	0.12	0.57	0.01	0.06	1.58
	SEOM	1.12	0.15	0.02	0.14	0.99	0.27	0.06	1.31

Table E.3: TEM EDS measurement on ROIs in FIB liftouts of T2-T6. Data reported in wt%.

Description	**ID**	**O**	**Na**	**Mg**	**Al**	**Si**	**K**	**Ca**	**Ti**	**Mn**	**Fe**
F11-T2											
Bulk	Area#2	38.620	0.830	0.540	3.750	15.770	1.430	0.780	0.090		37.690
L_{Si} in shell	Area#8	49.860	0.870	0.160	6.610	33.630	2.660	1.530	0.090	0.100	3.930
L_{Si} in shell	Area#9	48.400	1.260	0.200	6.640	34.010	3.120	1.660	0.070	0.110	4.060
L_{Si} in shell	Area#15	48.650	0.550	0.110	6.870	34.110	2.620	2.100	0.070	0.100	4.150
L_{Fe} Core	Area#13	31.860	0.570	0.700	2.020	4.840	0.540	0.280	0.070		58.590
L_{Si} Interm.	Area#14	41.660	0.870	0.440	4.930	22.470	1.920	1.210	0.100		25.810
L_{Fe} Shell	Area#16	36.810	0.830	0.620	3.010	11.660	1.130	0.490	0.090		44.910
Fe Oxide	Area#17	28.330	0.130	0.710	1.310	0.230	0.060	0.030	0.060		68.610
Fe Oxide	Area#18	28.540	0.440	0.780	1.380	0.500	0.030	0.250	0.110	0.060	67.300
Fe Oxide	Area#19	28.540	0.440	0.780	1.380	0.500	0.250	0.110	0.060		67.300
Fe Oxide	Area#20	29.470	0.520	0.760	1.410	0.930	0.370	0.100	0.060		65.750
Fe Oxide	Area#21	28.300	0.470	0.690	1.510	1.040	0.310	0.190	0.100		66.640
Fe Oxide	Area#22	33.070	0.540	1.160	1.220	0.470	0.270	0.040	0.110		62.180
Fe Oxide	Area#23	29.070	0.180	0.870	1.580	1.680	0.470	0.020	0.090		65.300
Fe Oxide	Area#24	34.310	0.450	0.990	1.130	0.190	0.060	0.080	0.080		62.170
Fe Oxide	Area#25	29.900	0.000	0.850	1.360	1.010	0.120	0.020	0.110		66.070
Fe Oxide	Area#26	30.430	0.270	0.800	1.380	0.610	0.090	0.080	0.080		65.670
Fe Oxide	Area#27	31.580	0.160	0.820	1.440	1.370	0.200	0.120	0.080		63.610
Fe Oxide	Area#28	33.150	0.770	0.870	1.440	1.560	0.330	0.070	0.060		61.210
Fe Oxide	Area#29	29.780	0.030	0.740	1.390	0.410	0.070	0.050	0.110		66.780
F11-T3											
Bulk	sp-6	20.450	0.560	0.790	2.860	12.840	1.790	1.430	0.130	1.600	57.530
L_{Si}	sp-4	32.400	0.530	0.560	6.680	38.300	4.500	4.380	0.170	0.270	11.870
L_{Si}	sp-5	35.040	0.750	0.590	6.340	35.760	4.180	3.770	0.010	0.280	13.000
L_{Si}	sp-6	32.740	0.400	0.610	6.940	38.460	4.620	5.090	0.200	0.240	10.420
L_{Si}	sp-7	33.240	0.930	0.470	6.570	37.560	4.980	4.820	0.190	0.250	10.850
L_{Si}	sp-8	33.520	0.520	0.540	6.480	37.190	4.670	4.460	0.160	0.240	11.920
L_{Si}	sp-19	32.440	0.840	0.680	6.930	36.590	4.750	4.320	0.180	0.240	13.020
L_{Si}	sp-20	32.440	0.870	0.610	6.540	34.570	4.670	4.140	0.170	0.280	15.700
L_{Si}	sp-21	31.160	0.840	0.660	6.010	32.300	4.590	4.160	0.150	0.340	19.780
L_{Si}	sp-22	34.390	0.970	0.700	6.420	33.220	4.080	3.470	0.150	0.290	16.280
L_{Si}	sp-23	31.660	0.790	0.640	7.050	36.170	4.790	4.790	0.190	0.260	13.640
L_{Si}	sp-24	32.700	0.860	0.580	6.760	35.750	4.790	4.280	0.170	0.250	13.850
L_{Fe}	sp-15	18.910	0.400	0.780	2.200	9.770	1.240	0.990	0.120	1.290	63.970
L_{Fe}	sp-30	18.520	0.240	0.440	1.880	9.020	1.250	0.810	0.120	1.840	65.870
F28-T4											
Bulk	sp-1	34.810	0.490	1.140	2.590	13.740	1.360	0.550	0.100	1.040	43.940
L_{Fe} 1	sp-2	29.360	0.000	0.720	0.800	4.010	0.430	0.180	0.130	1.380	62.710
L_{Fe} 2	sp-3	26.650	0.000	0.670	0.710	3.800	0.430	0.160	0.110	1.450	65.720
L_{Si}	sp-10	40.110	0.680	1.230	3.920	21.990	2.170	0.940	0.050	0.620	28.160
F28-T5											
Bulk	sp2	41.300	0.790	1.140	3.230	18.640	1.620	0.830	0.100	0.830	31.480
L_{Fe} 1	sp3	31.310	0.920	1.350	0.920	3.340	0.590	0.070	0.140	1.490	59.500
L_{Fe} 2	sp4	31.780	0.750	1.600	0.960	3.420	0.540	0.160	0.110	1.240	59.110
L_{Fe} 3	sp5	32.550	0.530	0.690	0.970	3.050	0.460	0.050	0.150	0.870	60.280
L_{Fe} 4	sp6	38.850	0.610	0.570	2.390	13.270	0.780	0.540	0.190	0.540	42.040
L_{Fe} 5	sp7	35.080	0.130	1.090	1.030	5.890	0.900	0.260	0.150	1.450	53.700

L_{Fe} 6	sp8	34.180	0.390	0.790	1.310	6.250	0.500	0.260	0.180	0.690	55.070
L_{Fe} 7	sp9	32.770	0.530	2.320	1.160	2.840	0.530	0.140	0.090	0.830	58.600
L_{Fe} 8	sp10	39.750	0.620	1.850	2.720	14.680	1.150	0.630	0.030	0.490	37.890
L_{Fe} 9	sp11	36.730	0.950	1.040	1.830	10.420	0.990	0.390	0.130	0.920	46.220
L_{Fe} 10	sp12	38.570	0.760	0.840	2.510	15.900	1.220	0.690	0.010	0.750	38.300
L_{Fe} 11	sp13	36.590	0.450	0.850	2.460	14.350	1.230	0.500	0.080	0.800	42.190
L_{Fe} 12	sp14	41.920	0.030	1.460	3.040	18.700	1.550	0.850	0.020	0.450	31.690
L_{Fe} 13	sp15	35.090	0.720	0.850	1.810	8.590	0.910	0.340	0.120	0.670	50.530
L_{Si} 1	sp16	49.830	0.900	0.140	4.660	33.050	3.240	1.720	0.050	0.120	5.960
L_{Si} 2	sp17	48.870	0.390	0.020	5.040	34.270	3.150	1.650	0.050	0.100	6.350
L_{Si} 3	sp18	50.960	0.410	0.070	4.840	33.160	2.660	1.660	0.070	0.110	5.700
L_{Si} 4	sp19	49.970	0.510	0.070	4.640	32.650	3.060	1.580	0.060	0.120	7.080
L_{Si} 5	sp20	48.990	1.360	0.670	5.050	31.140	2.730	1.330	0.060	0.150	8.440
F28-T6											
Bulk	sp1	43.360	0.000	0.310	1.730	17.890	1.260	0.440	0.000	0.870	34.020
L_{Fe} 1	sp6	35.480	0.040	1.870	1.110	4.740	0.520	0.150	0.030	0.770	55.190
L_{Fe} 2	sp7	34.980	0.000	2.240	1.000	2.270	0.340	0.120	0.020	0.750	58.140
L_{Fe} 3	sp8	35.260	0.000	2.070	1.350	4.680	0.380	0.140	0.020	0.770	55.220
L_{Fe} 4	sp9	39.110	0.520	1.990	2.210	10.660	0.740	0.260	0.030	0.620	43.740
L_{Fe} 5	sp10	35.090	0.030	2.070	1.040	2.840	0.370	0.080	0.030	0.740	57.630
L_{Fe} 6	sp11	34.990	0.160	2.010	0.840	2.350	0.510	0.060	0.040	0.830	58.120
L_{Fe} 7	sp12	36.070	0.000	2.080	0.890	2.480	0.580	0.100	0.090	0.800	56.820
L_{Fe} 8	sp13	35.800	0.510	1.740	0.720	3.820	0.660	0.070	0.090	0.820	55.430
L_{Fe} 9	sp14	38.890	0.390	1.690	1.420	10.200	0.430	0.180	0.020	0.690	45.920
L_{Fe} 10	sp15	43.370	0.860	1.590	2.230	16.810	1.910	0.390	0.100	0.500	32.100
L_{Fe} 11	sp16	39.790	0.730	1.950	1.670	11.390	1.670	0.330	0.050	0.600	41.540
L_{Fe} 12	sp17	40.930	0.020	1.340	1.670	12.810	0.610	0.260	0.090	0.630	41.450
L_{Fe} 13	sp18	42.460	0.550	1.560	2.610	17.670	0.940	0.430	0.080	0.510	33.030
L_{Fe} 14	sp19	41.210	0.770	1.780	1.940	13.760	1.940	0.230	0.090	0.550	37.520
L_{Fe} 15	sp20	45.990	0.040	0.680	2.420	22.290	0.670	0.510	0.070	0.410	26.770
L_{Si} 1	sp21	51.950	0.810	0.780	4.650	33.700	2.520	1.090	0.060	0.090	4.250
L_{Si} 2	sp22	52.930	0.430	0.700	4.330	34.720	1.560	1.000	0.080	0.070	4.150
L_{Si} 3	sp23	52.080	0.560	0.770	4.680	34.530	2.020	0.790	0.080	0.070	4.370

Table E.4: TEM EDS measurement uncertainties of ROIs in FIB liftouts of amoeboids T2-T6. Data reported in wt%.

ROI Name	**Analysis ID**	**O**	**Na**	**Mg**	**Al**	**Si**	**K**	**Ca**	**Ti**	**Mn**	**Fe**
F11-T2		**1-σ**	**1-σ**	**1-σ**	**1-σ**	**1-σ**	**1-σ**	**1-σ**	**1-σ**	**1-σ**	**1-σ**
Bulk	Area#2	1.916	0.019	0.007	0.052	0.563	0.016	0.005	0.000		2.111
L_{Si} in shell	Area#8	3.116	0.006	0.005	0.113	2.516	0.024	0.009	0.001	0.002	0.032
L_{Si} in shell	Area#9	2.836	0.013	0.006	0.130	2.585	0.041	0.008	0.001	0.003	0.034
L_{Si} in shell	Area#15	3.021	0.018	0.003	0.157	2.558	0.024	0.015	0.001	0.003	0.030
L_{Fe} Core	Area#13	1.501	0.012	0.004	0.026	0.049	0.009	0.001	0.001		5.384
L_{Si} Interm.	Area#14	2.129	0.018	0.004	0.085	1.128	0.028	0.004	0.000		1.007
L_{Fe} Shell	Area#16	1.907	0.024	0.002	0.036	0.316	0.010	0.001	0.000		3.054
Fe Oxide	Area#17	1.535	0.042	0.006	0.010	0.002	0.002	0.001	0.002		7.746
Fe Oxide	Area#18	1.553	0.019	0.013	0.035	0.007	0.002	0.002	0.002		6.804
Fe Oxide	Area#19	1.210	0.031	0.011	0.009	0.005	0.006	0.002	0.003		7.403
Fe Oxide	Area#20	1.232	0.012	0.006	0.016	0.019	0.004	0.001	0.002		6.950
Fe Oxide	Area#21	1.240	0.036	0.016	0.029	0.024	0.007	0.006	0.006		7.250
Fe Oxide	Area#22	1.776	0.068	0.021	0.022	0.016	0.015	0.008	0.011		6.317

Fe Oxide	Area#23	1.608	0.026	0.014	0.026	0.018	0.008	0.005	0.005		7.098
Fe Oxide	Area#24	1.705	0.014	0.007	0.010	0.004	0.003	0.001	0.002		6.248
Fe Oxide	Area#25	1.283	0.000	0.012	0.018	0.011	0.002	0.000	0.001		7.103
Fe Oxide	Area#26	1.308	0.015	0.006	0.012	0.005	0.001	0.001	0.001		6.974
Fe Oxide	Area#27	1.105	0.010	0.010	0.031	0.006	0.002	0.001	0.002		6.495
Fe Oxide	Area#28	1.727	0.014	0.023	0.021	0.024	0.005	0.001	0.001		5.962
Fe Oxide	Area#29	1.147	0.020	0.010	0.011	0.002	0.002	0.001	0.002		7.165
F11-T3											
Bulk	sp-6	0.346	0.002	0.005	0.025	0.408	0.013	0.004	0.000	0.018	5.189
L_{Si}	sp-4	1.358	0.023	0.002	0.105	3.083	0.068	0.043	0.001	0.010	0.223
L_{Si}	sp-5	1.500	0.022	0.001	0.113	2.714	0.043	0.027	0.001	0.010	0.289
L_{Si}	sp-6	1.457	0.011	0.004	0.135	3.100	0.058	0.046	0.001	0.005	0.202
L_{Si}	sp-7	1.256	0.020	0.002	0.111	3.136	0.089	0.042	0.001	0.005	0.206
L_{Si}	sp-8	1.381	0.007	0.004	0.127	3.024	0.078	0.043	0.001	0.013	0.225
L_{Si}	sp-19	1.051	0.004	0.004	0.103	2.956	0.074	0.055	0.002	0.011	0.305
L_{Si}	sp-20	0.986	0.006	0.003	0.149	2.541	0.063	0.034	0.002	0.014	0.397
L_{Si}	sp-21	0.969	0.011	0.010	0.108	2.416	0.063	0.036	0.002	0.020	0.609
L_{Si}	sp-22	0.984	0.011	0.005	0.129	2.296	0.044	0.026	0.001	0.017	0.417
L_{Si}	sp-23	0.871	0.015	0.003	0.124	3.031	0.073	0.049	0.001	0.009	0.291
L_{Si}	sp-24	1.033	0.004	0.004	0.117	2.924	0.057	0.037	0.002	0.013	0.330
L_{Fe}	sp-15	0.613	0.007	0.001	0.011	0.229	0.006	0.004	0.000	0.028	6.531
L_{Fe}	sp-30	0.370	0.010	0.001	0.021	0.220	0.011	0.001	0.000	0.014	7.015
F28-T4											
Bulk	sp-1	2.400	0.110	0.240	0.540	2.800	0.260	0.080	0.020	0.150	6.510
L_{Fe} 1	sp-2	2.630	0.010	0.160	0.170	0.850	0.080	0.030	0.020	0.220	9.880
L_{Fe} 2	sp-3	2.460	0.010	0.140	0.150	0.810	0.080	0.020	0.020	0.230	10.490
L_{Si}	sp-10	2.490	0.140	0.250	0.810	4.430	0.400	0.140	0.010	0.090	4.090
F28-T5											
Bulk	sp2	2.500	0.170	0.230	0.660	3.740	0.300	0.120	0.020	0.120	4.550
L_{Fe} 1	sp3	2.600	0.200	0.290	0.200	0.700	0.110	0.010	0.020	0.230	9.230
L_{Fe} 2	sp4	2.670	0.170	0.340	0.200	0.710	0.100	0.020	0.020	0.200	9.160
L_{Fe} 3	sp5	2.770	0.120	0.150	0.210	0.640	0.090	0.010	0.020	0.150	9.390
L_{Fe} 4	sp6	2.530	0.130	0.120	0.490	2.680	0.150	0.080	0.030	0.090	6.170
L_{Fe} 5	sp7	2.750	0.040	0.230	0.220	1.210	0.170	0.040	0.020	0.220	8.150
L_{Fe} 6	sp8	2.700	0.080	0.170	0.280	1.300	0.100	0.040	0.030	0.120	8.400
L_{Fe} 7	sp9	2.690	0.120	0.500	0.250	0.590	0.100	0.020	0.010	0.130	9.060
L_{Fe} 8	sp10	2.590	0.130	0.380	0.560	2.960	0.210	0.090	0.010	0.080	5.520
L_{Fe} 9	sp11	2.470	0.200	0.220	0.380	2.120	0.190	0.060	0.020	0.140	6.850
L_{Fe} 10	sp12	2.450	0.160	0.170	0.520	3.210	0.230	0.100	0.000	0.110	5.590
L_{Fe} 11	sp13	2.550	0.100	0.180	0.510	2.910	0.230	0.070	0.010	0.120	6.220
L_{Fe} 12	sp14	2.740	0.030	0.300	0.630	3.760	0.290	0.120	0.000	0.070	4.590
L_{Fe} 13	sp15	2.480	0.150	0.180	0.380	1.770	0.170	0.050	0.020	0.120	7.580
L_{Si} 1	sp16	3.600	0.190	0.030	0.980	6.730	0.610	0.260	0.010	0.020	0.890
L_{Si} 2	sp17	3.520	0.090	0.000	1.050	7.000	0.600	0.250	0.010	0.020	0.950
L_{Si} 3	sp18	3.540	0.090	0.020	1.010	6.750	0.500	0.250	0.010	0.020	0.850
L_{Si} 4	sp19	3.440	0.120	0.020	0.970	6.640	0.580	0.230	0.010	0.020	1.050
L_{Si} 5	sp20	3.240	0.300	0.140	1.050	6.320	0.510	0.200	0.010	0.020	1.240
F28-T6											
Bulk	sp1	2.480	0.000	0.070	0.360	3.600	0.230	0.060	0.000	0.130	4.920
L_{Fe} 1	sp6	2.640	0.020	0.400	0.230	0.980	0.100	0.020	0.000	0.120	8.410

L_{Fe} 2	sp7	2.720	0.010	0.480	0.210	0.470	0.060	0.020	0.000	0.120	8.950
L_{Fe} 3	sp8	2.620	0.020	0.440	0.280	0.970	0.070	0.020	0.000	0.120	8.410
L_{Fe} 4	sp9	2.430	0.110	0.410	0.460	2.160	0.140	0.040	0.000	0.100	6.420
L_{Fe} 5	sp10	2.740	0.020	0.440	0.220	0.590	0.070	0.010	0.010	0.120	8.860
L_{Fe} 6	sp11	2.720	0.040	0.430	0.180	0.490	0.100	0.010	0.010	0.130	8.950
L_{Fe} 7	sp12	2.740	0.010	0.440	0.190	0.510	0.110	0.020	0.010	0.130	8.700
L_{Fe} 8	sp13	2.700	0.110	0.370	0.150	0.790	0.130	0.010	0.010	0.130	8.450
L_{Fe} 9	sp14	2.540	0.080	0.350	0.290	2.070	0.080	0.030	0.000	0.100	6.790
L_{Fe} 10	sp15	2.360	0.180	0.330	0.460	3.360	0.350	0.060	0.010	0.080	4.610
L_{Fe} 11	sp16	2.410	0.150	0.400	0.340	2.300	0.310	0.050	0.010	0.090	6.060
L_{Fe} 12	sp17	2.520	0.020	0.280	0.350	2.580	0.110	0.040	0.010	0.100	6.060
L_{Fe} 13	sp18	2.410	0.110	0.320	0.540	3.550	0.170	0.060	0.010	0.080	4.770
L_{Fe} 14	sp19	2.370	0.160	0.370	0.400	2.770	0.360	0.030	0.010	0.080	5.430
L_{Fe} 15	sp20	2.580	0.010	0.140	0.500	4.470	0.120	0.070	0.010	0.060	3.860
L_{Si} 1	sp21	3.440	0.170	0.160	0.970	6.860	0.470	0.160	0.010	0.010	0.630
L_{Si} 2	sp22	3.650	0.090	0.150	0.900	7.090	0.290	0.150	0.010	0.010	0.620
L_{Si} 3	sp23	3.550	0.120	0.160	0.980	7.050	0.380	0.120	0.010	0.010	0.650

Appendix F

NanoSIMS Dataset

A subset of collected NanoSIMS data that was used for this work is displayed in Table F.1. The uncertainty in ^{239}Pu quantification represents measurement uncertainty and does not include uncertainty in the matrix effect of the RSF due to matrix mismatch.

NanoSIMS data - ^{239}Pu quantification uncertainty is measurement unccertainty only and does not include uncertainty in the matrix effect of the RSF due to matrix mismatch

Table F.1: NanoSIMS data - ^{239}Pu quantification uncertainty is measurement uncertainty only and does not include uncertainty in the matrix effect of the RSF due to matrix mismatch

Non-Immiscible Glass	^{30}Si cps	^{54}Fe cps	^{63}Cu cps	^{239}Pu cps	^{42}Ca cps	^{239}Pu/^{42}Ca	1-σ	^{239}Pu ppm	1-σ
F27 R1	ND	130444	235	22.8	14270	0.00160	0.00001	3.37	0.14
F27 R2	ND	250234	469	41.2	10871	0.00379	0.00004	6.20	0.28
F27 R3	ND	552097	1376	55.9	15522	0.00360	0.00005	7.73	0.35
F27 R4	ND	587246	1485	65.7	17880	0.00367	0.00005	9.93	0.44
F27 R5	ND	594416	1534	58.0	19891	0.00292	0.00004	6.71	0.33
F27 R6	ND	349832	876	34.8	10139	0.00343	0.00006	7.89	0.38
F29-R7	ND	255973	414	20.7	25948	0.00080	0.00002	3.39	0.19
IM-1									
F27 In Situ Immiscibility	405422.3	607451	1540	87.5	11615	0.00753	0.00014	10.38	0.54
F27 In Situ L_{Fe}	397426.2	703862	2071	69.6	10329	0.00673	0.00009	6.37	1.51
F27 In Situ L_{Si}	412477.9	522382	1072	103.2	12751	0.00810	0.00017	12.71	1.15
F27 Ex Situ Immiscibility	252028.9	587786	1639	179.5	7286	0.02461	0.00045	19.60	1.53
IM-2									
F29 In Situ Immiscibility	166717.2	442500.9	381.25	0.178773	1735.906	0.000103	0.000005	–	–
F29 In Situ L_{Fe}	154412.1	475679.1	346.2266	0.185482	1480.787	0.000125	0.000009	–	–
F29 IN Situ L_{Si}	184737.2	426315	435.2432	0.178688	2084.359	0.00009	0.000007	–	–
IM-3									
F29 In Situ Immiscibility	83533.81	145758.1	81.72797	0.035928	838.5355	0.00004	0.000009	–	–
F29 In Situ L_{Fe}	71584.11	189578.4	80.89189	0.048649	735.3135	0.00007	0.000016	–	–
F29 IN Situ L_{Si}	104146.3	70170.63	83.17017	0.013986	1016.587	0.00001	0.000008	–	–
IM-4									
F34 Ex Situ Cycles 3-7	ND	506084.2	1613.677	41.67806	9773.062	0.004238	0.000265	1.970972	0.211955
F34 Ex Situ Cycles 8-12	ND	529824.3	1736.243	46.36335	10447.06	0.004443	0.000121	2.065919	0.18948
F34 Ex Situ Cycles 13-17	ND	553603.6	1916.471	40.86835	10340.55	0.003932	0.000105	1.828419	0.167398
F34 Ex Situ Cycles 18-22	ND	544782.9	2068.222	37.93039	10056.99	0.003744	0.000149	1.741106	0.167538
F34 Ex Situ Cycles 23-27	ND	550236.7	2501.57	28.88081	9997.645	0.002836	0.000265	1.318659	0.168775
UPI Reference Glass									
UPI_9 box	266089.6	3119.5	47.0	338.7	102795.0	0.0033	0.00001	47.2	1
UPI_8 box	263205.6	3090.2	46.2	311.6	99388.4	0.0031	0.00001	47.2	1
UPI_6 box	248597.7	2945.0	41.6	303.1	92074.0	0.0033	0.00001	47.2	1
UPI_5@1_1 box	200315.2	1846.5	6637.7	212.6	53590.8	0.0040	0.00002	47.2	1
UPI_5@1_2 box	213238.2	2342.1	12037.6	236.4	72095.2	0.0033	0.00004	47.2	1
UPI_5@1_3 box	229826.4	2532.2	13355.9	258.9	78970.4	0.0033	0.00003	47.2	1
UPI_5@1_4 box	240814.4	2811.7	15554.4	277.4	88422.8	0.0031	0.00002	47.2	1
UPI_5@1_5 box	243176.5	2837.1	15968.0	280.9	89469.1	0.0031	0.00002	47.2	1
UPI_5@1_6 box	249705.0	2927.6	16734.5	289.1	92024.6	0.0031	0.00003	47.2	1
UPI_5@1_7 box	245961.0	2875.0	16184.1	285.5	90354.5	0.0032	0.00002	47.2	1
UPI_5@1_8 box	242257.0	2893.7	16373.9	284.7	91366.8	0.0031	0.00003	47.2	1

Table F.2: SEM EDS data for NanoSIMS regions (wt %)

EDS Data for NanoSIMS Regions in Wt%																			
Non-Immiscible Regions	**O**	**1-σ**	**Na**	**1-σ**	**Mg**	**1-σ**	**Al**	**1-σ**	**Si**	**1-σ**	**K**	**1-σ**	**Ca**	**1-σ**	**Ti**	**1-σ**	**Fe**	**1-σ**	**Sum**
F27 R1	45.92	5.19	1.36	0.11	0.93	0.08	8.66	0.44	29.63	1.29	3.12	0.12	1.67	0.08	0.27	0.04	4.92	0.16	96.49
F27 R2	45.37	5.14	1.14	0.10	0.85	0.07	6.09	0.32	30.40	1.32	2.67	0.11	1.30	0.07	0.29	0.04	8.12	0.25	96.24
F27 R3	41.79	4.72	1.16	0.10	1.00	0.08	6.31	0.33	23.35	1.02	1.83	0.08	1.70	0.08	0.24	0.03	19.10	0.53	96.48
F27 R4	40.62	4.60	1.14	0.10	1.05	0.09	7.24	0.37	21.33	0.93	1.79	0.08	2.15	0.09	0.25	0.03	19.37	0.54	94.94
F27 R5	38.94	4.41	0.90	0.09	1.10	0.09	8.59	0.44	17.83	0.79	1.48	0.07	2.50	0.10	0.30	0.04	22.04	0.61	93.79
F27 R6	37.60	4.24	1.17	0.10	0.88	0.08	6.15	0.32	18.19	0.80	2.09	0.09	1.83	0.08	0.18	0.03	23.83	0.66	91.91
F29 A3	45.10	5.09	1.55	0.13	1.54	0.11	9.11	0.46	25.90	1.13	2.37	0.10	3.37	0.13	0.29	0.04	10.13	0.30	99.49
UPI Standard	44.84	0.43	0.05	0.01	4.27	0.08	7.15	0.22	26.10	0.35	5.53	0.21	11.74	0.13	0.05	0.04	0.21	0.04	99.95
Immiscible Regions	O	1-σ	Na	1-σ	Mg	1-σ	Al	1-σ	Si	1-σ	K	1-σ	Ca		Ti	1-σ	Fe	1-σ	SUM
F27 In Situ Immiscibility Region	35.95	3.66	0.73	0.07	0.47	0.05	3.70	0.20	17.50	0.77	1.48	0.07	1.10	0.06	0.12	0.03	29.52	0.81	91.05
F27 Ex Situ Immiscibility Region	30.31	3.36	0.68	0.07	0.24	0.04	2.15	0.13	9.43	0.43	1.13	0.06	0.65	0.05	0.15	0.03	43.43	1.18	89.74
F27 L_{Fe} **and** L_{Si}	O	1-σ	Na	1-σ	Mg	1-σ	Al	1-σ	Si	1-σ	K	1-σ	Ca	1-σ	Ti	1-σ	Fe	1-σ	SUM
F27 L_{Fe} 2294	32.90	3.71	0.79	0.08	0.68	0.07	3.10	0.18	12.55	0.56	1.06	0.06	0.54	0.04	0.12	0.03	38.22	1.04	89.96
F27 L_{Fe} 2295	33.49	3.76	0.73	0.08	0.59	0.06	3.20	0.18	13.50	0.60	1.18	0.06	0.72	0.05	0.13	0.03	36.68	1.00	90.22
F27 L_{Fe} 2296	33.21	3.74	0.79	0.08	0.56	0.06	3.03	0.17	13.10	0.58	1.10	0.06	0.52	0.04	0.13	0.03	37.76	1.03	90.20
F27 L_{Fe} 2297	35.50	4.00	0.70	0.07	0.55	0.06	3.54	0.20	16.98	0.75	1.29	0.07	1.01	0.06	0.11	0.03	30.55	0.84	90.23
F27 L_{Fe} 2298	35.73	4.02	0.70	0.08	0.64	0.06	3.48	0.19	16.06	0.71	1.22	0.06	0.81	0.05	0.11	0.03	34.07	0.93	92.82
F27 L_{Fe} 2299	32.69	3.68	0.55	0.07	0.49	0.06	3.60	0.20	17.16	0.76	1.30	0.07	0.96	0.06	NM	NM	31.51	0.86	88.26
F27 L_{Fe} 2300	35.88	4.02	0.77	0.08	0.74	0.07	3.61	0.20	15.50	0.69	1.19	0.06	0.70	0.05	0.13	0.03	35.71	0.97	94.22
Average F27 L_{Fe}	**34.20**	**1.33**	**0.72**	**0.08**	**0.61**	**0.08**	**3.37**	**0.23**	**14.98**	**1.77**	**1.19**	**0.08**	**0.75**	**0.18**	**0.12**	**0.01**	**34.93**	**2.78**	
F27 L_{Si} 2289	37.22	4.21	0.68	0.07	0.50	0.06	4.12	0.22	19.86	0.87	1.49	0.07	1.20	0.06	0.14	0.03	24.83	0.69	90.04
F27 L_{Si} 2290	35.34	3.98	0.77	0.08	0.51	0.06	4.01	0.22	18.76	0.83	1.41	0.07	1.29	0.07	0.18	0.03	23.19	0.64	85.46
F27 L_{Si} 2291	37.51	4.23	0.47	0.06	0.49	0.05	4.17	0.23	20.53	0.90	1.40	0.07	1.33	0.07	0.15	0.03	23.57	0.65	89.63
F27 L_{Si} 2292	36.83	4.16	0.64	0.07	0.43	0.05	3.99	0.22	20.04	0.88	1.49	0.07	1.34	0.07	0.16	0.03	23.57	0.65	88.49
F27 L_{Si} 2293	37.38	4.20	0.89	0.09	0.49	0.05	4.07	0.22	19.63	0.86	1.51	0.07	1.07	0.06	0.15	0.03	25.99	0.72	91.17
Average F27 L_{Si}	**36.86**	**0.79**	**0.69**	**0.14**	**0.48**	**0.03**	**4.07**	**0.07**	**19.76**	**0.58**	**1.46**	**0.04**	**1.25**	**0.10**	**0.16**	**0.01**	**24.23**	**1.04**	
F29 L_{Fe} **and** L_{Si}	O	1-σ	Na	1-σ	Mg	1-σ	Al	1-σ	Si	1-σ	K	1-σ	Ca	1-σ	Ti	1-σ	Fe	1-σ	SUM
F29 L_{Fe} 2330	31.88	3.58	0.68	0.07	0.56	0.06	2.32	0.14	9.50	0.43	0.57	0.04	0.50	0.04	1.97	0.08	43.13	1.17	92.09
F29 L_{Fe} 2331	31.61	3.55	0.67	0.07	0.51	0.06	2.43	0.14	9.76	0.44	0.62	0.05	0.37	0.04	1.96	0.08	41.71	1.13	90.49
F29 L_{Fe} 2332	32.54	3.66	0.75	0.08	0.52	0.06	2.81	0.16	11.06	0.50	0.92	0.05	0.32	0.04	1.86	0.08	39.37	1.07	90.97
F29 L_{Fe} 2333	32.60	3.67	0.63	0.07	0.39	0.05	2.69	0.16	11.28	0.51	1.07	0.06	0.43	0.04	1.90	0.08	39.25	1.07	91.00
Average F29 L_{Fe}	**32.16**	**0.42**	**0.68**	**0.04**	**0.50**	**0.06**	**2.56**	**0.20**	**10.40**	**0.78**	**0.79**	**0.21**	**0.41**	**0.07**	**1.92**	**0.05**	**40.86**	**1.64**	
F29 L_{Si} 2336	37.32	4.21	1.63	0.13	0.16	0.04	4.86	0.26	18.90	0.83	1.85	0.08	0.82	0.05	1.06	0.06	24.06	0.67	91.32
F29 L_{Si} 2337	36.26	4.07	1.74	0.14	0.27	0.04	4.56	0.24	17.13	0.76	1.70	0.08	0.57	0.04	1.20	0.06	27.05	0.74	91.14
F29 L_{Si} 2334	29.81	3.37	1.18	0.11	0.29	0.04	4.59	0.25	17.57	0.77	1.70	0.08	0.50	0.04	1.38	0.07	28.36	0.78	86.10
F29 L_{Si} 2335	37.00	4.18	1.22	0.11	0.28	0.04	4.69	0.25	17.71	0.78	1.74	0.08	0.55	0.04	1.30	0.06	27.21	0.75	92.44
Average F29 L_{Si}	**35.10**	**3.08**	**1.44**	**0.24**	**0.25**	**0.05**	**4.67**	**0.12**	**17.83**	**0.65**	**1.75**	**0.06**	**0.61**	**0.12**	**1.24**	**0.12**	**26.67**	**1.59**	